Disordered systems under cyclic shear deformation and supercooled liquids at low temperatures

A Thesis

Submitted to the
Jawaharlal Nehru Center for Advanced Scientific Research, Bengaluru
for the Degree of Doctor of Philosophy

by

Pallabi Das

Jawaharlal Nehru Center for Advanced Scientific Research, Bengaluru,India.

SEPTEMBER 2022

I dedicate this thesis to my parents

DECLARATION

I hereby declare that the matter embodied in the thesis entitled "**Disordered systems under cyclic shear deformation and supercooled liquids at low temperatures**" is the result of investigations carried out by me at the, Theoretical Science Unit, Jawaharlal Nehru Centre for Advanced Scientific Research, Bangalore, India under the supervision of Prof. Srikanth Sastry and that it has not been submitted elsewhere for the award of any degree or diploma.

In keeping with the general practice in reporting scientific observations, due acknowledgement has been made whenever the work described is based on the findings of other investigators.

Pallabi Das

Pallabi Das

CERTIFICATE

I hereby certify that the matter embodied in this thesis entitled "**Disordered systems under cyclic shear deformation and supercooled liquids at low temperatures**" has been carried out by Ms.. Pallabi Das at the Theoretical Science Unit, Jawaharlal Nehru Centre for Advanced Scientific Research, Bangalore, India under my supervision and that it has not been submitted elsewhere for the award of any degree or diploma.

Prof. Srikanth Sastry
(Research Supervisor)

Acknowledgements

First and foremost, I thank my advisor, Prof. Srikanth Sastry. I thank him for giving me the opportunity to have this scientific journey. His passion for science and the way of doing science has inspired me throughout. I consider myself lucky that I have been his student.

I want to thank all my lab members who have been an integral part of this journey. I thank my seniors Vinutha and Anshul for their unconditional help. I thank my batchmate Yagyik and my immediate senior Monoj for not only being helpful lab members but also being very supportive friends. I thank Himangsu, Rajneesh, Arun, Sebastiano, Dheeraj, Varghese, Pushkar, Shiva, Krishna, Debarghya, Swarnendu, Aravind, Sourav, Saptarshi, Saheli. All my lab members have made these past years of my life a great learning experience and a fun ride.

I thank my course instructors and faculty members of TSU, Prof. Srikanth Sastry, Prof. Subir K Das, Prof. Umesh Waghmare, Prof. Shobhana Narasimhan, Prof. Swapan K Pati, Prof. Kavita Jain, Prof. N.S. Vidhyadhiraja, Prof. Meher K Prakash. I would specially like to thank my GSAC members, Prof. Shobhana Narasimhan and Prof. Subir K Das.

I thank my institute, JNCASR, for providing all the facilities CCMS, NSM, complab, admin, academic office, and Dhanwantari. I thank all the staff in JNCASR who have made our stay at the campus easy going and pleasant.

I thank Mini Bose, Thakurprasad Bhattacharya, Prof. Muktish Acharaya, Prof. Brijesh Kumar, and all the great teachers I have come across who have inspired me in various ways. I thank my school Holy Child, my college Presidency, and my university JNU, for instilling the motivation to do great things in life.

I thank my friends Bankim, Nilotpal, Riya, Richa, Augniva, Rohit, Anirban, Meghna, Ananya, Neha, Moumita, Anushka, Jayeta, Payel for always supporting me.

Finally, I thank all my family members for everything. I thank my parents for their unconditional support and faith in me. And I thank my husband, Shubhajit, for being there no matter what.

Synopsis

This is a summary of the work done under the title "**Disordered systems under cyclic shear deformation and relaxation of supercooled liquids at low temperatures**" by Pallabi Das.

The central theme of the thesis is the study of disordered systems under oscillatory shear deformation. Two kinds of systems, namely, athermal systems and thermal glassy systems, are studied. In the study of athermal systems, the amplitude of deformation and the density of the system are the control parameters. The exploration of a wide range of deformation amplitude and density leads to a rich phase diagram that reveals interesting similarities between various transitions observed at different density regimes. In the case of thermal glassy systems, the periodic mechanical perturbation in the presence of thermal fluctuation leads the system to access low energy states when driven with optimal amplitude and rate. At the very low temperature regime, where the system falls out of equilibrium, it ages faster in the presence of a mechanical drive. The last part of the thesis focuses on the study of a dynamical crossover in a supercooled liquid at substantially low temperatures and associated phenomena of dynamical heterogeneity and thermodynamics.

The response of disordered systems under externally imposed drive is of interest in various contexts. For a wide range of systems like low-density colloidal suspensions, dense glassy systems, or athermal granular systems, the applied deformation causes diverse phenomena like self-organization, transitions from reversible to irreversible behaviour, or macroscopic changes like yielding or failure of the system. But what specific phenomenon will occur depends on the extent of the deformation applied. The study of an athermal system under oscillatory shear deformation is performed for a range of densities, where the system at limiting densities shows very different behaviours (such as the behaviour of low-density colloids or high-density glasses). An attempt is made to establish a unified picture by constructing a phase diagram in the

amplitude-density plane by identifying the key underlying similarities of the different transitions in these different density regimes.

Cyclic deformation is of importance, specifically in the context of glass-forming liquids in terms of relaxation, as one finds that an optimal choice of the amplitude of deformation leads the glassy systems to access lower energy states. At substantially low temperatures where the glassy system enters an aging regime, the incorporation of periodic mechanical deformation is found to enhance the aging process. However, at a temperature regime where the system can still be equilibrated by thermal fluctuations alone, the inclusion of mechanical deformation does not lead to faster sampling. The study of glassy systems at such supercooled regimes but at substantially low temperatures concurrently reveals a crossover in dynamics that indicates a faster relaxation. The dynamical crossover in that glass-forming liquid and associated aspects of dynamical heterogeneity is studied. The study of the thermodynamics across the crossover temperature shows no indication of the change that can accompany the dynamic crossover. Furthermore, a careful estimate of the entropy is carried out to investigate whether the well-known Adam-Gibbs relation, which relates thermodynamics to dynamics, remains valid at low temperatures. Our results show that the Adam-Gibbs relation continues to hold across the crossover temperature when the vibrational entropy is calculated with anharmonic corrections.

The work in the thesis is organised in the following chapters:

Chapter 1

In this chapter, the relevance of the problems addressed in the thesis is discussed. It contains an overview of important transitions like the glass transition and the jamming transition in disordered systems. A discussion of different non-equilibrium transitions that occur under the application of external mechanical drive, emphasizing the effect of periodic driving, is provided. With this background, the importance of cyclic shear deformation in the context of exploring low energy minima in the glassy landscape is discussed. Recently it has been found that a range of well known fragile glass-forming liquids at such very low temperatures shows a change in the nature of relaxation. In this regard, the study of the low-temperature glassy dynamics and its resemblance to well known fragile to strong transition is discussed.

Chapter 2:

This chapter describes the model systems that are used to simulate granular and glassy systems. Further, it describes the simulation methods and the corresponding description of the analysis of the problems addressed in the thesis.

Chapter 3:

This chapter discusses the reversible-irreversible transition below, close to, and above

the jamming density ϕ_J. Different phases across the isotropic jamming density is characterized by studying different microscopic quantities like the mean squared displacement, percentage of new collisions, non-affine path length, stress, potential energy, and contact numbers. It is found that the reversible-irreversible transition corresponds to the yielding transition for high density jammed packings. The presence of an unjamming region close to but above the isotropic jamming density (ϕ_J) is found. A cyclic shear jamming density (ϕ_J^{cyc}) is identified, above which the soft sphere packings behave like an amorphous solid. Below ϕ_J, two different forms of reversible phases are present, namely, point and loop reversible. Quantities like non-affine path length and the percentage of new collisions clearly distinguish reversible and irreversible phases for the whole range of densities. The transition to irreversibility is always characterised by the onset of diffusive behaviour of the particles at all densities. All transitions are characterised by discontinuous changes in relevant quantities.

Chapter 4:

The study of yielding transition in glassy systems under oscillatory deformation has shown previously that the system shows maximum annealing when the driving amplitude is close to the yielding amplitude. This chapter discusses our findings from exploring the possibility of generating low energy configurations by employing cyclic shear deformation with the optimal combination of temperature, amplitude of deformation, and strain rate. The generated low energy structures are found to be free from anisotropy, and their other properties guarantee that generated structures are equilibrium-like. However, within the temperature regime where the system can be equilibrated by thermal fluctuations alone, the incorporation of a mechanical drive does not offer a faster sampling.

Chapter 5:

This chapter discusses the phenomena of 'overaging' in glassy systems under the application of oscillatory deformation. At comparatively higher temperatures where the system can be equilibrated by equilibrium thermal fluctuations, mechanical perturbation in the form of oscillatory deformation does not lead to accelerated sampling. But at significantly lower temperatures, where the system enters the aging regime, annealing arising from mechanical perturbation becomes more significant than thermal fluctuation. The mechanical drive helps the system access lower energies faster; in other words, it helps the system to overage or age faster.

Chapter 6:

This chapter involves the study of supercooled liquid at low temperatures. Glass-forming liquids are broadly classified as fragile and strong glass-forming liquids, which show non-Arrhenius and Arrhenius temperature dependence of dynamics, respectively, as the glass transition temperature is approached. In anomalous liquids like

water or silica, a fragile to strong crossover is observed at lower temperatures. Though most metallic glass-formers show fragile behaviour for a wide range of temperatures, it has recently been found that even metallic glass-forming liquids show a crossover in dynamics when really low temperatures are accessed. This chapter describes the study of the Kob-Andersen model for a wide range of temperatures extending up to really low temperatures below the mode coupling temperature (T_{MCT}). Signatures of a possible dynamical crossover below T_{MCT} are found that are consistent with recent findings in different metallic glass formers. Unlike the conventional fragile to strong transition in anomalous liquids, no accompanying thermodynamic changes are found across the crossover temperature. Interestingly the Adam-Gibbs relation describing the relation between relaxation times and configurational entropy holds well below the dynamical crossover temperature when anharmonic corrections to the vibrational entropy are included.

Chapter 7:

The key findings of the work of the thesis are summarized in this chapter. The implications of the results and possible future directions are briefly discussed.

Contents

List of Figures

Chapter 1

Introduction

It would hardly be an overstatement to claim that disordered materials are present everywhere. Commonplace, mundane objects like toothpaste, hair gel, mayonnaise, a bowl full of grains or a heap of sand are all disordered materials. Engineered materials like silicon panels in solar cells, the tempered glass on our phone screens, tyres of cars, amorphous solid dispersions in drug delivery technology are also disordered materials. Even exotic natural examples such as volcanic glass, the granular fault gouge in geological faults, embryonic tissue - all belong to the fascinating world of disordered systems. As the name suggests, disordered materials lack any long-range order. These disordered systems are structurally liquid-like, but they can display both solid-like or liquid-like mechanical behaviour. We encounter such examples in our daily lives as well. Traffic jams are a common occurrence in our daily life. This cessation of vehicular movement can be perceived as a flowing liquid system undergoing a transition to a solid-like state. Another prominent example is the beautiful work of glassblowers subjecting glass-forming materials to heating and cooling cycles. The system alternates between a flowing and an arrested state until the final rigid shape of the material has been acquired. Such prominent changes in mechanical behaviour are generally not accompanied by an easily discernible change in the structure. A key question that arises in both the examples of a traffic jam or glassy material is the nature of the onset of rigidity or dynamical arrest. Such puzzles are central themes in the study of disordered materials. The glass transition and the jamming transition have been investigated extensively in the context of the emergence of solid-like behaviour in disordered systems. Conversely, glassy systems and jammed systems can be perturbed to bring them to a liquid-like state. Melting the glass or shaking the container of rice to pour it into the bowl are such instances. In the case of glasses, whether the glassy material will melt or stay rigid depends on the ambient temperature. Whether there will be a complete halt on the highway will depend on the number of vehicles traveling on that highway. Grains will often get stuck at the neck of the jar as we try to pour it out. One

often needs to give it a shake for it to come unstuck. All these transitions in different disordered systems depend on the control parameters like temperature, density, or amplitude of applied force and so on. In this chapter, we will introduce the basic concepts of these systems and the transitions observed in them. Along with that, we will give an overview of the problems that we set out to study in the thesis.

1.1 Glass transition

Glasses are everywhere around us. They are of different kinds, and they have a wide range of applications ranging from everyday mundane objects to exotic and precise instruments. The use of glasses in human civilization dates back to as old as the Roman times when they were heavily used for architectural purposes. Till today, the most commonplace example of glass is the window glasses of our house, made of silica (SiO_2). Glasses have solid-like mechanical properties, but interestingly, their structure is liquid-like. They do not suffer from scattering from grain boundaries. Therefore glasses are preferred over crystalline materials to be used as optical fibers [1] for high capacity, cost-effective long-distance communication. All the touch-sensitive screens of our smartphones are made of glasses. Thus, various application of glasses has revolutionized our modern world of communication. Metallic glasses have long been used as transformer cores because they exhibit low-loss power transmission [2]. Organic glasses are used in making organic light-emitting diodes [3]. Glass sheets are used in solar panels, and glass fibers are used in wind turbines [4]. Nonallergenic biocompatible glasses are used in healthcare systems. Bioactive glasses [5] are a group of reactive materials that bond to bone tissue and are hence extensively used in the process of tissue regeneration in the field of biomedical area. Glasses are heavily used in space applications (i.e., lenses of space telescopes) for their extraordinary thermal stability and resistance, which guarantees the precision and reliability of the instruments in extreme atmospheric conditions. Finally, in recent times, when conservation of the environment is one of the most concerning issues, glassy materials are highly relevant as they are one of the most recyclable materials. In this way, extensive applications of glasses have made them an important topic of research. In the next sections we will discuss some of the most important concepts that are fundamental to the understanding of glassy systems.

1.1.1 Preliminaries

The hallmark of the glass transition is the slowdown in the dynamics of the material without pronounced structural changes. In the words of pioneering scientist Austin Angell [6]“Glass, in the popular and basically correct conception, is a liquid that has

lost its ability to flow". Even though there are many ways through which the glassy state can be reached, glasses are typically prepared by cooling a liquid below its melting temperature (supercooling) at a fast enough rate as to avoid crystallization. When a liquid is cooled below its melting temperature, crystallization occurs through a first-order phase transition. Crystallization initiates through the formation of nucleii of the bulk crystalline phase through rare thermal fluctuations. The system crystallizes when the nucleus attains a critical size, crossing the relevant free energy barrier over an associated timescale, $\tau_{nucleation}$. This nucleation time shows a non-monotonic temperature dependence arising from the competition between the mobility of particles in the supercooled liquid phase and the height of the free energy barrier. All physical systems have their characteristic relaxation time (τ_{relax}), which is the time taken for the system to reach equilibrium (no memory of initial state). Liquids have a characteristic relaxation time at each temperature that increases monotonically with decreasing temperature. The nucleation time, $\tau_{nucleation}$, is infinite at the melting temperature and decreases as temperature decreases. The non-monotonic temperature dependence of the nucleation time, (see Fig.1.1(a)) as well as the dependence of $\tau_{nucleation}$ on the dynamics in the liquid, has been understood to result in a situation where the nucleation time is always larger than the relaxation time. Thus, at lower temperatures, when these timescales are comparable, avoiding nucleation becomes a challenge, and a fast cooling rate becomes essential in preparing a glass. To give an idea of how fast a system should be cooled to avoid crystallization, we can mention that the standard laboratory cooling rate is 1 K/min [7]. As the system is cooled down further, satisfying the aforementioned criteria, at some temperature, the dynamics of the system in a practical sense stops, or it becomes impossible to relax the system within a physical time scale. The system falling out of equilibrium is called the laboratory glass transition, and the temperature at which it occurs is called the experimental glass transition temperature T_g. To get an idea of what is meant by the arrest of dynamics, one can compare the relaxation times in three regimes, namely liquid, supercooled liquid, and glass. The τ_{relax} in the three regimes are 10^{-13}s, 10^{-9}s, and 10^{2}s or higher respectively. The feature of the massive increase of relaxation time in the glass phase is also reflected in the transport coefficients, like viscosity or diffusivity. Often such glasses are referred to as structural glasses, to distinguish them from spin glass and other glassy systems. As the glass transition occurs, thermodynamic quantities such as the volume and the enthalpy show a deviation from the respective extrapolated equilibrium liquid lines (see Fig. 1.1.(b)). In calorimetric experiments, the specific heat shows a sharp yet continuous drop as the glass transition occurs. The absence of a discontinuity in the second derivative of the thermodynamic potential, i.e., the specific heat would usually be evidence for the absence of a second order phase transition. However, the fact that the liquid cannot be equilibrated at these conditions prevents one from drawing such

a conclusion on the basis of the behaviour of the specific heat.

The glass transition temperature mentioned here is not unique. It depends on the

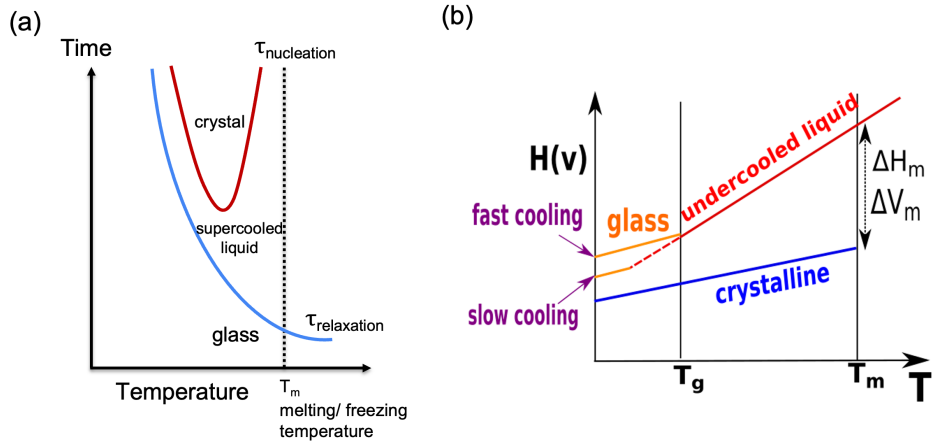

Figure 1.1: (a) The schematic representation showing the competition between nucleation time and relaxation time in glass forming liquids. (b) The schematic representation of the formation of glass by cooling a liquid below its melting temperature.

preparation history, which in this context is the cooling rate. Depending upon the cooling rate, different glasses can be obtained (see Fig.1.1 (b)). In the latter part of this chapter, we will discuss the relevance and the subsequent efforts to make different glasses.

Before proceeding further, we clarify a specific interchange of terminology used often in the literature and in this thesis. In studies of the glass transition, what one investigates are the changes that occur in the supercooled glass-forming liquid as the glass transition is approached. Supercooled liquids are, of course, metastable with respect to crystal. Given that the liquid is always in a supercooled state, we simply refer to it as the liquid for brevity. Further, the experimental/observation timescale, τ_{obs}, is usually greater than the relaxation time of the supercooled liquid, τ_{relax}, on the one hand, and smaller than the lifetime of the liquid in the metastable supercooled state, τ_{life}, on the other hand (the lifetime is the typical time before the transition to the globally stable crystalline state). Given this relationship between timescales, $\tau_{relax} << \tau_{obs} << \tau_{life}$, we drop the distinction between 'metastable' liquids and 'equilibrium' liquids (which are the globally stable state under the corresponding conditions and for which $\tau_{life} \rightarrow \infty$).

Unlike first-order transitions like freezing, where the change in the structure of the system is drastic, the glass transition is not accompanied by significant changes in structure. Subtle, gradual changes are observed as the temperature of the supercooled liquid is decreased. For instance, the slight modification in the peak of the pair correlation function (the probability of finding a particle at a distance from a central particle) occurs as the temperature is lowered. But this modest change is nowhere close to the

stark difference that the other phases of matter, like gas or liquid or crystal, have with respect to each other. Many interesting recent works have attempted to establish the role of structure in the dynamics of glass-forming liquids. Understanding the dynamics from the estimation of the entropy, where the information of two-body correlation is used, certainly connects the structural aspect to the dynamics in the system [8]. The structural ordering in the experiments of colloidal systems [9] also establishes a parallel connection. However, these structural signatures are not comparable to the degree of the dynamical changes that occur as the system approaches glass transition. We will start with the discussion of the prominent dynamical signatures of the transition, followed by the relevant thermodynamic aspects.

1.1.2 Non-exponential decay of time correlation functions

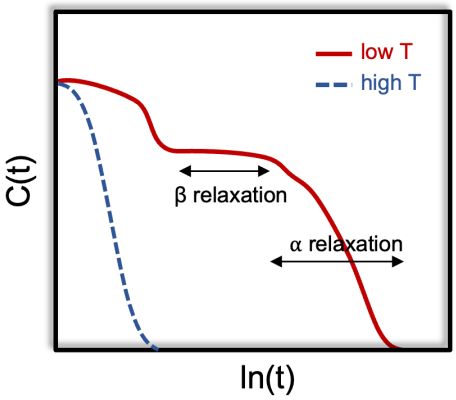

Figure 1.2: Schematic representation of the decay of the density correlation function at high and at low temperatures.

The dynamics of glassy systems show several non-trivial changes as the glass transition temperature is approached. The most prominent manifestation of these changes is the significant slowdown of relaxation of fluctuations or transport properties of the system. In experiments and theoretical studies of glasses, relaxation is measured using a number of methods. In experiments of supercooled liquids, relaxation is often measured from the dielectric susceptibility [10]. In simulations, these methods generally involve the measurement of dynamic correlation of relevant quantities. In the case of liquids, typically, density-density correlation is such a quantity of interest. The relaxation in the system can be measured by observing the time evolution of the correlation of the density fluctuation. At higher temperatures, the relaxation (the decay of the correlation function) of the system is exponential in nature. As lower temperatures are accessed, the nature of the decay of the correlation function changes. At very short times, the correlation rapidly decays. This fast decay occurs in the ballistic regime (common to both high and low temperature regimes), where the effect of the

velocity or the acceleration can be neglected. The ballistic regime is followed by an intermediate time window when the correlation function shows a plateau. This intermediate regime is the 'β' regime. The plateauing of the correlation function indicates the particles get caged by their neighbours. Beyond the β regime, when the particles break the cage, the correlation function finally decays to zero, that regime is termed the α relaxation regime. At lower temperatures, the α relaxation in the glass-forming liquids shows slower than exponential decay. This slower relaxation can be described by the stretched exponential function of the form (Kohlrausch-Williams-Watts function)

$$C(t) = C_0 \exp[-(t/\tau)^{\beta}] \tag{1.1}$$

where $C(t)$, is the relevant correlation function, C_0 is the prefactor, τ is the relaxation time and β is the stretching exponent. The value of β lies between 0 and 1, ensuring the slower than exponential decay. The existence of these two-step relaxation regimes (see Fig. 1.2) is an important feature of the dynamics of glass-forming liquids [6, 11, 12]. Numerical [13–17] and experimental [18, 19]evidence shows that close to the glass transition, the dynamics of the supercooled liquid is heterogeneous, with domains of different mobility and relaxation. The slower than exponential relaxation can thus be understood as the spatially averaged effect of separately relaxing regions where individual regions relax exponentially with characteristic relaxation time. If one calculates the variance of these different relaxation times, it can be shown that the relative variance of the relaxation times depends only on β_{kww}. The variance is inversely proportional to the β_{kww}, implying that as the relaxation of the system becomes more heterogeneous, β_{kww} decreases more, and the overall relaxation of the system becomes slower and slower. In this thesis, we have studied the behaviour of β_{kww} at very low temperatures in supercooled liquid in the context of dynamical heterogeneity, which we discuss in more detail later in this chapter.

1.1.3 Non-Arrhenius relaxation behaviour

We mentioned in the previous section that as the low temperatures are accessed, the time correlation functions measured in the supercooled liquids show prominent changes like two-step relaxation. Generally, by relaxation of the system, it is meant that the system has forgotten its initial state. In glass-forming liquids, the relaxation time is often measured as the time at which the time correlation function decays to $1/e$ of its initial value. The relaxation time also shows a prominent change in nature as the temperature decreases. At high temperature and low density, the relaxation behaviour of the liquid is described by the Arrhenius temperature dependence described as the

following

$$\tau = \tau_0 \exp[\frac{E}{k_B T}] \tag{1.2}$$

where τ is the structural relaxation time, E is the activation energy (constant), and T is the temperature. The same behaviour is reflected in the transport properties like viscosity or inverse diffusivity. For a large number of liquids, with the decreasing temperature, relaxation time increases faster than the exponential increase described by the Arrhenius relation. Such supercooled liquids with the super-Arrhenius increase of relaxation time are classified as fragile glass formers [20]. Metallic glass-forming liquids, many molecular liquids (a prominent example Ortho-terphenyl) fall under this category. Here the excess increase of relaxation time is ascribed to the emergence of temperature dependent activation energy barrier [20]. The crossover temperature at which transition from Arrhenius to super-Arrhenius dependence occurs is termed as the onset temperature T_{onset}. This temperature signifies the onset of activated dynamics in the system. The other category of glass formers called strong glass formers, where Arrhenius temperature dependence of relaxation times is followed till the glass transition temperature. Silica, the most commonplace example of glass, is a strong glass-forming liquid.

Understanding the super-Arrhenius increase of the relaxation time is a question of prime importance in glass physics. Despite extraordinary and extensive efforts, any universal consensus on this matter is still absent. Different empirical fitting forms have been used to describe such relaxation to various degrees of success. Among those, the most widely accepted and applicable fitting form is Vogel-Fulcher-Tammann or VFT fit.

$$\tau = \tau_0 \exp\left[\frac{1}{(K_{VFT}(T/T_{VFT} - 1))}\right], \tag{1.3}$$

In this fit form, T_{VFT} is the temperature at which the relaxation time for the system diverges. The other type of fit forms, such as parabolic fit [21] form ($\tau = \tau_0 exp[A(\frac{1}{T} - \frac{1}{T'})]$), indicate a zero temperature divergence of the relaxation times. However, as the systems fall out of equilibrium much before the temperature predicted for relaxation time divergence, it is almost impossible to empirically verify one form over the others though comparative studies have been done to compare different fitting forms [22,23].

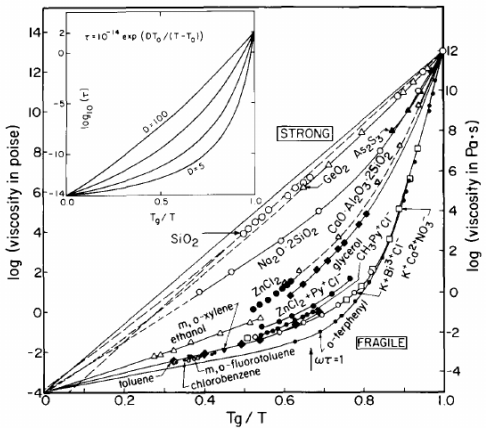

Figure 1.3: Angell plot of the logarithm of viscosity vs the scaled inverse temperature T/T_g [20]

1.1.4 Crossover of relaxation in glass forming liquids at low temperature

In the last section, we discussed about two broad categories of glass-forming liquids. The concept of fragility was introduced by Austen Angell (see Fig. 1.3) to categorize the diverse range of glass-forming liquids depending on their nature of Arrhenius or super-Arrhenius relaxation as the glass transition temperature is approached. As the glass transition temperature is approached, a fragile to strong crossover in supercooled water was observed [24–28]. A similar transition was observed in silica [29–32] and silicon [33–36]. In anomalous liquids like these, the fragile to strong transition is accompanied by a change in the liquid structure, like a change towards more tetrahedral geometry [37]. The dynamical transition is also accompanied by a change in thermodynamics like a heat capacity maximum. The existence of the fragile to strong transition in anomalous liquids has been investigated extensively. In recent times, there have been several findings of faster than expected relaxation at low temperatures in systems that are well known fragile glass formers. These systems include diverse systems like phase-change alloys [38, 39], metallic glass formers [40–43] etc. Some of these systems show a change in thermodynamic behaviour [42], and some do not. The nature of fragile to strong transition in such systems is not like the conventional fragile to strong transition observed in anomalous liquids. In Chapter 6, we have studied a dynamic crossover in a well studied fragile model glass former (Kob-Andersen 80:20 binary Lennard-Jones mixture) and the relevant thermodynamical aspects.

1.1.5 Dynamical Heterogeneity

Dynamical heterogeneity (DH) is at the heart of glassy dynamics, and it underlies significant dynamical behaviours such as slower than exponential decay of correlation

functions of glassy systems. The earliest evidence of dynamical heterogeneity was found in the NMR experiment of poly(vinyl acetate) [44]. The system is comprised of faster (mobile) and slower (immobile) particles. In a homogeneous liquid, the distribution of the displacement of the particles (quantified by the Van Hove function, see Chapter 2) is typically Gaussian [45]. The mobile particles can be those that move more than this estimated displacement in a homogeneous scenario [14]. Sometimes a certain percentage of the fastest moving particles are also considered to be the mobile particles [16]. Identifying immobile particles is a more nontrivial task. Apart from the consideration of the mobility, local packing is also considered to identify immobile particles [46–48]. Experimental and numerical findings have shown that these mobile or immobile particles are spatially correlated and form clusters [16, 49]. These clusters have typical lifetimes. Beyond this lifetime faster particles becomes slower and vice versa. The cluster size of such dynamically heterogeneous particles gives an estimate of the dynamical length scale associated with DH. The study of DH involves the study of this timescale of heterogeneity and the dynamical lengthscale emerging from such heterogeneity. We will elaborate on this in terms of quantities, such as the non-Gaussian parameter that is used to study DH in supercooled liquids.

One can think of DH simply in terms of the measure of the displacement of the particles [14]. The non-Gaussian distribution of displacement implies heterogeneous dynamics. The extent of the deviation of the distribution from the Gaussian beahviour (non-Gaussian parameter α_2, see Chapter 2) quantifies the heterogeneity present in the system. At very short time and at very long time the displacement distribution of the system stays Gaussian and non-Gaussian parameter α_2 stays zero. Therefore, the time evolution of α_2 shows nonmonotonicity and attains a maximum at a characteristic time [14]. This characteristic time t^* defines a timescale of the associated heterogeneity. This timescale increases with the decrease of the temperature. The size of the clusters formed by these particles also grows with the decreasing temperature [16]. This growing length scale has been of interest to study for its connection with dynamics. There are other quantities that are used to quantify dynamical heterogeneity. DH is studied from the fluctuation (χ_4, see Chapter 2) of the two-point correlation function that describes the relaxation of the system [50]. The time evolution of $\chi_4(t)$ also shows the existence of a characteristic time τ_4 at which it becomes maximum. The peak value of $\chi_4(t)$ also increases with decreasing temperature. The definitions used to identify mobile and immobile particles are not universal. The compactness of the clusters and geometry (fractal nature) also make the absolute estimation of lengthscale difficult. Therefore the lengthscale obtained from such cluster size does not necessarily guarantee very accurate quantification of lengthscales. As the measure of χ_4 is free from such ambiguity, this quantity has motivated the study of the associated dynamic length scale [51, 52].

The other quantity that gives the measure of DH present in the system is the stretching exponent β_{kww} as mentioned in the earlier sections. The relative variance of the different relaxations of the different regimes within the system depends only on β_{kww}. β_{kww} quantifies the extent of heterogeneous dynamics in the system. The decrease of β_{kww} indicates the increase of heterogeneity in the system [53].
Numerical and experimental studies have shown that DH increases as the glass transition temperature is approached. Some recent studies show non-trivial changes in DH in fragile glass-forming systems, when very low temperatures are accessed [41–43]. Some studies show the increase of DH becomes moderate at much lower temperature [43]. Some studies show the DH decrease at very low temperatures [42]. Some studies show a possible saturation of DH at such a substantial low-temperature regime [41]. We have investigated different aspects of dynamical heterogeneity, the morphology of heterogeneity of a model glass-former at very low temperatures to find a connection between the crossover in relaxation and the dynamical heterogeneity.
We discussed previously that the distribution of the relaxation times in a dynamically heterogeneous system gives rise to the stretched exponential decay of the correlation function. The other consequence of the DH is the decoupling of diffusivity and structural relaxation timescale, which we will discuss in the following section.

1.1.6 Violation of the Stokes-Einstein relation(SER)

The relaxation in the glassy systems is measured through time correlation of fluctuations such as structural relaxation (τ_α), or transport coefficients such as shear viscosity (η), and inverse diffusivity (D^{-1}). Stokes-Einstein relation (SER) describes the relation between viscosity and diffusivity at a given temperature. The Einstein relation explains the relation between the diffusion coefficient D, temperature T, and friction coefficient ξ through the relation $D = k_B T/\xi$. Stokes relation establishes the connection between friction coefficient and the viscosity through the relation $\xi = 6\pi\eta R/m$. Combining these two relations, we obtain the Stokes-Einstein relation as $D\eta/T$ =constant or equivalently $D\tau_\alpha$ =constant. SER has been found to be valid for many liquids at high temperatures. But as the low temperatures are approached, the violation of this relation has been observed in many systems [54–58]. The diffusivity and the structural relaxation timescale decouple. As the temperature is decreased, inverse diffusivity shows slower divergence compared to the structural relaxation time. The diffusivity and the structural relaxation becomes fractionally related by $D \propto \tau_\alpha^{-1+\omega}$ where $\omega > 0$. Various studies of supercooled liquids have shown that violation of SER occurs because of the dynamical heterogeneity in the system [50, 53, 59, 60]. When the dynamics in the system become heterogeneous, the contribution to the diffusivity in the systems

comes from the faster moving particles. Conversely, the contribution to structural relaxation comes from the slower particles, as this relaxation time is measured by the displacement of the particles beyond a certain cutoff distance. Hence the decoupling of D and τ_α occurs as they represent different moments of the wide-ranged distribution of the local relaxation times in supercooled systems. In chapter 6, we have studied SER relation for an extensive range of temperatures.

1.1.7 Thermodynamics

So far, we have discussed the significant features of glassy dynamics. Next, we discuss the thermodynamic aspects of the supercooled liquids approaching the glass transition. As the temperature decreases, various thermodynamic quantities like volume and enthalpy show a continuous but sharp change in slope as a consequence of the glass transition. The quantitative change depends on the preparation history, like the cooling rate. The entropy also shows similar behaviour, and there are a couple of crucial views regarding the entropy of these supercooled liquids, which we will briefly discuss.

1.1.7.1 Kauzmann's paradox

The relation between the entropy and the specific heat is described as follows

$$(\frac{\partial S}{\partial T})_V = \frac{C_V(T)}{T} \tag{1.4}$$

The specific heat of the liquid is more than the crystal. Hence, the entropy of the liquid decreases faster than that of the crystal. The difference between the liquid entropy and the crystal entropy is called the excess entropy of the liquid, defined as $\Delta S(T) = S_{liq}(T) - S_{crys}(T)$. The extrapolation of the liquid and crystal entropy predicts that the excess (configurational) entropy vanishes at some finite temperature. This temperature is called the Kauzmann temperature(T_K). It implies that at some temperature range ($T < T_k$), the entropy of a disordered solid becomes less than the entropy of the crystal at that temperature. It is quite counterintuitive. The crystal entropy becomes zero at the absolute zero temperature. Therefore the extrapolated liquid entropy at zero temperature should be negative at zero temperature. This is in direct violation of the third law of thermodynamics. This possibility is famously known as the Kauzmann's paradox [61]. In an attempt to resolve the paradox, it has been hypothesized that a thermodynamic transition at T_k occurs that produces "ideal glass," and beyond that temperature, the excess entropy vanishes. Kauzmann temperature lies well below the glass transition temperature T_g for all the known glass-forming liquids. Therefore the system cannot be equilibrated at around T_K. Therefore,

verifying if the excess entropy goes to zero at a finite temperature is almost impossible. In this context, we will describe various attempts that have been made to resolve such a situation. Systems have been studied where a finite fraction of particles are pinned; in other words, their positions do not evolve with time. Such a system is called the random-pinning glass-former. Using theoretical arguments [62] and simulations [63, 64], it has been shown that by increasing the fraction of pinned particles, excess entropy can be brought to zero at an accessible temperature range. In other words, by random pinning, the Kauzmann temperature of the system can be shifted to a much higher temperature. However, subsequent work [65] argued that such protocol changes the fragility of the system instead of shifting the Kauzmann temperature. Hence, to resolve the paradox, one needs to be able to equilibrate the system at as low temperatures as possible. In this context, in the latter part of the chapter, we will discuss recent developments in preparing well annealed (low temperature) glasses.

1.1.8 Adam-Gibbs Relation

Configurational entropy measures the number of distinct configurations a system can sample at a given temperature (or density) in the configuration space. The potential energy surface of the supercooled liquid has a number of local minima. These local minima are known as inherent structures. The system samples possible configurations within a basin, and it also jumps from one basin to the other. With that picture in mind, the total entropy of the system can be divided into two parts, namely, vibrational entropy and configurational entropy. The vibration of the system within a local minimum contributes to the vibrational entropy or basin entropy. The measure of the different independent minima contributes to the configurational entropy. Entropic theories like the Adam-Gibbs relation [66], Random first-order transition (RFOT) theory [67, 68] attempt to connect the dynamics and the thermodynamics of the glassy systems. Estimation of configurational entropy is of vital importance in these theories. In our discussion of dynamical heterogeneity, we mentioned that the dynamics of the system is heterogeneous, and the heterogeneous regions are spatially and temporally correlated. These spatially correlated regions show cooperative rearrangement [69] that simply implies a group of particles move in a cooperative fashion. Adam-Gibbs relation attempts to establish a connection between cooperativity and the relaxation of the system [66]. The particles involved in such cooperative motions are identified as the cooperatively rearranging region or the CRR. CRR is defined as a group of rearranging particles (atoms, molecules, etc., depending on the nature of the glass former) such that smaller groups of particles are incapable of rearrangement independently of

their surroundings. In experiments and numerical simulations, the signature of cooperative motion has been observed [16, 43, 69]. The probability of the arrangement of CRRs is considered dependent on the size of the CRR ($z(T)$) [66]. The configurational entropy per CRR is considered to be constant (S^*). So the configurational entropy per ($S_c(T)$) particle at a given temperature can be related to Z and S^* as, $S_c(T) = \frac{S^*}{z(T)}$. The free energy of these CRR for rearrangements is the Gibbs free energy $G = z\triangle\mu$, where $\triangle\mu$ is the chemical potential barrier per particle. Using the expression of z and separating the temperature dependent and independent terms, the relaxation time for the system can be written as the following [66].

$$\begin{aligned}\tau &= \tau_0 \exp[\frac{S^* k_B^{-1} \triangle\mu}{T S_c}] \\ &= \tau_0 \exp[\frac{K}{T S_c(T)}]\end{aligned} \tag{1.5}$$

where K is the temperature independent term. This is known as the Adam-Gibbs relation that predicts the dynamics of the system from the measure of the entropy of the system. It states that the relaxation of the system diverges as the configurational entropy goes to zero. Adam-Gibbs (AG) relation has been shown to hold for various glass-forming systems and a range of temperatures [70–74]. We have discussed that the relaxation time in glass-forming liquids can be represented by various timescale from correlation functions, transport coefficients, and so on. We have also discussed how these different timescales decouple from each other. Different works attempted to verify AG relation with respect to different timescales of the system [58, 75]. A few recent findings show that the Adam-Gibbs relation is violated at very low temperatures [43, 76]. In order to verify if the AG relation holds, the most important point is the accurate estimation of the configurational entropy. In this thesis, we have shown that in a model glass-forming liquid, the AG relation holds for an extensive range of temperatures when the basin entropy is calculated with caution, taking the anharmonic contribution into consideration.

1.1.9 Preparation of stable glasses

Up to this point, the discussion about significant dynamic and thermodynamic aspects of glass transition proves the study of glasses has been extensive. Earlier in this chapter, we have mentioned that the state of the glass depends on its preparation history. Such as, when we prepare a glass by cooling supercooled liquids, the slower we cool the system, the lower the energy of the glasses is. Therefore, one would always attempt to slow the cooling rate further down to obtain better glasses. But the limit of

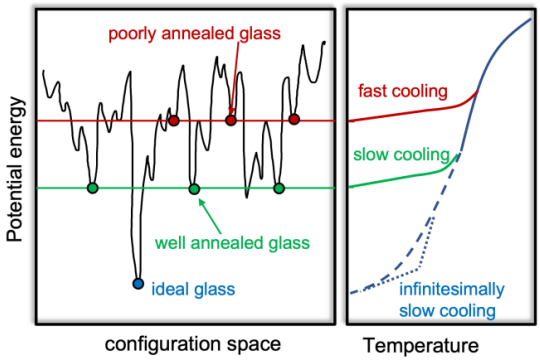

Figure 1.4: The schematic representation of potential energy landscape (PEL) and concept of annealing.

the lowest cooling rate is bounded by the issue of crystallization and the experimental or computational capacity. Hence one of the most enduring efforts in this field has always been to prepare glasses with lower energies to have a more refined understanding of the glass problem (see Fig.1.5).

In this context, a concept that we invoke is the potential energy landscape picture. Generally a well annealed glass is understood to be one where the system resides in a deeper local energy minimum. The potential energy is determined from the positions of the particles. In a $DN + 1$ dimensional space, the potential energy landscape can be represented by a hypersurface including the interactions of all the particles of a system of size N and at a dimension D. Each different glassy configuration can be thought of as a point on this surface. This energy landscape picture was first discussed by Goldstein [77] as an approach to comprehending the behavior of glass forming liquids. In this potential energy landscape (PEL) picture, the minimum corresponding to the crystalline state will be the global minimum. However, for amorphous systems, there will be many local minima corresponding to all the possible stable configurations. As described in the schematic one dimensional projection of the PEL (Fig. 1.4), the preparation history dictates the depth of the minimum in the PEL that the glassy system occupies. Glasses stuck at higher and lower energy minima are called poorly annealed glasses and well annealed glasses, respectively. As Fig. 1.1 illustrates, there exists multiple T_g depending on the protocol used [78]. Naturally, there have been numerous attempts to prepare glasses of progressively greater stability, or even the ideal glass [79]. The structural and dynamical nature of this putative ideal glass, and the question of whether the corresponding energy minimum is lower or higher than that of the crystalline state are all puzzles that remain to be solved. So far, we have discussed various aspects of the laboratory glass transition. Numerical simulations have been a very effective tool in expanding our understanding of glasses. Through such investigations, researchers have been able to directly probe microscopic changes

in the structure and in the dynamics of glassy systems as the glass transition is approached. One drawback of the computational study of glasses is that glasses prepared on computers get stuck in very high energy minima compared to their experimental counterparts. The slowest possible cooling rate on computers is still orders of magnitude faster than the typical laboratory cooling rates. Different sampling techniques are being pursued to address this drawback with a substantial degree of success. We will

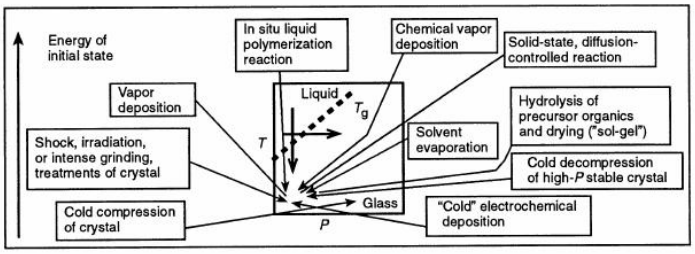

Figure 1.5: Different methods of preparing glasses [6]

discuss two well-known methods that have achieved considerable success in preparing well-annealed glasses.

The first is one that can produce glasses with extraordinarily low energy is the physical vapor deposition (PVD) method [80]. The preparation of glasses by the vapor deposition method has been in place for a long time [6]. But the fact that the method's ability to make extraordinarily stable glass lies in optimizing the control parameters has been found recently [80]. As the name suggests, such glasses are prepared by depositing the vapor of the material to a substrate maintained at a very low temperature. The first successful preparation of stable organic (indomethacin) vapor deposited glasses were carried out by Swallen *et al* [80]. The crucial control parameters to prepare such glasses are the deposition rate of vapor and the substrate temperature. In this method, glasses are prepared by depositing new layers on a substrate. This deposition of particles is repeated at a certain rate. A freshly deposited layer of particles will have more mobility [81] because of the presence of the interface. If the time between subsequent layers of particles being deposited is very long, there exists a possibility of crystallization. Also, a much faster rate of deposition will not provide sufficient time for the freshly deposited particles to sample suitable configurations. Therefore in the preparation of PVD glasses, deposition rate plays a very important role. For some organic glasses close to the glass transition temperature, the surface diffusivity has been found to be orders of magnitude($\sim 10^8$) higher compared to the bulk diffusivity [82]. The temperature of the substrate is also a crucial parameter in producing ultrastable glasses. Indomethacin glasses accessed a highly stable structure when the substrate temperature was maintained at $0.85T_g$. The glasses prepared using this method are 'stable' in many aspects. Apart from having lower energy, the vapor deposited glasses have a higher density. For comparison, it can be mentioned that glasses that are prepared

by isothermal annealing for six months have equivalent kinetic stability compared to glasses prepared by the PVD method within a few hours [80]. A variety of organic and polymeric stable glasses can be prepared using this method [7]. Vapor deposited glasses make better glasses with a range of properties such as high density, low enthalpy, high thermal stability, high modulus. These glasses show enhanced chemical stability. To destroy a vapor deposited glass structure, fifty times more intense photon flux is required compared to its liquid-cooled counterpart [83]. They show exceptional dynamical behaviour also. In ultrastable glasses, a substantial suppression of β relaxation has been observed [84]. Apart from organic or polymeric glasses, stable metallic glasses have also been prepared that show higher glass transition temperature and high elastic modulus. [85]. Vapor deposited glasses have also been prepared through numerical simulation of a standard model of metallic glass formers [86]. For glasses prepared by standard cooling, a two to three orders of magnitude slower colling rate than the available typical cooling rate is required to prepare as stable glasses as one can obtain using the PVD method [86]. However, the simulation shows the difficulty in preparing isotropic bulk glasses as substantial compositional heterogeneity is observed along the axis of deposition. In fact, vapor deposited glasses show a considerable degree of orientational anisotropy [87]. Hence this method is not useful for making isotropic bulk glasses. However, stable organic glasses have been found to be a very promising candidate for modern day technologies. Organic light emitting diode (OLED) in smartphones, organic semiconductors are products that require very stable glasses because the generic aging nature of glass can substantially reduce the effectiveness of a material [7]. Therefore the quest for making better annealed glasses is continuing actively.

In recent times an extensively used fast sampling method to prepare stable glasses on computers is the swap Monte Carlo method. Swap Monte Carlo method has been previously implemented in hard sphere [88], soft sphere [89] systems where they showed evidence of faster sampling. The applicability of this method has been extensively studied in many works till date [90–93]. We will briefly mention the general principle of the algorithm. Both in standard Monte Carlo simulation and swap Monte Carlo simulation, a randomly selected particle is given a displacement, where the displacement is accepted or rejected based on Metropolis acceptance rule. In the swap Monte Carlo method, in addition to that, diameters of two randomly chosen particles are exchanged. The exchange of diameters is again performed following the Metropolis acceptance rule. At every Monte Carlo step, this swap move is attempted with a finite probability. The two extrema of the swap probability represent two different scenarios. For $p = 0$, no swap moves occur, and swap Monte Carlo reduces to the standard Monte Carlo algorithm. For $p = 1$, the particles are always swapped. It has been shown that the maximum acceleration of the sampling occurs at an intermediate

value of the probability [90]. This optimum value of the probability shows robustness with the variation of temperatures and systems. The swap of diameters of the particles instead of the swap of particles is a modified concept used in the recent application of the algorithm so that the measurements of position dependent quantities that require particle index information stay meaningful. These probabilistic nonlocal moves help the system sampling configurations that are otherwise unattainable or associated with a much longer relaxation time. However, the efficiency of this method depends mainly on the polydispersity of the system. The swap acceptance probability determines the efficiency of the swap MC algorithm. This probability decreases logarithmically with the increase of the difference of radii of particles in the system [90]. Systems with continuous polydispersity show orders of magnitude faster relaxation compared to the standard methods. The method does not appear to be very useful for bidisperse systems like the binary Lennard-Jones system. But ternary or other discretely polydisperse systems of a higher degree of polydispersity can also achieve faster sampling using this technique [90]. In this method, Monte Carlo moves are equated to molecular dynamics timesteps to provide a mapping from MC steps to real time. This correspondence has been determined from the rescaling factor of the structural relaxation time in terms of MC steps to match with the corresponding MD steps. The significant reduction in the relaxation time for such systems has enabled a better understanding of glasses, in fact approaching laboratory conditions and allowing for more direct comparisons [92].
In Chapters 4 and 5, we explain how we explored the possibility of generating low energy glass by the application of mechanical deformation.

1.1.10 Well annealed glasses and equilibrium

A key issue that one needs to address is whether these energetically stabler and more rapidly relaxing states are sampling phase space in equilibrium corresponding to a thermodynamic ensemble. Thus, one needs to verify if the methods described in the previous section guarantee that the prepared glasses are equivalent to their equilibrium counterparts. For example, the non-local moves used in the swap Monte Carlo [89] scheme obey the detailed balance condition and thus generate configurations from an equilibrium ensemble. The ultrastable films generated using PVD show structural anisotropy [94] compared to their equilibrium bulk counterparts that are prepared using standard cooling techniques. In this thesis, we will discuss our efforts towards making well annealed glasses. In subsequent parts of this chapter, we will show that cyclic deformation anneals the system when the deformation amplitude is in the vicinity of the yielding transition amplitude [95]. The configurations generated

by oscillatory shear are not guaranteed to sample an equilibrium ensemble. This validation is beyond the scope of this thesis but has been discussed in Ref. [96]. In the spirit of the hybrid Monte Carlo scheme described in [97], cyclic deformation has been considered as a generation step for the trial move. The sheared configuration is accepted or rejected using a Metropolis acceptance rule with an appropriate modification to account for the non-equilibrium conditions [96]. In order to better understand whether these low energy configurations are comparable to those generated by straightforward molecular dynamics, one needs to thoroughly characterise the states generated in a molecular dynamics scheme at the corresponding conditions. In Chapter 4, we describe how we have investigated the possibility of generating low energy glasses by the application of cyclic shear and have confirmed that glasses prepared in this way under optimal conditions are, in fact, equivalent to glasses prepared by normal equilibrium dynamics.
In this thesis, we have studied various aspects of glassy systems discussed so far. We outline the problems that have been addressed in the following chapters in the context of glass physics.

- We have discussed how preparing stable glass, especially on computers, has been one of the most prominent directions of research in the area of glass physics. In this thesis (chapters 3 and 4), we have investigated the possibility of generating low-energy glassy states via periodic deformation of the systems(we discuss periodic drive in the later part of this chapter).

- We have discussed the broad classification of glass-forming liquids, namely strong and fragile liquids, in terms of their dependence of relaxation time on temperature. We have also demonstrated how recent studies of glassy systems at low temperatures that have not been accessed before have given evidence of fragile to strong transition in well-known fragile glass-forming liquids. In this thesis (chapter 6), we present a detailed study of a model fragile glass-forming liquid at significantly low temperatures that gives evidence of dynamical crossover at such a temperature regime.

- We have presented an elaborate account of various dynamical (such as non-exponential decay of relevant correlation functions, dynamical heterogeneity) and thermodynamic aspects (concept of excess entropy, entropy crisis) that are crucial to the study of glass physics. We have studied extensively all such dynamic and thermodynamic signatures of the above mention model glass-forming system (in chapter6) to understand the nature of the relaxation crossover at such low temperatures.

1.2 Jamming transition

So far, in the discussion of glass transition, we have primarily talked about the role of temperature being the control parameter (though the glassy state can be arrived upon by controlling density). Similarly, the non-equilibrium jamming transition can occur when the density of the system is varied in an athermal system [98]. Jamming transition is also a transition from a fluid state to a rigid state. One can think that the particles can move freely when the system is at a low enough density. This is a fluid-like state. If the density of the system is increased, it becomes harder for the particles to move freely. In fact, beyond a certain density, the particles can no longer move. This solid-like state is the *jammed* state. The transition from such a fluid-like state to a solid-like state is called *jamming transition*. Jamming transition is a transition to rigidity at zero temperature, unlike glass transition, where thermal fluctuation plays a crucial role. Therefore we can think of the systems to jam where temperature plays a negligible role. The grains, emulsions, colloids, and biological tissues with bigger constituent particles have interaction energy much higher than their kinetic energy and therefore undergo jamming transition [99, 100]. Jamming is a regular occurrence in our life. Starting from traffic jams to jammed grains in kitchen containers, interestingly have similar features to jamming.

Jammed packings are mechanically stable packings. The important aspect of studying the jammed system is the study of the packing and its structure. The study of the packing problem is extended across the field of physics, mathematics, information theory. Along with its broader range of applications, the history of the study of packing is also spread over a long period. In the year 1616, the Kepler Conjecture stated the densest packing in same sized spherical particles in three dimension is 74% and was proved afterwards [101]. The study of packing of disordered systems by Bernal [99] shows that the densest sphere packing beyond which the system stays jammed is 64%. Identification of such a jammed state can be viewed very simply by putting particles randomly in a big box and then isotropically compressing it in steps. At each step after compression, the system is allowed to relax and settle down. Continuing this compression procedure, we can arrive at a certain high packing fraction which is 64% Beyond this packing fraction, the system stays jammed. This density limit is identified as the random close packing limit (RCP). When the lower density configuration (that is compressed to obtain jammed structure) is generated randomly, the systems jams around 64% and indicates the existence of a unique jamming density [102]. But when the initial densities of the equilibrated configurations are different, that can give rise to a range of jamming densities [103, 104] with RCP being the lowest jamming point. Unlike glass transition, jamming transition is accompanied by easily observable structural changes. The role of structure is an important aspect in the study of packing. In

the study of structure, estimation of contacts of particles is significant as it determines the stability of the packings. The onset of rigidity signifies the system being able to support stress. From the argument of stability, it can be shown quite simply the stability is accompanied by a certain number of coordination $2D$ where D is the dimension. The system has to be in force balanced condition to generate a mechanically stable packing. We can say the number of constraints in the system $N_c = \frac{NZ}{2}$ where N and Z are the total number of particles and average contact number, respectively. For the packing to be stable, the number of constraints should equal the system's degrees of freedom (D_F). Degrees of freedom in the D dimension should be ND. This equality condition states the average contact number $Z = 2D$ [105]. This is the isostatic condition for the frictionless jammed packing. The jammed systems having densities within the RCP range satisfy this condition. This condition changes to be $D + 1$ in case of the presence of frictional force in the system as both force and torque is taken under consideration.
In chapter 3 of the thesis, we demonstrate the study of a system of sphere assemblies that interact via repulsive harmonic potential. Such a system has been studied in a vast range of densities, where different densities represent characteristically different systems. Very low-density limit shows response similar to low-density colloidal systems. High-density systems (much further away from isotropic jamming density) show responses similar to glassy systems. Interestingly it shows some unique behaviour when the system is close to the isotropically jammed systems. The concept of jamming transition and isotropic jamming has been crucial in understanding the range of responses observed in such a system.

1.3 Driven amorphous systems

The study of driven amorphous materials is of interest as their utility depends on their response to the applied external force or deformation. We discussed so far how the variation of thermodynamic variables like temperature and density brings out different non-equilibrium transitions in amorphous systems. In amorphous systems, external drives like the application of stress or the application of deformation or strain play a crucial role in exploring the phase space. Driven amorphous systems show various transitions ranging from complete failure of the system to self-organized interesting new phases. We will discuss some of these exciting transitions relevant to the works done in this thesis.

1.3.1 Shear jamming transition

Earlier, we have discussed that jamming transition occurs as the density of the system is increased. We have discussed the existence of an isotropic jamming density ϕ_J. The system can also be jammed by the application of shear. Among different forms of shear, we can consider simple shear (relevant for the discussion of the thesis), where the deformation keeps the parallel planes parallel to each other while translating them relative to each other. Such deformation can also rigidify the system, and the jamming under such deformation is called shear jamming transition. In the discussion of shear jamming phenomena, it is important to categorize the discussion about both frictional and frictionless systems.

A system where frictional force is present can be jammed by the application of shear deformation at lower densities than isotropic jamming [106]. Experiments of two-dimensional photoelastic disks and numerical simulations of frictional grains show such a jamming transition [107, 108] in the system. An exciting feature of shear jamming is that as the system is sheared, an intriguing intermediate transient state called the fragile state emerges between the initial unjammed and the final shear jammed state. The fragile state emerges for small applied stress in the system [106, 107]. In this state, the particles bearing strong forces (forces higher than the average force of the system) form networks. These networks percolate along the compressive direction only. Such states are unable to support stress in perpendicular directions. Now, as the deformation is further increased, the force network formed in the compressive direction buckles, and they percolate in all directions [109]. At that point, the system gets shear jammed.

Friction stabilizes structures [110] and is necessary to produce jammed states below ϕ_J. Recent studies of frictionless spheres when subjected to shear [109,110] show that shear deformation generates structures that have fingerprints of jamming at lower densities than ϕ_J, but are not jammed. Addition of friction to the contacts can only stabilize them. However, some investigations have reported shear jamming for densities below ϕ_J for small systems of frictionless particles [111], raising questions about possible finite-size effects. Recently, a study of frictionless sphere assemblies has shown that cyclic shear deformation can generate packings with isotropic jamming densities ϕ_j above the minimal jamming density ϕ_J [112]. This study is important as it investigates the emergence of shear-induced states in frictionless systems. In Chapter 3, we will discuss how in a frictionless sphere assembly, the unjammed states can be generated above isotropic jamming density ϕ_J by applying cyclic shear deformation. As those frictionless unjammed states can be shear jammed, we posit that our work has facilitated the study of shear jamming in frictionless systems.

1.3.2 Yielding transition

The shear jamming transition describes a transition from fluid-like states to solid states. The converse transition from a solid-like to a flowing state is called the yielding transition and is the subject of this section. The most obvious change that a solid undergoes, when subjected to a large deforming force, is that it breaks or *yields*. The yielding behaviour of a substance is an important material property with deep implications. From the study of landslides to the construction of a bridge or in the making of protective screen covers for our smartphones - understanding the yielding property of a material is vital. This understanding is pretty comprehensive for crystalline solids, compared to the understanding of the collapse of a simple sandcastle. The reason for this is the structural difference between crystalline material and disordered systems. Failure in crystalline solids is explained in terms of dislocations or defects, which is the irregularity in the crystal structure arising from an abrupt change in the arrangement of the atoms. Hence, in crystalline solids, identifying failure is relatively straightforward, with defects breaking its translational symmetry. Disordered materials lack translational symmetry and therefore the identification of failure in disordered materials requires a different framework.

As we have discussed earlier, there exists a variety of amorphous materials, and they show different behaviour in their yielding transition. But there exist some fundamental similarities transcending the specificity of the systems. Under small applied stress, all these materials show solid-like elastic responses where stress is proportional to applied strain. At large stress, the system shows plasticity. Plasticity in disordered systems is understood in terms of localized rearrangements of particles termed as plastic events. The onset of plasticity marks the yielding transition in amorphous solids. Hence characterisation of this plasticity is the most important aspect of the study of yielding.

As the study of yielding in disordered systems has been the study to understand plasticity, there have been various approaches to comprehend plasticity, the local rearrangements. One way of understanding local rearrangements has been devoted to study the phenomena by identifying the basic unit of plasticity, termed as shear transformation zone (STZ) [113–116]. The other way has been to understand plasticity in terms of the nature of the perturbation in the surrounding medium where the effect of shear strain applied at a point in the system is measured in terms of shear at a different point propagated through an elastic medium [117, 118]. Apart from the study of plasticity, the nature of the transition itself is a question of interest. Extensive experimental and simulational studies [95, 119–127] have been carried out in recent years. Simulational studies of yielding have provided the important understanding of yielding transition in the aspect of its dependence on shear rate, temperature [128, 129].

Yielding has also been extensively studied following athermal quasistatic protocol in which shear deformation is applied at zero temperature and a zero rate limit (see chapter 2). The system evolves successively through different energy minima in the potential energy landscape at each strain step. The zero-temperature limit of this deformation protocol is a good approximation for the granular systems and foams. Also, the approximation that the system remains in a mechanically stable state unless otherwise perturbed covers the range of atomic or metallic glasses at low temperatures. We briefly describe here some of the important works performed (following AQS protocol) that have contributed to the understanding of yielding significantly and constitute a relevant background for the yielding phenomena that we have studied in our thesis. Uniformly and periodically applied deformation has uncovered significant features of the transition. The nature of transition, whether brittle or ductile, has been found to be largely dependent on the material's preparation history [130, 131] such as the degree of annealing. Under uniform shear deformation, the poorly annealed glasses show a gradual, continuous transition. Whereas for the cyclically shear deformation, the stress shows a small but discontinuous drop at the yielding amplitude [95, 130]. In this regard, the system shows progressively annealing toward low energy states as the amplitude of deformation is increased until the yielding transition amplitude. A threshold energy that coincides with the inherent structure energy at the mode coupling temperature exists, dictating the limit of the annealing below which the yielding transition becomes brittle [130]. Recently, these interesting features of yielding under cyclic deformation have been well captured in the mesoscopic modelings [132, 133]. The yielding under cyclic shear deformation shows other notable features of shear banding [134], structural changes [135], which we refrain from further discussion considering the scope of this thesis.

One of the prominent features of yielding among the mentioned is that amorphous solids show an annealing effect or, in other words, access progressively low energy states when driven cyclically under optimal conditions [95]. In the thesis, we have described how we have explored the possibility of exploring such low energy states in glasses by oscillatory shear in the pre-yield regime. We have also studied (Chapter 3) how the microscopic picture of the yielding transition is similar to very different transitions observed in different systems. In the following section, we will discuss the connection of the yielding transition to the microscopic reversible-irreversible transition.

1.3.3 Reversible-irreversible transition

The non-equilibrium transition, like the yielding transition, is identified from the systems' response quantified by macroscopic quantities like stress or energy. In the yielding transition under oscillatory shear, the system keeps returning to the same state (absorbing) at the end of each cycle in the pre-yield regime. The particles of the system trace the same trajectory over and over again. But after the system yields, the system keeps moving on to new states. The displacement of the particles shows diffusive motion as a function of cycles. Yielding transition at a particle-scale level coincides with absorbing to diffusive transition [95, 136]. In the context of such microscopic transition, we will discuss the Absorbing phase transition (APT) in this section.

APT is a non-equilibrium transition observed in diverse systems. Such transition takes a system from a dynamically fluctuating state to an absorbing state. In the dynamically fluctuating state, the system fluctuates between different configurations. As we mentioned in the context of yielding, absorbing states are states that a system can reach by its dynamics but cannot come out of it. For example, a model that describes an epidemic spread of an infectious disease shows such transition [137]. The epidemic is modeled on a lattice site where a site can be infected or healthy. The infected sites heal by themselves or infect neighbouring sites and spread. Depending upon the infection rate, the infection either survives or goes to a state where the infection is eradicated, reaching a unique absorbing state. Absorbing states can also be degenerate in some other transitions. Similar transitions are also observed for other diverse phenomena like forest fires, turbulence, chemical catalytic reactions, etc.

Absorbing phase transitions are also observed in soft matter systems such as non-Brownian suspensions, granular materials, and soft glasses when the systems are subjected to periodic drive. The microscopic dynamics of such systems show these transitions are reversible-irreversible transitions in nature. It has been shown in the study of sheared suspensions [138] when the amplitude of the deformation is small, the particle trajectories are reversible, and they repeat the same path over the cycles. When the amplitude crosses a certain threshold value that depends on the density of the system, the trajectories of the particles become irreversible; they do not come back to the same position after one or many cycles. This reversible-irreversible transition is a form of absorbing phase transition (APT).

Such transitions have been captured in a simple yet elegant simulational model named random organization model [139]. The basic idea of this model is to give the particles a random displacement when the particles come in contact with their neighbouring particles in the course of deformation. This model shows below a density-dependent critical value of strain amplitude the system organizes so that no further collision between particles occurs and the system enters a reversible regime. But beyond the

critical value of strain, there always remains a fraction of particles, identified as active particles, that collide, and the system becomes irreversible and diffusive. The particles that collide as the shear deformation is applied are identified as the active particles, whereas the particles that do not collide are termed passive particles. The fraction of active particles that survive after repeated application of deformation cycles defines the activity of the system. When the system organizes to avoid a further collision, the system remains reversible with zero activity. The emergence of a finite number of active particles indicates the onset of irreversibility, hence finite activity.
This picture gives us an idea of how activity can be thought of as a relevant order parameter to study such transitions. These transitions have been studied in different models [140, 141] in the context of percolation. These models show that such transitions belong to a specific universality class called the conserved directed percolation (CDP) class. Such universality class describes the nature of the transition being continuous. But a recent study of a minimal particle model and a continuum theory by Mari et al. [142] shows when the mediated interaction from the active regions to the passive regions is considered, they show a deviation from the CDP universality class. It describes the discontinuous nature of the transitions observed in semi-dilute [143] and dense systems [124, 130, 134].
In Chapter 3, We have studied different transitions in sphere assemblies under oscillatory shear deformation. We have found similar discontinuous microscopic transitions interestingly coinciding with different macroscopic transitions like yielding transition, shear jamming transition, and unjamming transition.

1.3.4 Periodic drive and its effects

Subjecting systems to periodic drive is one of the most commonplace occurrences, whether we pack more rice by shaking the container or pour them from the container to the cookware. Application of periodic drive to disordered systems has shown intriguing responses [95, 121, 130, 130, 138]. Here we will discuss some of the phenomena that are relevant to this thesis.
The compaction of granular materials is one of the most visible effects of the periodic drive. We have mentioned earlier that the granular systems are athermal systems. We elaborate this by an example. The gravitational energy associated with moving a sand particle with a diameter of millimeter order by a height equal to its diameter is orders of magnitude (~ 12) more than its thermal energy at the room temperature ($k_B T$). Hence mechanical drive plays a significant role for such athermal systems to sample different configurations. Many experiments have been carried out to understand the evolution of the granular system under mechanical drive apart from the theoretical

approach to understand the statistical mechanics of the granular matter [144]. Tapping experiments [145, 146] have been carried out to study the evolution of packing in thermal systems. Experiments on the assembly of soda-lime glass beads show the system densifies as a series of tapping (vertical vibration) is applied. The steady state density depends upon the intensity of the taps applied. Recently it has been shown that assembly of hard cubic particles evolves to a densest ordered packing under periodic shear [147]. Numerical study of an assembly of spherical and non-spherical particles have shown similar compaction behaviour upon the intensity and the frequency of vibration [148]. There are many more experimental and numerical evidence of compaction of athermal systems under periodic drive.

Glasses under periodic drive also show interesting phenomena. Glassy systems have

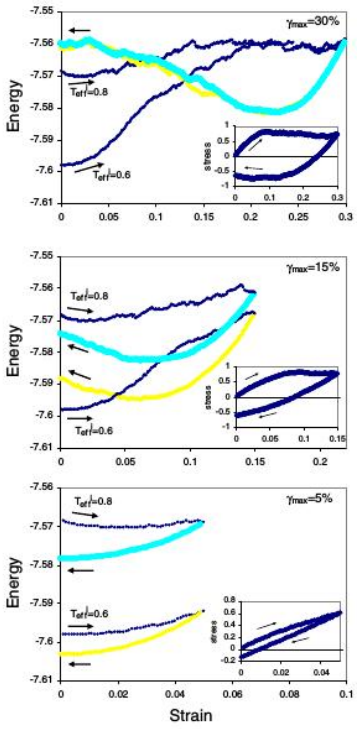

Figure 1.6: Exploration of potential energy landscape in an amorphous solid under periodic drive [149]

a rugged potential energy landscape (PEL). In the presence of thermal fluctuation, the system visits the energy basins accessible at that temperature. In glassy systems understanding the effect of the mechanical drive, decoupled from the thermal fluctuation is of importance, and many numerical studies have been carried out to investigate the role of mechanical deformation at zero temperature limit (following AQS protocol). Interestingly the study of glassy systems under periodic drive has shown that depending upon the initial state of the system and the extent of mechanical drive, different parts of the PEL (see Fig. 1.6) are accessed by the system. [149]. Glasses yield when deformed uniformly or cyclically beyond a certain threshold strain. Application of

cyclic deformation shows the nature of yielding changes depending upon the initial temperature at which the liquid has been equilibrated [95,130]. It has been shown that up to the yielding amplitude, the system descends to lower energy states or stays at the same energy state depending upon the initial temperature of equilibration. The annealing feature of the yielding transition becomes relevant in the context of the preparation of better glasses with lower and lower energy in the deeper energy minima of the PEL. The system rejuvenates or goes high up PEL when it is driven with amplitudes higher than the yielding amplitude. Interestingly, the system shows reversible-irreversible transition at the yielding transition amplitude [95, 136]. The absorbing states below yield show the ability to retain the memory of the deformation amplitude where the applied repeated cycles of deformation act as training cycles. [150,151]. Not only athermal oscillatory shearing of glasses but finite temperature finite rate shearing or thermomechanical processing of glasses is also useful for practical purposes. The experiments and simulations of metallic glasses show strain hardening under cyclic loading [152, 153], which implies yield stress value increases as repeated cycles of deformation are applied. This is of particular interest for the industrial application of glasses.

Thus we have discussed how periodic drive in disordered systems brings out a rich phenomenology that not only sheds light on the aspect of understanding the basic nature of the systems but also paves the way to make them useful in the application purpose.

So far, we have discussed various transitions such as yielding transition, shear jamming transition, reversible-irreversible transition occurring in a variety of driven disordered systems ranging from low-density colloids to granular material or high-density glassy systems. Further, we have discussed when the drive is of periodic nature, how these various transitions show further intriguing features. However, these diverse transitions occurring in characteristically different systems show intriguing similarities in their microscopic nature. One important theme of this thesis has been to have a unified understanding of these transitions under oscillatory shear deformation that we detail in chapter 3. Chapters 4 and 5 are also devoted to the study of the effect of the oscillatory shear but specific to the glassy system.

1.4 Aging and mechanical aging

In the discussion regarding glass transition, we have discussed the phenomenology of glassiness in terms of equilibrium properties in supercooled liquids approaching the glass transition. Such formalism cannot describe the system at temperatures below the glass transition temperature as the system falls out of equilibrium. Out-of-equilibrium

systems evolve over time and any properties measured at a given time become dependent on the time spent in the out-of-equilibrium state. This time is called the waiting time (t_w) and the dependence of measured system properties on the elapsed waiting time is a hallmark of *aging*. The dependence of measured properties on t_w poses an additional challenge in the study of glassy systems, however, the numerous implications of aging make such studies very important. The ubiquity of glasses in various applications make it imperative to have control of and an understanding of such changes over waiting time.

Usually, in the study of aging, the equilibrated system is quenched at $t = 0$ and driven out of equilibrium. The two-point time correlation functions (say density-density correlation function) clearly show the effect of aging through a dependence on the waiting time (the time elapsed since the quench at $t = 0$). Just after the quench, the relaxation in the system is faster compared to the relaxation at any later point. The study of aging systems is extensive, both in terms of experiments and simulations. Within the scope of this thesis, we can mention a couple of effects observed in an aging system. An aging system is often subjected to thermal cycling [154,155] to probe its non-equilibrium behavior. Thermal cycling implies that the system is subjected to two different extreme temperatures at a very fast rate. Depending on the temperatures through which the system is cycled, the system shows memory and rejuvenation effect [154]. Depending on the stages of cycling, either the system remembers the memory of the temperature, or it forgets its age and rejuvenates to higher energy states.

The response of out-of-equilibrium systems to external driving is an area of focus in this thesis. In particular, we will talk about mechanical aging resulting from mechanical driving. The study of this kind of aging is of importance in the context of aging in soil or in the manufacture of more ductile polymer glasses and so on. The application of drive enforces a new relaxation timescale in the system. In addition to rejuvenation, driven out-of-equilibrium systems sometimes display faster relaxation and a phenomenon termed *overaging* [156–159]. In Chapter 5, we study overaging in model glass-forming liquid under the application of cyclic deformation.

1.5 Scope of the thesis

Chapter 2 will summarise the model, methods and important definitions that have been used in this work.

Chapter 3 will describe a phase diagram in the amplitude-density plane, summarising various transitions observed in frictionless sphere assemblies under the application of cyclic shear deformation. It summarises key underlying similarities of the different transitions observed in different density regimes.

Chapter 4 will describe the study of exploring low energy configurations under optimal conditions in a model glass-forming system when driven cyclically at a finite rate and finite temperature.
Chapter 5 will describe the mechanical aging in a model glass-former when subjected to periodic deformation. We discuss here how mechanical drive overages or accelerates aging process.
Chapter 6 will contain the study of dynamical crossover in a model glass-former at substantially low temperatures. It will also describe the thermodynamics aspects accompanying the crossover.

Chapter 2

Models and methods

In this chapter, we briefly describe the models along with the different simulation methods employed in the subsequent chapters. Several important quantities critical for the interpretation of the results are also addressed. This chapter is arranged as follows. The first section outlines the model potentials accompanied by a short review of the simulation techniques. Next, we define various quantities and discuss the context in which they have been used to analyse the results.

2.1 Models

2.1.1 Kob-Andersen model

In the computational study of glass formers, Kob-Andersen (KA) 80:20 binary mixture [160] has been used extensively to improve the understanding of glass physics significantly. We have used this model in the study of annealing of glasses as well as in the low temperature study of supercooled liquids. In this model the interaction between particles is defined in the following manner:

$$\begin{aligned} U_{\alpha\beta}(r) &= 4\epsilon_{\alpha\beta}\left[\left(\frac{\sigma_{\alpha\beta}}{r}\right)^{12} - \left(\frac{\sigma_{\alpha\beta}}{r}\right)^{6}\right] \\ &\quad + 4\epsilon_{\alpha\beta}\left[c_0 + c_2\left(\frac{r}{\sigma_{\alpha\beta}}\right)^{2}\right], r_{\alpha\beta} \le r_{c\alpha\beta} \\ &= 0, \qquad\qquad r_{\alpha\beta} > r_{c\alpha\beta}. \end{aligned} \tag{2.1}$$

c_0 and c_2 are chosen such that the potential and force between particles go to zero continuously at the cutoff distance. Here, indices (α, β) represent particle type (A or B) in the binary mixture. We report results in reduced units, with units of length,

energy and time scales being σ_{AA}, ϵ_{AA} and $\sqrt{\sigma_{AA}^2 m_{AA}/\epsilon_{AA}}$, respectively. The model parameters are $\epsilon_{AB}/\epsilon_{AA} = \epsilon_{BA}/\epsilon_{AA} = 1.5$, $\epsilon_{BB}/\epsilon_{AA} = 0.5$, and $\sigma_{AB}/\sigma_{AA} = \sigma_{BA}/\sigma_{AA} = 0.8$, $\sigma_{BB}/\sigma_{AA} = 0.88$. Energy values reported are energies per particle.

2.1.2 Soft-sphere model

Assembly of soft spheres interacting via repulsive harmonic potential is a well studied model for a range of systems from foams [161] to dense glassy systems [162]. In our study of a wide range of athermal systems under mechanical deformation, we have used a binary mixture (50:50) of such particles whose interaction potential is defined in the following manner:

$$\begin{aligned} U_{\alpha\beta} &= \frac{1}{2}\epsilon_{\alpha\beta}(1 - \frac{r_{\alpha\beta}}{\sigma_{\alpha\beta}})^2, r_{\alpha\beta} \leq \sigma_{\alpha\beta} \\ &= 0 \end{aligned} \tag{2.2}$$

We report results in reduced units, with units of length, energy and time scales being σ_{AA}, ϵ_{AA} and $\sqrt{\sigma_{AA}^2 m_{AA}/\epsilon_{AA}}$, respectively. Here, indices (α, β) represent particle type (A or B) in the binary mixture.The model parameters are $\epsilon_{AA} = \epsilon_{AB} = \epsilon_{BB}$ and $\sigma_{AB}/\sigma_{AA} = \sigma_{BA}/\sigma_{AA} = 1.2$, $\sigma_{BB}/\sigma_{AA} = 1.4$. Energy values reported are energies per particle.

2.2 Simulation methods

2.2.1 Athermal quasistatic cyclic shear deformation

The soft sphere assemblies have been subjected to an athermal quasistatic (AQS) shear deformation for a range of densities and a range of deformation amplitudes. We first describe the simulation protocol followed by relevant simulation details.

2.2.1.1 AQS protocol

AQS protocol consists of two steps.

- In the first step, the particle coordinates are given affine transformation. Affine transformation is a linear mapping that preserves points, straight lines, and planes. We apply the transformation with the following transformation matrix (in xz shear plane), which preserves volume.

$$\begin{bmatrix} x' \\ y' \\ z' \end{bmatrix} = \begin{bmatrix} 1 & 0 & d\gamma \\ 0 & 1 & 0 \\ 0 & 0 & 1 \end{bmatrix} \begin{bmatrix} x \\ y \\ z \end{bmatrix}$$

- In the next step the potential energy function is minimized using standard minimization methods like conjugate gradient (CG) or FIRE [163] or Steepest descent (SD) algorithm.

In our work, $d\gamma$ is the small shear strain step which is the ratio of the change in length along the shear direction to the original length in the perpendicular direction on the shear plane (dx/L_z, dx is the change in length, L_z is the undeformed length of the box along the z direction, in our case).
Athermal quasistatic deformation is a limit where the system is probed when the temperature $T \to 0$ and the rate of deformation $\dot{\gamma} \to 0$. The system can be studied under the sole effect of mechanical deformation as there is no thermal fluctuation involved. The timescale of the relaxation of the system stays well within the time scale imposed by the rate of applied deformation.

2.2.1.2 Cyclic shear deformation protocol

The system is deformed with an amplitude γ_{max} in small $d\gamma$ strain steps followed by minimization. The strain within a cycle varies as $0 \to \gamma_{max} \to 0 \to -\gamma_{max} \to 0$. The strain step used in our work is 10^{-3} for packing fractions (ϕ) below 0.661 and 10^{-4} for higher packing fractions. The cycles are applied repeatedly till the system reaches a steady state. The terminology “steady state" repeatedly used in our work refers to the state of the system when the characterising properties (such as contact number or potential energy) do not change statistically with the number of deformation cycles. To reach the steady state, we perform $\sim 10^2$ cycles in the irreversible regime and up to $10^3 \sim 10^4$ cycles in the reversible regime. All the measurements are done for stroboscopic or the strain zero configurations. γ_{accum} which is measured as $4 \times N_{cycle} \times \gamma_{max}$ can be considered as an equivalent time as there is no real time involved in this method.

2.2.1.3 Simulation details

Initial configurations in the density range $0.54 - 0.627$ are obtained from hard sphere fluid configurations at $\phi = 0.363$, subjected to fast compression using Monte Carlo simulations.The isotropic jamming density is estimated to be $\phi_J = 0.648$, following the method in [103]. Configurations close to ϕ_J ($\phi = 0.638 - 0.647$ and $\phi =$

$0.650 - 0.661$) are obtained by a single step decompression or compression of configurations at ϕ_J, and configurations well above ϕ_J are obtained by multiple step compression of configurations at ϕ_J. Each compression or decompression step is followed by the energy minimization (CG).The range of packing fraction for our study is $[0.54 - 0.72]$. The strain amplitude range is $[0.001 - 0.2]$ and $[0.01 - 1.0]$ for above and below ϕ_J respectively. For $\phi = 0.56, 0.54$, γ_{max} ranges from $[0.1 - 8.0]$. Approximately 2000 independent simulations are used to construct the complete phase diagram. The number of independent samples used in different density ranges are - 10 for $0.661 - 0.72$, $10 - 20$ for $0.650 - 0.661$, $4 - 10$ for $0.638 - 0.648$, $6 - 10$ for $0.54 - 0.627$, and $1 - 2$ samples at the lowest densities at high amplitudes.

In this context, we will have a brief discussion about a few more important things as follows:

- **Minimization methods:** We have mostly used conjugate gradient(CG) method to minimize the potential energy function. CG is an optimization method for both linear and non-linear systems. An iterative algorithm (the Polak-Ribiere version used in package LAMMPS) has been used to minimize the energy. In this iterative approach the new search direction is made perpendicular or conjugate to all previous search directions. CG is a more efficient optimization method compared to the steepest descent (SD) where search direction is just set as the negative gradient of the energy function at every iteration. Another minimization method that has been used in our work is the fast intertial relaxation engine or the FIRE [163] algorithm. This is a molecular dynamics (MD) scheme with an adaptive timestep. The principle followed in this minimization method can be thought of as a blind skier searching the fastest route to reach the bottom of the valley. The skier can steer his way through the valley, the potential energy landscape governed by an equation of motion. The skier can choose acceleration to a steeper direction or can stop when the direction is uphill, tracking the power at a time $P(t) = F(t).v(t)$, where $F(t)$ and $v(t)$ are force an acceleration at a given time. In the right direction, the timestep is increased, and minima can be reached in a faster way. We have found in our work this algorithm finds lower energy minima than minima obtained through the conjugate gradient method (see Chapter 3). We will further discuss the effect of different minimization methods in the next chapter. The stopping criterion for minimization is that the energy change between successive line minimizations, normalized to the energy value or the magnitude of the maximum component of force, falls below 10^{-16}, whichever is satisfied earlier.

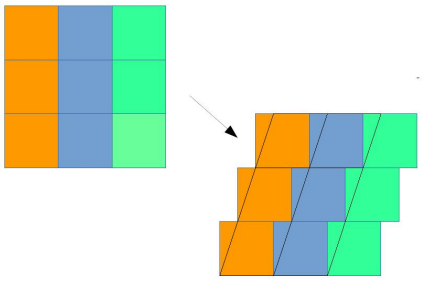

Figure 2.1: Sliding-brick and deformed cube representation of system with flow.

- **Lees-Edwards boundary conditions:** Lees-Edwards (LE) boundary condition is a periodic boundary condition (PBC) [164] employed in a system with a shear flow. We represent the LE PBC in a sliding brick representation (shown in coloured boxes in Fig.2.1) along with the deformed cube representation (shown in black outline). When a box is deformed we can assume the particles of an upper layer will move more along the sheared direction (right in this case). Hence when a particle crosses the boundary it is important to take into account from which layer it escaped and accordingly with an adjusting term along with normal periodic boundary conditions the extra or less displacement, caused be the deformation of the box itself, should be taken care of when the particle is put back in the original simulation box. In our sheared simulation to determine the position of particles or to calculate quantities like force or energy where positions of two particles are required, LE PBC is used. Needless to say, LE PBC reduces to normal PBC at undeformed condition.

2.2.2 Equilibrium molecular dynamics in a canonical ensemble

Equilibrium molecular dynamics simulation has been performed in a constant temperature (T) constant volume (V) and a constant number of particles (N) ensemble or a canonical (NVT) ensemble of KA 80:20 binary mixture. Simulation of an NVT ensemble involves the system being in contact with a heat bath. The coupling of the system to the heat bath can be of stochastic nature as well as of deterministic nature. In our simulation, we have used Nosé-Hoover thermostat [165] which couples to the system in a deterministic way. The application of the Nosé-Hoover thermostat is an application of extended Lagrangian where artificial coordinates and velocities are used. Along with the degree of freedom of the particles in the system the dynamical equation involves the bath variables. Further in works of Maryna et al [166] it has been shown that the Nosé-Hoover chain removes the shortcomings of a single Nosé-Hoover

thermostat.

2.2.2.1 Nosé-Hoover thermostat

The dynamical equation of motion in terms of real varaibles can be written as follows:

$$\begin{aligned}
\dot{\mathbf{r}} &= \frac{\mathbf{p}_i}{m} \\
\dot{\mathbf{p}}_i &= \mathbf{F}_i - \frac{p_{\xi_1}}{Q_1}\mathbf{p}_i \\
\dot{\xi}_k &= \frac{p_{\xi_k}}{Q_k} \\
\dot{p}_{\xi_1} &= (\sum_i \frac{p_i^2}{m_i} - LK_BT) - \frac{p_{\xi_2}}{Q_2}p_{\xi_1} \\
\dot{p}_{\xi_k} &= (\frac{p_{\xi_{k-1}}^2}{Q_{k-1}} - K_BT) - \frac{p_{\xi_{k+1}}}{Q_{k+1}}p_{\xi_k} \\
\dot{p}_{\xi_M} &= (\frac{p_{\xi_{M-1}}^2}{Q_{M-1}} - K_BT)
\end{aligned} \tag{2.3}$$

The equations together describe the evolution of the canonical ensemble where $\mathbf{r}_i$ and $\mathbf{p}_i$ is the position and momenta of the i^{th} particle in the system. L is the number of degrees of freedom. M number of chains are coupled together where $k = 1,...M$. p_{ξ_k} and Q_k are the momenta and mass like variables of the thermostat. ξ is the friction coefficient that can assume a positive or negative value.
For such non-Hamiltonian dynamics, it has been shown that the conserved quantity is an extended Hamiltonian-like quantity that involves thermostat variables, stated as follows.

$$H'(p,q,\xi,p_{xi}) = H(p,q) + \sum_{k=1}^{M}\frac{p_{\xi_k}^2}{2Q_k} + LK_BT\xi_1 + \sum_{k=2}^{M}k_BT\xi_k \tag{2.4}$$

The dynamical equations are solved through the construction of a Liouville operator where along with particles' position and momenta, thermostat variables are considered as phase space variable. The operator is implemented using the Trotter identity. Liouville equation combined with Trotter formula is a powerful tool to solve time-reversible dynamical equations.

2.2.2.2 Simulation details:

The simulations has been performed in a KA 80:20 binary mixture of 4000 system size. The initial configurations for the simulations below $T = 0.466$ are prepared by

quenching equilibrated configurations from $T = 0.466$ and for the simulations above $T = 0.466$ configurations are obtained by quenching equilibrated configurations from $T = 1.0$ to respective target temperatures. We have performed equilibrium simulations for a range of $T = 0.9 \sim T = 0.365$. The density (ρ) has been kept constant at 1.2. 16-25 independent trajectories have been studied (unless otherwise crystallized). The equilibration run varies from 20-100 times of the structural relation time depending upon the simulation temperature. The system at low temperatures shows crystallization [167]. The crystallizing samples have been discarded to study the equilibrium properties. We will describe how the crystallization in the system has been identified and taken care of in the following discussion. The timestep below and above T_{MCT} are respectively 0.01 and 0.005.
In this context we will briefly discuss the crystalization in the system at low temperatures.

Crystallization: We analyse the crystallization kinetics employing standard meth-

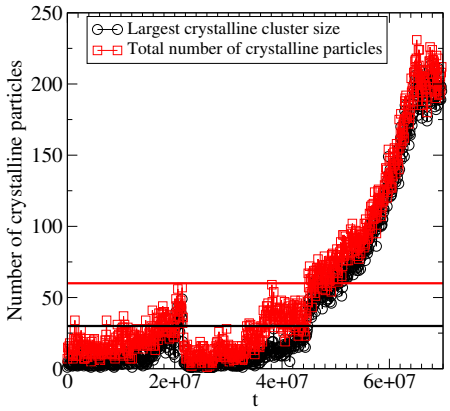

Figure 2.2: A crystallizing sample at $T = 0.37$ is hown

ods [167,168] that are based on defining bond orientational order parameters for each particle i, $q_{lm}(i) = \frac{1}{n_b(i)} \sum_{j=1}^{n_b(i)} Y_{lm}(\theta_{ij}, \phi_{ij})$, where θ_{ij} and ϕ_{ij} are angles formed by separation vectors $\mathbf{r}_{ij}$ between particles i and neighbors j. The l value used is 6. We employ cutoffs for defining neighbors from the location of the first minimum of the pair correlation functions $g_{\alpha\beta}(r)$, which are, $r_{AA}^{cut} = 1.4$, $r_{AB}^{cut} = 1.25$ and $r_{BB}^{cut} = 1.1$. Following [167], we define two neighbors to be bonded if the normalised dot product $\mathbf{q}_6(i).\mathbf{q}_6(j)/|\mathbf{q}_6(i)||\mathbf{q}_6(j)|$ is bigger than 0.7, and a particle is labeled as crystalline if it has at least 7 such bonds. Crystalline particles are then connected if they are within a cutoff distance, for which we use slightly larger values $r_{AA}^{clust} = 1.5$, $r_{AB}^{clust} = 1.4$ and $r_{BB}^{clust} = 1.2$. We then perform a cluster finding procedure to identify all clusters of connected crystalline particles and report the largest cluster size of crystalline particles. Because the largest cluster size may not fully reflect the degree of crystallinity in cases

where the cluster sizes are small, and the clustering definition may not capture physical proximity, we also report the total number of crystalline particles. These are shown in Fig. 2.2. In our analysis, when a trajectory exhibits persistently a largest crystalline cluster size of 30 or above, or the total number of crystalline particles is above 60 in a persistent fashion, or even otherwise, when the growth of crystallinity suggests the onset of crystallization, we exclude the corresponding trajectory segments (*i. e.* parts of the trajectory thereafter) from the computation of averages and statistics.

2.2.3 Cyclic shear deformation at a finite rate and a finite temperature

We have employed cyclic shear deformation in a KA 80:20 binary mixture using the SLLOD equation of motion. We give a brief description of the SLLOD equations and the cyclic shear protocol in the following sections.

2.2.3.1 SLLOD: dynamical equations for non-equilibrium molecular dynamics simulation

In the work by Hoover et al [169] the bulk viscosity in soft sphere dense fluids has been measured via a non-equilibrium molecular dynamics study. The dynamical equations used in this work to study the evolution of the system under shear flow were derived from a Hamiltonian named DOLLS Hamiltonian. Amusingly the name originated from the qp term in the Hamiltonian in resemblance to the “Kewpie" dolls. Later it was found the mentioned dynamical equations do not provide a correct description of normal stress difference. Evans and Morriss in 1984 [170] proposed a set of dynamical equations to simulate shear flow. These equations are named SLLOD equations of motions. Because of its close connection to the equations derived from DOLLS Hamiltonian, the equations were named this way. SLLOD equations are non-Hamiltonian equations. The general form of the SLLOD equation of motions are described as the following:

$$\begin{aligned} \dot{\mathbf{r}}_i &= \frac{\mathbf{p}_i}{m_i} + \mathbf{r}_i.\nabla\mathbf{v} \\ \dot{\mathbf{p}} &= \mathbf{F}_i - \mathbf{p}_i.\nabla\mathbf{v} \end{aligned} \tag{2.5}$$

Where m_i, $\mathbf{r}_i$ and $\mathbf{p}_i$ are mass, position vector and momentum vector of the i^{th} particle. $\mathbf{F}_i$ is the force on the i^{th} particle due to all the other particles in the system.$\nabla\mathbf{u}$ is the velocity gradient tensor. In a simple planar shear with flow in the x direction and gradient in the y direction, the tensor takes the following form.

$$\nabla \mathbf{v} = \begin{bmatrix} 0 & 0 & 0 \\ \dot{\gamma} & 0 & 0 \\ 0 & 0 & 0 \end{bmatrix}$$

SLLOD equations are first order linear equations of laboratory position and thermal velocity or peculiar velocity. It represents an equivalent of Newton's equation for a system with a homogeneous flow [171]. A thermostatting mechanism is required to achieve a steady state. The form of SLLOD equations when coupled to a thermostat (Nose Hoover here) is the following [172].

$$\begin{aligned} \dot{\mathbf{r}}_i &= \frac{\mathbf{p}_i}{m_i} + \mathbf{i}\dot{\gamma} r_{yi} \\ \dot{\mathbf{p}} &= \mathbf{F}_i - \mathbf{i}\dot{\gamma} p_{yi} - \mathbf{p}_i \frac{p_\xi}{Q} \\ \dot{\xi} &= \frac{p_\xi}{Q} \\ \dot{p}_\xi &= \sum_{i=1}^{N} \frac{\mathbf{p}_i^2}{m_i} - N_f k_B T \end{aligned} \tag{2.6}$$

Where Q is the effective mass of the thermostat, ξ is the friction coefficient, p_ξ is momentum like variable of the thermostat, $N_f = 3N$ or the number of degrees of freedom of the system. These are the equations for a system under simple shear along the x-axis with a strain rate $\dot{\gamma}$ in the xy plane.

2.2.3.2 Cyclic shear protocol (at a finite temperature, at a finite rate)

The system has been subjected to an oscillatory shear where the strain $\gamma(t)$ and the strain rate $\dot{\gamma}(t)$ at time t varies as:

$$\gamma(t) = \gamma_{max} sin(\omega t)$$

$$\dot{\gamma}(t) = \gamma_{max} \omega cos(\omega t)$$

where ω is the frequency, time period of T_p is $T_p = 2\pi/\omega$, γ_{max} is the amplitude of the shear. In our simulation when we talk about a fixed rate we mean the shear rate at $t = 0$. The simulation time is calculated as $t = N_{cycle} \times t_p$. All the quantities are calculated for the stroboscopic or the strain zero configurations unless otherwise mentioned.

2.2.3.3 Simulation details:

We consider $N = 4000$ particles at the reduced density $\rho = 1.2$ and perform simulations for a range of temperatures ($T \in [0.25, 0.4]$) across the Kauzmann temperature estimated in previous work to be ($T_K \approx 0.3$), shear rates ($\dot{\gamma}(0) \in [10^{-6}, 10^{-3}]$), and strain amplitudes (γ_{max}) up to 0.06. We perform conjugate gradient minimization on the simulated (stroboscopic) configurations to obtain energy minimum configurations (inherent structures). The initial configurations are generated by quenching high temperature ($T = 0.466$) equilibrated liquid to the desired simulation temperature at one step. 8 independent samples (a few cases 4) have been simulated. As all the studied temperatures were pretty low, we have used 0.01 timestep throughout. The crystallizing samples have been discarded following the same protocol mentioned earlier in this chapter.

2.3 Definitions

2.3.1 Contacts

In Chapter 3, we describe the study of jammed and unjammed soft sphere assemblies. In the study of such sphere packings, the geometry of the packings is of primary interest, and it is described by the contacts the particles have. We present a detailed description of such contacts enumerated in different ways.
Average contact number (Z): Z is defined as

$$Z = \frac{C}{N} \tag{2.7}$$

where C is the number of where C is the sum of the number of contacts of all particles, and contact implies $r_{ij} \leq \sigma_{ij}$ after energy minimization.
Average non-rattler contact number (Z_{NR}): Z_{NR} is defined as

$$Z_{NR} = \frac{C_{NR}}{N_{NR}} \tag{2.8}$$

where N_{NR} is the number of non-rattlers in the system (rattlers are particles with less than $D + 1$ contacts, D being the dimension), and C_{NR} is the sum of the number of contacts of the non-rattler particles.
Average mechanical contact number (Z_M): Z_M is defined as:

$$Z_M = \frac{C_M}{N_M} \tag{2.9}$$

where C_M is the sum of the number of mechanical contacts of N_M particles, each of which experiences finite force or stress. A mechanical contact is identified when the overlap of a pair is greater than (10^{-10}). N_M is the number of particles that have finite force or stress. Z_M can take values as 6 ($2D$ where D is the dimension) or zero, depending on a jammed or unjammed phase respectively.
We have performed a geometric bootstrap method to count rattlers where we keep removing rattlers and redefine the rattler count. This is required because once a rattler is identified and removed from the count, its neighbouring particles also experience a reduction in contact counts. This way after an iterative process, only particles with contact greater than $D+1$ survives or we end up with 0 contacts. We have checked an iterative count of Z_{NR} matches well with Z_M(see Fig. 2.3).

We have mentioned earlier the time to attain convergence and the quality of the

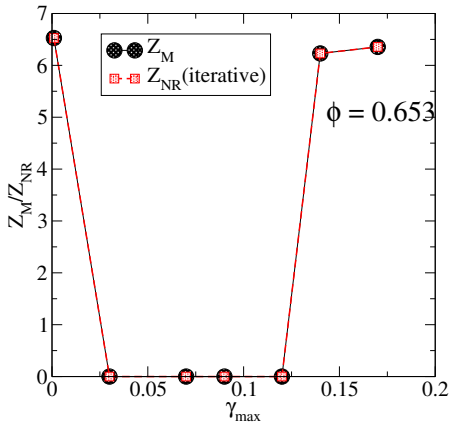

Figure 2.3: Z_M, calculated at a given packing fraction for a range of deformation amplitudes, has been compared with Z_{NR} estimated iteratively or using the 'bootstrap' procedure for one sample density. They show complete agreement.

minima depends on the minimization method used. Though most of our simulations have been done using the CG method, a few cases where the FIRE or the SD method becomes more relevant to use. We will discuss a few things in this regard.
In the study of packings, an important measure is the cumulative distribution of contacts $Z(r)$. This is the cumulative probability distribution of contact numbers as a function of distance(r) between particles. A plot of $Z(r)$ vs $r-\sigma$, depicts the nature of the packing beyond the overlap, ranging from proximity to very far away.

ust above isotropic jamming density (ϕ_J), we will show in Chapter 3 that the FIRE minimization method finds lower energy minima than CG.. At very high density CG and FIRE work reasonably similar ways. But below ϕ_J we can see a significant difference in the generation of packings as we vary the minimization method.(see Fig. 2.4). In this low density regime CG (as well as FIRE) generally pushes the particles much further away compared to SD. Ideally, in the soft sphere potential model, the minimization should stop just as the distance (r) becomes equal to the diameter (σ)

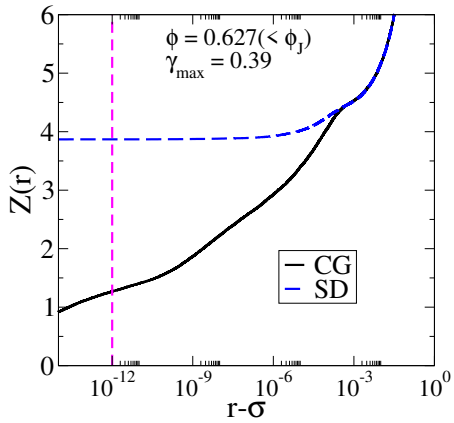

Figure 2.4: The cumulative distribution of contact numbers has been shown for a low density packing where two different kinds of minimization namely CG and SD have been used. For SD, the plateau of $Z(r)$ entends to much higher precision. A decrease in strain step shows a gradual increase of plateau to lower values in the case of CG. the vertical line shows the tolerance value used to define contact at low density.

value. SD performs in a better way in this scenario as we can see the plateau value of $Z(r)$ vs $r-\sigma$ extends to much higher precision compared to CG. For structural characterization of low density packing, we have used the SD minimization method. we discuss further details in this regard in the next chapter.

2.3.2 Mean squared displacement and cycle to cycle displacement

We have measured diffusivity in various contexts in our work. Diffusivity D defined as $\Delta r^2(t) = 6Dt$ (for a three dimensional system) where $\Delta r^2(t)$ is the mean squared displacement. Mean squared displacement (MSD) is defined as:

$$\triangle r^2(t) = \frac{1}{N}\sum_{i=1}^{N} |r_i(t+t_o) - r_i(t_o)|^2 \tag{2.10}$$

where $r_i(t)$ is the position of the i^{th} particle at time t. In the case of study of cyclically sheared configurations $r_i(t)$ can be replaced with $r_i(k)$ where $r_i(k)$ is the position at zero strain of i^{th} particle in cycle number k. MSD is averaged over time origin t_0 or equivalently reference cycles k^o.
In this regard displacement between cycles of deformation is also an important quantity and average displacement between cycles(Δr) is defined as the following:

$$\triangle r(k,N) = \frac{1}{N}\sum_{i=1}^{N} r_i(k+N) - r_i(k) \tag{2.11}$$

N is the number of the interval of cycles. N is kept fixed (preferably 1) and the cycle index k is varied. It gives an idea of how the average movement of particles within a fixed time window evolves with time.
All these quantities have been calculated for strain zero or stroboscopic configurations in the case of shear simulations.

2.3.3 Correlation functions

We have measured different relevant correlation functions in the study of the glassy system (Chapter 6). Here we describe the relevant details of the different correlation functions.
We introduce correlation functions that describe time, space, or frequency dependent response in the system. A time correlation function between two quantities A and B is generally defined as follows:

$$C_{AB}(t', t'') =< A(t)B(t) >$$

$< ... >$ implies equilibrium average. A and B being the same quantity it is called auto-correlation function.
In the study of glassy dynamics, density correlation is widely studied. Local density is defined as the following for a system comprising of N particles.

$$\rho(\mathbf{r}, t) = \sum_{i=1}^{N} \delta(\mathbf{r} - \mathbf{r}_i(t)) \tag{2.12}$$

- **Overlap function:** The dynamics in the glassy system is widely studied by the time correlation function of the local density function, the overlap function($q(t)$).

$$\begin{aligned} q(t) &= \int d\mathbf{r}\rho(\mathbf{r}, t)\rho(\mathbf{r}, t + t_0) \\ &= \sum_i \sum_j \delta(\mathbf{r}_j(t_0) - \mathbf{r}_i(t + t_0)) \end{aligned} \tag{2.13}$$

  $q(t)$ can be divided into self part and distinct part:

$$\begin{aligned} q(t)_s &= \sum_i \delta(\mathbf{r}_i(t_0) - \mathbf{r}_i(t + t_0)) \\ q(t)_d &= \sum_i \sum_{i \neq j} \delta(\mathbf{r}_i(t_0) - \mathbf{r}_j(t + t_0)) \end{aligned} \tag{2.14}$$

  In simulation δ function is approximated by a window function $w(x)$ described

as below

$$q(t) = \sum_j \sum_i w(|\mathbf{r}_j(t_0) - \mathbf{r}_i(t+t_0)|) \quad \text{where} \quad w(x) = \begin{cases} 1.0 & \text{if } x \leq a \\ 0 & \text{otherwise.} \end{cases} \tag{2.15}$$

The value of the overlap function depends on the choice of the cutoff parameter a. This parameter is chosen in such a way that the particle positions separated due to vibrational motion are treated as the same as a. It is chosen from the plateau region on the MSD curve as shown in [173].

- **Van Hove function**: It is defined as the probability density of finding a particle i in the vicinity of r at time t given that the particle j was in the vicinity of origin at time $t = 0$.

$$\begin{aligned} G(\mathbf{r},t) &= \frac{1}{N}\langle \rho(\mathbf{r},t)\rho(0,0)\rangle \\ &= \frac{1}{N}\left\langle \sum_j \sum_i \delta(\mathbf{r} - \mathbf{r}_j(t) + \mathbf{r}_i(0))\right\rangle \text{ using Eq. 2.12} \end{aligned} \tag{2.16}$$

$G(\mathbf{r},t)$ has two parts as described below.

$$G(\mathbf{r},t) = G_s(\mathbf{r},t) + G_d(\mathbf{r},t) \tag{2.17}$$

$$G_s(\mathbf{r},t) = \frac{1}{N}\left\langle \sum_i \delta(\mathbf{r} - \mathbf{r}_i(t) + \mathbf{r}_i(0))\right\rangle$$

$$G_d(\mathbf{r},t) = \frac{1}{N}\left\langle \sum_i \sum_{j\neq i} \delta(\mathbf{r} - \mathbf{r}_j(t) + \mathbf{r}_i(0))\right\rangle$$

- **Intermediate scattering function:** The Fourier transform of $G(\mathbf{r},t)$ is called the intermediate scattering function $F(\mathbf{k},t)$ defined as the following.

$$\begin{aligned} F(\mathbf{k},t) &= \int d\mathbf{r} G(\mathbf{r},t)\exp(-i\mathbf{k}.\mathbf{r}) \\ &= \frac{1}{N}\langle \rho(\mathbf{k},t)\rho(-\mathbf{k},0)\rangle \end{aligned} \tag{2.18}$$

Where

$$\rho(\mathbf{k},t) = \int d\mathbf{r}\rho(\mathbf{r},t)\exp(-i\mathbf{k}.\mathbf{r}) \tag{2.19}$$

$F(\mathbf{k},t)$ can be also be divided into self part and distinct part :

$$F(\mathbf{k},t) = F_s(\mathbf{k},t) + F_d(\mathbf{k},t)$$

$$F_s(\mathbf{k},t) = \int d\mathbf{r} G_s(\mathbf{r},t)\exp(-i\mathbf{k}.\mathbf{r})$$
$$F_d(\mathbf{k},t) = \int d\mathbf{r} G_d(\mathbf{r},t)\exp(-i\mathbf{k}.\mathbf{r}) \tag{2.20}$$

- **Dynamical heterogeneity:** Dynamical heterogeneity has been studied calculating the four point correlation function χ_4, the standard deviation of the overlap function.

$$\chi_4(t) = \frac{1}{N}\left(\langle q(t)^2\rangle - \langle q(t)\rangle^2\right) \tag{2.21}$$

The quantity, $\chi_4(t)$ can be written as an integral to a higher order, four point correlation function $g_4(\mathbf{r},t)$ commonly used in the context of dynamical heterogeneity.

$$\begin{aligned} g_4(\mathbf{r},t) &= \frac{1}{N}\langle\rho(0,0)\rho(0,t)\rho(\mathbf{r},0)\rho(\mathbf{r},t)\rangle - \langle\rho(0,0)\rangle\langle\rho(0,t)\rangle\langle\rho(\mathbf{r},0)\rangle\langle\rho(\mathbf{r},t)\rangle \\ \chi_4(t) &= \int d\mathbf{r} g_4(\mathbf{r},t) \end{aligned} \tag{2.22}$$

2.3.4 Structural quantities

Though in the study of glass transition, structural properties do not show significant changes a few quantities mentioned below are widely used in various structural studies.

- **radial distribution function:** The radial distribution function in a simple liquid is defined as:

$$g(\mathbf{r}) = \frac{1}{N\rho}\langle\sum_i^N\sum_{i\neq j}^N \delta(\mathbf{r}-\mathbf{r}_i+\mathbf{r}_j)\rangle \tag{2.23}$$

The definition of g(r) implies that on average the number of particles lying within the range r to $r+dr$ from a reference particle is $4\pi r^2\rho g(r)dr$ and the peaks in $g(r)$ represent shells of neighbours around the reference particle.

- **Static structure factor:** The static structure factor $S(\mathbf{k})$ is defined as the following:

$$S(\mathbf{k}) = \langle\frac{1}{N}\rho_{\mathbf{k}}\rho_{-\mathbf{k}}\rangle \tag{2.24}$$

The static structure factor and the radial distribution function is related by the following relation:

$$S(\mathbf{k}) = 1 + \rho\int g(r)exp(-i\mathbf{k}.\mathbf{r})d\mathbf{r} \tag{2.25}$$

In experiments the structure factor is determined from measurements of the cross-section for scattering of neutrons or x-rays.

2.3.5 Configurational entropy

The configurational entropy (S_c) is calculated by subtracting the *vibrational* entropy (S_{vib}) associated with individual *glasses* (or basins of free/potential energy minima or inherent structures) from the total entropy (S) of the liquid.

$$S_c = S - S_{vib} \tag{2.26}$$

2.3.5.1 Total entropy

The total entropy is computed from the Helmholtz free energy A, and subtracting the internal energy from it. The Helmholtz free energy is obtained by performing thermodynamic integration numerically from the ideal gas reference state at a high temperature T_r, to the desired density, and and a thermodynamic integration at fixed density to the desired low temperature, using the thermodynamic identities:

$$\left(\frac{\partial A}{\partial V}\right)_{N,T} = -P \tag{2.27}$$

$$\left(\frac{\partial (A/T)}{\partial (1/T)}\right)_{N,V} = U \tag{2.28}$$

where U is the internal energy and P is the pressure. We choose a thermodynamic path from zero density to the simulation density ($\rho = 1.2$, at $T_r = 3.0$ for Kob-Andersen (KA) 80:20 binary mixture). Writing the total free energy A as a sum of the ideal and excess parts, we have $A(\rho, T) = A_{id}(\rho, T) + A_{ex}(\rho, T)$, with $A_{id}(\rho, T) = NT(3ln\ \Lambda + ln\ \rho - 1)$, $\Lambda = \frac{h}{\sqrt{2\pi T}}$. Though not strictly necessary, we use the numerical value of the Planck's constant $h = 0.1858$ using Argon units, in computing the numbers we report. Thermodynamic integration is performed for the excess free energy, first with respect to density:

$$A_{ex}(\rho, T_r) - A_{ex}(0, T_r) = NT_r \int_0^\rho d\rho \left(\frac{\beta_r P}{\rho^2} - \frac{1}{\rho}\right) \tag{2.29}$$

where the reference excess free energy is

$$A_{ex}(0, T_r) = -T_r ln\left(\frac{N!}{N_A! N_B!}\right), \tag{2.30}$$

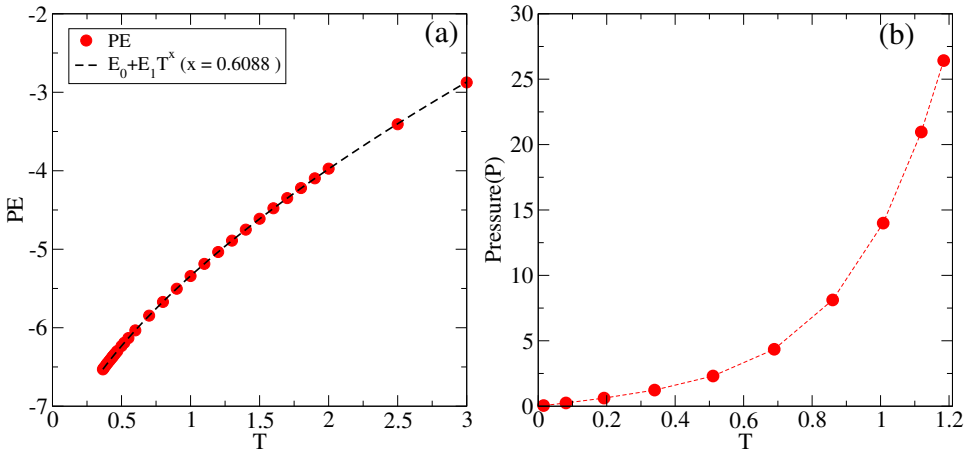

Figure 2.5: (a) Potential energy (at $\rho = 1.2$ for Kob-Andersen (KA) 80:20 binary mixture) as a function of temperature, and (b) pressure as a function of density ρ at reference temperature ($T_r = 3.0$ Kob-Andersen (KA) 80:20 binary mixture). The potential energies are well described by the Rosenfeld-Tarazona scaling of $E = a + bT^{3/5}$, but we use a best fit exponent of 0.6088 in performing the thermodynamic integration.

and $\beta = (k_B T)^{-1}$. The pressures employed for the above numerical integration are shown in Fig. 2.5. The thermodynamic integration to the desired temperature is then performed by integrating the potential energy E.

$$A_{ex,T} = T(\beta_r A_{ex}(\rho, T_r) + \int_{\beta_r}^{\beta} d\beta^{'} E(\rho, \beta^{'})) \tag{2.31}$$

The potential energy, shown in Fig. 2.5, follows the Rozenfeld-Tarazona scaling ($E = a + bT^{3/5}$) quite well, as noted before [174], but we use the best fit to the numerical data with an exponent of 0.6088 for the numerical integration. The entropy is then obtained from

$$S = -\left[\frac{A(\rho, T)}{T} - \frac{E(\rho, T)}{T} - \frac{3N}{2}\right]. \tag{2.32}$$

2.3.5.2 Vibrational entropy (harmonic approximation)

The vibrational entropy is computed, in the harmonic approximation, by expanding the energy around a local energy minimum of energy e_{IS} as

$$E = e_{IS} + \frac{1}{2}\sum_{ij\alpha\beta} \frac{\partial^2 U}{\partial r_{i\alpha}\partial r_{j\beta}} \delta r_{i\alpha}\delta r_{j\beta}, \tag{2.33}$$

truncated at the second order. Diagonalizing the Hessian H, with

$$H_{i\alpha j\beta} = \frac{\partial^2 E}{\partial r_{i\alpha}\partial r_{j\beta}} \tag{2.34}$$

one obtains $3N-3$ non-zero eigen values λ_i (and 3 zero eigen values corresponding to global translations), and the corresponding frequencies $\omega_i = \sqrt{\lambda_i}$. The vibrational free energy (with energies measured with respect to the minumum values e_{IS}) can be written as

$$\beta f_{vib} =< \sum_{i=1}^{3N-3} \ln(\beta\hbar\omega_i) - \ln z_0^3 > \tag{2.35}$$

where

$$z_0 = \left[\frac{1}{h}\sqrt{\frac{2\pi}{\beta}}V^{1/3}\right] \tag{2.36}$$

corresponds to the 3 zero frequency modes. The vibrational entropy is obtained as

$$S_{vib} = -\frac{\partial f_{vib}}{\partial T}. \tag{2.37}$$

2.3.5.3 Vibrational entropy (anharmonic correction)

In the harmonic approximation, the (vibrational) potential energy as a function of temperature can be written as

$$E_{vib}(T) =< e_{IS} > + \frac{3N}{2}k_B T. \tag{2.38}$$

Thus, if one considers the instantaneous potential energy and subtracts e_{IS} where e_{IS} is the local energy minimum to which the instantaneous configuration maps, the difference should equal $\frac{3N}{2}k_B T$. While this is found to be nearly the case for the KA-BMLJ [175], there is a non-negligible anharmonic component. Thus, if one considers the system to be thermalised within the basin of an inherent structure, one can write the anharmonic component as

$$E_{anh}(T) =< E_{vib}(T) - e_{IS} > - \frac{3N}{2}k_B T. \tag{2.39}$$

In order to compute the contribution of this anharmonicity, for inherent structures obtained at a temperature T_p, one considers that $E_{anh}(T)$ has a temperature dependence that can be expressed as [176]

$$E_{anh}(T) = \sum_{n=2}^{n_{max}} c_n T^n. \tag{2.40}$$

The derivative of $E_{anh}(T)$ is the anharmonic component of the vibrational specific heat, and therefore one has, with

$$S_{anh}(T_p) = \int_{T=0}^{T_p} dT \frac{1}{T}\frac{\partial E_{anh}(T)}{\partial T}, \tag{2.41}$$

$$S_{anh}(T_p) = \sum_{n=2}^{n_{max}} \frac{n\ c_n}{(n-1)} T_p^{n-1}. \tag{2.42}$$

Chapter 3

Unified phase diagram of reversible-irreversible, jamming and yielding transitions in cyclically sheared soft sphere packings

3.1 Introduction

The response of disordered assemblies of particles to externally imposed stresses or deformation is of importance in wide ranging investigations addressing transitions between rigid and flowing states of soft matter systems, and characterizing the rigid and flowing states. Questions in this regard pertain to the rheology of complex fluids, in particular, dense particulate suspensions [177–181], jamming in granular matter [107, 109, 182–187] [108] and the mechanical behaviour, yielding and shear banding in amorphous solids (from metallic glasses to yield stress soft materials) [95, 116, 119, 124, 125, 127, 188–192]. Investigations on these questions inform geophysical phenomena such as earthquakes and landslides [193–195], material properties of metallic glasses [196, 197], the control of rheological response of suspensions [198], origins of irreversible behaviour [138, 139, 199, 200], and memory formation in a variety of condensed matter systems [150, 151, 201–205], to name a few examples. A number of experimental and computational investigations addressing such questions have employed the protocol of oscillatory or cyclic shear deformation, often in the *athermal* limit, when thermal fluctuations do not play a significant role.

At low densities, cyclically sheared colloidal suspensions (and models thereof) exhibit a continuous transition from reversible behaviour (wherein particles return to the same position at the end of each cycle) to irreversible behaviour [138, 139], with time scales to reach steady states apparently diverging at the transition. At high densities,

dense glasses exhibit a sharp, discontinuous yielding transition [95, 122, 124, 136, 200, 206], nevertheless with apparent divergence of times to reach the steady state. These two regimes also display memory effects with significant differences in behaviour [150, 151, 204, 205]. At intermediate densities, where jamming behaviour has been explored [102–104], mechanical measurements reveal interesting phenomena such as softening and yielding [184, 207], which are not fully or well characterized. Thus, depending on the density regime, one finds transitions from reversible to irreversible behaviour with varying characteristics.

Given the diversity of observed behaviours, it is of interest to comprehend the relationship between these seemingly different but related phenomena. Such a comprehensive understanding is hampered by the fact that these different regimes have been probed on physically very different experimental systems (colloidal suspensions, granular matter, molecular or atomic glasses), or different computational models and methods. It is thus desirable to interrogate all these phenomena in a single system to establish the relationship between different regimes of behaviour. In the present work, we address this goal by studying the model system of athermal soft sphere assemblies, which have been used to model, depending on the density of the packings, the behaviour of colloidal suspensions, granular matter and dense glasses. We study the behaviour of a binary (50:50) mixture of soft spheres interacting through a harmonic potential, subjected to athermal cyclic deformation of varying amplitudes over a density range that encompasses all these regimes. By doing so, we observe reversible to irreversible transitions at the high and low density regimes, analogous to previous studies, but our results illuminate several new aspects not previously addressed. At intermediate densities, we further observe a window in which cyclic shear deformation unjams initially jammed configurations. This window is sandwiched between a reversible regime at low amplitudes and an irreversible regime at high amplitudes. Interestingly, this unjamming window allows us to probe a phenomenon that hitherto has largely been addressed in the context of frictional granular packings, namely shear jamming. Owing to the unjamming we obtain by cyclic shear deformation, we can study shear jamming in a frictionless system. We present our findings below by considering three distinct density regimes, and finally, construct a unified phase diagram that integrates all the observed regimes and transitions among them. Related results in two dimensions are presented in [208].

3.2 Methods

We have subjected a binary (50:50) mixture of soft spheres interacting through a harmonic potential to athermal quasistatic shear (see Chapter 2 for further details). Initial configurations in the density range $0.54 - 0.627$ are obtained from hard sphere fluid

configurations at $\phi = 0.363$, subjected to fast compression using Monte Carlo simulations.The isotropic jamming density is estimated to be $\phi_J = 0.648$, following the method in [103]. Configurations close to ϕ_J ($0.638 - 0.647$ and $0.650 - 0.661$) are obtained by a single step decompression or compression of configurations at ϕ_J, and configurations well above ϕ_J are obtained by multiple step compression of configurations at ϕ_J. Each compression or decompression step is followed by the energy minimization (CG).The range of packing fraction for our study is $[0.54 - 0.72]$. The strain amplitude range is $[0.001 - 0.2]$ and $[0.01 - 1.0]$ for above and below ϕ_J respectively. For $\phi = 0.56, 0.54$, γ_{max} ranges from $[0.1 - 8.0]$. Approximately 1950 independent simulations are used to construct the complete phase diagram. The number of independent samples used in different density ranges are - 10 for $0.661 - 0.72$, $10 - 20$ for $0.650 - 0.661$, $4 - 10$ for $0.638 - 0.648$, $6 - 10$ for $0.54 - 0.627$, and $1 - 2$ samples at the lowest densities at high amplitudes.

3.3 Results

3.3.1 Reversible-irreversible and yielding transition well above the isotropic jamming density

The soft sphere model system well above ϕ_J has been studied and observed to behave as a good glass former [162, 209]. It has been shown previously that amorphous solids under cyclic shear deformation yield at a well defined strain at which they undergo (in the steady states reached after repeated cycles of strain, which we always focus on unless otherwise stated) a transition from a reversible state (where particles return to the same position after each cycle) to an irreversible, diffusive, state [95, 136, 200]. Therefore we identify the yield strain at which the slope of the mean squared displacement (MSD) of particle positions measured stroboscopically changes from zero (reversible or absorbing phase, A) to finite values (irreversible or diffusive or yielding phase Y) in a discontinuous fashion. The yield strain can also be identified by the non-monotonic, and discontinuous change in the steady state value of the potential energy (PE) [95, 134, 200]. In Fig. 3.1, we show the mean squared displacement (MSD) for different shear amplitudes at one high packing fraction, $\phi = 0.72$, above the jamming density ϕ_J (the *minimum* value of ϕ_J in this system is estimated to be 0.648). For small amplitudes, the MSD is negligible and non-increasing with cycles, whereas above a strain amplitude of $\gamma_{max} = 0.075$, it exhibits a linear increase with accumulated strain $\gamma_{accum} = 4 \times \gamma_{max} \times N_{cycles}$ (Fig. 3.1). The diffusion coefficients obtained (treating γ_{accum} as time variable), from $MSD = 6D\gamma_{accum}$, shown in the inset

of Fig.3.1, display a discontinuous jump at $\gamma_{max} = 0.076$, as observed in previous studies [124,134]. In Fig. 3.2(b), we show the steady state per particle potential energy (PE) as a function of the strain amplitude, which shows a discontinuity at $\gamma_{max} = 0.075$, as seen previously for a binary Lennard-Jones glass [95, 134]. We identify the steady state by monitoring PE as a function of γ_{accum}. From these two characterizations, we identify $\gamma_y = 0.075$ as the yield strain value. These results illustrate yielding behaviour observed over a range of densities at roughly a constant $\gamma_{max} \approx 0.075$, which is consistent with the characterization of the yielding transition in previous work.

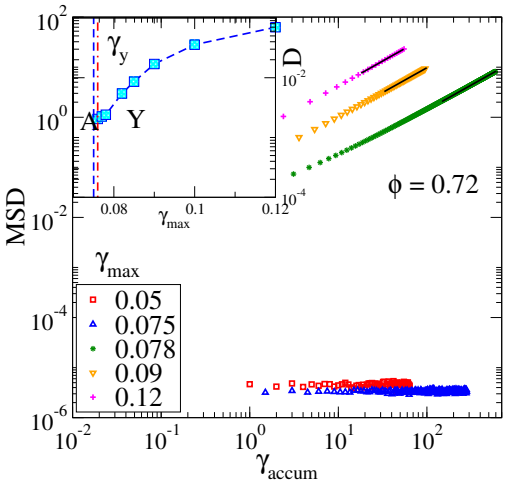

Figure 3.1: Mean square displacement (MSD) as a function of γ_{accum}, shown for different strain amplitudes. MSD shows a diffusive behavior above $\gamma_{max} = 0.075$. Blue and red vertical lines in the inset indicate the lower and upper transition strain amplitudes when the transition is approached from the two different phases. (Inset): Above $\gamma_{max} = 0.075$, the diffusion coefficient (D) jumps from zero to a finite value.

We identify the yield strain by two properties in this work. Firstly, the system achieves the lowest potential energy when driven cyclically at γ_y. Secondly, the system becomes diffusive when driven with higher amplitude than γ_y. We show in Fig. 3.3 that for a range of packing fractions (at the higher density limit), the system attains the lowest energy at around $\gamma_{max} = 0.07$. Attaining the steady state close to the transition to obtain reliable MSD is time consuming because of an apparent divergence of the number of cycles required to reach steady states (as discussed at length in [95, 136]), and we do not show those results here, but note that in all cases, we have ensured that the states are diffusive above $\gamma_{max} = 0.07$. We would mention one thing here: we have shown most of the results of the dense regime using $\phi = 0.72$ as a representative packing fraction. A finer grid of scanning of deformation amplitudes at this packing fraction shows that the potential energy minimum occurs at $\gamma_{max} = 0.075$ for $\phi = 0.72$. For other packing fractions, as we have shown in Fig. 3.3, the potential energy minimum occurs at around $\gamma_{max} = 0.07$

We show next, the shear stress-strain plots within a cycle for a range of amplitudes for

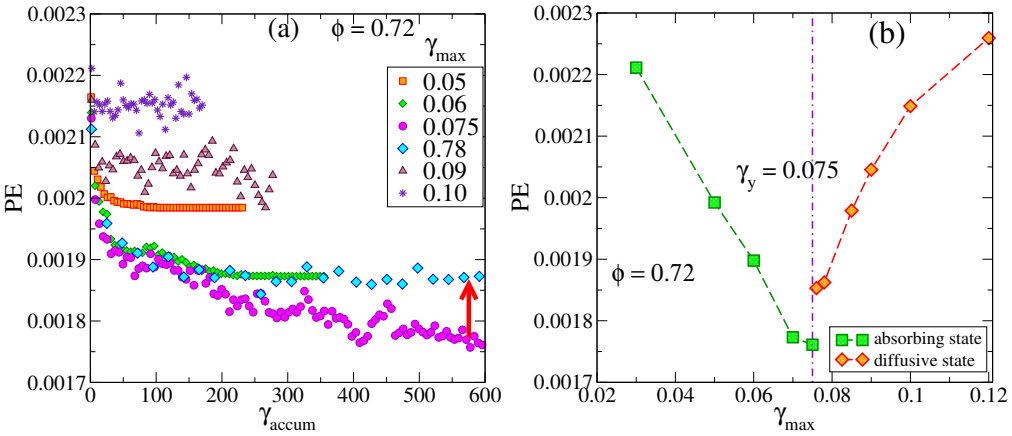

Figure 3.2: (a) The potential energy PE attains a minimum value at the yielding transition amplitude which is identified as $\gamma_y = 0.075$ in our system. PE shows a discontinuous jump (red arrow) as the yielding point is crossed. (b) The steady state potential energy (PE) value as a function of γ_{max} is shown. The potential energy attains a minimum value at the yielding strain amplitude, indicated as $\gamma_y = 0.075$. At the yielding strain, the potential energy shows a discontinuity.

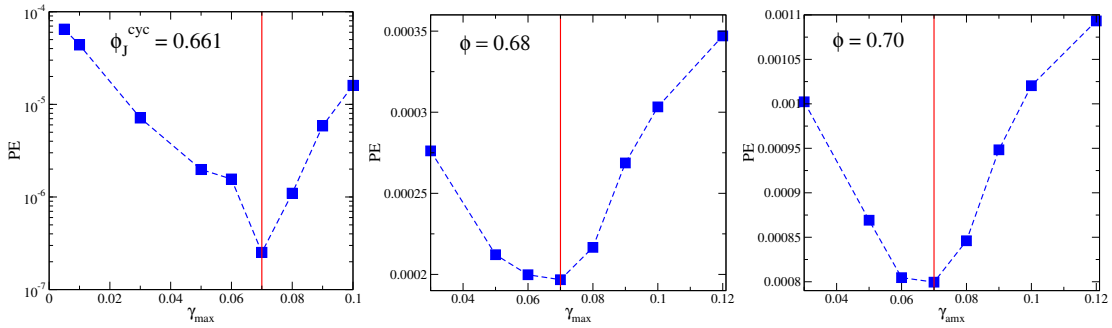

Figure 3.3: The γ_y, identified from the potential energy minimum, is almost constant over a range of packing fractions at the high density limit.

a given packing fraction ($\phi = 0.72$) after the system has reached a steady state (see Fig. 3.4 (a)). We can see for amplitudes greater than 0.075 (γ_y a finite area under the stress-strain curve emerges, which signifies the onset of dissipation, in other words, yielding in the system. Yielding is identified by a stress drop in the system under uniform shear. In the cyclic shear scenario, we consider the stress at the maximum deformation (γ_{max}) which clearly shows a drop as the strain amplitude is increased beyond 0.07 (see Fig. 3.4 (b)). Therefore, the identification of the yielding strain amplitude from the mechanical response of the system matches with earlier characterisation described in the here.

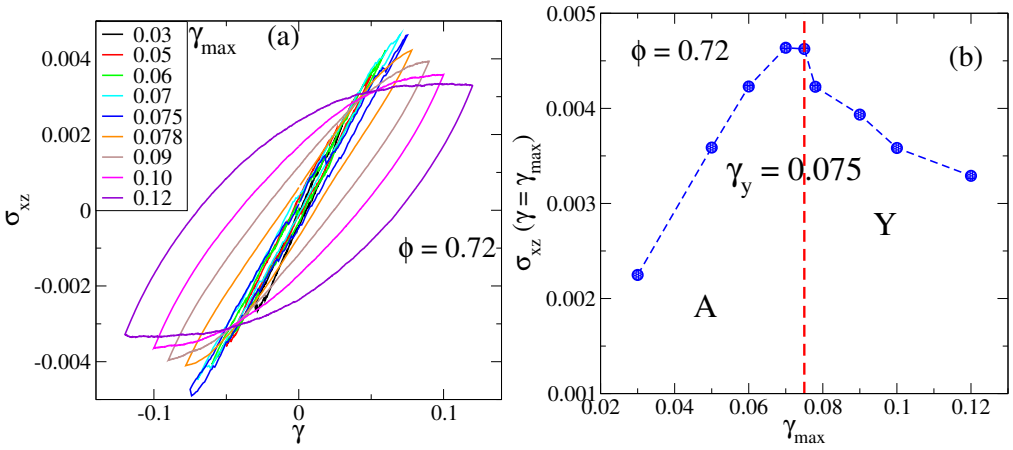

Figure 3.4: (a) The shear stress (σ_{xz}) within a cycle is shown for a range of amplitudes after the system reaches a steady state. As the yielding strain amplitude ($\gamma_y = 0.075$ here) is crossed, a finite area under stress-strain curve emerges signifying dissipation in the system in the post yielding regime. (b) The steady state value of the shear stress σ_{xz} at the strain $\gamma = \gamma_{max}$ is shown as a function of γ_{max}. The shear stress passes through a maximum as the yielding strain amplitude ($\gamma_y = 0.075$ for $\phi = 0.72$) is crossed and drops to a smaller value for higher strain amplitudes (starting from the point at $\gamma_{max} = 0.078$).

3.3.2 Unjamming and shear jamming just above the isotropic jamming density

3.3.2.1 Unjamming

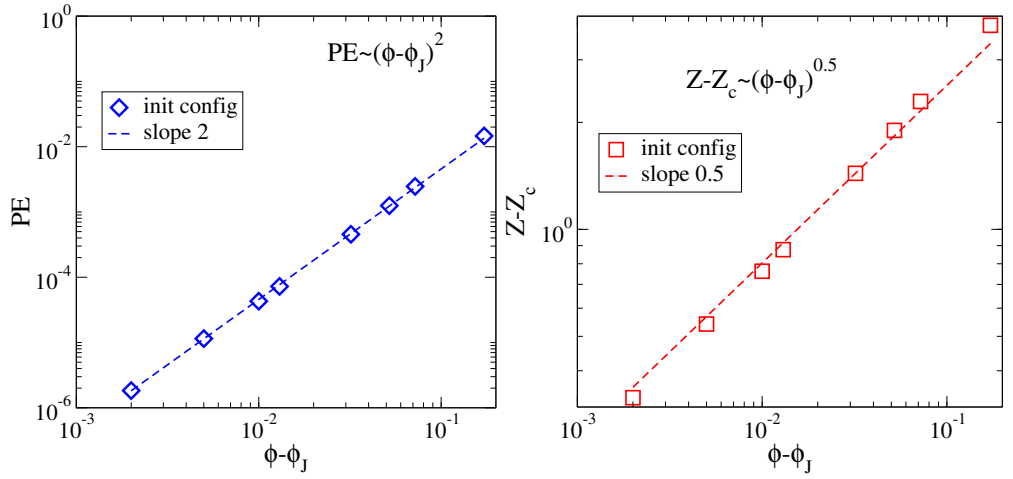

Figure 3.5: The scaling behaviour of the energy (PE) and the excess contact number ($Z - Z_c$) of the initial jammed packings above the isotropic jamming point obeys the scaling behaviour.

We next consider the density range just above the isotropic jamming density, ϕ_J, estimated to be 0.648 using previously employed methods [102, 103] of compressing

low density configurations. First, we show the scaling behaviour of the potential energy (PE) and excess contact number ($Z-Z_c$, Z_c is 6, the average contact numbers at the isostatic condition) in Fig.3.5 of the configurations generated close to the isotropic jamming density. The scaling exponents match the previously known results [102,103]. As noted before, the jamming density is not unique [103,104,111,189,210], and jammed packings just above ϕ_J exhibit peculiar mechanical properties [102,211]. We thus expect interesting responses to cyclic deformation in this regime. We observe that for a

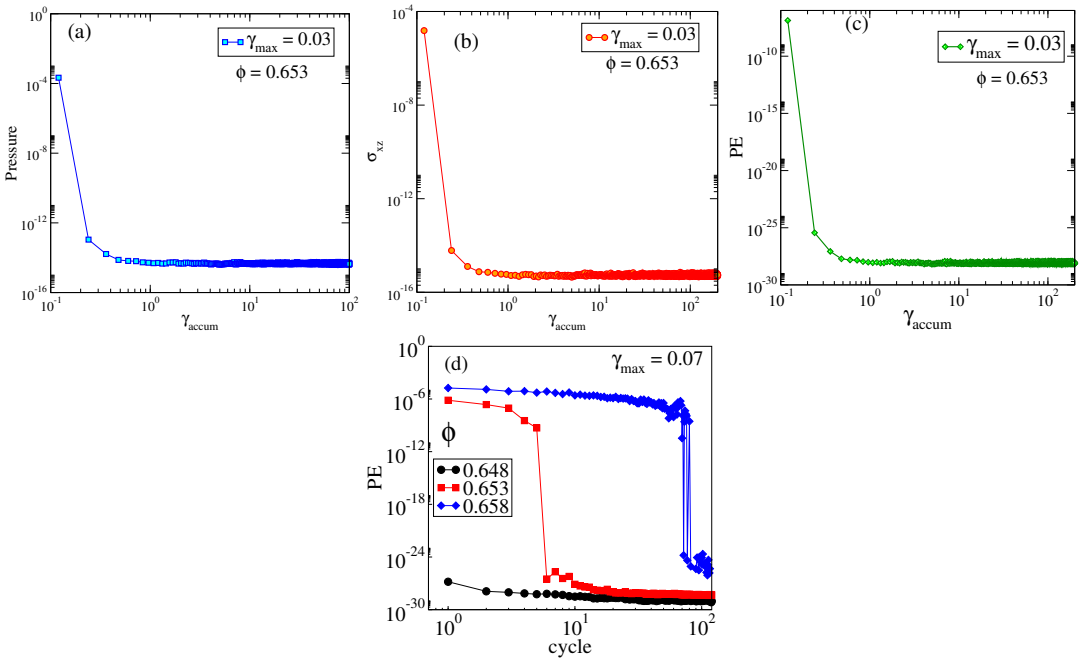

Figure 3.6: (a)-(c)The evolution of pressure,shear stress (σ_{xz}) and potential energy(PE) for an unjamming configuration with $\phi = 0.653$, $\gamma_{max} = 0.03$. (d) Potential energy as a function of cycle, for a fixed amplitude across a range of densities. The number of cycles required to unjam the system increases with the increase of density.

range of packing fractions close to ϕ_J the system unjams for an intermediate range of amplitudes, *i.e.,* pressure and shear stress go to zero. It takes more cycles to unjam the system as we move to higher densities(see Fig.3.6). In Fig. 3.7, we show how the stress varies at different strain steps within cycles. The cycle numbers are chosen to demonstrate different stages of the unjamming, ranging from transient to steady state. In the further analysis of the unjamming region, we do not focus on transients or variations through the cycle, (discussed in detail in [111,210]) and analyse stroboscopic steady state configurations unless otherwise indicated. In Fig. 3.8, we show the steady state value of the stroboscopic average mechanical contact number Z_M (defined in Chapter 2), and the shear stress in Fig. 3.8, for different densities, as a function of strain amplitude. In Fig. 3.9, we show the steady state value of the average contact numbers Z and Z_{NR}, for different densities. Details of the dependence of the contact numbers on the minimization protocol are described in the Appendix. In Fig. 3.9, we show the

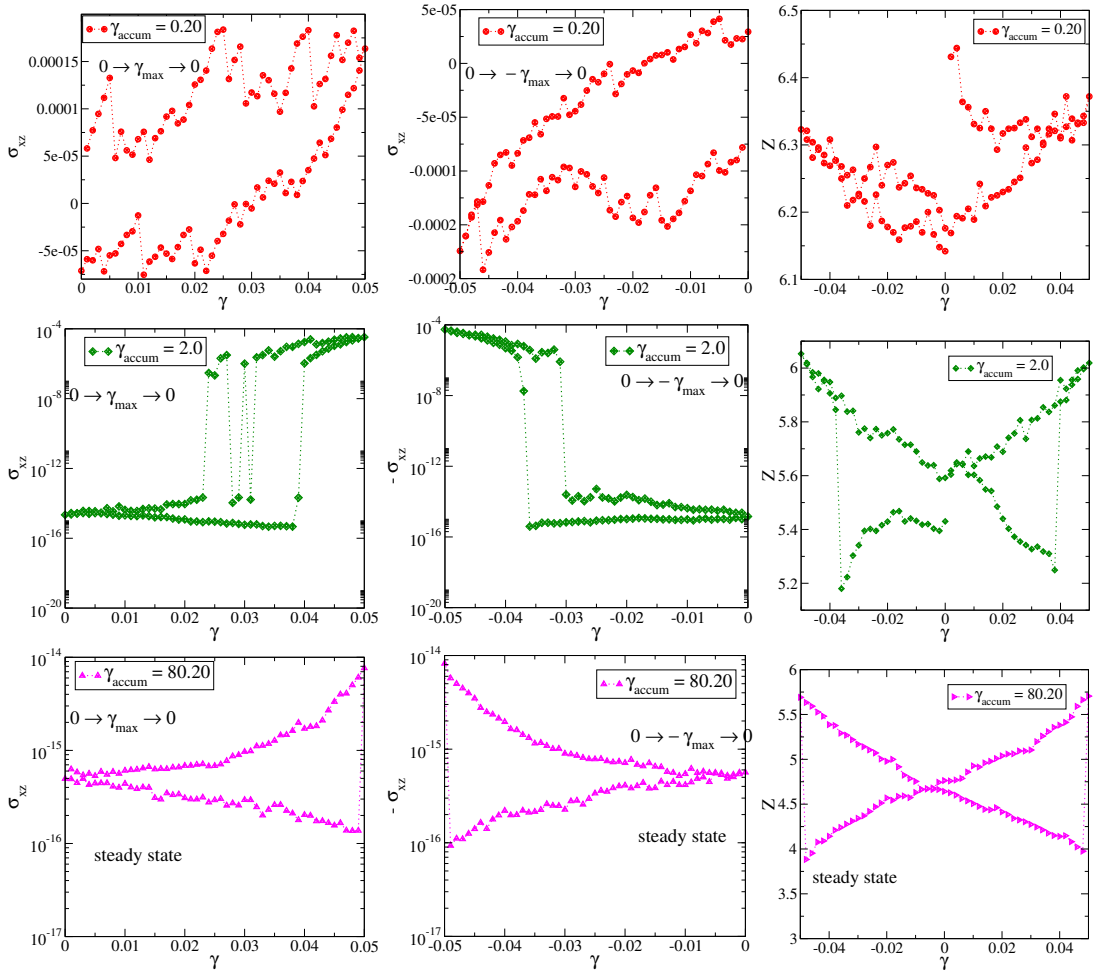

Figure 3.7: The first column for all the rows shows the stress vs strain value for the first half cycle of the deformation. The second column shows the stress vs strain value for the next half cycle of the deformation for the first row and the negative of stress vs strain value for the next half cycle of the deformation for the next two rows. The last column shows the evolution of average contact number versus strain within a cycle. The stress and contact number evolution within a cycle of an unjammed phase ($\phi_J = 0.653, \gamma_{max} = 0.05$)has been shown as the system gradually unjams. Figures in the first row show that the shear stress initially stays finite, and the average contact number stays above $2D$ though it decreases gradually as more cycles are applied. For intermediate cycles (second row), the stroboscopic configurations stay unjammed but get jammed within a cycle when the strain is increased from zero to γ_{max} (or decreased to $-\gamma_{max}$. During the reversal of shear direction (from γ_{max} or $-\gamma_{max}$), stress and contact number decrease and show a jump to zero and less than $2D$ value, respectively. Finally, (third row) stress remains zero for all values of strain within a cycle, and the average contact number always stays below $2D$ in the unjammed phase.

evolution of stroboscopic Z_{NR} for $\phi = 0.653$ and different strain amplitudes, which belongs to the unjamming region. We use this to identify steady state configurations. We observe that for $\gamma_{max} = 0.001$ and $\gamma_{max} > 0.12$, the system in the jammed (finite stress) state and in the intermediate range of γ_{max} the system is in the unjammed state.

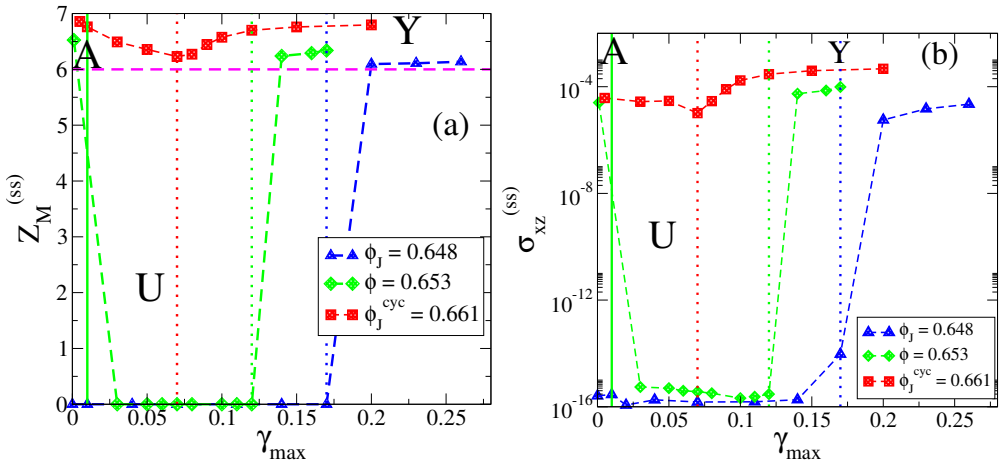

Figure 3.8: (a) The average mechanical contact number in the steady state, computed with only force bearing contacts, jumps to 0 in the unjamming regime, as does (b) the steady state shear stress $(\sigma_{xz})_{ss}$.The vertical green solid line indicates the absorbing and unjammed phase boundary. The vertical dotted lines indicate the strain amplitude beyond which the system enters the yielded phase from an unjammed phase (blue and green) or an absorbing phase (red).

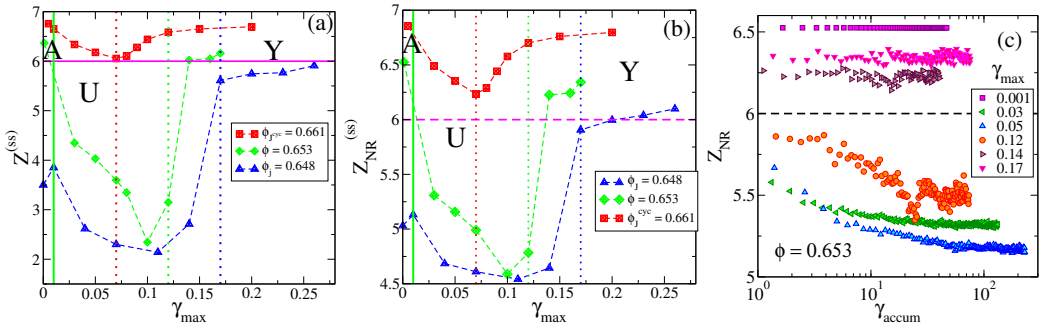

Figure 3.9: (a),(b) The steady state average contact number Z and contact number calculated without rattlers Z_{NR} are shown as a function of strain amplitude, for $\phi_J \leq \phi < \phi_J^{cyc} = 0.661$. Z and Z_{NR} drop to values below the isostatic contact value of 6. The vertical green solid line indicates the absorbing and unjammed phase boundary. The vertical dotted lines indicate the strain amplitude beyond which the system enters the yielded phase from an unjammed phase (blue and green) or an absorbing phase (red). (c) The evolution of Z_{NR} with γ_{accum} for $\phi = 0.653$ is shown.

The shear stress jumps to zero when Z_M (also Z, Z_{NR}) goes below $2D(= 6)$, the *isostatic* value for jamming in frictionless packings(see Appendix for further details). The unjamming range of shear amplitudes is largest at ϕ_J, and decreases with increasing density, till it vanishes at $\phi = 0.661$. At $\phi \geq \phi_J$, both for high amplitudes and very low amplitudes, the system has a finite value of stress. We identify the finite stress packings at low amplitudes as the absorbing phase, and at high amplitudes as the yielded phase. We interpret the presence of an unjamming regime as a reflection of the jamming density moving to higher values upon cyclic deformation. Thus, we

identify $\phi = 0.661$ as the ϕ_J^{cyc} or the cyclic jamming point, the highest jamming density obtained under athermal cyclic shear. The meaning of this limit jamming density, the range in density and character of jammed configurations obtained from different protocols [103, 104, 111, 189], merits further comparative investigation. Our results concerning unjamming are consistent with the observation of softening behaviour of jammed solids close to ϕ_J, for an intermediate range of strain amplitudes [207]. All the different measures of the average contact number also represent the potential energy behavior. This non-monotonicity of the contact numbers is comparable to the variation of the potential energy shown earlier (Fig. 3.2(b)). However, in the density regime of $\phi_J < \phi < \phi_J^{cyc}$, the strain amplitude at which the contact number starts increasing after a minimum value, that amplitude depends on the packing fraction. This is unlike the density-independent behaviour of the potential energy observed in the high density regime (Fig. 3.3). This behaviour of the intermediate density regime is described in the later part of the chapter where the phase diagram is described. The system enters a yielded regime at a higher value of deformation as the density is decreased from ϕ_J^{cyc} to ϕ_J.

In Fig. 3.10, we show the shear stress as a function of Z_{NR}, for one sample per density and strain amplitude (in the same range as Fig. 3.9). Each point in the scatter plot corresponds to all the stroboscopic configurations, from the initial configuration up to cycle numbers when the steady state is reached. For $\phi < \phi_J^{cyc}$, Fig. 3.10 exhibits two branches, one with close to zero stress and one with finite stress when $Z_{NR} \geq 6$, above the isostatic contact number. The re-entrant finite stress regime with $Z_{NR} \geq 6$ at high strain amplitudes corresponds to shear jamming, explored in great detail for frictional granular packings [107, 109, 187, 212–215], but also as a possibility in recent

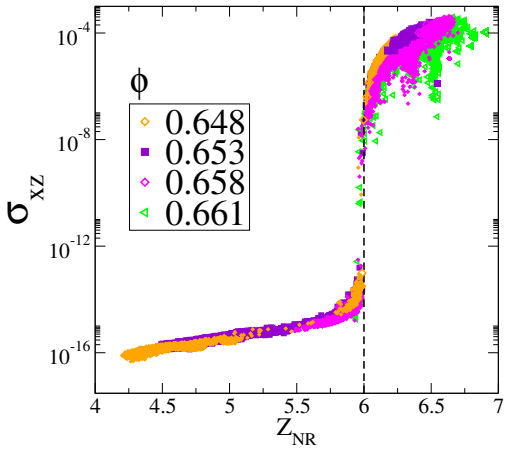

Figure 3.10: (a) Shear stress (σ_{xy}) *vs* the average contact number (Z_{NR}), for stroboscopic configurations, shown for different densities and strain amplitudes. Packings in the range $\phi_J \leq \phi < \phi_J^{cyc}$ exhibit two distinct branches of finite or zero stress. The shear stress jumps to a finite value at $Z_{NR} = 6$.

times for frictionless packings [111, 185, 189]. Our results open a novel route to generating unjammed packings above the isotropic jamming point ϕ_J, which can shear jam upon the application of shear. We note that a related approach to unjamming by cyclic deformation was explored in [111] employing volume cycling (see [216]) for related experimental results for frictional grains), leading to a range of jamming densities, followed by shear deformation leading to shear jamming.

Since the shear jamming is analogous to and contiguous with the yielding transition at higher densities, it is interesting to analyse their comparison further. To this end, we show in Fig 3.11 the MSD in the steady state for a range of shear amplitudes spanning the absorbing, unjamming and shear jamming regimes. The MSD shown correspond to zero diffusivity for the absorbing (jammed) and the unjamming regimes (and therefore does not distinguish these phases), but a finite diffusivity in the shear jamming phase. As shown in the inset of Fig 3.11(a) and Fig 3.11(b), the diffusivities display a discontinuous jump upon entering the shear jamming regime, analogous to the irreversible, yielded regime at higher densities (see Fig. 3.1), above ϕ_J^{cyc}. Although diffusivity does not distinguish the absorbing and unjammed regimes, they are distinguished by the presence of zero *vs.* finite stresses.

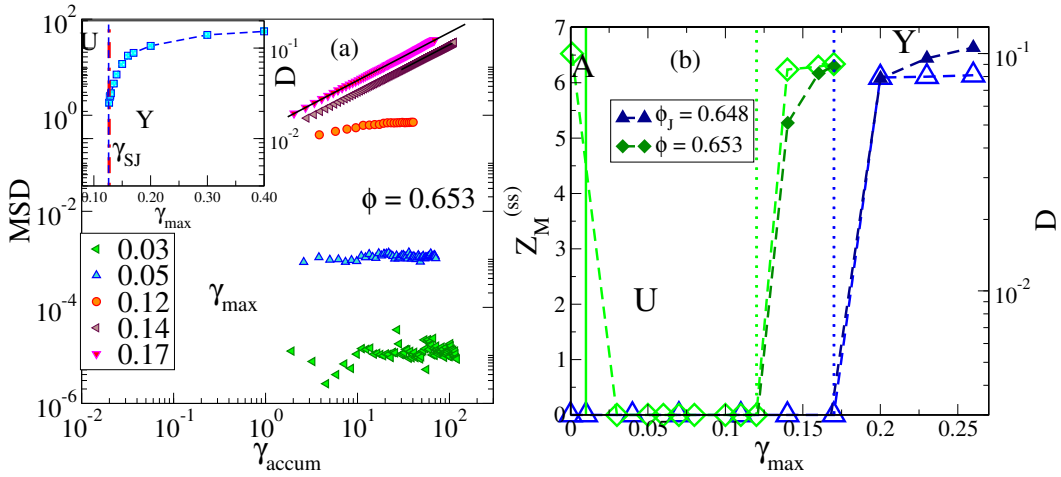

Figure 3.11: (a) The MSD for the jammed (absorbing) and unjammed regimes exhibit non-diffusive behaviour whereas the shear jamming regime exhibits diffusive behaviour. The diffusion coefficients (inset) show a discontinuity at the re-entrant shear jamming transition.(b) The diffusivity changes discontinuously from unjammed to yielded phase, in a similar fashion to the change of the contact numbers. The filled symbols represent diffusivity and the open symbols represent average mechanical contact numbers.

3.3.2.2 shear jamming of the unjammed phase

Here we show the response of all the three phases subjected to uniform shear (see Fig.3.12). The unjammed phase facilitates the study of frictionless shear jamming

above ϕ_j, achieved by cyclic shear deformation. We now take these unjammed configurations and then subject them to uniform shear. We see that the system jams again when subjected to uniform shear. We see a jump in stress for unjammed configurations, trained at amplitude 0.07 at different densities. As expected, the stress jump occurs above a certain threshold value of strain (Fig. 3.13) greater than the training amplitude strain value. As one moves further away from the isotropic jamming density, the distance between the training amplitude and the strain value at which the system jams decreases. Detailed analysis of shear jamming for this unjammed phase has been carried out by Babu et al. [112].

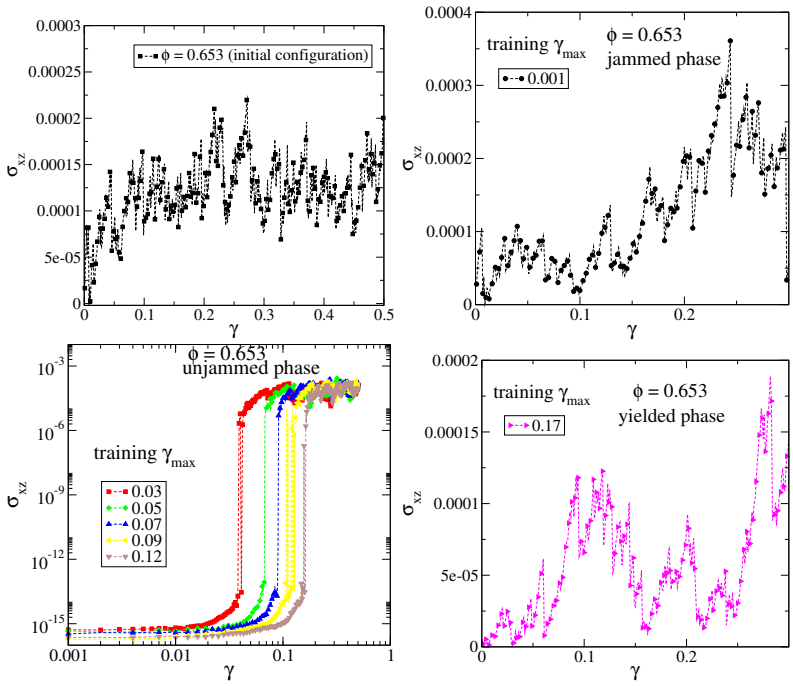

Figure 3.12: Uniform shear has been applied to the initial configurations, configurations obtained by training them with the mentioned amplitudes, corresponding to jammed phase, unjammed phase, and yielded phase. Uniform shear stress vs strain plot has been shown for $\phi = 0.653$.

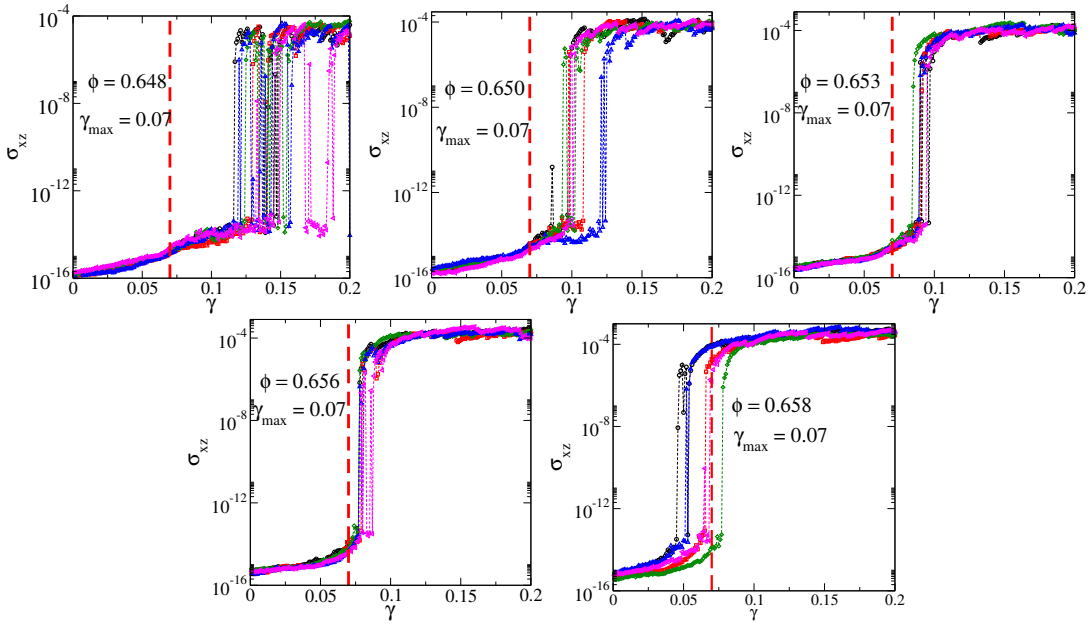

Figure 3.13: The unjammed configurations attained through cyclic shearing by a particular strain amplitude (γ_{max} = 0.07 shown here) have been subjected to uniform shear. The shear stress jumps beyond a particular threshold value. The jump occurs at a lower value of strain as we move further away from the isotropic jamming density. Different colours correspond to different samples. Five samples for each packing fraction have been shown. (For $\phi = 0.658$, it requires an excessive number of cycles to attain unjamming at $\gamma = \gamma_{max}$, Only one such configuration could be shown here.)

3.3.2.3 Structural analysis of the unjammed phase

We have analysed the partial radial distribution functions $g(r)_{ij}$ (where i, j are particle type indices) of the system in the unjammed (U) phase and compared them with the absorbing phase (A), the yielded phase (Y), and the jammed structures (see Fig. 3.14) we obtain by compression, before shear is applied. The radial distribution does not show any signature of a long range order or significant differences from the other two cases (A and Y) observed above isotropic jamming density or the initial isotropic jammed structures. We have also computed and analysed the evolution of the global orientational order parameter Q_6 to detect any global order present. The global Q_6 value of the unjammed phase does not change with γ_{accum} (apart from the scatter), and the average steady state value remains close to the value of the initial isotropic jammed structures (see Fig. 3.15). From these analyses, we can conclude that the unjammed phase (or the A and Y cases) does not show any indication of crystallization. We have

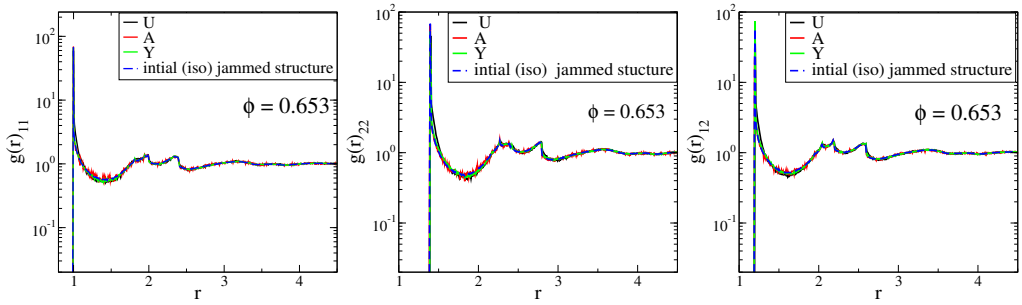

Figure 3.14: Partial radial distribution functions $(g(r))$ of the unjammed(U) phase are shown in comparison with the absorbing phase (A), the yielded phase (Y) and the initial isotropic jammed phase. The unjammed phase does not show any signature of long range order or any significant differences from other cases.

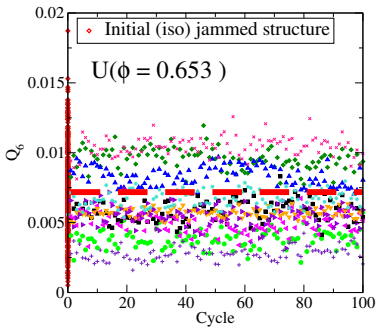

Figure 3.15: The global orientational order parameter Q_6 of the different initial isotropically jammed structures has been shown as red dots at cycle number zero. The horizontal red line indicates the average of Q_6 of the initial isotropically jammed structures. The scatter plot shows the evolution of the Q_6 in the steady state unjammed phase. Different symbols correspond to independent runs from different initial configurations.

also shown the partial radial distribution function near the contacts (see Fig. 3.16).

The overlap distribution (see Fig. 3.17) for the initial jammed and final unjammed configurations. The distribution significantly changes once the system unjams from the initial jammed configuration and, after that, does not show significant changes over the cycles of deformation.

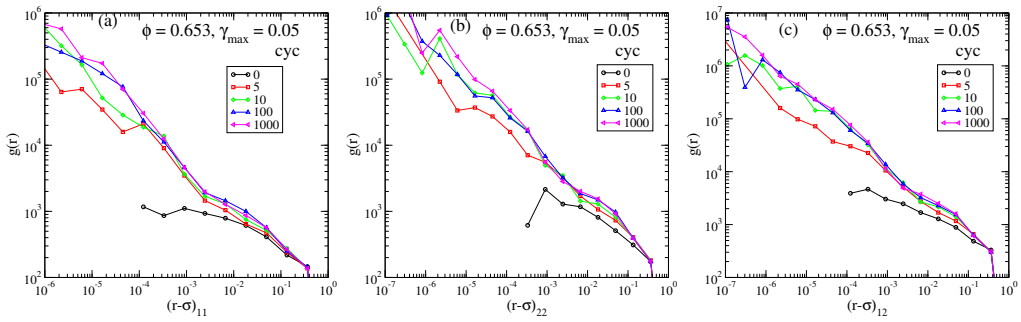

Figure 3.16: Evolution of $g(r)$ near contact as a function of cycle number, as the system unjams, for type 1 pairs (a), type 2 pairs (b), and type 1 and 2 pairs (c).

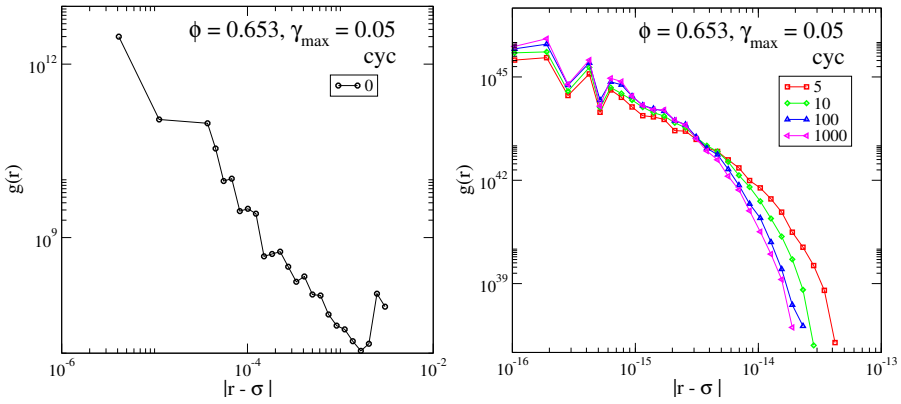

Figure 3.17: Overlap distribution for the initial jammed configuration and overlap distribution for the unjammed configurations have been shown

3.3.3 Reversible-irreversible transitions below the isotropic jamming density

We next study cyclically sheared sphere assemblies below ϕ_J, which show more complex behaviour in the reversible regime [199] than initially analysed for colloidal suspensions [138, 139]. Schreck *et al.* [199] showed that for such packings, two kinds of reversible states are present, referred to as point reversible states (PR) and loop reversible states (LR). In PR states, particles self organize during the initial cycles of strain so that they do not collide with each other. In the LR state, particle continue to collide in the steady state, but return to their original positions at the end of each cycle.

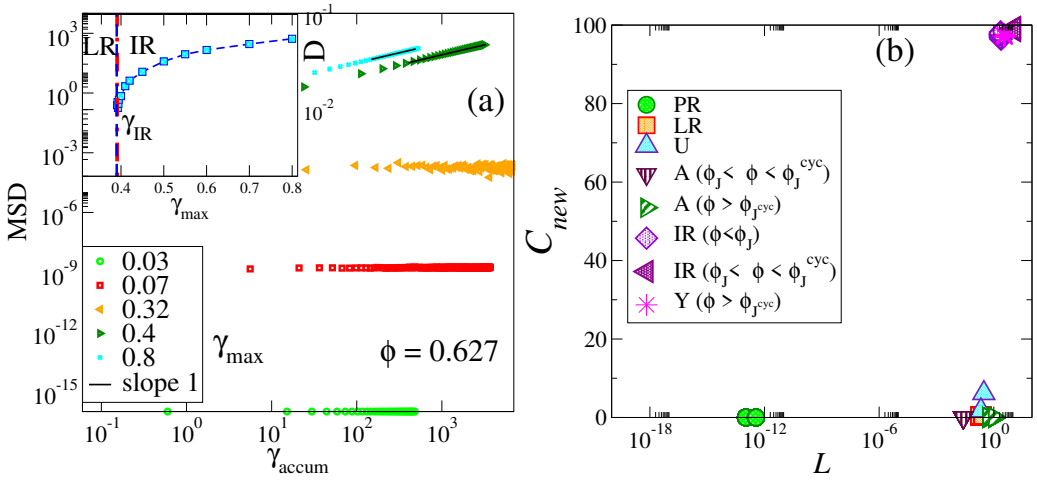

Figure 3.18: (a) MSD as a function of accumulated strain, shown at $\phi = 0.627$ for different amplitudes. We show a discontinuous jump in diffusivity as a function of strain amplitude. (b) Plot of the non-affine path length L and the percentage of new collisions C_{new}, which clearly differentiate all the different phases at all densities. PR: Point reversible; LR: Loop reversible; IR: Irreversible; Y: Yielded phase; U: Unjammed phase; A: Absorbing phase.

For packings below ϕ_J, potential energies and stresses are always zero. Thus, we characterise the trajectories of particles in the steady state in various ways to distinguish different phases and transitions. In addition to the MSD, we compute the non-affine path length (L) (the length of the path traversed by particles in excess of affine displacements due to global shear strain), and the percentage of new collisions (C_{new}) in a given cycle, compared to a reference cycle in the steady state. We will mention here the precise definitions of these two quatities.

Non-affine path length (L): The non-affine path length is the average of the magnitude of non-affine displacement per particle within a cycle [199].

$$L^2(k) = N^{-1} \sum_i \{ \sum_n [(X^i_{k,n+1} - X^i_{k,n})^2 + (Y^i_{k,n+1} - Y^i_{k,n})^2 + (Z^i_{k,n+1} - Z^i_{k,n})^2]^{\frac{1}{2}} \}^2 \tag{3.1}$$

where k is cycle, n is strain step, $X^i_{k,n} = x^i_{k,n} - \gamma_n z_{k,n}$, $Y^i_{k,n} = y^i_{k,n}$ and $Z^i_{k,n} = z^i_{k,n}$.The Non-affine pathlength is an indicator of collisions happening in the system. After the coordinates of particles are affinely transformed if overlaps are created, the minimization method displaces the particles to attain an energy minimized configuration. This gives rise to non-affine displacement in the system. $L(k)$ is an average measure of such displacement at k^{th} cycle.

Percentage of new collisions (C_{new}): We compute the number of collisions that take place during a given cycle by number of pairs of particles that overlap ($r_{ij} < \sigma_{ij}$ when a

stain step is applied, and before energy minimization.). Considering a reference cycle m in the steady state, we compute the number of collisions $C(m+k)$ at a later cycle $m+k$. The number of such collisions which also occurred in the m cycle is defined as $C_m(m+k)$. The percentage of new collisions for the k^{th} cycle (we typically use $k \geq 10$) after the reference cycle m is thus:

$$C_{new}(k) = (1 - \frac{C_m(m+k)}{C(m+k)}) \times 100 \tag{3.2}$$

As we will see when particles collide they can self organize to a reversible state or can reach an irreversible diffusive state. This quantity is used to distinguish the nature of collisions that leads to this two different behaviour.

Here we will mention that because of the finite precision of the minimization, we find overlaps close to the machine precision even in the PR phase, where particles are not supposed to have overlaps. To compute the collisions that take place, we, therefore, impose a cut-off of 10^{-10} for the overlaps ($r_{ij} \leq \sigma_{ij}$) arising between particles after the affine strain step but before minimization resulting in the final configuration.

First, we characterize the phases in terms of mean squared displacement. As shown in Fig. 3.18, the MSD saturates for small amplitudes and shows diffusive behaviour at higher amplitudes, identified as the irreversible phase (IR). The diffusion coefficient shows a discontinuity (inset of Fig. 3.18) in a manner analogous to the shear jamming and yielding transitions. Although the discontinuity is weaker, analysis supports the conclusion that the transition is discontinuous. MSD fails to identify the transition from the point reversible to the loop reversible state. However, the non-affine path length L does. L is negligible for point reversible states whereas it is finite for loop reversible states (see Figure. 3.19). The number of new collisions C_{new} further distinguishes the reversible states from the irreversible states, being zero for reversible states and finite for irreversible states (see Fig. 3.19). As shown in Fig. 3.18, the combination of L and C_{new} helps organize all the regimes we observe across densities into three groups: (i) vanishing L, C_{new} (point reversible), (ii) finite L, vanishing C_{new} (loop reversible, unjamming and absorbing states), and (iii) finite L and finite C_{new} (irreversible, shear jammed and yielded states).

We compute the non-affine path length, collisions, percentage of new collisions (C_{new}) and fraction of active particles to characterise different phases and to identify the transitions. For the point reversible states (PR), particles trace the same path in a cycle (as there are no collisions) and hence L and C_{new} is zero. For the loop reversible states (LR), collisions occur in a cycle, and hence the non-affine path length is finite. Also, in the loop reversible states, even though collisions occur, they occur between the same pairs and hence $C_{new} = 0$, see Fig. 3.19. Only in the diffusive region, irreversible states (IR), C_{new} is finite. In Fig. 3.19, we show L and C_{new} as a function of γ_{accum}, which we

have used to identify the steady state configurations. When a particle at least collides once within a cycle during the affine transformation, in its steady state, we identify such a particle as an active particle. Even though the number of collisions shows a strain dependent increase (see Fig. 3.19) beyond PR phase, almost all the particles seem to collide at least once in a cycle in LR or IR phase (Fig. 3.19). We compute the collision number within one cycle, in the steady state, for different γ_{max} and we count an overlapping pair only once in a cycle. As mentioned in the previous work [199] cycle to cycle displacement Δr (see Chapter 2) has also been measured. They show characteristic features in different reversible-irreversible regimes as shown in Fig.3.20. To summarise the behaviour of all the quantities mentioned, the PR to LR transition is identified by the discontinuous jump in L, number of collisions and fraction of active particles whereas the LR to IR transition is captured through the discontinuous increase of C_{new}. Surprisingly, the number of collisions, and the fraction of particles undergoing collisions, change discontinuously at the PR-LR transition, at variance with expectations based on previous work [138, 139, 217], where continuous changes with respect to deformation amplitude have been reported.

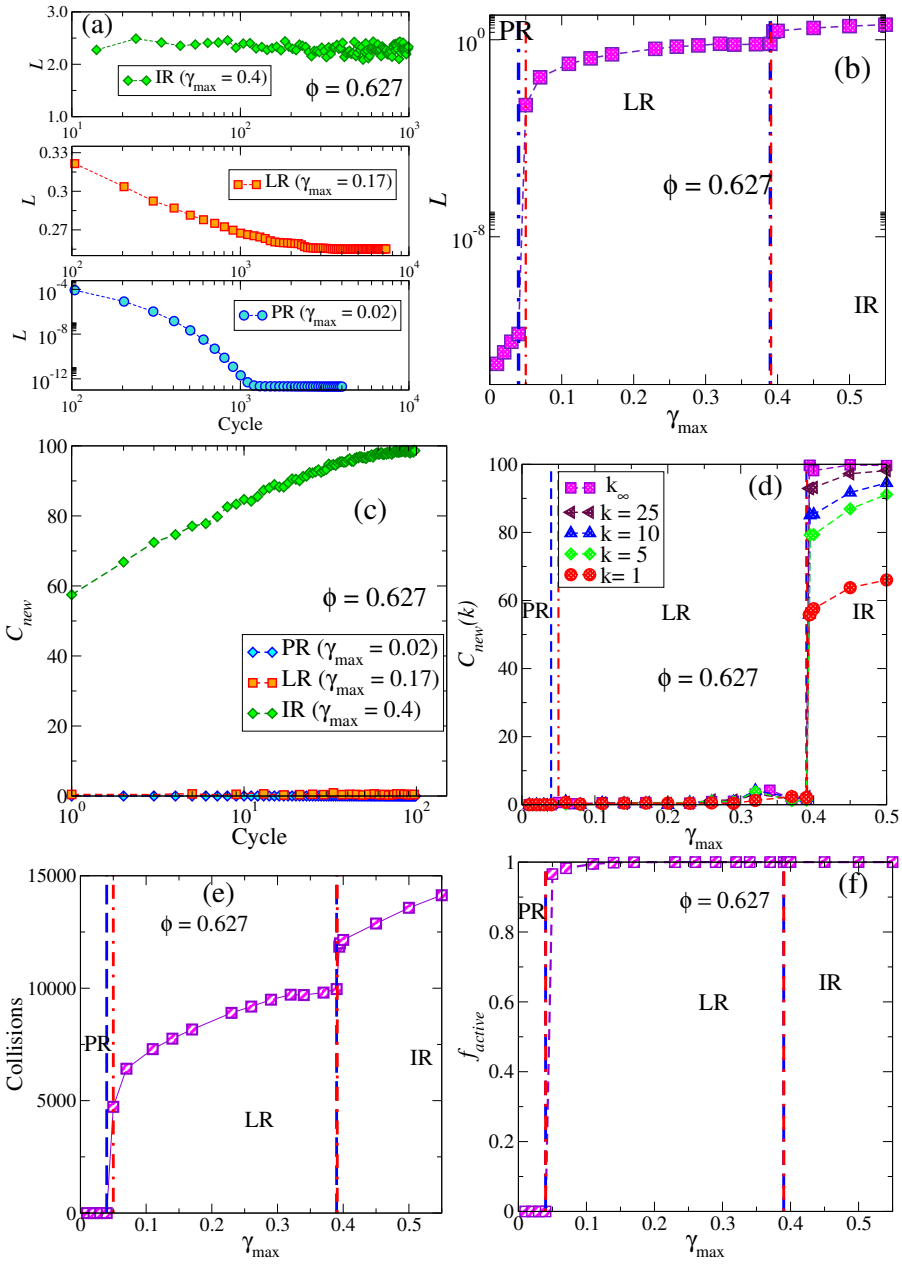

Figure 3.19: (a) Steady states are achieved as the non-affine path length reaches a steady state. (b) The non-affine path length captures the transition from point reversible phase to loop reversible and irreversible states. (c) C_{new} as a function of γ_{accum}, shown for $\phi = 0.627$ for all three phases. For PR and LR, $C_{new} = 0$ in the steady state and finite only for the IR state. (d) Percentage of new collisions differentiates point and loop reversible states from the irreversible state. (e) Total number of collisions, within a cycle, have been shown as a function strain amplitude, exhibiting a discontinuous jump across PR-LR boundary and shows a strain amplitude dependent increase across LR and IR phase. (f) Fraction of active particles captures PR-LR transition through a discontinuous jump from 0 (in the PR phase) to almost 1 (in the LR phase).

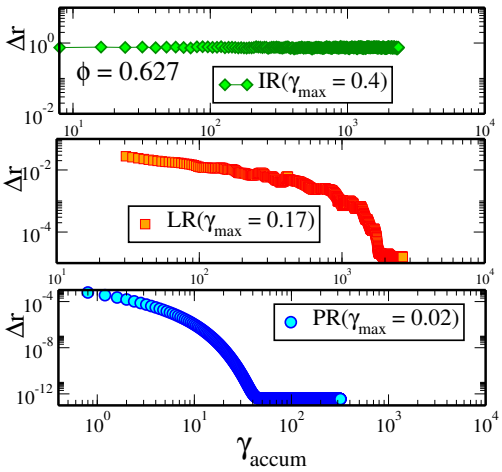

Figure 3.20: Cycle to cycle displacement Δr has been shown as a function of γ_{accum} in point reversible(PR), loop reversible (LR), and irreversible (IR) states. Here displacement has been measured at an interval of five cycles.

The time taken to reach steady state (measured through the decay of L, shows non-monotonic change across both the PR-LR and LR-IR transitions (see Fig. 3.21), consistently with previous results near reversible-irreversible transitions [95, 136, 138, 139]. L captures the slow down of relaxation to the steady state near the PR - LR and LR - IR transitions. Keeping in mind that the accumulated strain γ_{accum} would translate to a time at a constant rate of strain, we characterise the rate of relaxation by a time scale τ (more appropriately a strain scale.) The time scale (τ) has been extracted from the relaxation of L as the system approaches a steady state with increasing γ_{accum}. The point reversible phase exhibits exponential decay of ($L(\gamma_{accum})$ which we use to evaluate a relaxation time scale, whereas the loop reversible phase shows more complex behavior and in the irreversible phase L reaches the statistically stationary regime very rapidly. Since our purpose is only to illustrate the non-monotonic dependence (on γ_{max}) of the relaxation to the steady state, we employ (for LR and IR) a simple procedure of evaluating the value of γ_{accum} at which the difference between the initial and final values of $L(t)$ decreases to $1/e$ of its initial value. *i. e.* writing $L(\gamma_{accum}) = (L(0) - L(\infty))f(\gamma_{accum}/\tau) + L(\infty)$, where $f(x)$ is a function that decreases from 1 to 0, we find the time at which $(L(\gamma_{accum}) - L(\infty)) = (1/e) \times (L(0) - L(\infty))$. We see an initial increase of τ as we approach PR-LR boundary (see Fig 3.21) and we see a similar increase in time scale across the LR-IR boundary after an intermediate decrease of τ in the middle region of the LR phase. This behaviour indicates the existence of two different transitions at the upper and lower limit of the loop reversible phase. The results shown do not permit us to conclude that the time scales diverge at the transitions, and a more careful analysis close to the transitions is required to make any definite statements in this regard.

Among the phases we identify, the low density phase that we identify as loop reversible

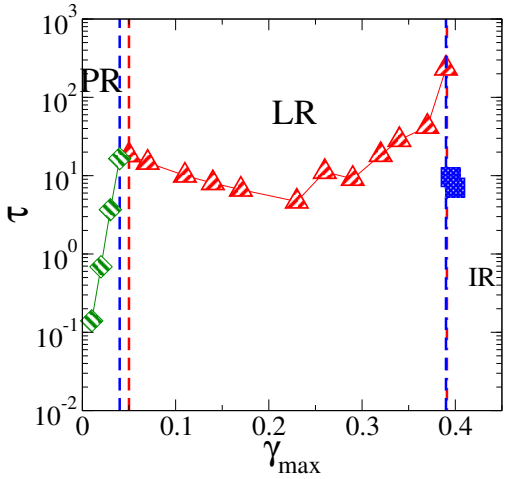

Figure 3.21: The time scale extracted from the relaxation of L shows a non-monotonic change across the PR-LR and LR-IR boundaries.

(LR), the unjammed phase (U), and the absorbing phase (A), all share the property of undergoing non-affine displacements due to collisions (or more generally interactions) with other particles, but in such a fashion that they return to the same position at the end of each cycle. We illustrate this feature for the LR, U and A phases Fig. 3.22, in which the Y component of the position of a sample particle is shown after the system has reached the steady state. The displacements along the Y direction are purely non-affine as our shear plane is the XZ plane. In the steady state, particles converge to trajectories which, despite collisions/interactions during the cycle, form closed loops. Above ϕ_J, loop reversibility is accompanied by transitions of the system between local energy minima, the sequence of which remain the same cycle after cycle, and which bring all particles in the system to the same positions at the end of the cycle [151], as illustrated in Fig. 3.22. This picture has been studied using a formulation in terms of directed graphs, to understand memory effects in cyclically sheared glasses [218].

We have looked at the general behaviour of the diffusivity across the packing fraction and amplitude axis. We have performed additional simulations close to the transition points. We show below the diffusivity(D) vs γ_{max} plots for three different regimes of packing fraction respectively below ϕ_J, above ϕ_J but below ϕ_J^{cyc} and above ϕ_J^{cyc}, see Fig. 3.23. We also show D vs $(\gamma_{max} - \gamma_c)$ plots where γ_C is the irreversible transition amplitude. We have shown a range of transition amplitudes as the possible location of the transition, chosen to lie between two adjacent simulated γ_{max} values across which the transition occurs. All three regimes show a similar nature of the diffusivity close to the transition. In a log-log plot of D $vs.$ $(\gamma_{max} - \gamma_c)$, a power law will appear to be a straight line, whereas a finite value of D on one side of the transition will correspond to a plateauing in a log-log plot, see Fig. 3.24. The plateauing nature of the diffusivity

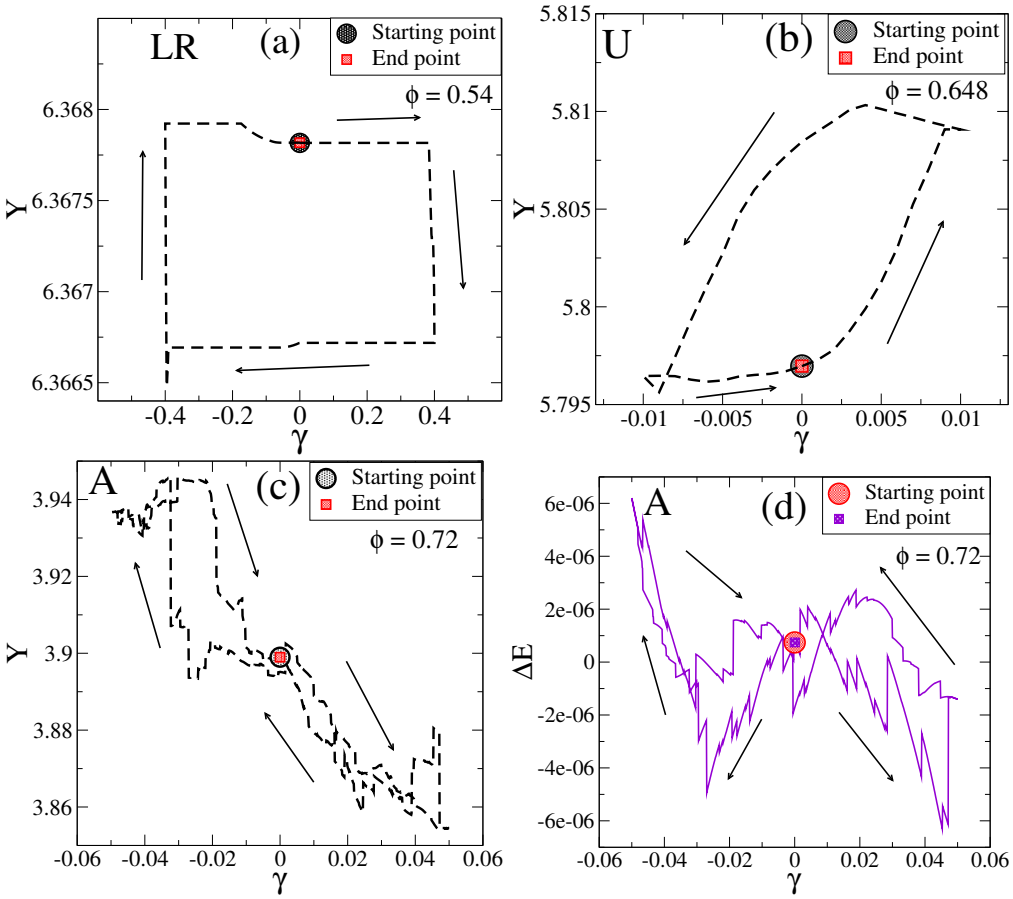

Figure 3.22: (a) We show the evolution of the Y coordinate of a particle in the loop reversible phase (LR), at $\phi = 0.54, \gamma_{max} = 0.4$. The black dashed line shows the trajectory of the particle (a). The particle comes back to the same position after one cycle of deformation. The initial and the final coordinates are highlighted by black and red symbols. We show the Y coordinate of a particle in the unjammed phase (b), at $\phi = 0.648, \gamma_{max} = 0.01$. We show the Y coordinate of a particle (c) and We show the energy (d) of the system after subtracting a harmonic fit curve (to highlight the basin changes, see [151]), ΔE, in the absorbing phase, at $\phi = 0.72, \gamma_{max} = 0.05$.

close to the transition indicates the discontinuous nature of the transition, and we see that in all three density regimes, this is indeed the case.

Of the three regimes we show, data for the density $\phi = 0.627$ appear the least clear. We can indeed fit the data to a power law form with a $\gamma_c \sim 0.384$, but with an exponent $\beta \sim 0.41$ which is smaller than those reported in literature, of $\beta = 0.67$ (barring the ROM model results reported by Corte *et al* (which report a value of $\beta = 0.45$). However, our simulations at $\gamma_{max} = 0.39$ show that the system reaches a loop reversible absorbing state, and therefore the transition amplitude γ_c needs to be equal to or greater than $\gamma_c = 0.39$. Data shown for assumed γ_c values above 0.39 show the same kind of deviations in a log-log plot of D *vs.* $\gamma_{max} - \gamma_c$, albeit weaker. Thus, we conclude that, to the best of our ability to judge, the transition is discontinuous in D at

$\phi = 0.627$ as at higher densities. Close to the transition, the systems show interesting bi-stable behaviour which further support the idea of a discontinuous transition, but a discussion of it will both require additional work.

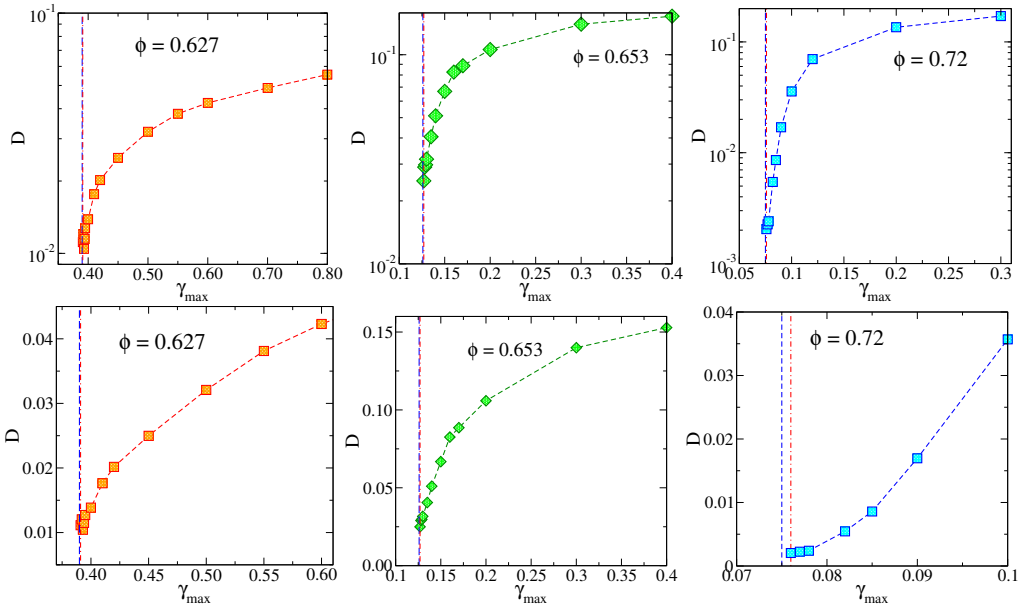

Figure 3.23: The diffusivity as a function of strain amplitude is shown with a denser set (than the previous version of the MS) of data points near the transition in the three regimes, $\phi < \phi_J$, $\phi_J < \phi < \phi_J^{cyc}$ and $\phi > \phi_J^{cyc}$ in both log and linear scale.

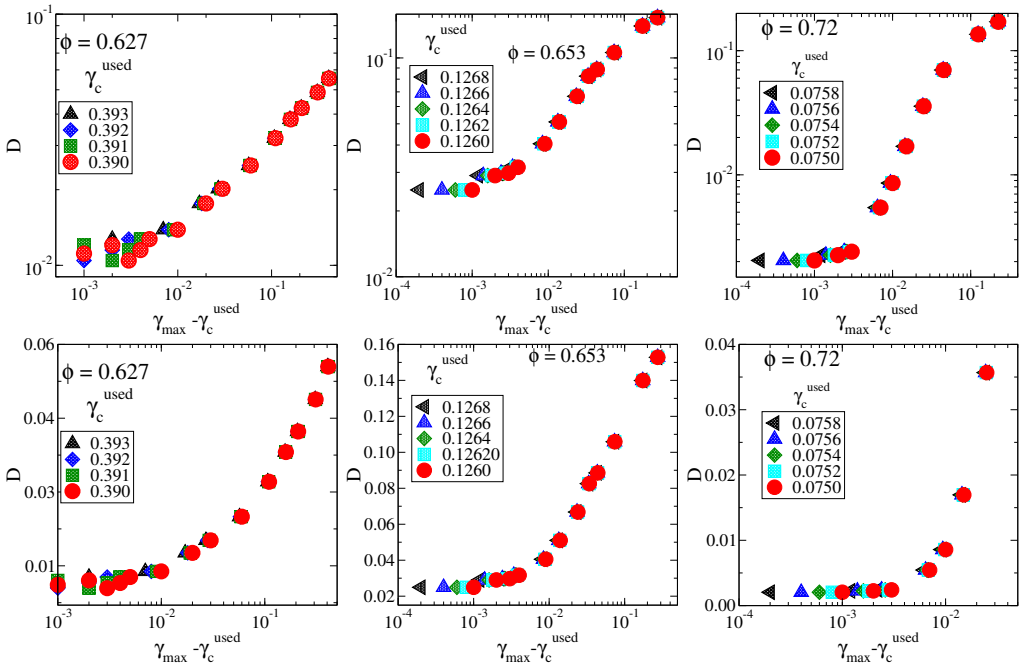

Figure 3.24: Log-log plot (upper panel) and linear-log plot (lower panel) of the diffusivity as a function $\gamma_{max} - \gamma_c^{used}$ for $\phi = 0.627$, $\phi = 0.653$, and $\phi = 0.72$. We use different values for γ_c to illustrate the dependence of diffusivity curves on the value of critical strain amplitude. For $\phi = 0.627$, when using γ_c values above 0.39, we do not show points which lie below the chosen γ_c values.

The reversible-irreversible transition line for packings above ϕ_J corresponds to the yielding (above $\phi_J^{cyc} = 0.661$) and shear jamming transitions ($\phi_J(0.648) < \phi < \phi_J^{cyc}(0.661)$). Below ϕ_J no such obvious correspondence can be drawn. There are recent studies suggesting the possibility of connecting the reversible-irreversible transition line to the shear jamming transition in frictional packings [109, 110, 212, 213]. We have shown that packings below ϕ_j also show a reversible-irreversible transition under cyclic deformation and this transition amplitude increases rapidly with a decrease in density. We have studied shear jamming in cyclically sheared frictionless packings below ϕ_j adding friction to the system. We present some initial findings of the possible correspondence of the cyclic shear jamming and LR-LR transition line. The details of the enumeration of the contact numbers in this regime are described in the Appendix.

Experiments performed on photoelastic discs showed that the application of shear deformation could lead to jamming for a range of densities even below RCP or ϕ_j [107]. Previous studies of monodisperse frictionless spheres under shear deformation below RCP [110, 187, 219] have been shown that shear alone can generate structures that resemble jammed packings even below RCP and that these structures can support jamming in the presence of friction [110, 187]. The geometric criterion on the contact number Z for shear jamming is $Z = D + 1$, where D is the spatial dimensionality. This condition is independent of friction coefficient, spatial dimensions, and jamming

protocols [219]. Here, we subject the low density packings to uniform shear deformation and then generate contact networks or structures that support jamming in the presence of friction, see Fig. 3.25. In Fig. 3.25, we show Z as a function of strain, for different densities, under uniform shear deformation. We take these sheared packings at different strain values and obtain contact forces in the presence of friction by solving for the force, and the torque balance conditions [219]. We compute force balance solutions for these contact networks in the limit of infinite friction. The strain value at which stress shows a discontinuous jump is identified as the shear jamming strain, see Fig. 3.25(b). When the $Z = D + 1$ condition is reached, stress shows a discontinuous jump for all densities. Therefore, $Z = D + 1$ is the geometric criterion for shear jamming. Note that the Z value reaches $D+1(= 4)$ in steady state for $\phi = 0.56$. So we identify $\phi = 0.56$ as the lower limit for shear jamming in the case of uniform shear.
Next we attempt to identify the shear jamming strain amplitude for cyclically sheared configurations below ϕ_j. In Fig. 3.25, we show the steady state Z as a function of deformation amplitude for different densities. We define contacts using a tolerance value from the plateau of $Z(r)$ curves for different amplitudes and densities. We take the steady state configurations and then obtain force solutions using the protocol mentioned in [219]. We further show that for the amplitudes, where stroboscopically $Z = D + 1$, the system can support stress. Unlike uniform shear, we could did not observe shear jamming at and below $\phi = 0.58$. In Fig. 3.25, we show the shear jamming curve and $Z = D + 1$ for both uniform and cyclically shear deformed packings. Interestingly we notice that similar to shifting of the isotropic jamming point under cyclic shear, we can also shift the shear jamming line to higher strain values under cyclic shear compared to uniform shear cases. We observe a correspondence between LR-IR line and shear jamming line below ϕ_J. Though any firm statement requires further investigation.

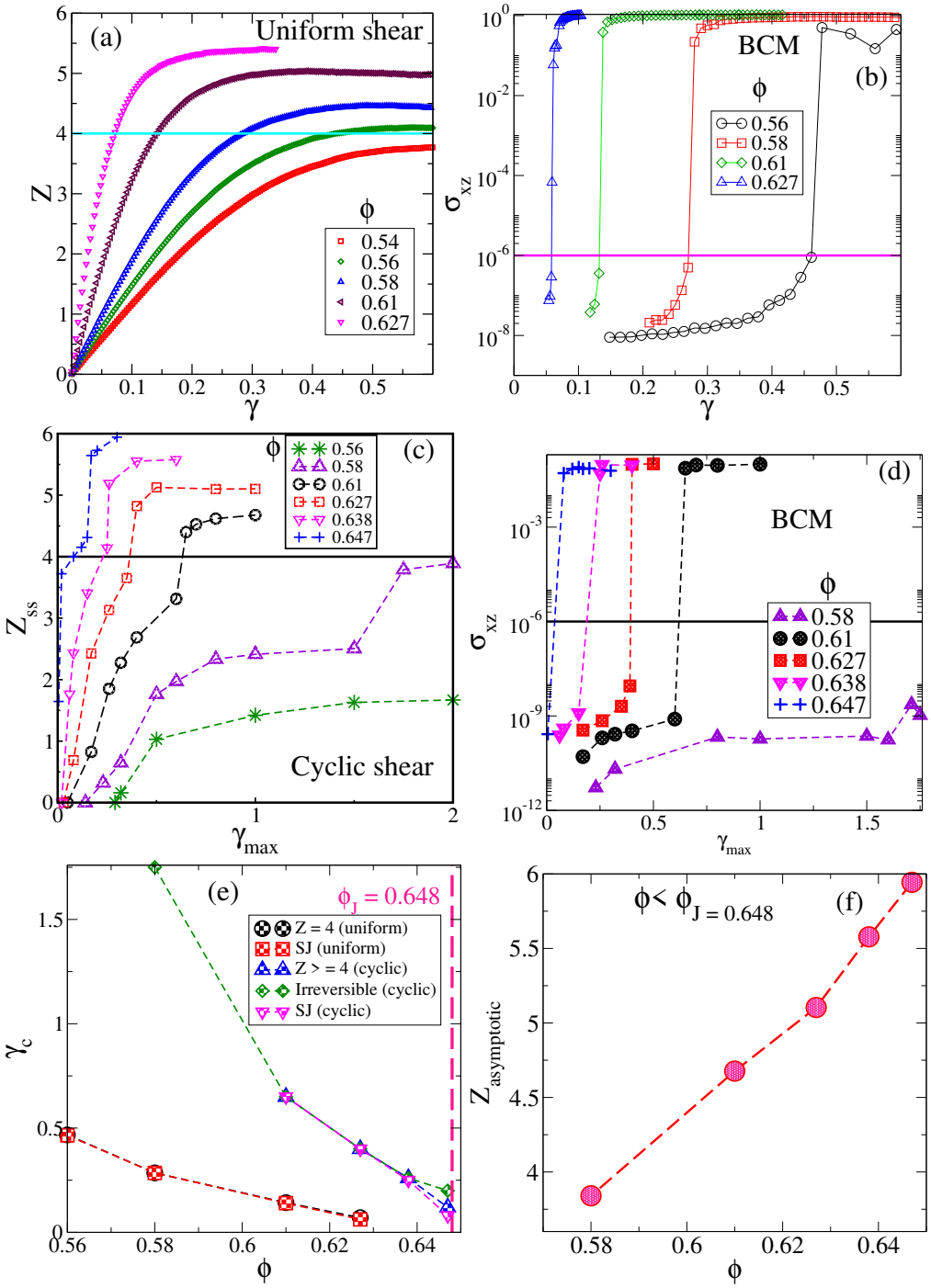

Figure 3.25: (a) Evolution of Z as a function of strain under uniform shear deformation, shown for different densities. (b) Shear stress shows a jump at a strain value where Z reaches $4(D+1)$. The strain value corresponding to discontinuity is the shear jamming strain is shown. Forces are obtained for sheared packings in the presence of tangential forces (or friction) and in the limit of infinite friction. (c) Evolution of Z_{ss} as a function of cyclic shear amplitude, shown for different densities. (d) Shear stress shows a jump at a strain value where Z reaches $4(D+1)$ in the cyclic shearing case. (e) The jamming phase diagram is obtained. We observe that under cyclic shear deformation, the shear jamming line shifts to higher strain values. Also, an irreversible phase emerges as the system produces a jammed like structure. (f) The $Z_{asymptotic}$ value of Z as a function of packing fraction

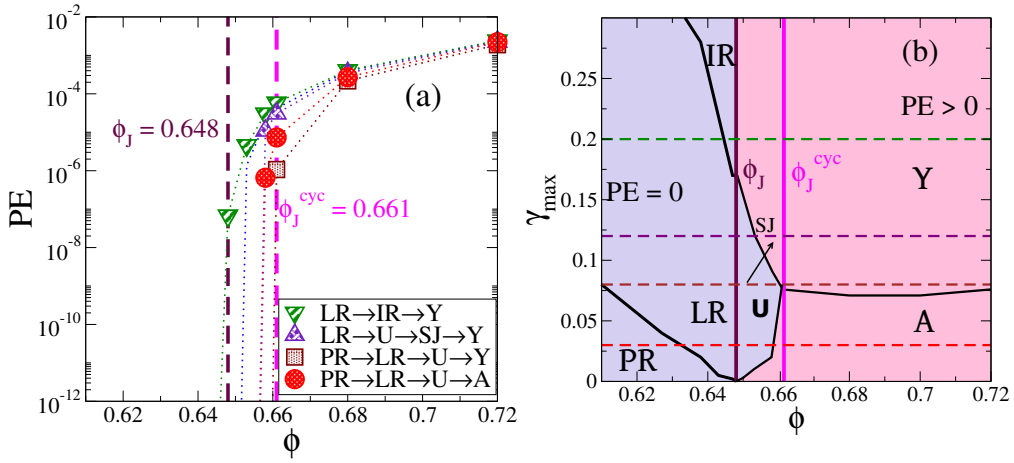

Figure 3.26: Average stroboscopic steady state value of the potential energies shown as a function of ϕ, for four different γ_{max} (a). At these γ_{max} values, potential energy shows a discontinuous change to finite values, but at different densities depending on γ_{max}. For small γ_{max}, the jump occurs at the transition from the unjamming to absorbing or shear jamming states, whereas at larger γ_{max}, it occurs at ϕ_J. (b)The horizontal lines in (b) indicate the strain amplitude at which PE energy shown in (a) are monitored across the density axis.

3.3.4 Phase diagram

Although all the analysis apparently offers a tidy grouping of all observed regimes into three types, one may ask if no further boundaries and transitions separate them further. There is indeed such a separation, in the form of zero or finite energies and stresses. These quantities separate states below ϕ_J and those above, but with a curious exception, illustrated in Fig. 3.26. Moving from low to high densities at intermediate strain amplitudes at which the unjamming phase exists, energies do not become finite at ϕ_J but at higher densities ($\phi > \phi_J^{cyc}$) that correspond to the transition from the unjamming phase to the absorbing phase, or the shear jamming phase. For strain amplitudes larger than the shear jamming value at ϕ_J, the jump to finite energies occurs at ϕ_J. Thus, the unjamming phase forms a curious zero energy and stress pocket in a finite energy regime for densities $\phi \geq \phi_J$.We show the contact number variation across the density (see Fig.3.27) along the irreversible transition line and correspondingly the shear stress.

The global phase diagram that emerges, shown in different density regimes in Fig. 3.28 (a) - (c) and in its entirety in 3.28 (d), has the point reversible phase at low densities and strain amplitudes, that terminates at the isotropic jamming density ϕ_J. Starting with the loop reversible states below ϕ_J that lie at larger strains, moving to larger densities, one has a sequence of loop reversible states in the form of the unjammed phase, and the absorbing phase. At all densities, at still higher strain amplitudes, one sees a

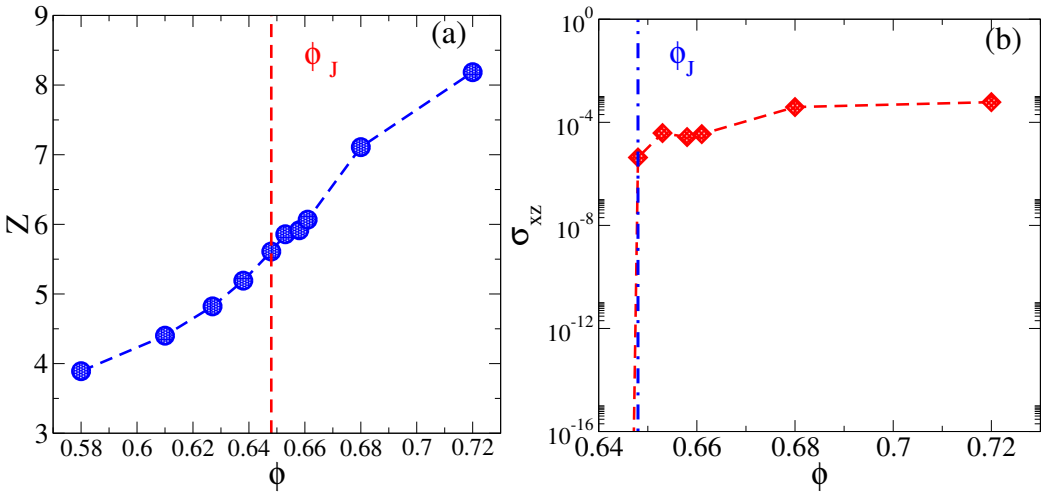

Figure 3.27: contact number Z (a) and shear stress (b) σ_{xz} has been shown across the irreversible transition line.

transition to the irreversible states. Interestingly, at all densities, the transition to the irreversible phase is characterized by a discontinuous jump in diffusion coefficients, which has in the past been shown to characterize the yielding transition in glasses under cyclic shear [124, 134]. The new remarkable observation is that all the transitions we analyse are associated with discontinuous changes in characterisations of trajectories (except the absorbing to unjammed states, characterised instead by a jump in contact number). The presence of loop reversible states at all densities is another general feature that is revealed by our results. Whether these special states are robust in the presence of thermal and other forms of noise remains to be investigated, but they are a common feature of athermally driven systems. Following recent work [151, 218], analyzing memory effects in the the different reversible regimes in light of the behaviour outlined in this work is of great interest. Although the unjamming phase is closely associated with the presence of a line of jamming points along the density axis, the isotropic jamming density (or minimum jamming density) ϕ_J emerges as a non-trivial threshold density. Point reversible states are confined to densities below this value, and energies and stresses become finite in the irreversible phase beyond this density. As noted however, energies and stresses remain zero above this density in the unjamming *pocket*, the origins of which merit further investigation.

3.4 Summary and conclusions

In summary, we have studied the reversible-irreversible transition below, close to and above the jamming density ϕ_J. We have characterised different phases across the isotropic jamming density in detail by studying different microscopic quantities like the mean squared displacement, percentage of new collisions, non-affine path length,

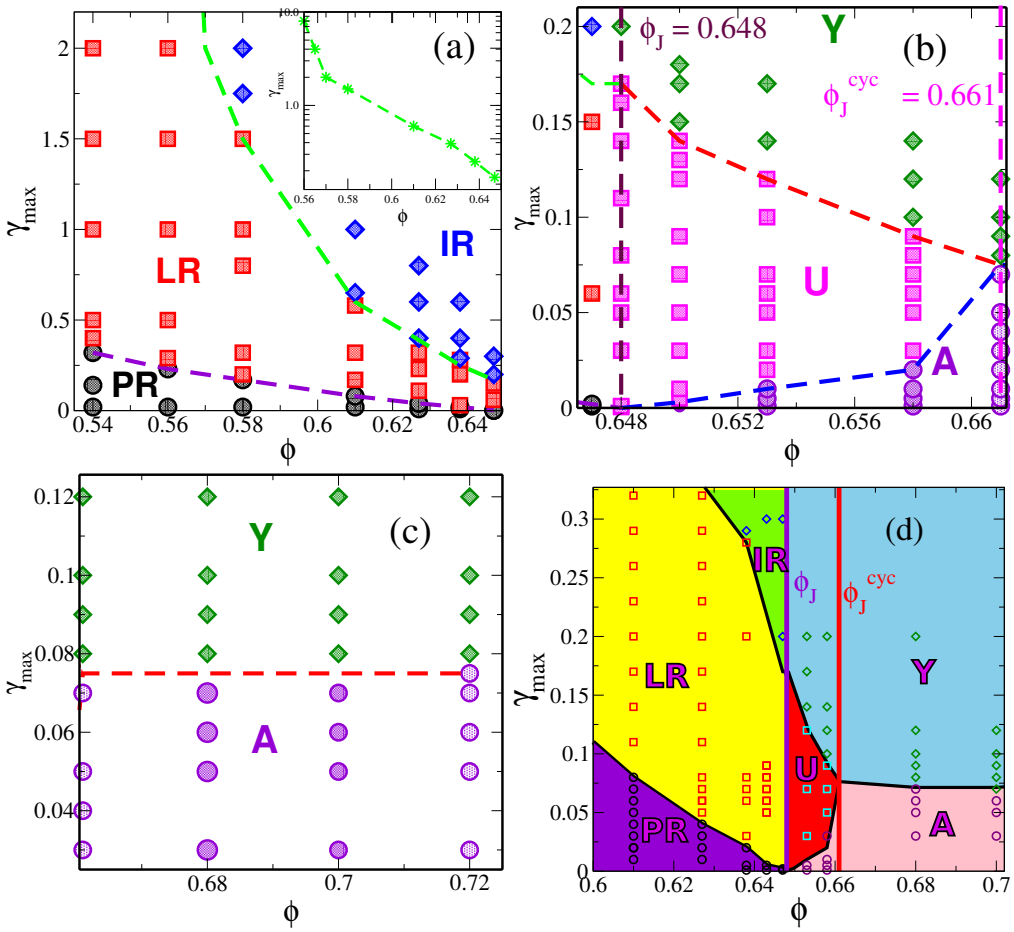

Figure 3.28: The phase diagrams showing different transitions for different range of packing fractions ((a)-(c)) and the global phase diagram (d). Symbols in the legends indicate the following phases: PR: Point reversible; LR: Loop reversible; IR: Irreversible; Y: Yielded phase; U: Unjammed phase; A: Absorbing phase. **(a)** Below ϕ_J. **(b)** $\phi_J \geq \phi < \phi_J^{cyc}$. **(c)** $\phi > \phi_J^{cyc}$. (d) Complete phase diagram showing different phases and transitions across the isotropic jamming density.

stress, potential energy, and contact numbers. For high density jammed packings, the reversible-irreversible transition corresponds to the yielding transition. We have confirmed the presence of an unjamming region close to but above ϕ_J. We identified $\phi_J^{cyc} = 0.661$ as the cyclic shear jamming density, above which the soft sphere packings behave like an elastic amorphous solid. Below ϕ_J, two different forms of reversible phases are present, namely, point and loop reversible. We showed that the non-affine path length and percentage of new collisions clearly distinguish reversible phases and irreversible phases for the whole range of densities. The transition to irreversible behavior is always characterised by the onset of diffusive behaviour of the particles at all densities. All transitions are characterised by discontinuous changes in relevant quantities.

Our work offers a comprehensive view of the response of particle assemblies to cyclic deformation, and is of relevance to a wide range of problems concerning the behaviour of driven amorphous particle assemblies. There are many other obvious directions in which our work can be extended, and we close by a brief discussion of some such directions. Despite much work, the origin of irreversible behaviour, in particular as a transition from periodic to chaotic states [203, 220] remains incompletely elucidated. Our work has focused exclusively on frictionless sphere packings, but the role of friction in shear jamming is well appreciated and therefore understanding the implications of results for frictionless packings to the frictional case and extending the analysis here to the frictional case is of obvious importance. Some progress in that direction has been recently made [109, 110, 213]. The other direction for further investigation is the role of thermal and other forms of noise on the behaviour revealed by our study. The observation of unjamming opens the exciting possibility of systematically studying shear jamming and the related phenomenon of dilatancy in frictionless systems, and the possibility of a unified understanding of frictionless and frictional shear jamming.

Chapter 4

Annealing glasses by cyclic shear deformation

4.1 Introduction

The hallmark of glassy behaviour is the enormous slow down of dynamics upon decreasing temperature as the glass transition is approached. In studies of glass forming liquids through experiments and in computer simulations, such a slow down means that the observed glass transition is always a kinetic phenomenon whereby the liquid falls out of equilibrium in a protocol dependent fashion. Importantly, because glass formers fall out of equilibrium too far away from a putative ideal glass transition, definitive validation or refutation of proposed explanations for glassy behaviour becomes difficult [51, 67, 68, 79, 221]. A telling example is the growth of length scales that are considered to be associated with the approach to the glass transition. Whereas such length scales are expected to diverge at the glass transition, their growth in the observed range of temperatures is modest, varying by less than an order of magnitude [51]. Thus, extending the range of states that can be analysed is of great importance in developing a better understanding of the behaviour of glass forming systems. The reasons for the difficulty in accessing low temperature states is often expressed in terms of the complex energy landscape possessed by glassy systems [12, 77], and going beyond glass formers, the "rugged energy landscape" problem is of relevance to a wide variety of physical systems and contexts.

Recent years have witnessed encouraging progress in addressing the problem of preparing and simulating glass formers and glasses in well annealed, low temperature (or high density) states. Seminal work by Ediger *et al.* opened new directions in experiments and simulations in generating deeper energy states in an efficient manner [80, 221]. It has been shown experimentally that through physical vapour deposition (PVD) of particles on a substrate, maintained at an optimal temperature (15 %

below T_g), glasses that correspond to much lower temperatures compared to conventional methods can be prepared [80, 221]. Enthalpic measurements suggest that the PVD technique results in much lower enthalpy and higher density glasses, termed *ultrastable* glasses, compared to conventional approaches [80, 221]. In computer simulations, time scales accessible to conventional molecular dynamics and Monte Carlo simulations are many orders of magnitude shorter than in experiments. Some approaches using non-local moves and other methods have been attempted [88, 89, 222–226] with varying degrees of success. The experimental PVD method has motivated the corresponding method *in silico* to generate extremely well annealed glass films [81, 86, 227], by optimizing deposition rates and substrate temperature. A limitation of this approach, however, is that it is restricted to the specific geometry required, namely that of a film, and the glasses prepared *via* PVD are inhomogeneous, *i.e.*, the bulk density differs from that of the surface [86]. In simulations of polymeric glasses, the stability is correlated with the high degree of anisotropy, appearing from the layering of polymer along the normal direction to the substrate [94]. More recently, the swap Monte Carlo method [88–91, 224, 228], in which non-local swaps of distinguishable particles are employed to achieve accelerated sampling of configuration space, have been employed with great success in simulating glass forming liquids [90, 91, 228], and also promises to lead to other new simulation approaches [229]. A shortcoming currently of the swap Monte Carlo approach is that it relies on the presence of polydispersity in the simulated systems, although ways of circumventing this limitation are being explored [93]. Even without doing so, the approach allows regimes previously unexplored in simulations to be explored [92, 130, 131, 230]. These developments have greatly advanced the ability to simulate glass formers at low temperatures, and prompted the exploration of other approaches.

Here, we set out to attempt an exploration of the energy landscape of a model glass-former by applying mechanical deformation. The behaviour of glasses (or *inherent structures* (IS), local energy minima generated by energy minimization of liquid configurations) under (typically, but not restricted to) athermal quasistatic (AQS) shear deformation have recently been investigated in order to study the mechanical behaviour of glasses [95, 122, 124, 126, 130, 131, 136, 230–234]. Under cyclic, or oscillatory, shear deformation, the energies of the glasses are found both to decrease from cycle to cycle, or increase, depending on relevant parameters [95, 136, 149]. A detailed analysis of a model glass by Leishangthem *et al.* [95], with the amplitude of shear deformation as the relevant variable, showed that below the yielding strain amplitude, progressively deeper energy minima are sampled, whereas above the yielding amplitude, energies become larger, accompanied by the formation of shear bands [134]. The lowest energy, homogeneous, structures are attained at (but below) the yielding point. This observation (consistent with various theoretical investigations describing the yielding point

as a limit of vanishing or low barriers to rearrangements [119, 189, 235, 236]) suggests cyclic deformation at suitably chosen shear amplitudes as an approach to generate low energy configurations.

We set out to investigate this possibility. In order to incorporate thermal relaxation and explore the role of additional parameters, we study oscillatory shear deformation of liquids at finite temperature and shear rates. We found that the incorporation of finite rate and finite temperature allowed the system to access lower energies compared to the energies accessed by athermal shearing. We compared the energies obtained from cyclic driving with the energies accessed when the system has evolved by equilibrium thermal fluctuation. We make two important observations in this regard. First, in a regime where the temperature is substantially low, but the system can still be equilibrated by equilibrium thermal fluctuations alone, the incorporation of mechanical perturbation does not offer a faster sampling (see conclusion and Chapter 5). In this temperature regime, when the system is driven with the deformation amplitude in the vicinity of the yielding amplitude, it accesses energies similar to the energies accessed by equilibrium dynamics within an equal time. We, in fact, found that the well known fragile glass-forming systems show much faster relaxation (in the absence of any mechanical drive) than expected at low temperatures, which leads to the work described in Chapter 6 of the thesis. However, we made a second important observation that the mechanical perturbation becomes significant at much lower temperatures when the system enters the aging regime. Here, mechanical deformation in the presence of thermal fluctuation drives the system to access lower energies faster(overage) than the energies accessed by aging. We discuss this aspect in the next chapter. In the present chapter, we describe how cyclic deformation generates configurations that have properties of equilibrated liquids and therefore provide a useful benchmark.

4.2 Methods

We perform non-equilibrium molecular dynamics simulations (NEMD) to shear deform a model glass former at finite temperatures and strain rates. The trajectories are generated *via* the SLLOD algorithm [170], employing LAMMPS [237] with a Nosé-Hoover thermostat (or for simulations of equilibrium sampling). We study the Kob-Andersen 80:20 mixture [160] with a quadratic cutoff at $r_{c\alpha\beta} = 2.5\sigma_{\alpha\beta}$, applying Lees-Edwards periodic boundary conditions [164]. The model parameters are $\epsilon_{AB}/\epsilon_{AA} = \epsilon_{BA}/\epsilon_{AA} = 1.5$, $\epsilon_{BB}/\ \epsilon_{AA} = 0.5$, and $\sigma_{AB}/\sigma_{AA} = \sigma_{BA}/\sigma_{AA} = 0.8$, $\sigma_{BB}/\sigma_{AA} = 0.88$. Energy values reported are energies per particle, in units of ϵ_{AA}. Unit of timescale is $\sqrt{\sigma_{AA}^2 m_{AA}/\epsilon_{AA}}$.

The initial liquid configurations are generated *via* equilibrium molecular dynamics (MD) simulation (typically, at temperature $T = 0.466$). Then, these configurations are

subjected to oscillatory shear deformations for a range of temperatures, strain rates and amplitudes, solving the SLLOD equations:

$$\dot{\mathbf{r}}_i = \frac{\mathbf{p}_i}{m} + \mathbf{r}_i.\nabla\mathbf{v} \tag{4.1}$$

$$\dot{\mathbf{p}}_i = \frac{\mathbf{F}_i}{m} - \mathbf{p}_i.\nabla\mathbf{v} - \alpha(t)\ \mathbf{p}_i \tag{4.2}$$

where the strain rate tensor has only the xy component being non-zero, and given by $\gamma_{xy}(t) = \gamma_{max}\sin(\omega t)$, where ω is the frequency, and γ_{max} is the amplitude of strain. The strain rates $\dot{\gamma}$ reported are the strain rate values at the initial time of each cycle, *i.e.* $\dot{\gamma} = \gamma_{max}\omega$. The friction coefficient α depends on the thermostat used (see Chapter 2 for further details). The relaxation time from the equilibrium MD simulation is denoted as τ, whereas the time in the NEMD simulation is denoted by t. We consider $N = 4000$ particles at the reduced density $\rho = 1.2$ and perform simulations for a range of temperatures ($T \in [0.25, 0.4]$) across the Kauzmann temperature estimated in previous work to be ($T_K \approx 0.3$), shear rates ($\dot{\gamma}(0) \in [10^{-6}, 10^{-3}]$), and strain amplitudes (γ_{max}) up to 0.06. We perform conjugate gradient minimization on the simulated (stroboscopic) configurations to obtain energy minimum configurations (inherent structures). We evaluate the potential energy of sheared liquid configurations and inherent structures (IS), stress anisotropy and two dimensional pair correlation functions to characterize their anisotropy, if present. The error bars on γ_{max} indicate the grid spacing with which we sample γ_{max}. The error bars on energies are the standard error of the mean of block averaged energies, with 20 block considered within the measurement window.

We carry out a series of simulations for different shear amplitudes, for each of a set of shear rates and temperatures. The grid of values is limited by the significant computational effort for each data set. To find out the amplitude dependence of the IS energy (which we report stroboscopically, *i. e.*, at the end of each cycle, unless otherwise noted).

4.3 Results

4.3.1 Characterization of the optimal strain amplitude

Onset of yielding in athermally sheared glasses has been studied by considering the energy and stress within a strain cycle and as function of cycles. At the yield strain amplitude (γ_y), the system accesses the minimum energy states based on past work [95]. Beyond the yielding point, the location of the minimum of energy shifts from zero strain to finite strain values, and the area enclosed by the stress-strain curve becomes

finite, indicating the onset of plasticity in the system (see Fig. 4.1). We show here that the optimal strain amplitude, which we identify as the strain at which the inherent structure energy is minimum (stroboscopically), compared to the inherent structure energies obtained when driven with bigger or smaller amplitudes, also displays the characteristic features mentioned above. Within the temperature regime of our interest, the system does not necessarily reach a steady state for all the shear amplitudes. So for such cases (typically for amplitudes up to yielding amplitude), we have chosen a suitable time window within which the energies are averaged and compared. Here, we show the variation of energy at some intermediate time at which a steady state has not necessarily been reached. The average e_{IS} we report as at time $t \approx 10^7$ corresponds to the average energy calculated within a time window of $t \approx 8\times10^6 - t \approx 10^7$. The Error bars shown are the standard error of the mean of block averaged energies obtained for 20 blocks within this time window. At the highest temperature, (T=0.4) as the system equilibrates faster, we have chosen the time window to be $t \approx 2\times10^5 - t \approx 6\times10^5$ and indicate the average within this block to be the long time average.

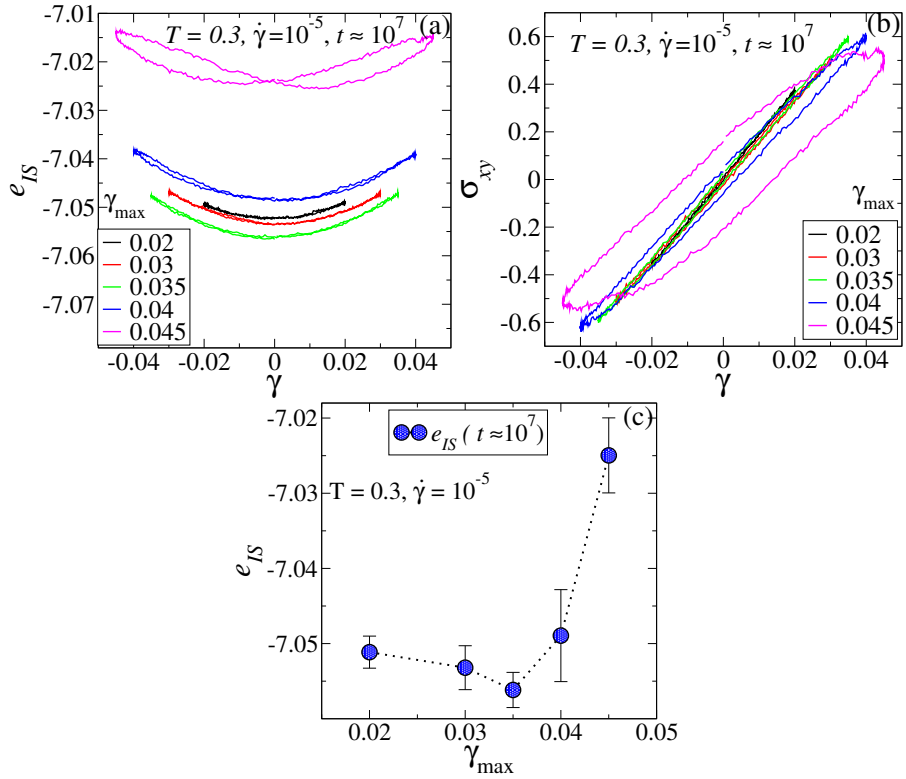

Figure 4.1: (*a*) Inherent structure energy variation within a cycle for different amplitudes at a fixed rate and a fixed temperature. The energy minimum at zero strain shifts to finite strain values above a certain strain amplitude. (*b*) Variation of stress σ_{xy} of inherent structures over a cycle. After a certain amplitude of strain, the stress-strain curves begin to enclose a finite area. (*c*) The optimal strain identified is the location of the minimum in the energy at zero strain is consistent with criteria for the yield strain in earlier work.

4.3.2 Dependence on shear amplitude and rate

In this section, we show results of the inherent structure energy variation with time for a range of temperatures and strain rates (see Fig. 4.2-4.5). The deformation amplitude corresponding to the minimum e_{IS} in a long time window is identified as the optimal amplitude. As noted earlier, such an optimal strain amplitude shares characteristics with the yielding strain amplitude previously studied in athermally sheared glasses. The optimal point shifts to higher values of strain amplitude as the strain rate is increased and it shifts to a lower value as the temperature is increased. At the highest temperature, even though we have analysed amplitudes below $\gamma_{max} = 0.005$, the behavior for such amplitudes are not significantly distinguishable from that of $\gamma_{max} = 0.005$ (see Fig. 4.5) and no clear minimum in the evaluated energies is present. However, above $\gamma_{max} = 0.005$ the energies increase to higher than the equilibrium energy at T=0.4, and hence we identify for this temperature $\gamma_{max} = 0.005$ as the optimal amplitude.

We note that the decrease of energies is generally logarithmic, a feature observed in aging systems, granular compaction, *etc.* [145, 216, 238, 239]. We leave for future work an investigation of how such behaviour may arise in the present context.

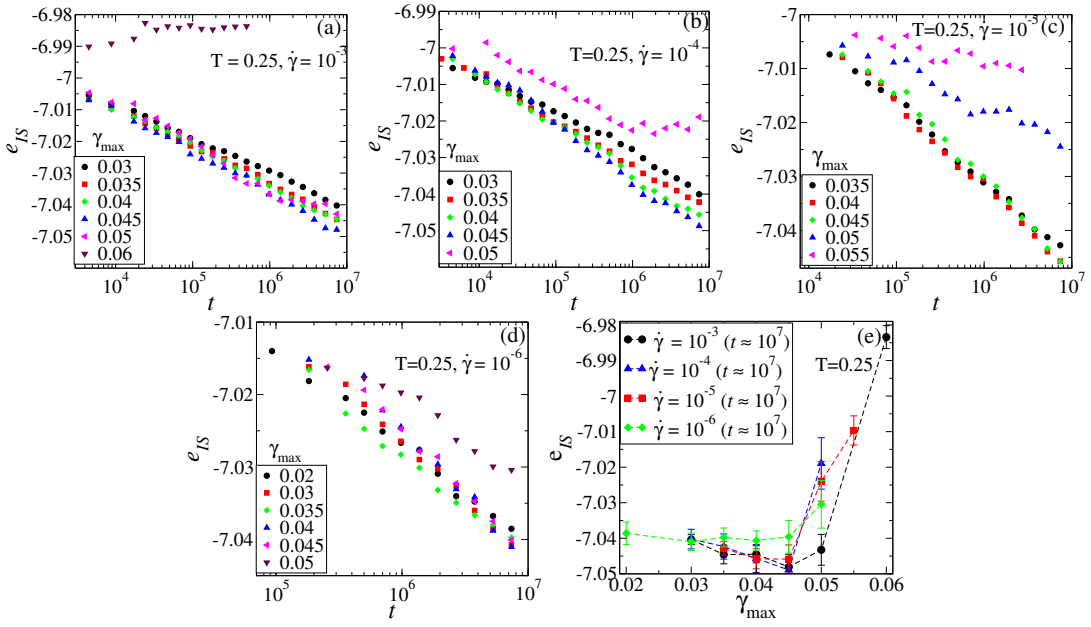

Figure 4.2: (*a*)-(*d*) The evolution of IS energy for different shear rates has been shown for $T = 0.25$. The amplitude at which the long time energy value reaches a minimum is identified as the optimal amplitude γ_y . (*e*) The long time values of IS energies *vs.* strain amplitude, obtained as an average for $t = 8 \times 10^6$ to $t = 10^7$.

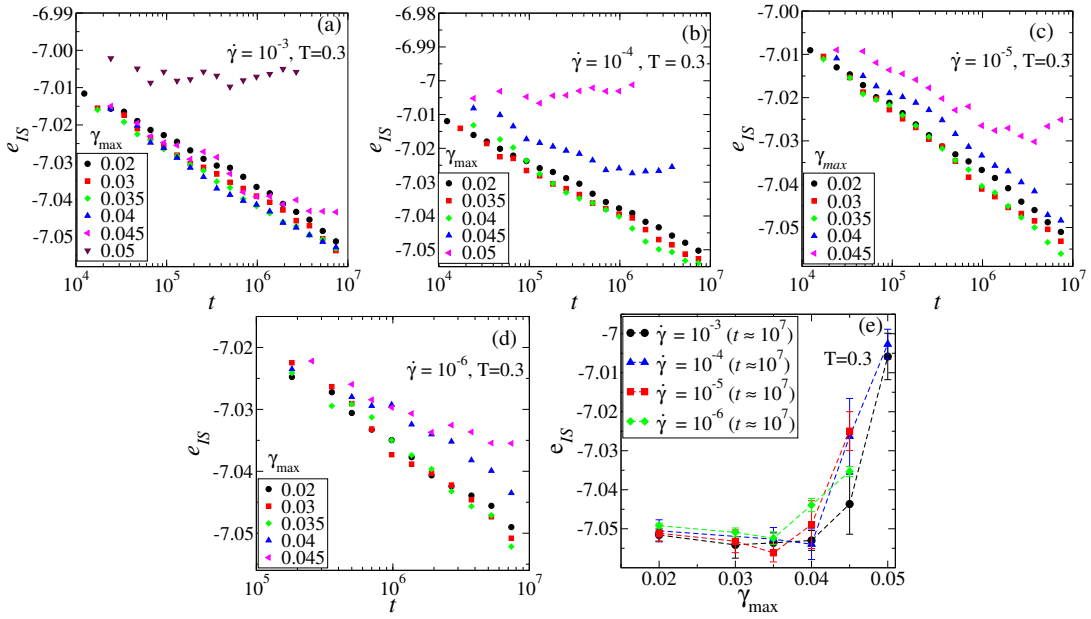

Figure 4.3: (*a*)-(*d*) The evolution of IS energy for different shear rates has been shown for $T = 0.3$. The amplitude at which the long time energy value reaches a minimum is identified as the optimal amplitude γ_y. (*e*) The long time values of IS energies *vs.* strain amplitude, obtained as an average for $t = 8 \times 10^6$ to $t = 10^7$.

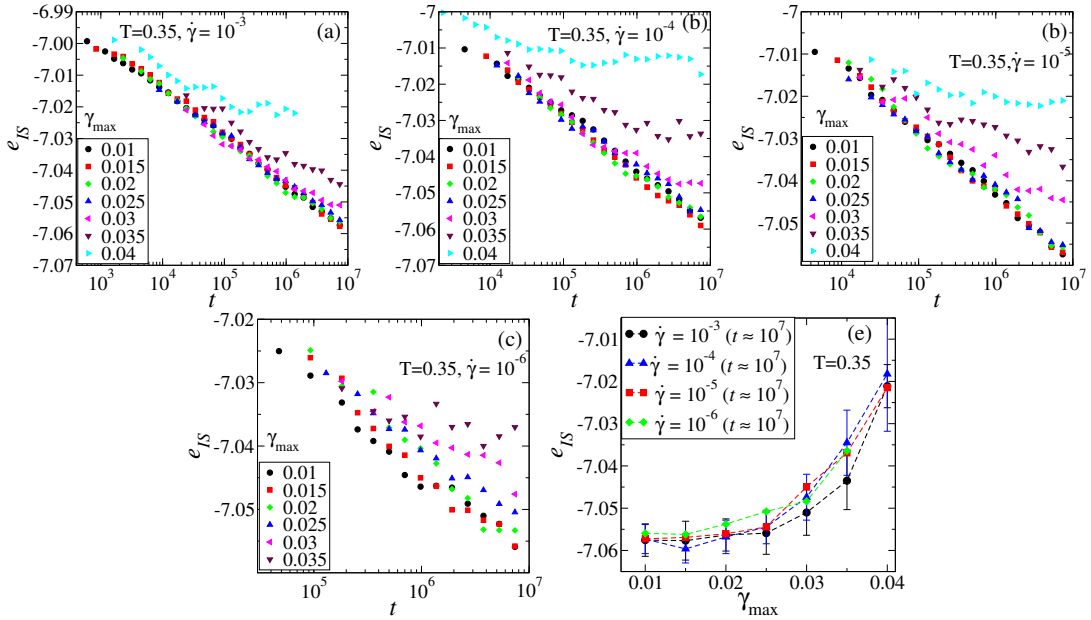

Figure 4.4: (*a*)-(*d*) The evolution of IS energy for different shear rates has been shown for $T = 0.35$. The amplitude at which the long time energy value reaches a minimum is identified as the optimal amplitude γ_y. (*e*) The long time values of IS energies *vs.* strain amplitude, obtained as an average for $t = 8 \times 10^6$ to $t = 10^7$.

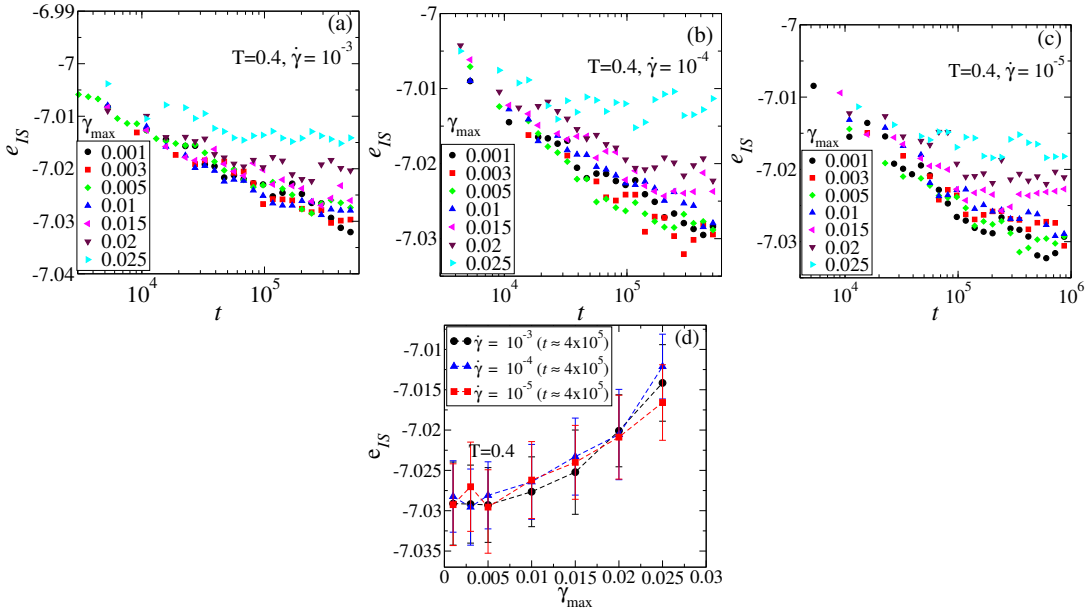

Figure 4.5: (*a*)-(*c*) The evolution of IS energy for different shear rates has been shown for $T = 0.4$. The amplitude at which the long time energy value reaches a minimum is identified as the optimal amplitude γ_y. (*d*) The long time values of IS energies *vs.* strain amplitude, obtained as an average within a time window from $t = 2 \times 10^5$ to 6×10^5.

We next consider the strain rate and temperature dependence of the optimal strain amplitude considering a range of strain rates ($\dot{\gamma} \in [10^{-3}, 10^{-6}]$) and temperatures ($T \in [0.25, 0.4]$). Although with limited data, we see that with increasing strain rates, the yield strain shifts towards higher values , consistently with previous results [128, 129]. Likewise, as the temperature is lowered the yield strain shifts towards higher strain amplitudes, as shown in Fig. 4.6 (a). For each strain rate, we consider the IS energies obtained at the optimal strain amplitude γ_{max} and plot it as a function of temperature in Fig. 4.6 (b). Similar to observations for PVD [86], we find the maximum extent of annealing for $T = 0.35$, near the estimated Kauzmann temperature ($T_K \approx 0.3$), and we perform further analysis at Kauzmann temperature.

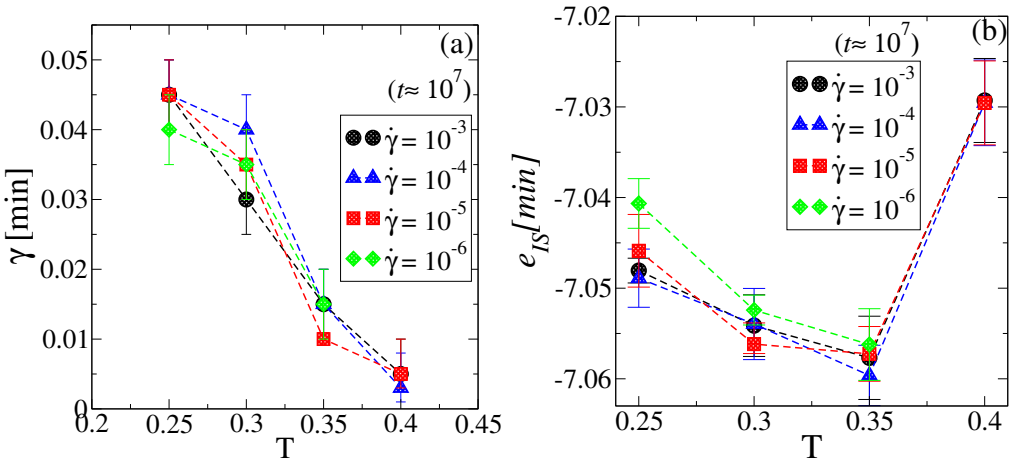

Figure 4.6: (*c*) The strain amplitude for minimum IS energy is a decreasing function of temperature. (*d*) The minimum inherent structure energy attained *vs.* temperature, shown for different shear rates. The results indicate that the optimum temperature for annealing is $T \approx 0.35$.

4.3.3 Cyclic shear and equilibrium relaxation

As the optimal strain amplitude depends on the temperature and rate, we focus below on the amplitude $\gamma_{max} = 0.035$, the optimal value for strain rate 10^{-5} at Kauzmann temperature $T = 0.3$. So far, we have shown that for an optimal combination of shear rate and temperature, the system accesses the lowest possible energy when driven close to the yielding transition amplitude. But in order to estimate the efficiency of the approach, we need a mapping of the inherent structure energies and temperatures. For this, we use the observation [74] that the inherent structure energies at low temperatures display the behaviour

$$e_{IS}(T) = E_{\infty} - \mathcal{A}/T, \tag{4.3}$$

where E_{∞} is the extrapolated infinite temperature IS energy and $\mathcal{A}$ represent the slope of e_{IS} *vs.* $1/T$. Fitting the energies to the above mentioned form we are able to map IS energies and temperatures, as illustrated in Fig. 4.7. The fit parameters are $E_{\infty} = -6.7264$ and $\mathcal{A} = 0.12065$. We have checked that this relation holds well enough to the lower temperature regime. We estimate the equilibrium temperature corresponding to a given inherent structure energy using this relationship. As an extrapolation, however, the meaning of the temperature so estimated should be treated with due caution (see Appendix for further details). Next, we compute relaxation times corresponding to a given temperature using the Vogel Fulcher Tamman relation (VFT) expression $\tau = \tau_0 \exp\left[(K_{VFT}(T/T_{VFT} - 1))^{-1}\right]$ where parameters τ_0, K_{VFT} and T_{VFT} are obtained from fits to MD simulations [240] (see Appendix/chapter 6). A comparison of the estimated temperature reached for a given simulation time with the relaxation time at that temperature provides a way of judging the extent to which cyclic shear may accelerate the accessing of low energy configurations. Fig. 4.8 (b) shows the estimated temperatures *vs.* simulation time, along with reference curves that indicates the dependence of the relaxation times on temperature. A long run of duration $t \sim 6 \times 10^8$ at $\dot{\gamma} = 10^{-5}$ shows the lowest temperature accessed is approximately $T = 0.34$ ($e_{IS} \approx -7.08$, to be compared with the lowest estimated value of -7.15; see Appendix).

We show extrapolated VFT curves for two cases in Fig.4.8 (b). The first curve (black) is the VFT fit to relaxation times for temperatures above $T_{MCT} = 0.435$, which is extrapolated for lower temperatures. A comparison with this VFT fit leads to the conclusion that the relaxation to low energy configurations is significantly accelerated by the application of cyclic shear. To make a direct comparison, MD runs are performed at low temperatures (reported in [240]), with the lowest temperature being $T = 0.365$. These simulations reveal that the temperature dependence of relaxation times undergoes a crossover, with low temperature relaxation times being significantly smaller than the

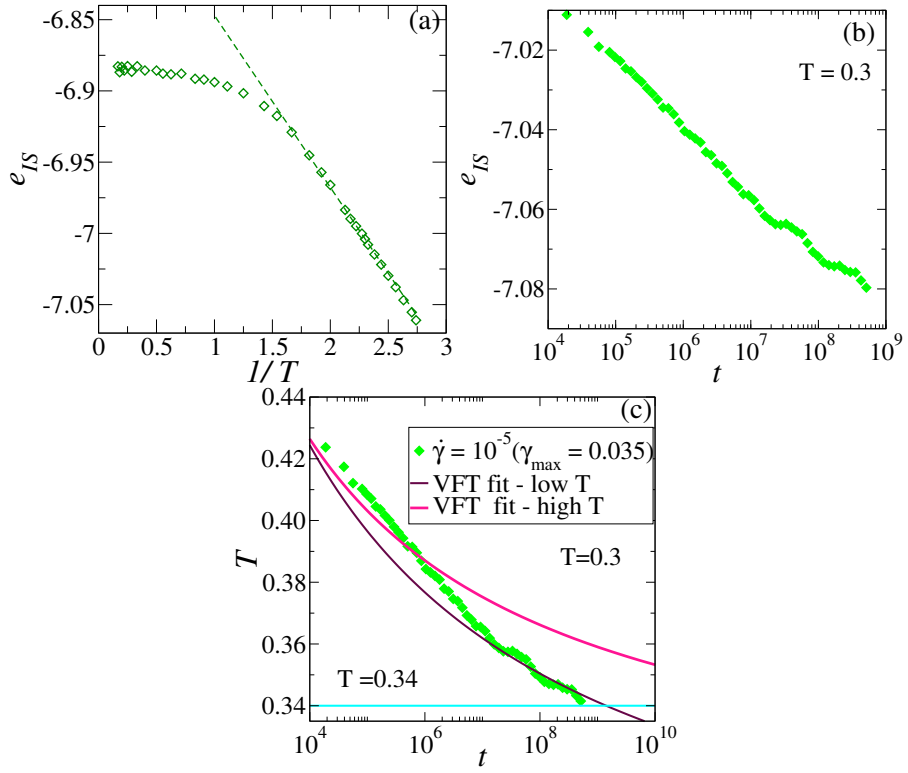

Figure 4.7: (*a*) Temperature dependence of the inherent structure (IS) energy for a liquid equilibrated in a molecular dynamics simulation. The equilibrium molecular dynamics simulation data has been fitted below temperature $T = 0.7$ to obtain a mapping between the IS energy and temperature, which is used to map the IS energy *vs.* time data in panel (*b*) to the temperature values in panel (*c*). Panel (*c*) also shows the VFT relationship between temperature T and relaxation times τ when fitted to two different temperature regime.

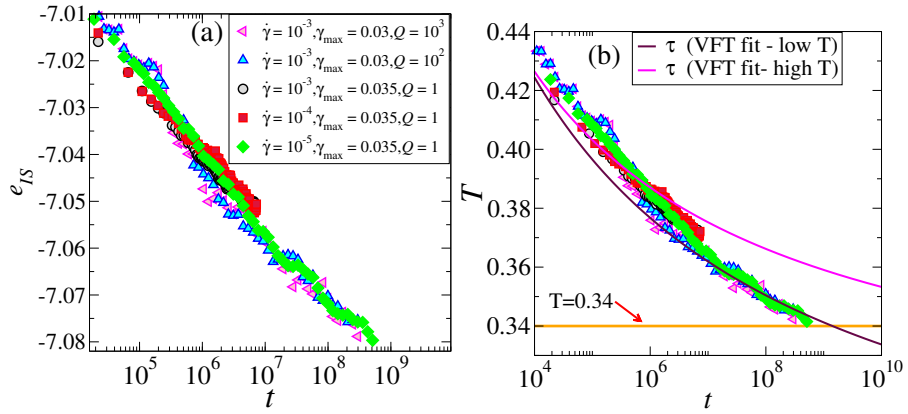

Figure 4.8: (a) Inherent structure energies e_{IS} *vs.* time for different shear rates and different damping parameters (Q), at the simulation temperature $T = 0.3$. (*b*) The energies e_{IS} is transformed to temperatures corresponding to those energies for equilibrated samples. Two extrapolated VFT curves are shown as they are fitted to two different temperature regimes (up to T_{MCT} and up to substantially low temperatures below T_{MCT}).

VFT extrapolation from temperatures above $T = 0.435$. The relaxation times over this extended temperature range are also fitted to the VFT form, which is also shown in Fig.4.8 (b) (maroon curve). A comparison of the cyclic shear results with results from low temperature MD simulations indicates that, contrary to the earlier conclusion, no significant acceleration is obtained through the application of cyclic shear. Although the application of cyclic shear deformation does not therefore appear promising as an approach to performing accelerated sampling at low temperatures, it does lead to overaging when simulations are performed at temperatures lower than $T = 0.3$. We have discussed this elaborately in the next chapter.

4.3.4 Properties of sheared configurations

Apart from the question of whether cyclic shear induces acceleration of relaxation, addressed in previous section, it is of importance to ascertain whether the properties of the sheared liquids are comparable to the equilibrium liquid. We perform a comparison of properties of the sheared liquid and that simulated with conventional MD. Results presented here show that the configurations generated by cyclic shear are isotropic, homogeneous, and have properties that are indistinguishable from the equilibrated liquid configurations. We have chosen $T = 0.4$ (and higher temperatures) for a comparison of the structures generated by conventional constant temperature MD and cyclic shear, at which the liquid can easily be equilibrated with moderate effort in a constant temperature molecular dynamics simulation and (as described later) cyclic shear simulations reach steady states within the simulated time window. For cyclic shear, we have kept our shear rate fixed at $\dot{\gamma} = 10^{-5}$ and based on short runs across different strain amplitudes, identify $\gamma_{max} = 0.005$ as being a reasonable choice based on data shown in Fig. 4.5, for comparison with MD simulations. In Fig. 4.9 we compare the average inherent structure energy obtained from molecular dynamics simulations and finite temperature, finite shear rate, cyclic deformation, as a function of temperature, and show that the energies in these cases are comparable to each other and follow $1/T$ behaviour in the low temperature range.Fig.4.10 shows that the distribution of energies in the steady state for the cyclic shear simulations is identical to the MD trajectory.

Fig. 4.11 shows that the partial radial distribution functions of the inherent structures obtained by NVT MD and cyclic shear simulations agree with each other quantitatively, which implies that the structures generated by cyclic shear are the same as those generated by MD.

We also show, in Fig. 4.12, that the vibrational density of states of configurations ob-

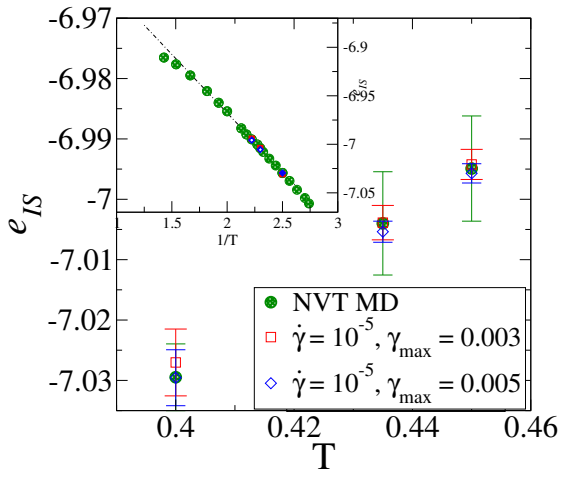

Figure 4.9: The e_{IS} energies obtained from the equilibrium MD is compared to the e_{IS} energy obtained from sheared configurations at amplitudes of $\gamma_{max} = 0.003, 0.005$. The energies show good quantitative agreement. The temperature varies in the range $[0.4 - 0.45]$, where the system can be equilibrated easily by normal molecular dynamics. The shear rate has been kept fixed at $\dot{\gamma} = 10^{-5}$. The inset shows the inherent structure energies against inverse temperature, indicating that the energy obeys a $1/T$ dependence on T.

tained by NVT MD and cyclic shear at $T = 0.4$ are the same, whereas they are clearly different from those of configurations generated by MD at higher temperatures.

To obtain an estimate of the energy barriers surrounding the minima obtained from sheared simulations we have looked at the strain interval distribution for the first plastic drop when these configurations are sheared. This gives us the idea of the measure of the potential energy barriers of the corresponding minima [188]. Here we have taken the inherent structures obtained from equilibrium MD and cyclic shearing at $T = 0.4$. These configurations are subjected to a uniform athermal quasistatic deformation with a strain step of 10^{-5}. With the application of uniform shear, the elastic energy of the system increases and this increase is punctuated by local plastic drops as long as the strain is below the yield strain. The strain value ($\Delta\gamma_{iso}$) at which the inherent structure energy decreases discontinuously, as opposed to the expected elastic increase as a result of shearing, has been identified as the occurrence of a plastic event or a barrier crossing. This strain value gives us the estimate of the energy barrier [188] surrounding the minima obtained from our simulations. For both the cases of equilibrium MD and non-equilibrium shearing, the distributions shown are qualitatively and quantitatively comparable. From this observation, we can conclude that the energy barriers surrounding the minima obtained through cyclic shearing is similar to the minima visited in a normal molecular dynamics simulation at constant temperature. In order to ensure that the apparent agreement is meaningful, we compare these distributions to the strain interval ($\Delta\gamma_{iso}$) distributions for higher temperatures (obtained by molecular dynamics), and note that indeed, these higher temperature distributions

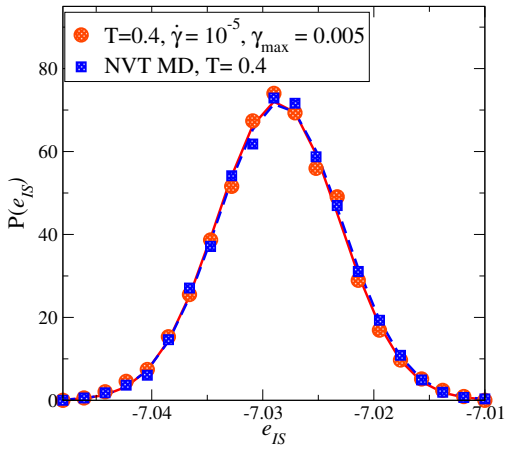

Figure 4.10: The inherent structure energy distribution is shown for the MD and sheared configurations at $T = 0.4$ after the system reaches equilibrium or steady state respectively. The distribution of IS energies from the sheared simulations and MD simulations are indistinguishable.

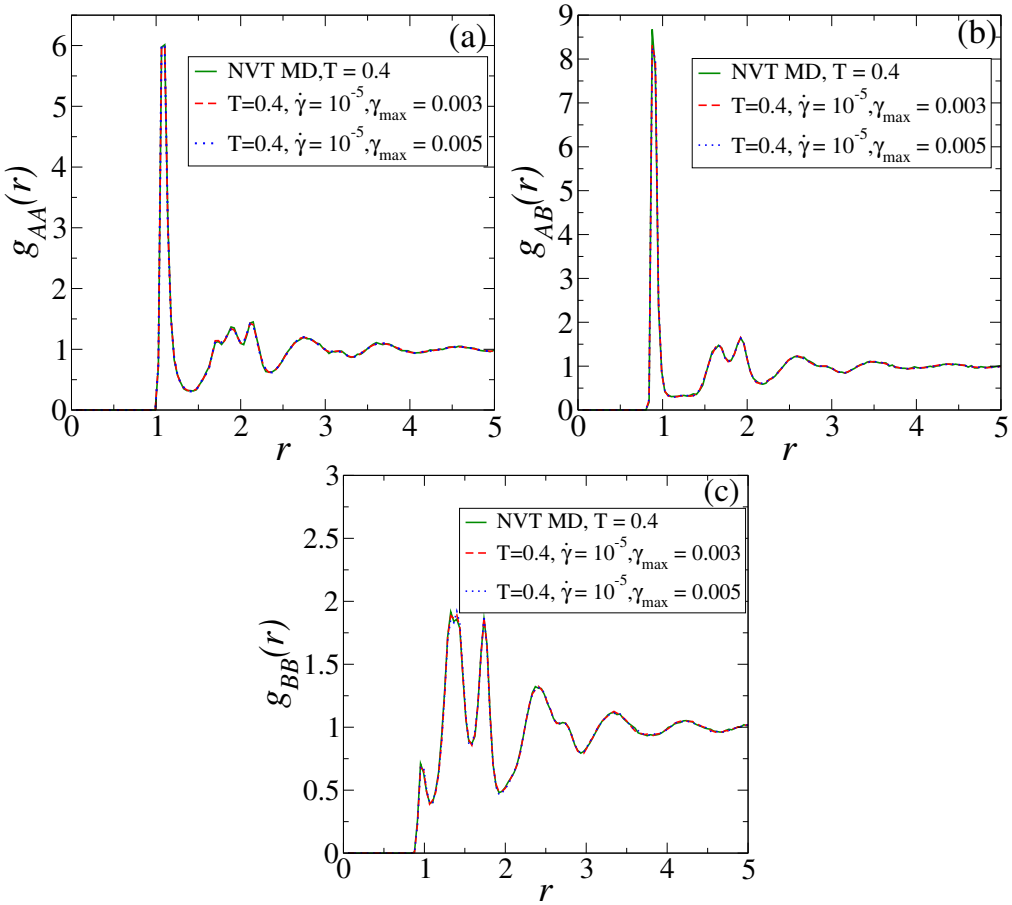

Figure 4.11: The partial radial distribution functions of the IS configurations obtained through equilibrium MD and cyclic shear at a high enough temperature, ($T = 0.4$) where the system can be equilibrated easily through conventional MD. The data show that there is no significant structural difference between the configurations generated from the two approaches.

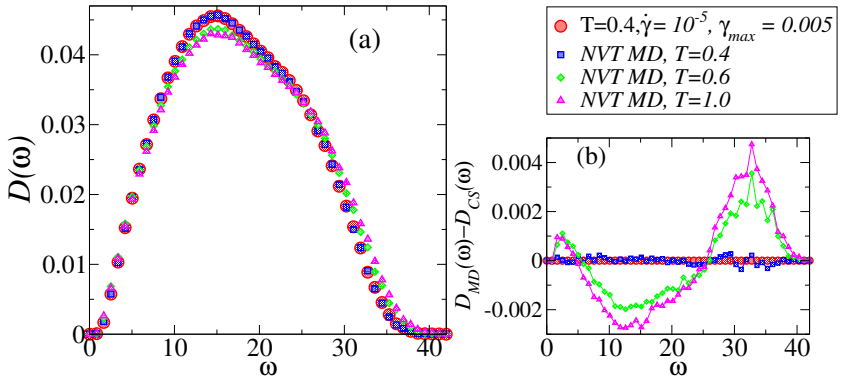

Figure 4.12: *(a)* Vibrational density of states (DOS) for cyclically sheared configurations at $T = 0.4$, and configurations generated by molecular dynamics at $T = 0.4, 0.6, 1.0$. The DOS at $T = 0.4$ are indistinguishable for molecular dynamics and cyclic shear, whereas they are clearly different from those at $T = 0.6, 1.0$ obtained from MD simulations. (b) The difference of the DOS at different temperatures from the cyclically sheared configurations at $T = 0.4$, indicating that MD and cyclic shear results at $T = 0.4$ are indistinguishable.

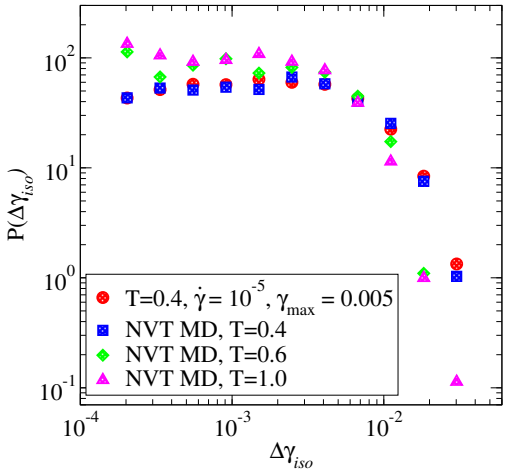

Figure 4.13: The distribution of the strain intervals ($\Delta\gamma_{iso}$) at which the first plastic deformation event occurs for inherent structures obtained through cyclic shear and from NVT molecular dynamics. The strain interval values are a measure of the energy barriers surrounding the undeformed inherent structures. For $T = 0.4$, the distributions from MD and cyclic shear are quantitatively the same, whereas they are easily distinguishable from higher temperature MD results.

are distinguishably different (see Fig. 4.13).

We next examine possible anisotropies in the structures we generate. The ultrastable glasses produced by physical vapor deposition (PVD) method have shown features that can be connected to more anisotropic packing, compared to its ordinary glass counterpart formed by cooling the liquid. Since we perform shear in a given plane, anisotropies are also possible in our case. We also consider the effect of shearing in alternating shear planes (xy, xz, and yz, repeated after 3 cycles). As shown in Fig. 4.14 (a)

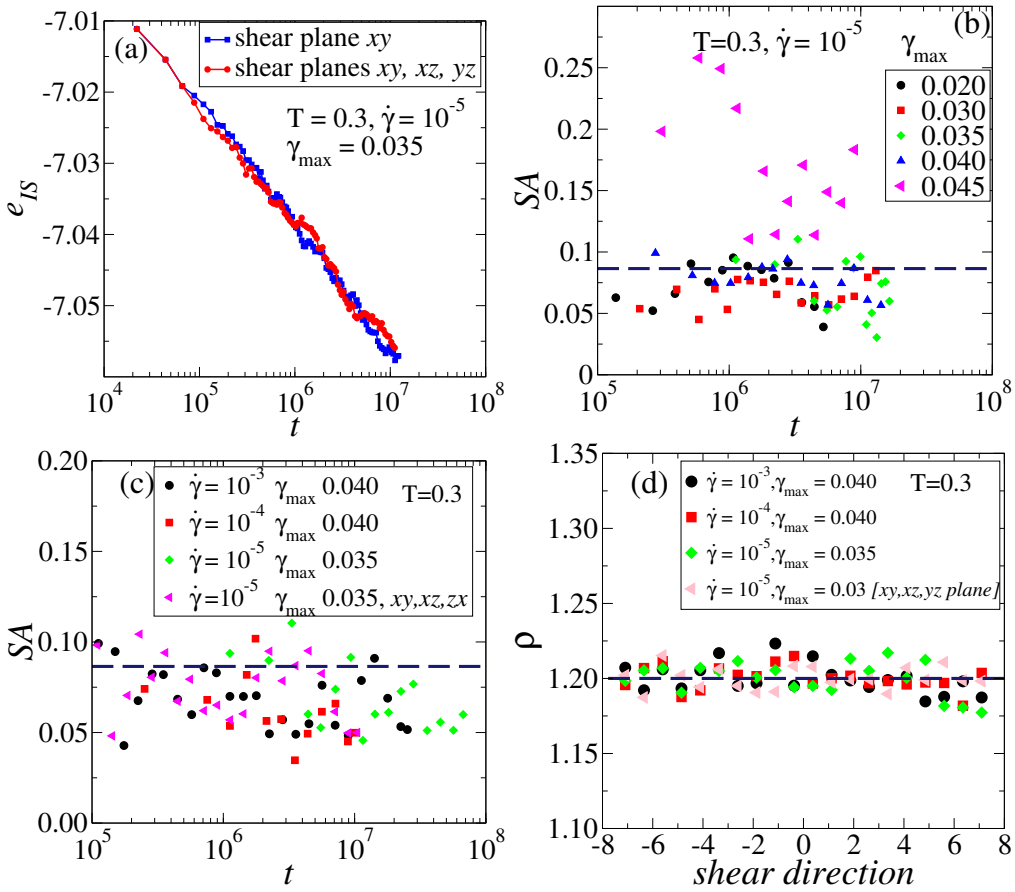

Figure 4.14: (*a*) Inherent structure (IS) energies (when shear is applied in alternating planes) vary in the same way with time as when only xy shear is applied. (*b*) For strain amplitudes lower than or close to the yielding amplitude, stress anisotropies for strain rate 10^{-5} compare with those of isotropic inherent structures (indicated by the horizontal line). (*c*) The same observation holds for different strain rates indicated, and also when shear in applied in alternating shear planes. (*d*) Variation of density in the shear direction indicating that the system is homogeneous in all cases.

the generated energies are essentially the same (however, it has been reported that for larger systems at lower temperatures and shear amplitudes, alternating shear planes leads to better annealing [234, 241]). To characterise anisotropy and inhomonegeity, we first consider the stress anisotropy, which is defined as $SA = (S_1 - S_3)/(S_1 + S_2 + S_3)$, where S_i ($S_1 > S_2 > S_3$) are the eigenvalues of the stress tensor. Excepting for very large strain amplitudes, we find the stress anisotropies to be small, and comparable to those of inherent structures quenched directly from liquid configurations, as shown in Fig.s 4.14 (b) and (c). We also test for the possibility of shear localisation accompanied by inhomogeneities in the local density. Density values obtained for slabs in the shear direction show no evidence of strain localisation (as they do beyond the yield strain in AQS simulations [134], although for larger samples), as shown in 4.14 (d).

We also compute the radially averaged and two dimensional (partial) pair correlation

functions, for stroboscopic configurations, in order to analyse the structure. For temperature T = 0.3 $\dot{\gamma}_{xy} = 10^{-5}$, $\gamma_{max} = 0.035$ has been identified as the yielding strain amplitude. For this amplitude, the radially averaged pair correlation function is calculated after 0 (newly quenched from the liquid), 5, 50 and 500 cycles. The Increase in the number of shear cycles corresponds to a decrease in energy and the temperature. The pair correlation functions show very small amounts of change, comparable to what is observed in the equilibrium liquid at different temperatures (Fig.4.15).
We calculate the two dimensional radial distribution function ($g(x,y)$), in the $xy-$ (shear) plane, defined as

$$g(x,y) = \frac{1}{2Na\rho} \times \left\langle \sum_{i=1}^{N-1} \sum_{j \neq i}^{N} \delta(x-(x_i-x_j))\delta(y-(y_i-y_j))\theta(a-|z_i-z_j|) \right\rangle, \tag{4.4}$$

where "$\langle\rangle$" represents the averaging over independent samples. x_i, y_i, and z_i are coordinates of particles. A pair of particles is considered to be in the same plane if the separation between them does not exceed a threshold value $a = 0.2\sigma_{AA}$, which is enforced by the Heaviside function above.
As shown in Fig. 4.16, these correlation functions do not reveal any indications of anisotropy.

All the above comparisons show that the IS configurations obtained by cyclic shear

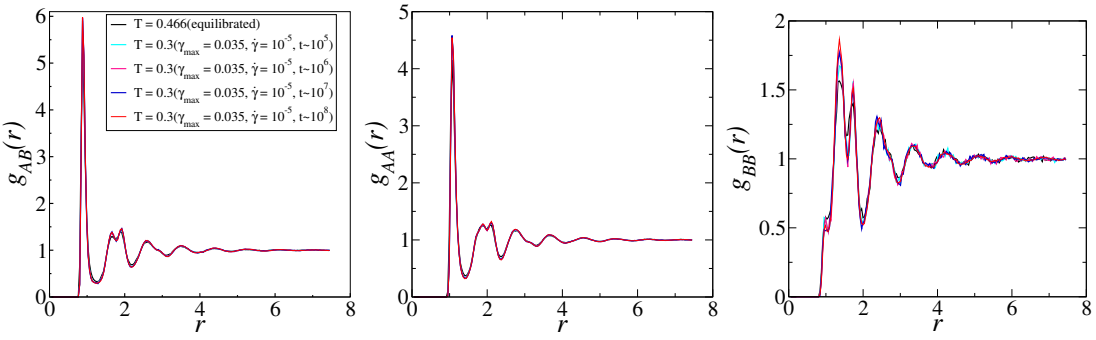

Figure 4.15: The partial pair correlation functions of the liquid configurations at the end of different cycles compared with the initial configuration.

are isotropic. Such isotropy is surprising, but has previously been noted in the context of both symmetric [151] and asymmetric [242] cyclic shear of glasses. It appears that such isotropy arises from the high density of the systems, the cyclic nature of the deformation, and the presence of plastic rearrangements, which needs better understanding. This is in contrast with low density systems subjected to cyclic [243] and uniform [244] driving. They also show that they exhibit the same response to shear (in the form of the distribution of strain required to undergo a plastic rearrangement) as those obtained from conventional MD.

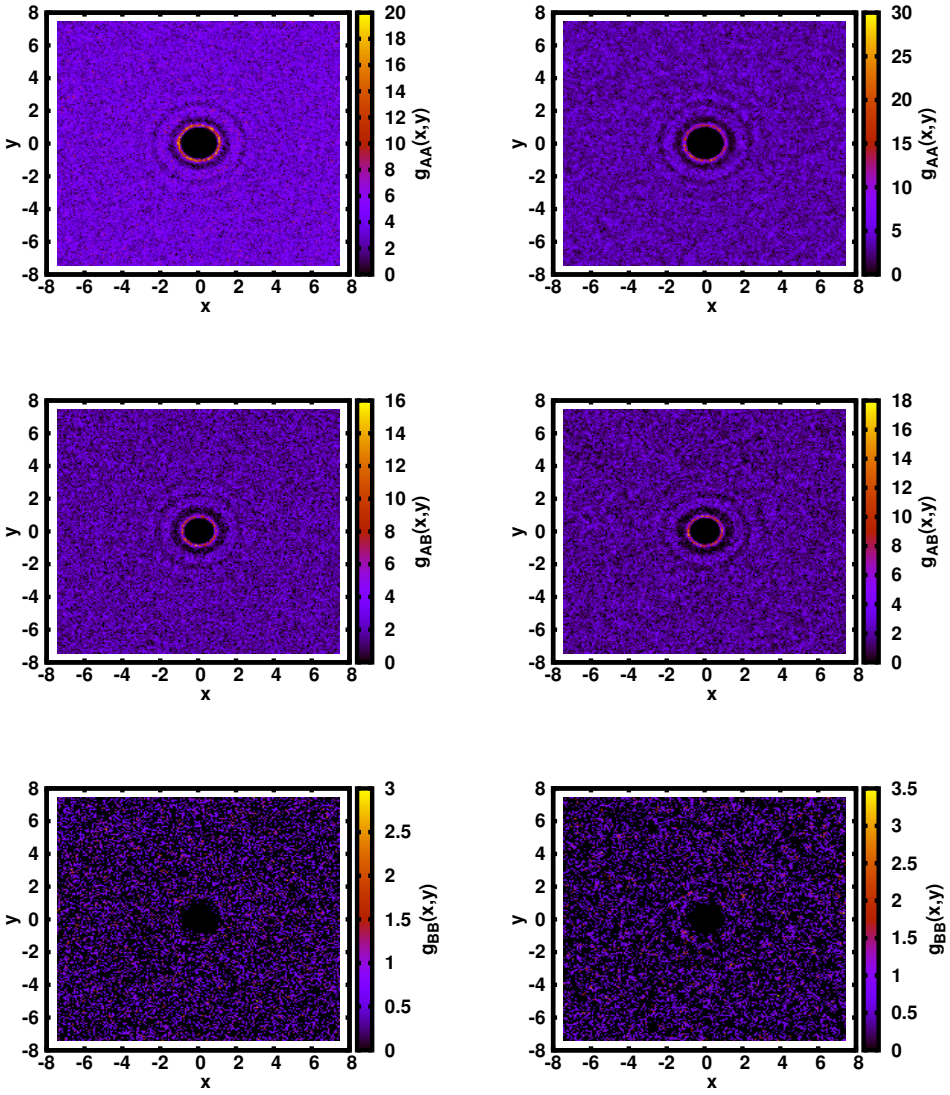

Figure 4.16: Two dimensional, partial pair correlation functions in the shear plane for (left panel) the initial configurations at $T = 0.466$, and (right panel) after 2000 shear cycles (t $4x10^7$). No indications of anisotropy is observed.

4.4 Conclusion

To summarise, we have explored the possibility of generating low energy configurations by the application of cyclic shear deformation and have attempted to find optimal conditions for doing so, namely temperatures close to the Kauzmann temperature ($T = 0.35$), strain amplitudes close to yield strain ($\gamma_{max} \approx \gamma_y$) and small strain rates. According to the extrapolated VFT prediction, the obtained low energy configurations

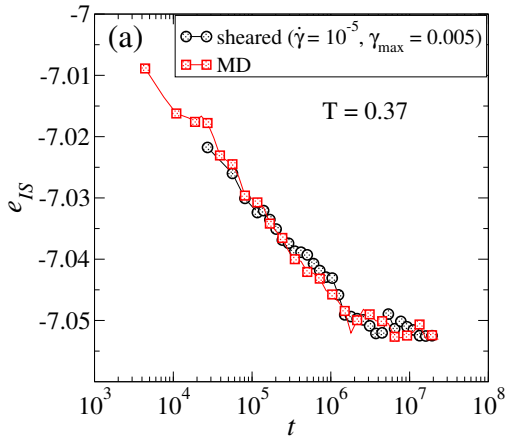

Figure 4.17: The energy relaxation of MD and sheared simulation is very similar at T = 0.37.)

are generated faster than configurations obtained by performing normal molecular dynamics simulation. But verification of the validity of the VFT prediction leads us to the work described in Chapter 6 of this thesis. We observe that faster relaxation by normal equilibrium dynamics occurs at a low temperature regime. Extrapolated VFT fit gives an overestimation of the relaxation times at substantially low temperatures when the actual simulation data used for fitting and extrapolation is limited to a comparatively high temperature regime (up to T_{MCT}). We find that the temperature regime where the system can still be equilibrated with long computational simulation, the cyclic shear method does not offer effective acceleration. In this regard, we will mention that In Chapter 6, we have been able to equilibrate the same system via equilibrium molecular dynamics down to the temperature $T = 0.365$. As we have seen earlier, at the temperature range $T = 0.4 - 0.45$ (see Fig. 4.9) and further down to temperature $T = 0.37$ (see Fig. 4.17), (temperatures within the equilibrium range), the system does not show faster sampling when driven with deformation amplitude close to the yielding amplitude. However, we will show that cyclic shear does overage the system in the aging regime. So even if cyclic shear cannot be employed as an effective equilibrium sampling method, the phenomena of reaching lower energy states by cyclic driving than by thermal aging still remains. But beyond which temperature thermal fluctuation becomes more prominent than mechanical perturbation, this remains to be investigated and understood in our future work. Nonetheless, cyclic shear with the optimal choice of deformation amplitude and strain rate generates anisotropy free equilibrium like configurations in the temperature regime where the system can be equilibrated.

Chapter 5

Overaging by cyclic shear deformation

5.1 Overaging by cyclic shear deformation

The aging of glasses is an important matter of practical interest. A huge range of polymer glasses used in everyday life is the systems that have undergone glass transition. Hence the system stays out of equilibrium. Any property of such aging systems becomes a function of time. Therefore any measurements in such glassy systems have a crucial parameter called the waiting time t_w. Waiting time is the time elapsed from the time when the glass is formed. Aging alters properties like embrittlement or dielectric strength that are crucial for the application purpose of the material. Therefore, it is essential to understand the nature and predict the amount of aging that can happen in material to determine its sustainability when used in various applications. As the system ages further, the relaxation in the system becomes progressively slower. Hence, the more aged the system is, the slower the change of the properties of concern can be.

Aging behaviour can be affected by the application of mechanical drive. The mechanical drive can take the system to such parts of the landscape where the structural relaxation becomes slower. This phenomenon is known as overaging or mechanical aging. The driving can also lead the system to such parts of the landscape where the relaxation becomes faster. This phenomenon is known as the rejuvenation of glasses. In several computational studies and experiments, the effects of mechanical driving on aging have been observed and studied. Studies have shown that mechanical aging changes the mechanical properties of the system, such as making them stronger glasses by increasing the modulus [245]. Studies in polymer glasses show that mechanical drive leads the system to such parts of the landscape that are qualitatively and quantitatively different from the results of thermal treatment of the system [246]. Again study of polymer glasses shows overaging in glasses prepared by quenching, but the effect recedes when the system is well annealed. The overaging phenomenon

depends on different timescales in the system like β relaxation timescale or cooling timescales [247]. Nonetheless, in various systems, overaging in the pre-yield regime has been reported. However, the absence of overaging and recovery of the relaxation in the absence of mechanical drive has also been observed in the study of polymer glasses [158].
In our work, we find that when a model metallic glass former is subjected to cyclic driving, a significant amount of overaging occurs in the pre-yield regime at certain low temperature regimes. In this chapter, we discuss different aspects of overaging under cyclic shear deformation.

5.2 Methods

We study the Kob-Andersen 80:20 mixture [160] with a quadratic cutoff at $r_{c\alpha\beta} = 2.5\sigma_{\alpha\beta}$, applying Lees-Edwards periodic boundary conditions [164]. The model parameters are $\epsilon_{AB}/\epsilon_{AA} = \epsilon_{BA}/\epsilon_{AA} = 1.5$, $\epsilon_{BB}/\ \epsilon_{AA} = 0.5$, and $\sigma_{AB}/\sigma_{AA} = \sigma_{BA}/\sigma_{AA} = 0.8$, $\sigma_{BB}/\sigma_{AA} = 0.88$. Energy values reported are energies per particle, in units of ϵ_{AA}. Unit of timescale is $\sqrt{\sigma_{AA}^2 m_{AA}/\epsilon_{AA}}$. We perform non-equilibrium molecular dynamics simulations (NEMD) to shear deform a model glass former at finite temperatures and strain rates. The trajectories are generated via the SLLOD algorithm [170], employing LAMMPS [237] with a Nosé-Hoover thermostat (or for simulations of equilibrium sampling). Equilibrium molecular dynamics simulations have been performed in the NVT ensemble for a range of temperatures $t = 0.37-0.1$. We consider a system of size N = 4000 particles at the reduced density $\rho = 1.2$. The simulation run length has been mostly till $t \sim 10^7$. We have performed simulations in the aging regime. We have chosen simulation time $t = 10^7$ to be the long time approximation in this work. We have compared the energies of different cases, taking an average of quantities within the time block of $t \approx 8\times10^6 - 10^7$. Eight independent configurations have been quenched from equilibrated $T = 0.466$ liquid configurations to the target temperature, and subsequently, the NVT MD simulations and cyclic shear simulations have been performed.

5.3 Results

5.3.1 Faster equilibrium relaxation at low temperatures

We have discussed how cyclic shear generates low energy configurations for suitable combinations of temperature, shear rate, and shear deformation amplitude. In the previous chapter, we performed a comparative study of deformed and undeformed systems in the temperature regime where the system can be equilibrated by normal

molecular dynamics simulation (such as at $T = 0.4$). We have concluded that sheared configurations are similar to the undeformed equilibrated configurations in the pre-yield regime. We have seen that in equilibrium and sheared simulations, the system reaches similar low energy configurations at comparable times. But the extrapolated VFT prediction indicates one should expect faster sampling at further lower temperatures, such as at $T = 0.37$.

Most metallic glasses are fragile glass-forming liquids. Their relaxation time shows a faster divergence than relaxation time predicted by Arrhenius law at lower temperatures. But a couple of recent studies of metallic glasses [40, 42, 248–251] that are generally known as fragile glass formers show a possible dynamical crossover to strong glass formers-like behaviour at low-temperature regime, implying their relaxation time divergence becomes milder than expected. At this point, carrying out an equilibrium molecular dynamics simulation at further low temperatures like $T = 0.37$, we find that the relaxation time predicted by VFT extrapolation overestimates the relaxation times at this low-temperature regime (see appendix). Similar to the recent dynamical crossover mentioned in different metallic glasses, we also find evidence of a dynamical crossover at low temperatures in our system (further discussion in Chapter 6) that causes slower divergence of relaxation time at lower temperatures. Next, We performed cyclic shear at $T = 0.37$, $\dot{\gamma} = 10^{-5}$ and $\gamma_{max} = 0.005(\leq \gamma_y)$. Comparing equilibrium MD and the cyclically sheared trajectory, we find thermal fluctuation alone is sufficient for the optimum relaxation at such a temperature range (see Fig. 5.1). The time evolution of the e_{IS} for the equilibrium dynamics and the sheared simulation do not show any significant difference. But in this chapter, we will discuss how mechanical perturbation becomes more significant than thermal fluctuation at further low temperatures, where the system enters the aging regime. This implies when cyclic deformation is applied to the system (under optimal conditions), it accesses lower energies faster compared to the energies accessed by the system when evolving under thermal fluctuation alone. We further show in this chapter how the variation of different parameters (such as temperature, rate, and amplitude) provides a better route to access lower energies faster or to overage the system.

5.3.2 Comparison between normal molecular dynamics and cyclic shear deformation lower temperatures

We carried out cycle shear and molecular dynamics simulations at very low temperatures, ranging from $T = 0.35 - 0.10$. As mentioned in the previous chapter, we have considered t 10^7 as our long-time observation timescale. The long time values of IS energies (or temperature), obtained as an average for $t = 8 \times 10^6$ to $t = 10^7$. We have shown comparisons of e_{IS} between sheared configurations and configurations

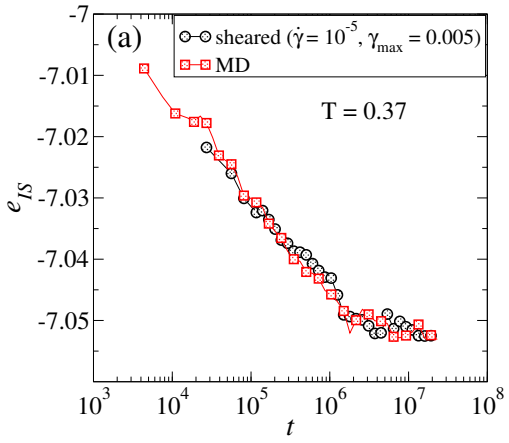

Figure 5.1: The energy relaxation of MD and sheared simulation is very similar at T = 0.37.)

obtained from equilibrium simulations for combinations of temperature, shear rate, and amplitude. The temperature regime mentioned here is substantially low, and the system does not equilibrate within a computationally feasible timescale. The system ages. When the system is driven with amplitudes close to or lower than the yielding amplitude(γ_y), it accesses lower energies faster than the energies achieved when the system evolves under equilibrium fluctuation. As mentioned earlier, γ_y is the amplitude of deformation that drives the system to the lowest possible energy. The evolution of e_{IS} has been shown as a function of time for temperatures within $T = 0.2 - 0.1$ (e_{IS} vs in Fig. 5.2 (t data for $T = 0.25$ and $T = 0.3$ has been shown already in Chapter 4). Under the mechanical drive system reaches lower energy faster or overages. We see around $T = 0.3$ the system starts showing the effect of overaging (see Fig. 5.3). As the temperature decreases further, the amount of overaging increases, implying mechanical perturbation becomes progressively important for the system to access available energy states.

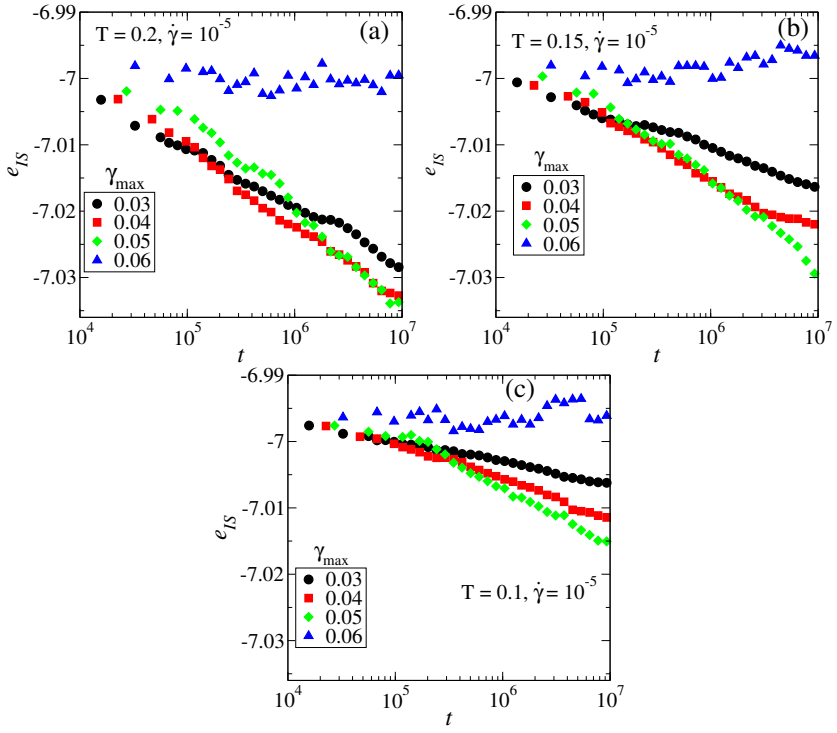

Figure 5.2: (*a*)-(*c*)The evolution of IS energy for the three lowest temperatures ($T = 0.1, 0.15, 0.2$) has been shown. The amplitude at which the long time energy value reaches a minimum is identified as the optimal amplitude γ_y.

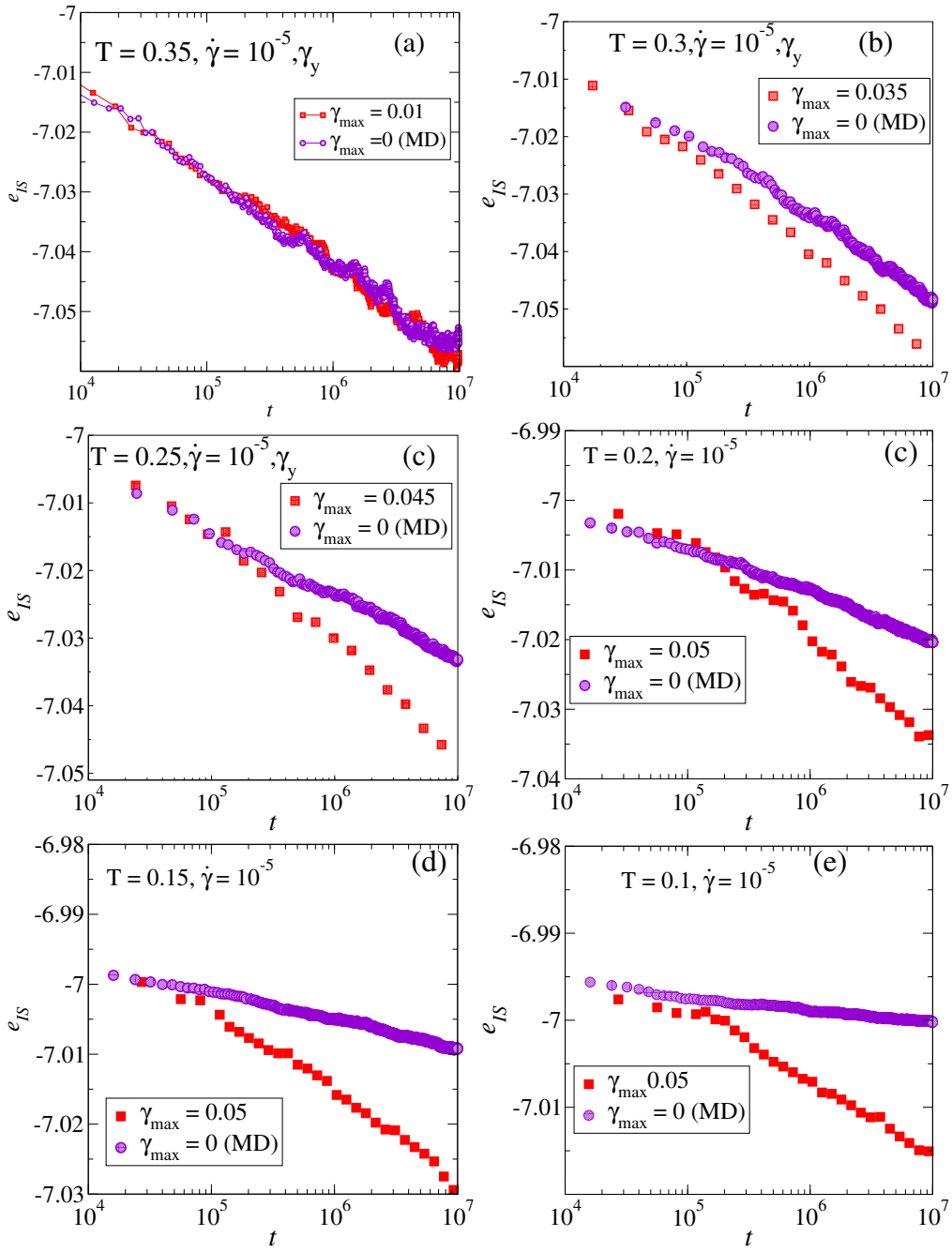

Figure 5.3: Beyond temperature $T = 0.3$ the system starts showing overaging behaviour under mechanical deformation. Inherent structure energy evolution has been looked at for a range of temeperatures.

5.3.3 Dependence on deformation amplitude and rate

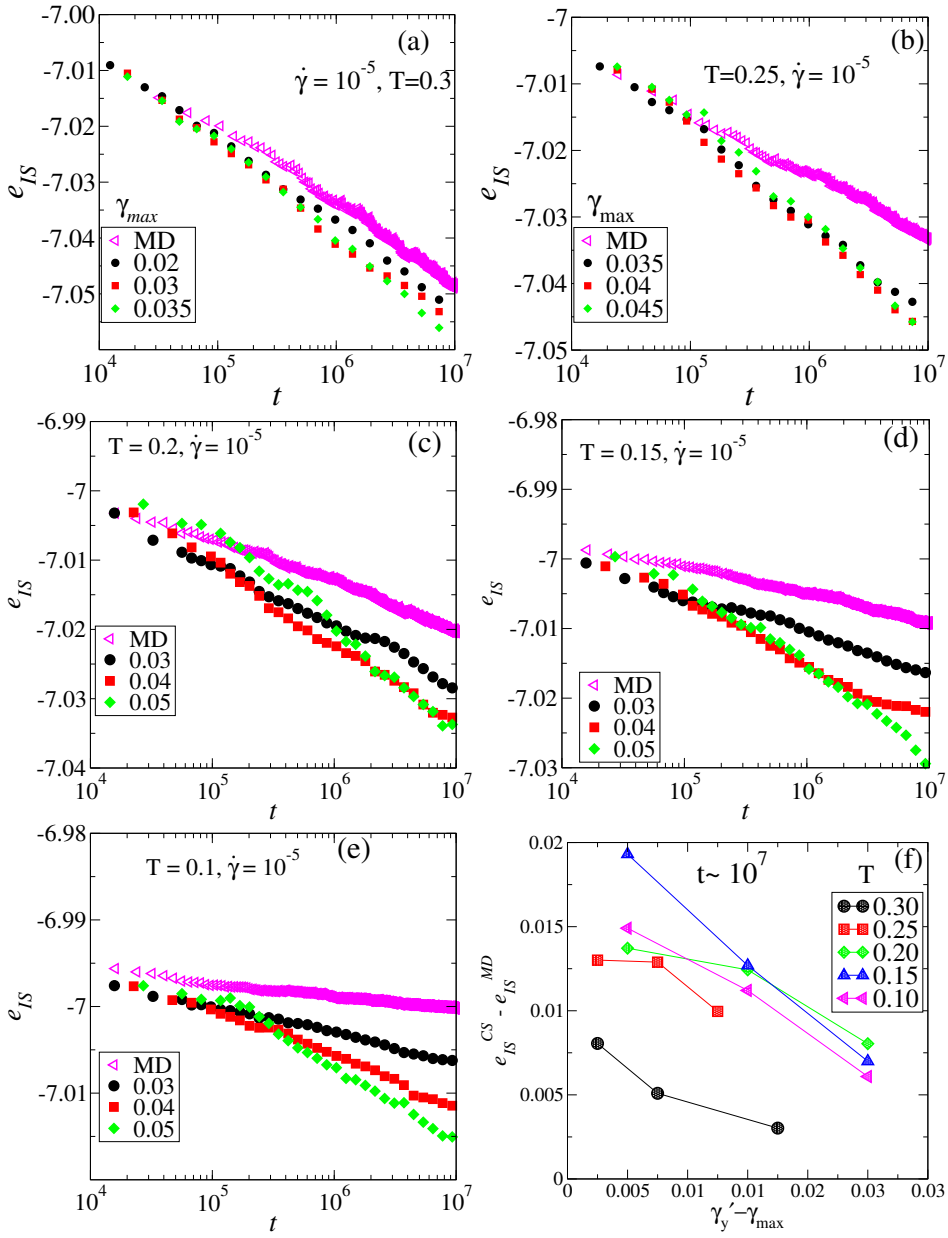

Figure 5.4: MD run from $T = 0.3 - 0.1$ has been compared to the sheared runs for a fixed shear rate and $\gamma_{max} \leq \gamma_y$. Significant overaging (energy difference between sheared and unsheared configurations at $t \sim 10^7$) at the pre-yield regime. The effect of overaging increases as the driving amplitude is increased up to the yielding amplitude.

In the aging regime, the amount of overaging increaes when driven with amplitude progressively closer to the yielding amplitude. Though the effect is marginal we have shown in Fig. 5.4 that for a given temperature ($T = 0.3 - 0.1$) and a given rate ($\dot{\gamma} = 10^{-5}$) the system shows maximum overaging closest to their yielding points. The amount of overaging has been measured by the difference in inherent structure energy ($e_{IS}^{MD} - e_{IS}^{CS}$) at $t \sim 10^7$. In Fig.5.4 we show the e_{IS} averaged between the time window $t \sim 8x10^6 - 10^7$. We see that the amount of overaging increases as the γ_y' is approached. γ_y' is the average of the deformation amplitude at which e_{IS} attains a minimum value and the next higher amplitude at which e_{IS} increases again.

The overaging behaviour has a shear rate dependence. We compared the evolution of

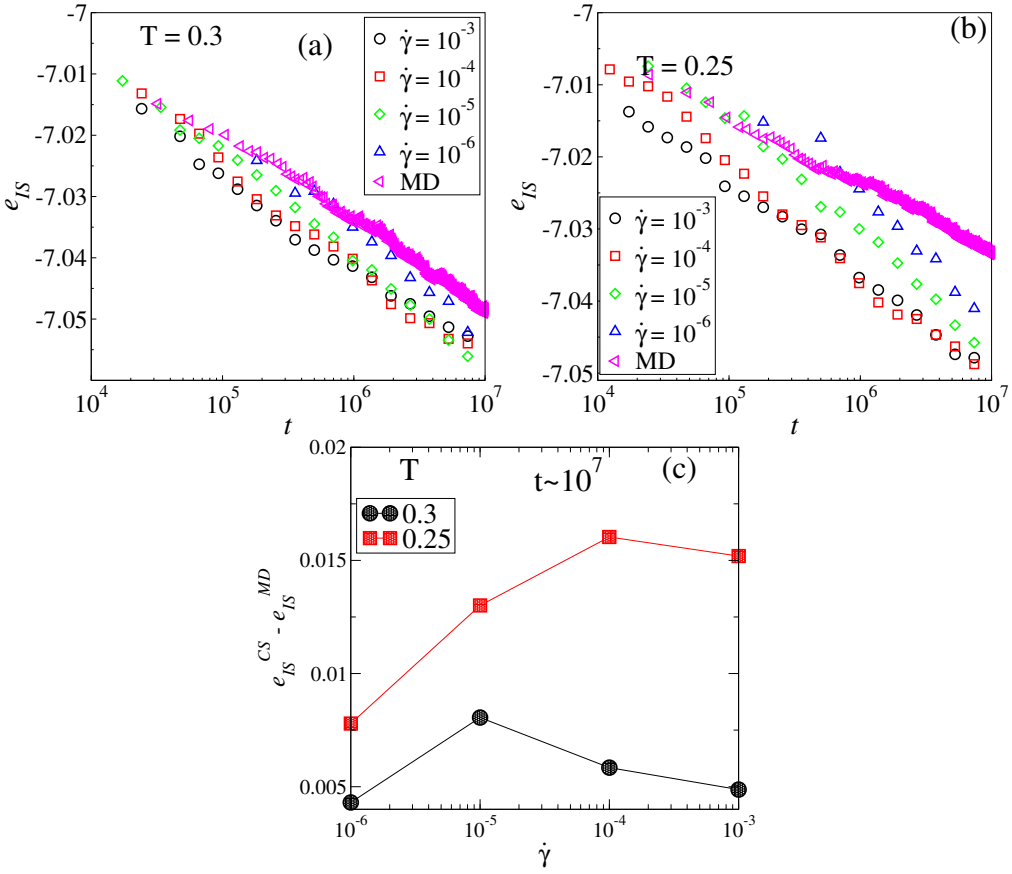

Figure 5.5: MD run at $T = 0.3, 0.25$ has been compared to the sheared runs for different shear rate and $\gamma_{max} \sim \gamma_y$. we see a significant overaging effect (energy difference between sheared and unsheared configurations at $t \sim 10^7$) at the high shear rate end.

the energies under deformation to the energies in the case of the equilibrium dynamics for two temperatures ($T = 0.3, 0.25$)and four shear rates ($10^{-3} - 10^{-6}$). The shear amplitudes are the yielding amplitudes (γ_y) shown in Fig. 5.5. The amount of overaging has been measured by the difference in inherent structure energy ($e_{IS}^{MD} - e_{IS}^{CS}$) at $t \sim 10^7$. In Fig.5.5 we show the e_{IS} averaged between the time window $t \sim 8x10^6 - 10^7$. Even though there is a mild trend of overaging increasing with increasing shear rate,

the dependence is not very prominent. However, for the lowest shear rate, the energy curve stays closest to the energy curves of the corresponding equilibrium dynamics, implying the lowest Δe_{IS} and the least amount of overaging. Here the mechanical perturbation is smaller, and hence the system ages more like the system aging under thermal fluctuation.

A gap between the energies reached in MD simulations and cyclic shear simulations increases upon lowering the temperature. To quantify this, we compute the difference between the energy reached at $t \approx 10^7$ and the initial value, Δe_{IS}, in MD and cyclic shear simulations respectively. The ratio $\Delta e_{IS}^{cs}/\Delta e_{IS}^{md}$, shown in Fig. 5.6, indeed grows as the temperature decreases, indicating a greater degree of overaging induced by the cyclic shear deformation, the lower the temperature.

Fig. 5.7 summarizes how the combination of the shear rate and the shear amplitude

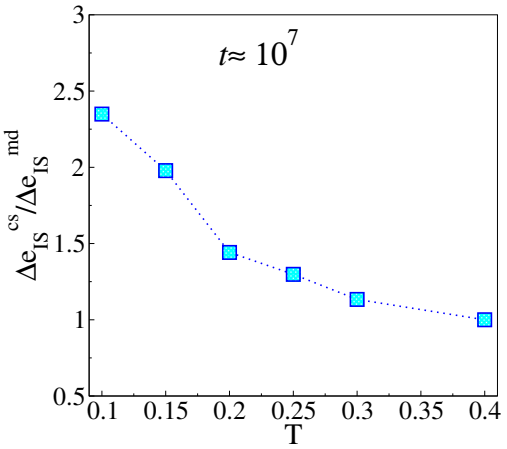

Figure 5.6: The ratio of the difference between the energy reached at ($t \sim 10^7$) and the initial value, for cyclic shear and MD(Δe_{IS}^{cs} and Δe_{IS}^{md} respectively), as a function of the simulation temperature. The ratio increases above 1 with decreasing temperature, signifying the amount of overaging increases as the temperature is decreased.

together clearly makes a case of mechanical aging at a lower temperature. Mechanical aging at low temperature can be achieved by increasing strain rate and amplitude (still maintaining the amplitude stays below or around the yielding amplitude). The normal equilibrium dynamics appear to be the zero strain rate and zero amplitude limit at these temperature regimes.

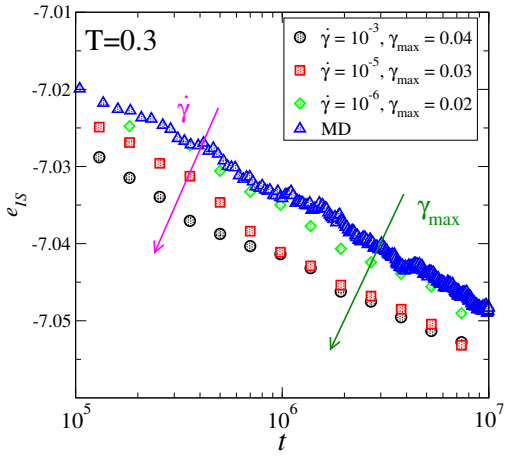

Figure 5.7: The evolution of the inherent structure energies as the system is deformed at $T = 0.3$, for sets of shear rates and strain amplitudes that approach the limit of vanishing shear rate and strain amplitude together. Comparison with normal molecular dynamics shows that energies in the aging regime deviate from the normal dynamics as amplitude and shear rate are increased together. The arrows indicate the direction of increasing strain amplitude and increasing shear rate.

5.4 Conclusions

To summarize, in our system, overaging under mechanical deformation is observed at temperatures $T \sim T_{VFT}$ and below. The amount of overaging increases with approaching yielding amplitude and higher shear rate. Though why at comparatively higher temperatures, thermal fluctuation becomes the effective relaxation mechanism is not understood at this moment. At this point, it remains an interesting question to investigate and understand the existence of the optimum temperature that dictates thermal fluctuation or mechanical perturbation to be the more significant medium of relaxation at low temperature glass-forming liquids.

Chapter 6

Crossover in dynamics in the Kob-Andersen binary mixture glass-forming liquid

6.1 Introduction

The concept of fragility was introduced by Angell [6, 252, 253] as a way of organizing the diversity of the remarkable slow down of dynamics in glass forming liquids as the glass transition is approached. Glass formers such as silica near the glass transition display an Arrhenius variation of viscosity, whereas other commonly investigated glass formers exhibit super-Arrhenius dependence of viscosity and relaxation times on temperature, to various degrees. Glass formers exhibiting Arrhenius temperature dependence are termed strong and those exhibiting super-Arrhenius temperature dependence as termed fragile. Fragility quantifies the degree of deviation from Arrhenius behavior, and has been investigated extensively [254].

In attempting to rationalise experimental results close to the glass transition of water with those obtained at considerably higher temperatures in supercooled water, Angell [24] proposed the possibility of a crossover from fragile behaviour at the higher temperatures to strong behaviour close to the glass transition. In addition to water [25–28], such a fragile to strong transition has been investigated in computer simulations of silica [29–32], and silicon [33–36]. In these liquids, all of which exhibit several well known anomalous properties arising from low density, open tetrahedral order that becomes dominant at low temperatures. The fragile to strong crossover is associated with a change in liquid structure towards more tetrahedral local geometries upon lowering temperature, a possible liquid-liquid transition [31, 255], and with the crossover being characterised by the presence of a heat capacity maximum.

In recent years, the fragile to strong crossover in dynamics has also been reported in a

variety of other glass formers, including phase change alloys [38, 39] used in memory devices, and several metallic glasses [42, 249, 250, 256, 257]. In many of these instances, though not all, the fragile to strong crossover has been shown to be accompanied by a heat capacity maximum. Unlike the cases such as silica discussed above, however, there is no broadly applicable picture of structural change that may drive such a crossover.

Interestingly, a well studied computational model glass former that is commonly described as a fragile glass former, the Kob-Andersen 80 : 20 binary Lennard-Jones mixture (KA-BMLJ), also exhibits a crossover in dynamics [40, 41] that is reminiscent of the transition seen in computer simulations of silica [30]. Such a crossover has also been recently investigated for the same model potential but for different compositions (2 : 1 and 3 : 1 rather than 4 : 1) [43] and for a soft sphere mixture [258]. In the KA-BMLJ model, below the mode coupling temperature T_{MCT}, the relaxation times exhibit a crossover from non-Arrhenius to Arrhenius temperature dependence. We perform molecular dynamics simulations which are roughly an order of magnitude longer than those reported in [41], and characterise the dynamics in detail, including several aspects of dynamical heterogeneity. We perform an analysis of the structure of clusters of mobile particles, to understand the changes in the geometry of such clusters across the dynamical crossover. We investigate the relation between the dynamics to thermodynamic changes. Specifically, we consider the behaviour of the heat capacity. Although the presence of a heat capacity maximum was reported in an earlier study [259], the recent work reported in [41] does not find evidence for such a maximum, a result which we confirm to hold to lower temperatures. We also investigate the validity of the Adam-Gibbs relation, found to be valid in computer simulations of the KA-BMLJ [52, 74, 75] as well as other systems [16, 31, 73]. However, recent work [76] concludes that a generalised form of the Adam-Gibbs relation is required to describe the relaxation times at temperatures significantly lower than previously investigated, as also observed for two dimensions in [75]. We find deviations from the Adam-Gibbs prediction below the dynamical crossover temperature, when the configurational entropy is evaluated with a harmonic approximation to the vibrational entropy (as has been done in the past for the studied system [52, 74, 75]). However, when anharmonic correction to the vibrational entropy estimates are included, the relaxation times are found to obey the Adam-Gibbs relation across all the temperatures investigated.

We first describe the model studied and the simulation details, followed by a description of the simulation results. We conclude with a discussion of the significance and implication of these results.

6.2 Methods

We study the Kob-Andersen (KA) 80 : 20 binary mixture [160], with the interaction potential between particles given by

$$\begin{aligned} U_{\alpha\beta}(r) &= 4\epsilon_{\alpha\beta}\left[\left(\frac{\sigma_{\alpha\beta}}{r}\right)^{12} - \left(\frac{\sigma_{\alpha\beta}}{r}\right)^{6}\right] \\ &\quad + 4\epsilon_{\alpha\beta}\left[c_0 + c_2\left(\frac{r}{\sigma_{\alpha\beta}}\right)^{2}\right], r_{\alpha\beta} \leq r_{c\ \alpha\beta} \\ &= 0, \qquad\qquad r_{\alpha\beta} > r_{c\ \alpha\beta}. \end{aligned} \tag{6.1}$$

Here, c_0 and c_2 are chosen such that the potential and force between particles go to zero continuously at the cutoff distance $r_{c\ \alpha\beta}$ ($= 2.5\sigma_{\alpha\beta}$). The indices (α, β) represent particle type (A or B) in the binary mixture. We report results in reduced units, with units of length, energy and time scales being σ_{AA}, ϵ_{AA} and $\sqrt{\sigma_{AA}^2 m_{AA}/\epsilon_{AA}}$, respectively. The model parameters are $\epsilon_{AB}/\epsilon_{AA} = \epsilon_{BA}/\epsilon_{AA} = 1.5$, $\epsilon_{BB}/\ \epsilon_{AA} = 0.5$, and $\sigma_{AB}/\sigma_{AA} = \sigma_{BA}/\sigma_{AA} = 0.8$, $\sigma_{BB}/\sigma_{AA} = 0.88$. Energy values reported are energies per particle. Constant volume, temperature (NVT) simulations have been performed for the system size $N = 4000$ using the Nosé–Hoover thermostat. The initial configurations for the simulation below $T = 0.466$ are prepared by quenching equilibrated configurations from $T = 0.466$ and for the simulations above $T = 0.466$ configurations are obtained by quenching equilibrated configurations from $T = 1.0$ to respective target temperatures. We have performed equilibrium simulation for a range of temperatures, from $T = 0.9$ to $T = 0.365$. The number density ($\rho = N/V$, where V is the volume) has been kept constant at 1.2. At each temperature, $16 - 24$ independent trajectories have been studied. The time step below and above the mode coupling temperature $T_{MCT} = 0.435$ are respectively $dt = 0.01$ and $dt = 0.005$. We note, however, that the use of the larger time step at low temperatures leads to a shift in the per particle energy of $\approx 5 \times 10^{-3}$. We perform additional runs with the smaller time step of 0.005 to rectify this shift in the energy values employed. At the lowest temperatures, run lengths extend up to 2×10^{10} integration time steps or a time duration of 2×10^{8}. All simulations have been performed using LAMMPS [237]. The relevant quantities are reported for the A type of particles unless otherwise mentioned. The system is prone to crystallization at low temperatures. In the range of temperatures from T_{MCT} to the lowest simulated temperature, the percentage of runs that crystallize increases from 5% to 80%. The crystallizing samples have been identified using standard methods employing bond orientational order parameters [260], as described in [41, 96, 167] and discarded from the analysis.

6.3 Results

We present results concerning the structural relaxation times, and several measures of dynamical heterogeneity, which display a crossover around the mode coupling temperature. We describe next the results concerning the thermodynamic changes with temperature and their relationship with the observed dynamical crossover.

6.3.1 Structural Relaxation

Structural relaxation times are computed by considering the overlap function $q(t)$ and the self intermediate scattering function $F_s(k,t)$.

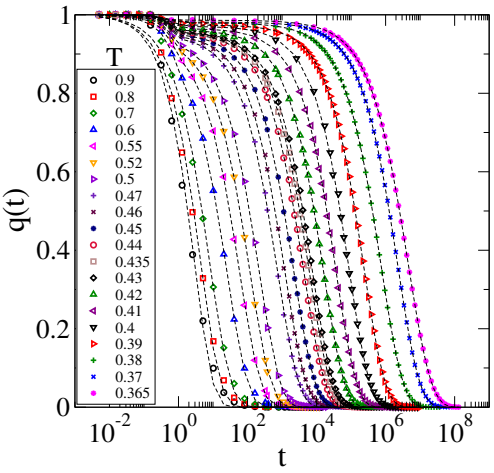

Figure 6.1: The self part of the overlap function is shown for A of particles. The dotted lines are fits to the data.

The overlap function $q(t)$, defined as

$$\begin{aligned} q(t) &= \frac{1}{N}\int d\mathbf{r}\rho(\mathbf{r},t)\rho(\mathbf{r},t+t_0) \\ &= \frac{1}{N}\sum_i\sum_j \delta(\mathbf{r}_j(t_0)-\mathbf{r}_i(t+t_0)) \end{aligned} \tag{6.2}$$

where $\rho(\mathbf{r},t)$ is the local density of particles at position r at time t, can be divided into a self part and a distinct part. In the present work, we will employ the self part, $q(t)_s$, defined as

$$q(t)_s = \frac{1}{N}\sum_i \delta(\mathbf{r}_i(t_0)-\mathbf{r}_i(t+t_0)) \tag{6.3}$$

as a good approximation to the full overlap function. In simulations, the δ function is approximated by a window function $w(x)$ described below, where we further define the function considering the A particles only. Thus, we consider

$$q(t) = \frac{1}{N_A} \sum_{i=1}^{N_A} w(|\mathbf{r}_i(t_0) - \mathbf{r}_i(t + t_0)|)$$

where $w(x) = 1.0$ if $x \leq a$ and $= 0$ otherwise. Here, t_0 is the time origin and the overlap function is calculated with an average over multiple time origins. The value of the overlap function depends on the choice of the cutoff parameter a. This parameter is chosen in such a way that the particle positions separated due to vibrational motion are treated as the same. We choose $a = 0.3$, which corresponds to displacements at the plateau region of the mean squared displacement (MSD) curves, as shown in, *e. g.*, [173] and used in previous literature. The overalp function for all the temperatures has been shown in Fig. 6.1. The structural relaxation time has also been calculated from the self part of the intermediate scattering function $F(\mathbf{k}, t)$ defined as:

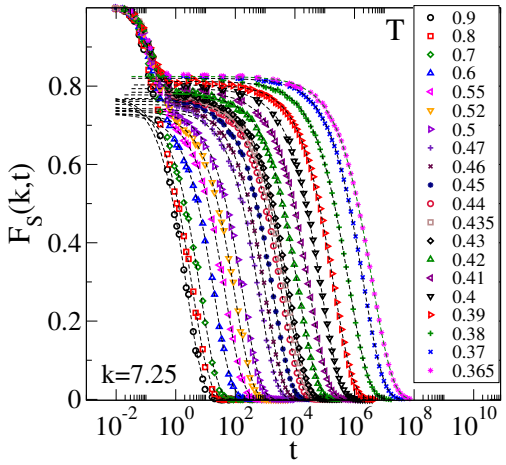

Figure 6.2: The self part of the intermediate scattering function $F_s(k, t)$ is shown for a range of k values. The dotted lines are fits to the data.

$$F_s(\mathbf{k}, t) = \frac{1}{N_A} \sum_{i=1}^{N_A} e^{-i.\mathbf{k}.(\mathbf{r}_i(t_0) - (\mathbf{r}_i(t+t_0))} \tag{6.4}$$

where we calculate $F_s(k, t)$ for the A type of particles, performing an isotropic average over the directions of $\mathbf{k}$. The structural relaxation time is measured from the $F_s(k, t)$, with $k = |\mathbf{k}| = 7.25$, the first peak of the structure factor, unless otherwise noted (see Fig. 6.2). $F_s(k, t)$ values we report are obtained by averaging over multiple time origins (t_0). $F_s(k, t)$ for different values of k has been shown in the Appendix.

These time correlation functions are fitted with a four parameter functional form, which is expressed for $q(t)$ as

$$q(t) = (1 - f_c)exp(-(t/\tau_s))^n + f_c exp(-t/\tau_\alpha)^{\beta_{kww}} \tag{6.5}$$

where f_c is the non-ergodicity parameter, τ_α is the structural relaxation time, β_{kww} is the Kohlrausch-Williams-Watts stretching exponent, and τ_s is a relaxation time that describes the short time decay of the correlation functions. The exponent n describing the short time decay, based on results in [53], is chosen to be $n = 2$. The τ_α extracted from the fitted form for $q(t)$ are plotted as the function of the temperature (see Fig. 6.3). We next fit the structural relaxation time τ_α with the the Vogel Fulcher Tamman

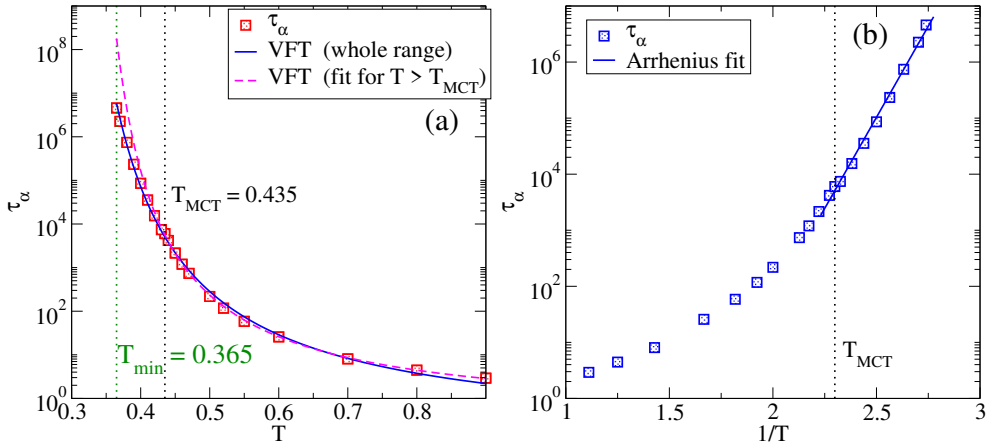

Figure 6.3: (a) Relaxation times τ_α extracted from the decay of the overlap $q(t)$ for temperatures across T_{MCT} are shown, along with VFT fits to data for $T > T_{MCT}$ (red dashed line) and the full range of T values (blue solid line). The fit to high temperature data overestimates relaxation times at lower temperatures, whereas the fit to the entire range shows deviations from the data points at the higher temperatures. (b) Relaxation times τ_α from the decay of $q(t)$ *vs.* $1/T$. The fit line through the data for $T < T_{MCT}$ demonstrates that at low temperatures, relaxation times can be better approximated by an Arrhenius temperature dependence.

relation (VFT) expression.

$$\tau = \tau_0 \exp\left[\frac{1}{(K_{VFT}(T/T_{VFT} - 1))}\right], \tag{6.6}$$

that is often employed to describe relaxation times in glass formers. Previous work has estimated the mode coupling temperature T_{MCT} to be $T = 0.435$ from power law fits of relaxation times for higher temperatures ($\tau = \tau_0(T - T_{MCT})^{-\gamma}$) [160]. In Fig. 6.3 (a), we show VFT fits to the relaxation times, by considering data only for $T > T_{MCT}$ ($\tau_0 = 0.3101$, $K_{VFT} = 0.2243$, $T_{VFT} = 0.2989$), as well as the entire range available. The VFT fits to the high temperature data clearly overestimate the relaxation times for $T < T_{MCT}$. On the other hand, for the VFT fit to the full range

($\tau_0 = 0.1175, K_{VFT} = 0.1383, T_{VFT} = 0.2592.$), the VFT form does not provide a good description of the data at higher temperatures. Fig. 6.3 (b) shows the same results in an Arrhenius plot, which shows that at temperatures below T_{MCT}, the slower increase of relaxation times can be better approximated by an Arrhenius form. The value of the activation energy barrier from the fit is ~ 15, which agrees well with the the previously reported value in [41] at which the activation energy shows a possible saturation. Such a crossover from super-Arrhenius to Arrhenius behavior has indeed previously been observed [40, 41, 43]. Our results extend the range of temperatures explored.

6.3.2 Dynamical heterogeneity

We next discuss three quantities that are associated with dynamical heterogeneity, namely the stretching exponent in the stretched exponential fits to the relaxation functions, β_{KWW}, the non-Gaussian parameter α_2, and the dynamical susceptibility χ_4. Stretching exponent(β_{kww}): Dynamical heterogeneity in supercooled liquids is understood in terms of the existence of regions with their inherent exponential relaxation with different relaxation timescales. The superposition of these differently relaxing regions gives rise to the overall stretched exponential behaviour, and this behaviour is identified by the stretching exponent or the Kohlrausch-William-Watts (KWW) exponent mentioned as β_{kww} previously in the long time relaxation of the correlation functions. It is shown [261] that the relative variance of these different relaxation times increases monotonically with the decrease of the stretching exponent. Hence, The decrease of the exponent clearly indicates the increase of the heterogeneity in the system. We have extracted β_{kww} from the four parameters fit mentioned earlier. After an initial decrease, β_{kww} almost saturates at further lowering of the temperatures [262, 263]. We have also extracted β_{kww} linearizing the stretched exponential form for a better estimate of the exponent.

6.3.2.1 Stretching exponent (β_{kww})

The Kohlrausch-William-Watts (KWW) stretched exponential form exhibited by correlation functions ($q(t)$ and $F_s(k,t)$ in our study) have been investigated as a manifestation of heterogeneous dynamics [53, 264]. We extract the exponent β_{kww} from the fits as expressed in Eq. 6.5, from $q(t)$ as well as $F_s(k,t)$ at $k = 7.25$, as shown in Fig. 6.4 (a). We also estimate β_{kww} by linearizing the long time behavior of $q(t)$, which can be written as $q(t) = f_c exp(-(t/\tau)^{\beta})$. From this, we can write (along the lines in [265]).

$$\ln[-\frac{d}{dt}[\ln\ q(t)]] = \ln(\frac{\beta}{\tau^{\beta}}) + (\beta - 1) ln\ t \tag{6.7}$$

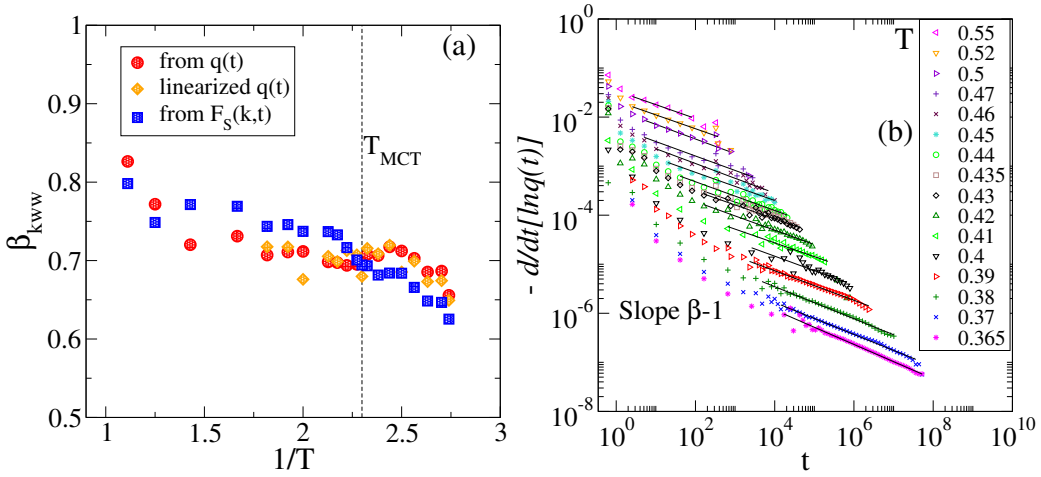

Figure 6.4: (a) The stretching exponent β_{kww} is shown here as a function of the temperature, obtained from stretched exponential fits of the overlap function $q(t)$ and $F_s(k,t)$, as well as by transforming the $q(t)$ to obtain β_{kww} from the resulting linearisation of the data. (b) The transformation of $q(t)$ used to estimate β_{kww} from the linearised data. The smallest $q(t)$ value used is $q(t) = 3 \times 10^{-3}$.

6.3.2.2 Non-Gaussian parameter ($\alpha_2(t)$)

The non-Gaussian parameter $\alpha_2(t)$ is defined as

$$\alpha_2(t) = \frac{3 < r^4(t) >}{5 < r^2(t) >^2} - 1 \tag{6.8}$$

and is a measure of how non-Gaussian the distribution of single particle displacements is. In the case of normal diffusive dynamics the displacement distribution is Gaussian and α_2 is zero. In glass forming liquids, below the onset temperature [175, 266], the parameter goes through a maximum at a characteristic time t^* and is zero in the short and the long time limits [14, 16, 53]. The peak value is taken as a measure of the degree of heterogeneity, which increases with the decrease of the temperature. The time at which the peak occurs, t^*, is considerably shorter than the alpha relaxation time τ_α. Analysis presented in [16] showed that the heterogeneity reflected in the behavior of $\alpha_2(t)$ is associated with clusters of spatially correlated *mobile* particles, and that the time scale at which such heterogeneity is maximum is closely related to the diffusive time scale $(D/T)^{-1}$. We will return to these considerations below.

Fig. 6.5 (a) shows the $\alpha_2(t)$ values for the range of temperatures studied, indicating that both the peak value α_2^{peak}, and the time at which it occurs, t^*, increases upon lowering temperature. We will discuss the behavior of t^* further below when we compare different time scales emerging from our study. Fig. 6.5 (b) shows the temperature dependence of the peak value α_2^{peak}, which displays a change in the temperature dependence below T_{MCT}, with values at lower temperatures falling below values one may expect from an extrapolation of the high temperature behavior. The same trend

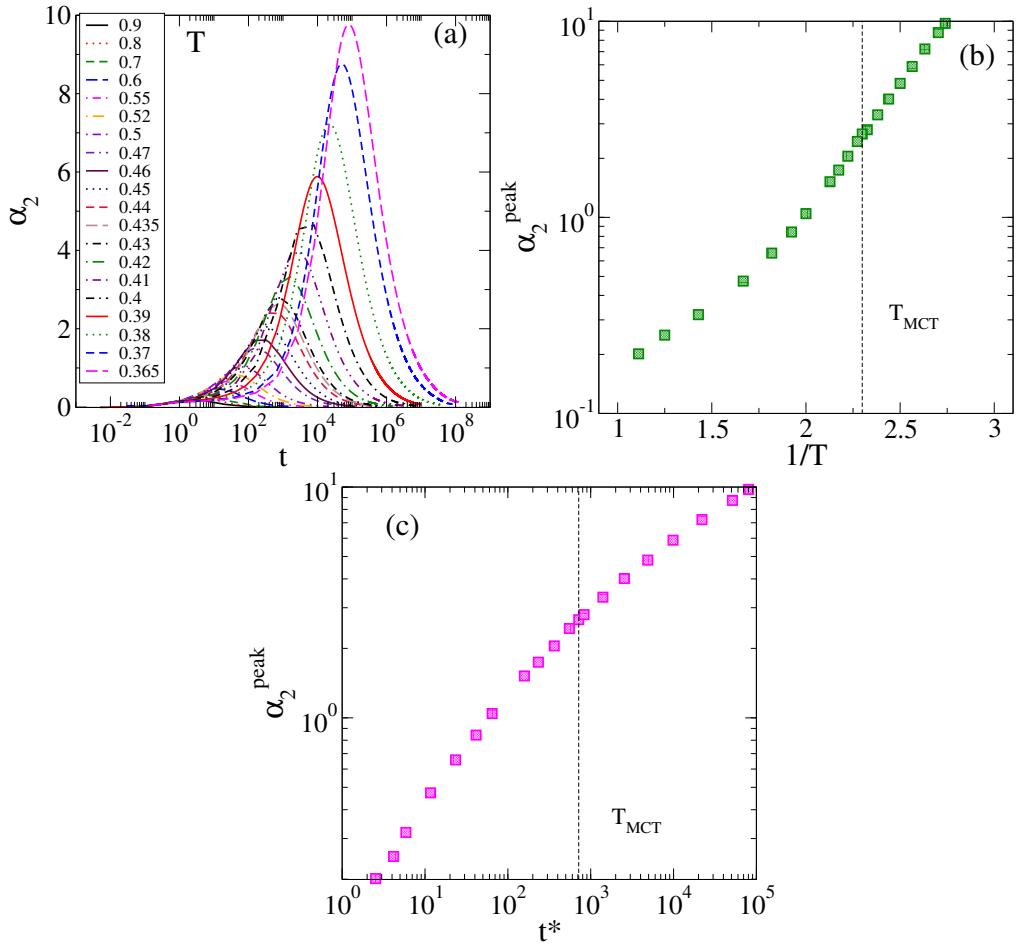

Figure 6.5: (a) The non-Gaussian parameter $\alpha_2(t)$ as a function of time. The temperatures are indicated in the legends. (b) The peak value of the non-Gaussian parameter α_2^{peak}, increases monotonically upon lowering temperature, but displays a change in the manner of increase around T_{MCT}. (c) The same behaviour of α_2^{peak} is reflected in when plotted with the charactersitic time t^*

is reflected in the the α_2^{peak} vs $t*$ plot in Fig6.5 (c).

6.3.2.3 Dynamical susceptibility (χ_4)

The dynamical susceptibility $\chi_4(t)$ measures the fluctuations of the overlap function $q(t)$, and is defined (considering only A particles) as

$$\chi_4(t) = N_A[< q(t)^2 > - < q(t) >^2]. \tag{6.9}$$

The peak of the $\chi_4(t)$ [50, 52] gives a measure of the amount of heterogeneity in the system. In Fig. 6.6 (a), we show $\chi_4(t)$ for the different temperatures studied. Like $\alpha_2(t)$, $\chi_4(t)$ exhibits a peak at a characteristic time τ_4. We compare τ_4 with other characteristic time scales below. The peak height χ_4^{peak}, shown in Fig. 6.6 (b), clearly

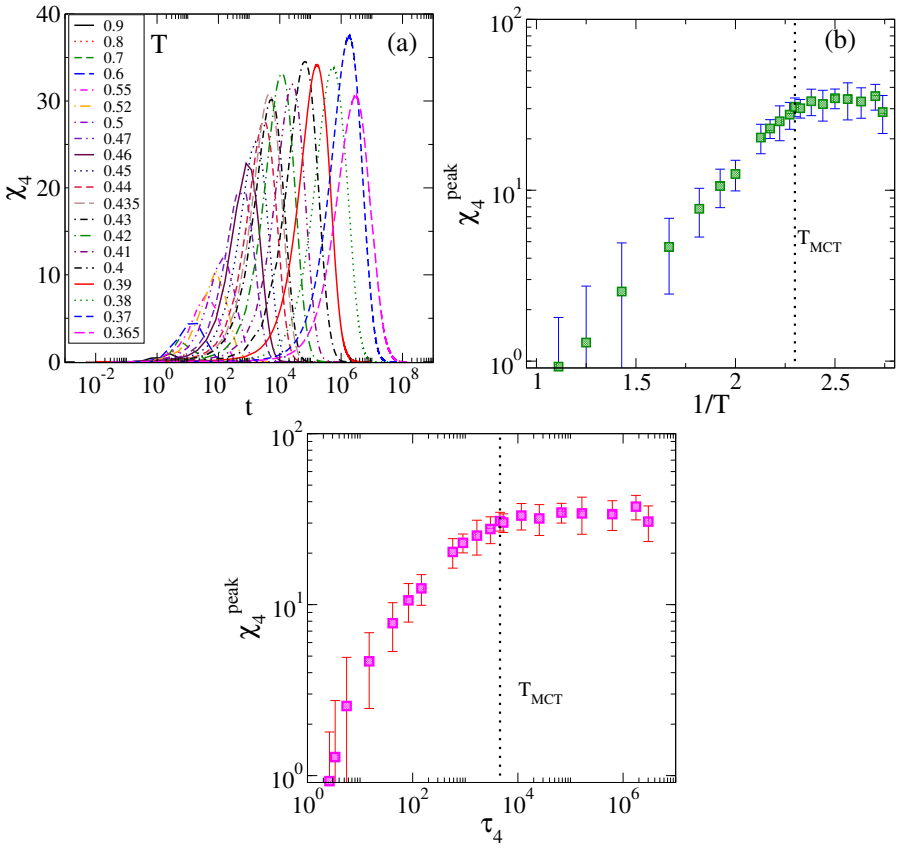

Figure 6.6: (a) The dynamical susceptibility χ_4 as a function of time. The temperatures are indicated in the legends. (b) The peak value of χ_4 shows a saturation at the lower temperatures. (c)The χ_4 *vs* characteristic time τ_4 behaviour shows the change in behaviour of the peak value across mode coupling temperature.

displays a crossover in behavior upon crossing T_{MCT}, becoming nearly constant, and possibly exhibiting a weak maximum. Our results are consistent with those obtained in [41], and the change in behavior of $\chi_4(t)$ observed for the $2:1$ and $3:1$ KA-BMLJ model reported in [43]. In recent work on a metallic glass model [42], a clear peak in the χ_4^{peak} values is observed, along with a specific heat maximum, which are described as manifestations of a fragile to strong crossover. As described later and in [41], no evidence of a specific heat maximum is found in the present model. Further, it is argued in [41] that the occurrence of the crossover near T_{MCT} may be accidental. Our results are not able to clarify the issue further, although the change in behavior in χ_4^{peak} occurs quite convincingly when T_{MCT} is crossed. The χ_4 *vs* characteristic time τ_4 behaviour shows the change in behaviour of the peak value across mode coupling temperature (see Fig. 6.6 (c)).

To summarise briefly the results so far, we see a change in the nature of dynamical heterogeneity when the temperature is decreased below T_{MCT}, most convincingly in the case of χ_4, but also in the case of $\alpha_2(t)$. The stretching exponent β_{kww} results we have are sufficiently noisy that we can not draw any conclusions of a crossover in

behavior, although they do indicate that the dynamics becomes more heterogeneous as temperature decreases.

6.3.3 Mobile particle clusters and strings

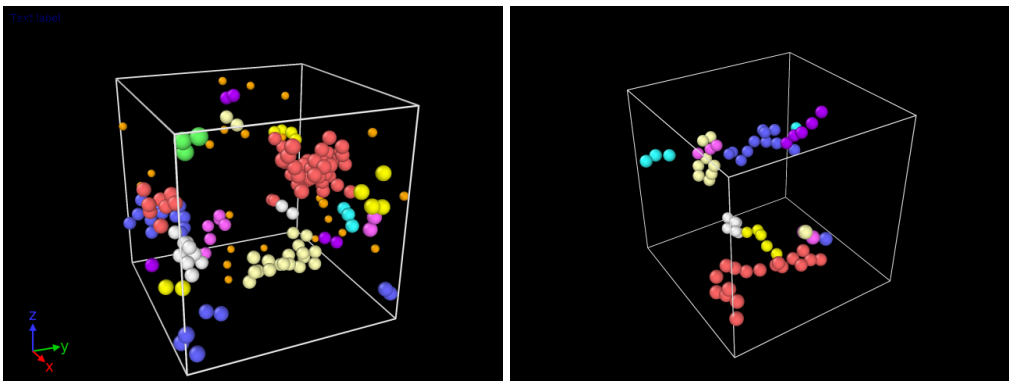

Figure 6.7: Different mobile clusters (left,in different colours) and strings of mobile particles (strings with more than four particles)has been shown in the system.

We next consider the statistics and morphology of clusters of particles that move in a correlated fashion, which have been a subject of considerable study [15, 16, 42, 43, 48, 50, 51, 69, 267]. In particular, the time dependent size of spatially correlated clusters of mobile and immobile particles, as well as string-like correlated mobile particles were investigated in [16], as also the morphologies of such clusters. It was found that the mean size of mobile particle clusters as well as strings displayed a non-monotonic time dependence, exhibiting a peak size at a time scale $t_{n_M}^{peak}$ and t_L^{peak} respectively. These time scales were found to closely track the time t^* at which $\alpha_2(t)$ exhibits a maximum, and in turn, the diffusion time scale $(D/T)^{-1}$. It was found further in [16] that clusters of immobile particles exhibit a maximum mean size at a time that corresponds to the alpha relaxation time. In the present work, we do not investigate immobile particle clusters, but focus attention on clusters of mobile particles and strings.
The large values of the non-Gaussian parameter for times $\sim t^*$ has been shown in several works [14, 48] to correspond to the presence of a sub-population of particles that move much farther than the remaining particles. Such particles have further been shown to be spatially correlated. In these investigations, analysis of spatially correlated clusters was performed by considering the top 5% most mobile particles, which we also follow here (other works employ slightly different fractions; while the choice of the subset of mobile particles is thus arbitrary, qualitative behavior that emerges from such choices is not sensitively dependent on the choice). For any given time t, *mobile* particles identified as the 5% most mobile particles at that time are defined to belong to the same cluster (see Fig. 6.7) if they are within a distance $1.4\sigma_{AA}$ of each other (We consider distances at the time the clusters are identified, but do not find

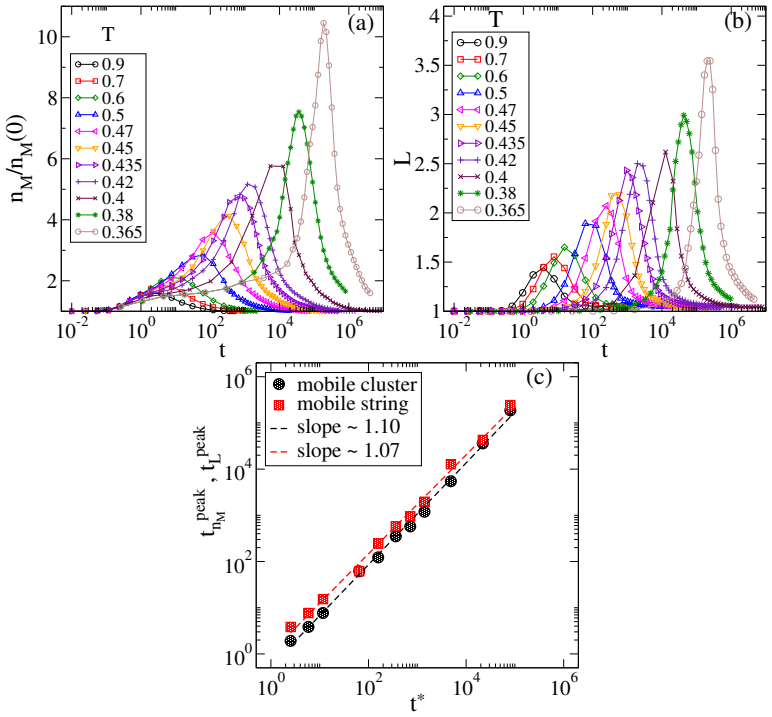

Figure 6.8: The average size of mobile clusters and strings, shown in (a) and (b), exhibit maxima at characteristic time scales $t_{n_M}^{peak}$ and t_L^{peak} respectively. (b) The time scales $t_{n_M}^{peak}$ and t_L^{peak} plotted as functions of time t^*.

significant changes in the distribution of clusters if the separation of particles at the initial time is considered instead). The average of the sizes of these clusters is normalised by the average cluster size when the subset labeled as mobile is randomly chosen in the initial configuration. In practice, we compute the normalisation based on labeling particles as mobile considering their displacements in the first integration step at the time origin.

We next consider string-like cooperatively moving particles. Strings have been identified as groups of mobile particles such that the position of one of the particles is occupied by another particle at a later time [15]. After we identify mobile particles at a time t, we check if the i^{th} mobile particle has been replaced by the j^{th} mobile particle within the radius δ over the interval t. If so, those two particles are considered to form a string (see Fig. 6.7). Here, two particles are identified as belonging to the same string if $|r_j(0) - r_i(t)|] < 0.6\sigma_{AA}$. It has been observed that for a given i, multiple other particles may satisfy such a criterion, in which case, the particle j which has the minimum distance $|r_j(0) - r_i(t)|]$ is identified as the particle that replaces i. In computing the average string length, we include particles that are not connected with any other as strings of length 1, so that at very short and very long times, the average length of a string tends to a value of 1.

Fig. 6.8 (a) shows the time dependence of the mean size of mobile clusters, which exhibit a maximum at a characteristic time $t_{n_M}^{peak}$. The mean length of strings is shown as a function of time in Fig. 6.8 (b), which exhibits a maximum at a characteristic time t_L^{peak}. These times are plotted against the time t^* at which $\alpha_2(t)$ is maximum, in Fig. 6.8 (c). Consistently with observations in [16], these times are seen to be essentially the same (but see below for further discussion on this point).

6.3.4 Summary of various timescales

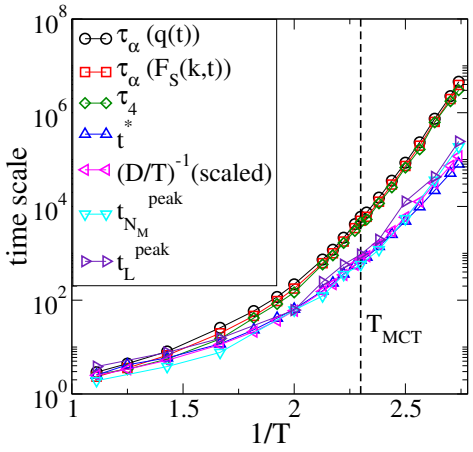

Figure 6.9: Different time scales, τ_α (from $q(t)$ and $F_s(k,t)$), τ_4, t^*, $(D/T)^{-1}$, $t_{n_M}^{peak}$, t_L^{peak}, plotted against $1/T$ in an Arrhenius plot. All time scales show a crossover to Arrhenius behavior at low temperatures. They fall in to two groups: τ_α and τ_4 are larger and have stronger T dependence, whereas t^*, $(D/T)^{-1}$, $t_{n_M}^{peak}$, and t_L^{peak}, are smaller, and show weaker T dependence.

We have reported above on different characteristic times, defined with respect to structural relaxation and dynamical heterogeneity. We summarise the temperature dependence of these time scales here and compare them with each other. Fig. 6.9 shows an Arrhenius plot of the alpha relaxation time τ_α (from $q(t)$ and $F_s(k,t)$), the diffusion time scale $(D/T)^{-1}$, the time at which χ_4, α_2, the size of mobile particles n_M, string length L show maximum values, which are, respectively, τ_4, t^*, $t_{n_M}^{peak}$, and t_L^{peak}. The time scales shown fall into two groups: The time scales τ_α and τ_4 are essentially the same, as previously observed [50–52, 59, 268]. The remaining time scales, $(D/T)^{-1}$ (which has been scaled to match the magnitude of the others at one reference temperature), t^*, $t_{n_M}^{peak}$, and t_L^{peak}, also exhibit the same temperature dependence, which is milder than that of τ_α [16, 59]. We note that recent work on a metallic glass former indicates that $t_{n_M}^{peak}$ is larger than $t^* \sim t_L^{peak}$ and is equal to the time scale associated with the Johari-Goldstein process [42], although all these time scales exhibit a milder temperature dependence than the alpha relaxation time τ_α. Such a distinction is not

apparent from our present results.

The decoupling of the diffusion time scale and the alpha relaxation time scale have

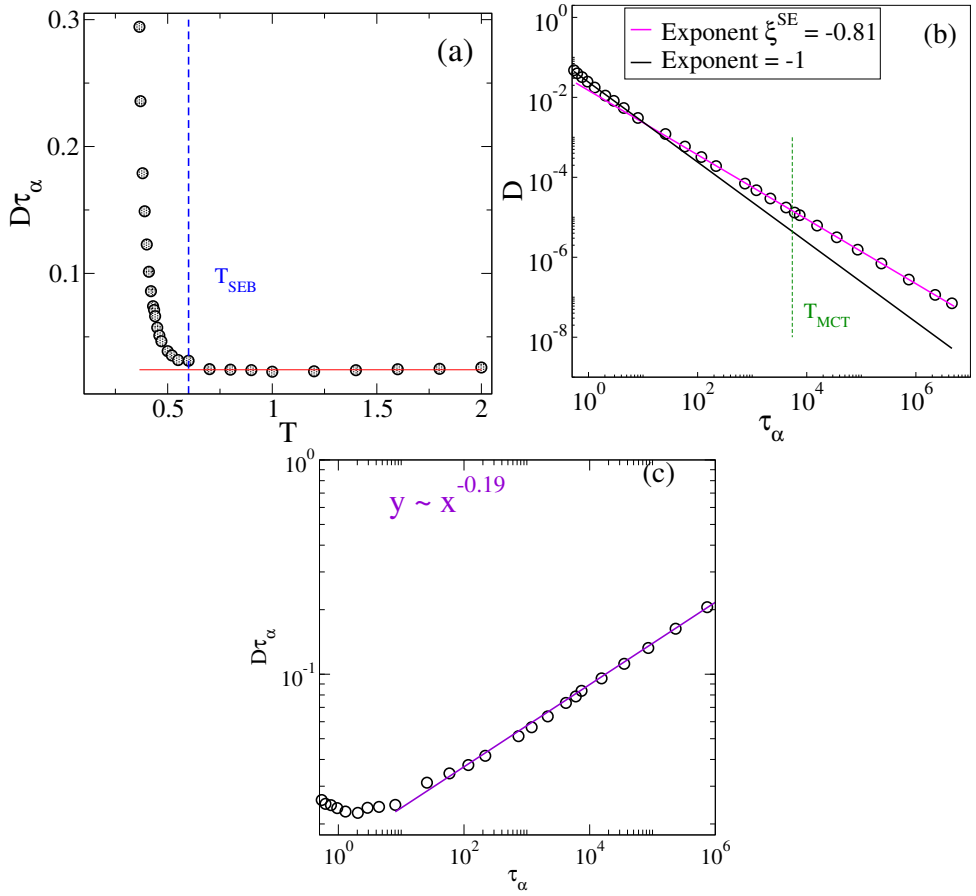

Figure 6.10: (a) the vertical blue line in the $D\tau_\alpha$ *vs* T plot represents the T_{SEB} at which the Stokes-Einstein relation breaks down. The temperature T_{SEB} is identified as the temperature ($T \sim 0.55$) at which $D\tau_\alpha$ significantly increases from the $D\tau_\alpha = const.$ value at high temperature, shown by the horizontal red line. (b)The diffusion coefficient D is shown against τ_α exhibiting the breakdown of the Stokes-Einstein relation. A fit to high temperature data with exponent -1 is shown for reference. Results below $T = 0.8$ exhibit a best fit exponent of -0.81 and the behavior in this regime does not show any indication of a crossover around T_{MCT}. The $D\tau_\alpha$ *vs* τ_α^ω plot show fractional positive value of $\omega = 0.19$. The relation between ξ^{AG} and ω satisfies with the relation $1 + \xi^{AG} = \omega$.

been investigated extensively ([53–55, 58, 59, 269–278] and references therein), in the context of the breakdown of the Stokes-Einstein relation, employing τ_α as being proportional to the viscosity [53]. We consider the breakdown of the Stokes-Einstein relation in order to investigate whether it reveals any indication of the crossover in dynamics around T_{MCT}, as reported in [42]. In the plot of $D\tau_\alpha$ *vs* T, the vertical blue line shows the temperature at which SER breaks down. The data points at high temperatures have been fitted into a horizontal red line. When the $D\tau_\alpha$ value substantially varies from this constant value, we identify that temperature as the breakdown

temperature or T_{SEB}. The significant deviation of $D\tau_\alpha$ from the constant value occurs around $T \sim 0.55$, which matches well as shown in Ref. [53] at around $T \sim 0.52$. We plot the diffusion coefficient D *vs.* τ_α in Fig. 6.10. The results clearly display a breakdown of the Stokes-Einstein relation, consistently with previous results in [53, 58], but do not exhibit any marked change in behavior around T_{MCT}. The breakdown exponent ξ we obtain by fitting the D values to the form $D \propto \tau_\alpha^{-\xi^{SE}}$ is $\xi^{SE} = 0.81$, which is consistent with values in the range 0.78 to 0.83 previously reported [53, 58]. In another representation we have shown $D\tau_\alpha$ *vs* τ_α (see Fig. 6.10). We have fitted a power-law fit of $D\tau_\alpha$ *vs* τ_α^ω. The positive fractional value of ω (0.19) indicates the SER breakdown. The relation between ξ^{SE} and ω satisfies with the relation $1 + \xi^{SE} = \omega$. As it has been shown previously [16, 59], we also see t^* is the inverse relaxation time that corresponds to D/T. The plot of t^* *vs* $(D/T)^{-1}$ shows an exponent of ~ 0.95 for the whole temperature range (see Fig.6.11). Even though there is a recent finding of decoupling of these two timescales at lower temperature [42] for metallic glasses, we do not see any significant difference across the crossover temperature.

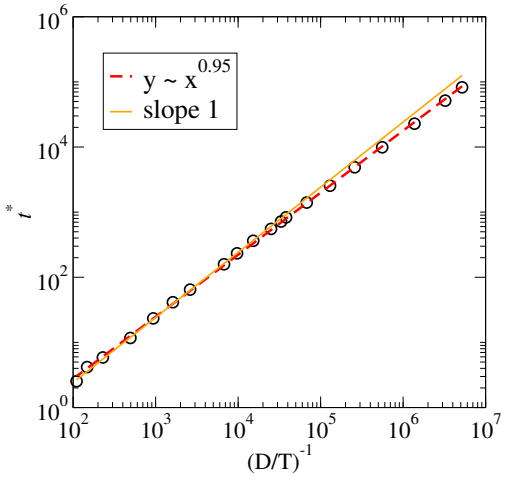

Figure 6.11: t^* *vs* $(D/T)^{-1}$ shows an exponent of ~ 0.95 for the entire temperature regime. The orange line is of exponent of 1.

6.3.5 Morphology of correlated rearrangements

In addition to the sizes of rearranging regions, there has been considerable interest in analysing the morphology of the correlated rearranging regions. In addition to investigations of string-like cooperative motion already mentioned [15], the observation of string-like rearrangements at temperatures accessed in computer simulations had led to theoretical analysis within the framework of the random first order transition theory (RFOT) [69], leading to the prediction of a crossover of rearranging regions from compact to fractal morphology at the dynamical transition temperature, identified with the mode coupling transition. In [16], the fractal dimensions of mobile,

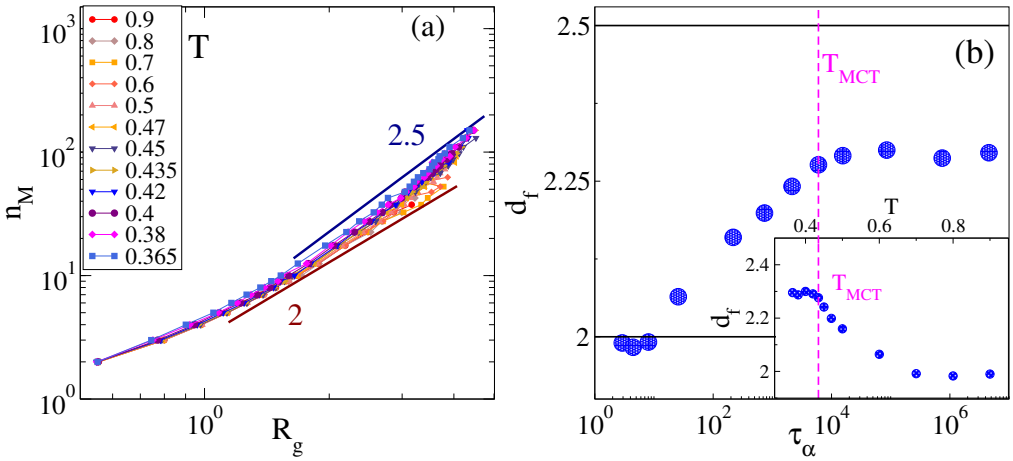

Figure 6.12: The fractal dimension of mobile clusters: (a) The dependence of the size of the clusters on the radius of gyration, for different temperatures. (b) The fractal dimensions d_f shown as a function of τ_α or temperature (inset) reveal a marked change as T_{MCT} is traversed. The horizontal lines mark $d_f = 2.0$ and $d_f = 2.5$ respectively, for reference.

immobile clusters and strings were analysed. It was found that mobile and immobile clusters exhibited a change in the fractal dimension from $d_f \sim 2$ to $d_f \sim 2.5$ as the temperature was lowered, and strings exhibited a change from $d_f \sim 5/3$ to $d_f \sim 2$. For mobile and immobile clusters, the fractal dimensions found were described as being in the range of the d_f value of 2 for lattice animals, to $d_f = 2.5$ observed for branched polymers with screened excluded volume interactions. Similarly, $d_f = 5/3$ is the fractal dimension for self-avoiding walks, and $d_f = 2$ is the fractal dimension for self-avoiding walks with screened excluded volume interactions. We consider here the fractal dimensions for mobile clusters, following the results in [16], to investigate whether a crossover in the cluster morphology is observed that accompanies the dynamical crossover.

For a cluster of size n, we may define the fractal dimension d_f from its dependence of the radius of gyration,

$$n \sim R_g^{d_f} \tag{6.10}$$

where,

$$R_g^2 = \frac{1}{2n^2} \sum_{i,j} (r_i - r_j)^2 \tag{6.11}$$

The results obtained at different temperatures of the dependence of the cluster size on the radius of gyration are shown in Fig. 6.12 (a) for mobile clusters. As observed in [16], the cluster size does not depend on R_g with a single power law exponent, which indicates that as the clusters grow larger, their morphology changes. We consider clusters of size > 5 and at each temperature, and obtain the fractal dimension

with a single best fit to the form in Eq. 6.10. Such a procedure will provide an underestimate of the fractal dimension of the largest clusters, but alternate procedures lead to comparable estimates. The fractal dimensions so obtained are shown in Fig. 6.12 (b), both as a function of temperature (inset) and of τ_α. Remarkably, we find that a clear crossover is observed for the fractal dimension in each case, showing that the dynamical transition we observe is indeed accompanies by a change in the morphology of correlated rearranging regions. Although Fig. 6.12 (a) suggests that the largest clusters approach a fractal dimension of $d_f = 2.5$, our numerical estimates saturate at a lower value.

6.3.6 Thermodynamics

We consider next the thermodynamic aspects of the dynamical crossover observed. As mentioned in the introduction, the fragile to strong crossover has been associated with the presence of a specific heat maximum. We thus first consider the constant volume specific heat C_v obtained by differentiating numerically the internal energy with temperature. The resulting specific heat, shown in Fig. 6.13 (a), displays a monotonic increase as the temperature is decreased, consistently with [41]. We note that the presence of a specific heat maximum has been reported in [259, 279] for the model studied here and a similar binary mixture glass former in a similar temperature range as the lowest temperatures we study, which may have arisen either as a result of a lack of equilibration or system size effects. Such a maximum has also been reported in a metallic glass model which exhibits a more marked fragile to strong crossover [42]. Our results indicate that the dynamical crossover we observe is not related to the presence of a specific heat maximum, at least in the temperature range investigated.

A related quantity that has been investigated in the context of the fragile to strong crossover (*e. g.*, in the context of silica [32, 280]) is the average energy of local energy minima, or inherent structures, e_{IS}, as a function of temperature. The average inherent structure energy displays a $1/T$ dependence for, *e. g.*, KA-BMLJ [74, 281], but displays deviations for liquids displaying a fragile to strong crossover. The inherent structure energies shown in Fig. 6.13 (b) do indeed show a $1/T$ temperature dependence below $T \sim 0.7$, and more importantly, do not show any indication of a deviation from the $1/T$ behavior down to the lowest temperatures investigated.

We next consider the Adam-Gibbs relation, which relates dynamical properties such as relaxation times in glass forming liquids, to the configurational entropy, a thermodynamic quantity. The relationship can be written as

$$\tau = \tau_0 \, exp\left(\frac{A}{TS_c}\right) \tag{6.12}$$

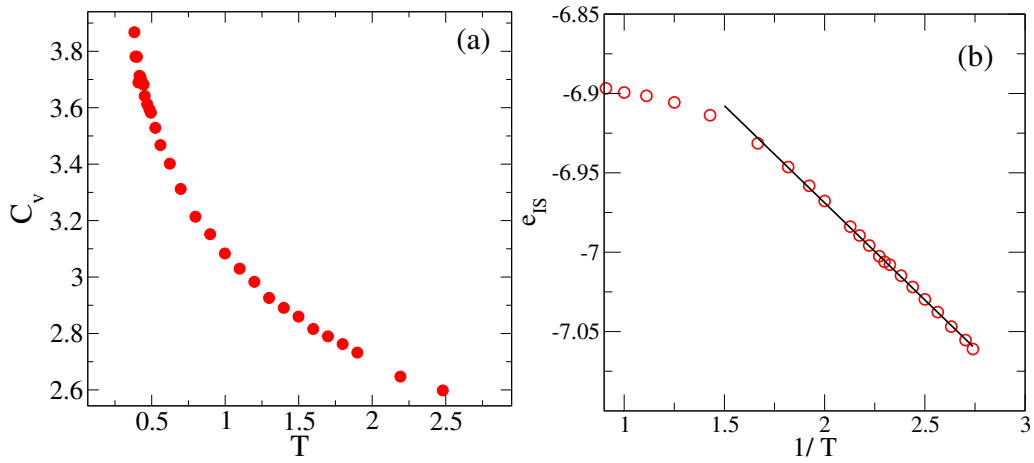

Figure 6.13: (a) The specific heat C_v, plotted against temperature, shows a monotonic increase as the temperature is lowered. (b) The inherent structure energy e_{IS} plotted against inverse temperature, shows a $1/T$ dependence at all temperatures below $T \sim 0.7$.

and has been investigated extensively, both experimentally and in computer simulations [16, 31, 52, 73–75, 176, 282] (where τ is a relaxation time scale, either τ_α or the diffusion time $(D/T)^{-1}$ in most studies, including here). While several computational investigations find the Adam-Gibbs relationship to be valid, recent work [43,76] raises questions about whether results from an extended range of temperatures would continue to validate the relationship. We note in particular that in [76], an extrapolation of relaxation times were performed using a parabolic law, which, however, has been found to be valid for the present system in only a limited temperature range, with deviations at higher temperatures and indication of deviations at lower temperatures as well [41]. Thus, accessing directly the relaxation times over a temperature window across which the character of dynamics may change provides a more reliable test. Given the crossover in dynamics in the system investigated here, by performing simulations over a much wider range of relaxation times than the previous studies mentioned, we consider whether the Adam-Gibbs relation continues to hold in this extended range of temperatures.

The configurational entropy is calculated by subtracting the *vibrational* entropy associated with individual *glasses* (or basins of free/potential energy minima or inherent structures) from the total entropy of the liquid. Based on the observation that a harmonic approximation to the basin free energy provided a satisfactory description [174, 175] below the onset temperature for the KA-BMLJ, the vibrational entropy has been evaluated in the harmonic approximation [52, 58, 74, 75, 174, 281]. However, it has been found necessary to incorporate anharmonic corrections for other systems investigated, which have been done in several ways, as reviewed in [176]. The procedure used to obtain the total entropy, and the vibrational entropy, at a given temperature T

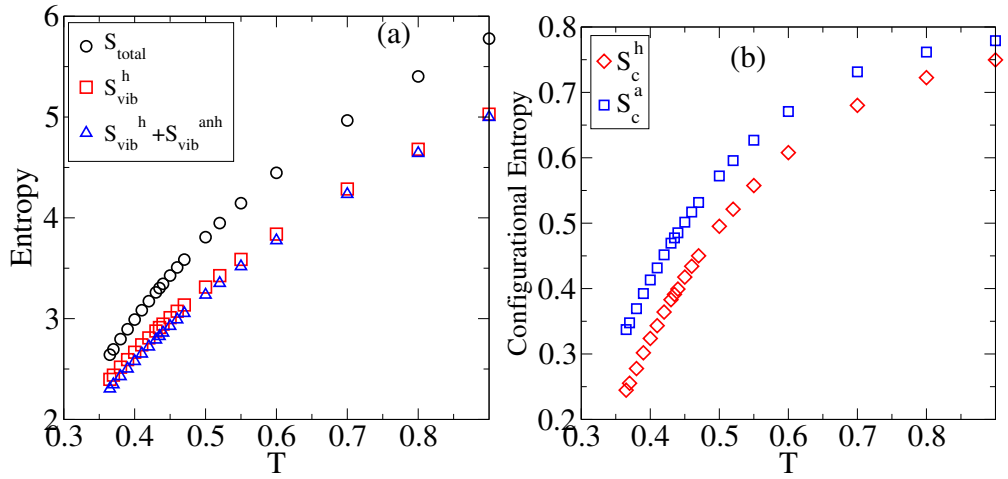

Figure 6.14: (a) The vibrational entropy along with the total entropy is shown as a function of the temperature. The vibrational entropy computed according to the harmonic approximation (S^h_{vib}) as well as by including the anharmonic correction (S^{anh}_{vib}), are shown. (b) The configurational entropy is shown as a function of the temperature, obtained by subtracting from the total entropy the vibrational entropy without (S^h_c) and with (S^a_c) the anharmonic correction.

and density ρ are described in Chapter 2. [283].

Accordingly, we first compute the configurational entropy employing the harmonic approximation for the basin entropy. The computed entropies, and the configurational entropies, are shown in Fig. 6.14 (a) and (b) respectively.
In Fig. 6.15 we show the Adam-Gibbs plots for $\log \tau_\alpha$ and the diffusion time scale $\log (D/T)^{-1}$, plotted as a function of $\left(T S^h_c\right)^{-1}$, where S^h_c is the configurational entropy in the harmonic approximation. The Adam-Gibbs plots, for both τ_α and $(D/T)^{-1}$, show that for temperatures below T_{MCT}, a deviation is observed from the linear behavior observed at temperatures above T_{MCT}.
Although similar results have been reported in various contexts [43,75,76], the observation of deviations raise questions about the relevance of anharmonic effects, since several results clearly show a change in the energy landscape topology when the mode coupling temperature is crossed [130,284–287]. We thus compute the anharmonic correction to the vibrational entropy and the configurational entropy [16, 176, 288–290] as we describe below.

The vibrational entropy with anharmonic corrections are shown in Fig. 6.14 (a), and the configurational entropies with anharmonic corrections are shown in Fig. 6.14 (b). Although the change in vibrational entropies appears small in Fig. 6.14 (a), inclusion of anharmonic contributions leads to a substantial change in the configurational

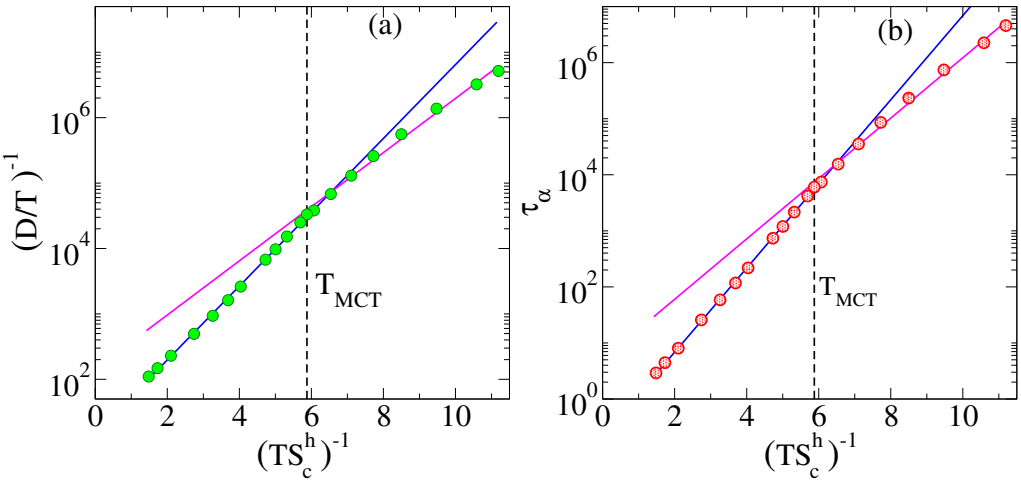

Figure 6.15: Adam-Gibbs plots of diffusion time $(D/T)^{-1}$ and τ_{α_A} employing configurational entropies S_c^h obtained with the harmonic approximation to the vibrational entropies. A change in slope is observed around T_{MCT}, indicated by the vertical line. The fitted Adam-Gibbs coefficient A for diffusion times is $A_D = 1.30, 0.95$ ($D_0 = 2.69, 4.96$) at temperatures above and below T_{MCT}. Similarly, for τ_α, $A_\tau = 1.73, 1.24$ ($\tau_0 = -1.53, 1.62$) at temperatures above and below T_{MCT}. The blue lines are fit lines for the data in the range of $T > T_{MCT}$ which are extrapolated to $T < T_{MCT}$ and the magenta lines are fit lines for the data in the range of $T < T_{MCT}$ which are extrapolated to $T > T_{MCT}$.

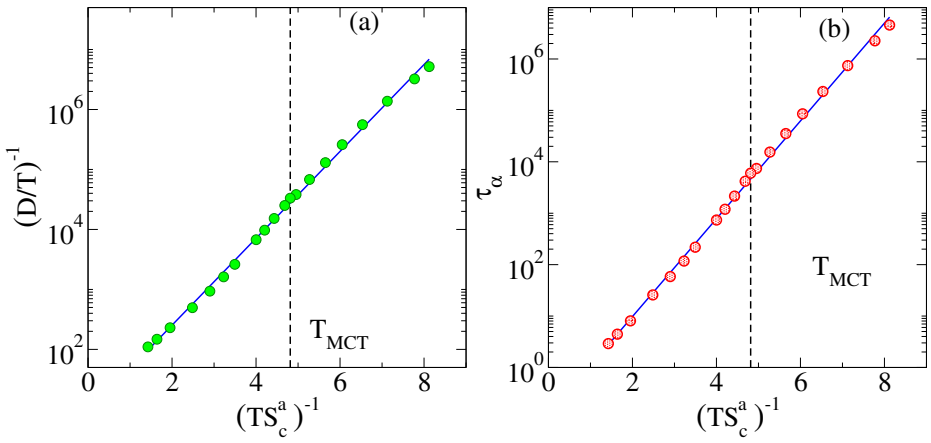

Figure 6.16: Adam-Gibbs plots of diffusion time $(D/T)^{-1}$ and τ_α employing configurational entropies S_c^a obtained with the anharmonic corrections included in evaluating the vibrational entropies. The Adam-Gibbs relation is valid across T_{MCT}, indicated by the vertical line. The fitted Adam-Gibbs coefficient A for diffusion times is $A_D = 1.67$ ($D_0 = 2.2$)„ and similarly, for τ_α, $A_\tau = 2.19$ ($\tau_0 = -2.1$). The blue lines are fit lines for the whole temperature range.

entropies, as seen in Fig. 6.14 (b). The corresponding Adam-Gibbs plots are shown in Fig. 6.16. Both $\log \tau_\alpha$ and $\log (D/T)^{-1}$ are linear in $(TS_c^a)^{-1}$ (where S_c^a is the configurational entropy obtained after including anharmonic corrections), indicating that they obey the Adam-Gibbs relation across the entire temperature range as was found

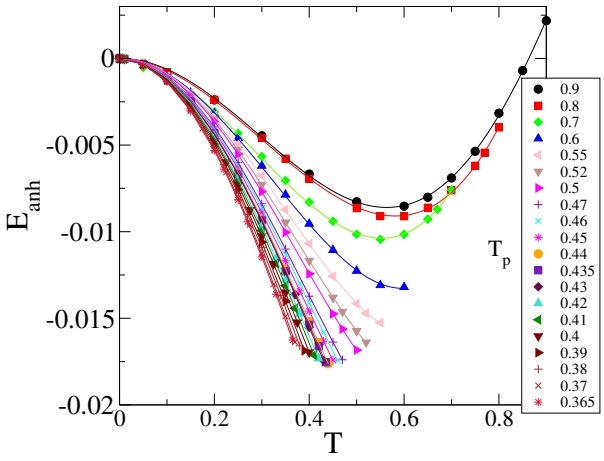

Figure 6.17: Anharmonic corrections to the energy, along with polynomial fits according to Eq. 2.40.

in previous studies of water [288,289]. We note that the results in this case are noisier, owing to the numerical errors involved in obtaining the anharmonic correction, which needs to be improved upon. However, no systematic deviation from the high temperature Adam-Gibbs behavior is seen at low temperatures, barring small deviations at the lowest two temperatures for which the results are the least reliable. We thus conclude that the observed deviations when the harmonic approximation is used are an artefact of an improper accounting of the vibrational entropy. It is important to note further that, even disregarding the data at temperatures above T_{MCT}, the Adam-Gibbs relation is seen to be valid for roughly three decades of relaxation times below T_{MCT}. In order to evaluate the anharmonic contribution to vibrational entropy, we consider 1000 inherent structures at each temperature T_p. For each of them, a short simulation (of 1000 integration steps, using a time step of 0.005) is performed for a range of temperatures T from close to 0 to T_p. The simulation is chosen so that (a) it is longer than the time required for the system to thermalize (as we verify), and (b) not much longer than the caging time, as judged by the plateau of the mean squared displacement, so that a roughly constant energy is obtained in this time window. The energies from 150 to 650 (150 to 500 for the highest two temperatures) steps are averaged to obtain estimates of $E_{vib}(T)$, from which $E_{anh}(T)$ is calculated. The resulting data, for each T_p is fitted to the form Eq. 2.40, with $n_{max} = 4$ (except for $T_p = 0.9$ for which we use $n_{max} = 5$, from which $S_{anh}(T_p)$ is computed. The fit coeffcients for selected temperatures are shown in Table I below.We show the anharmonic corrections to the energy, along with the fit lines, in Fig. 6.17.

T_p	c_2	c_3	c_4
0.8	-0.0765996	0.0787235	0.011623
0.7	-0.0973854	0.10679	0.0143602
0.6	-0.0922832	0.0587472	0.056073
0.55	-0.0914617	0.0269616	0.0859847
0.52	-0.0964523	0.026074	0.0820558
0.5	-0.09677	0.00530751	c=0.10677
0.47	-0.101674	-0.00922972	0.123299
0.46	-0.104524	-0.00645234	0.117956
0.45	-0.105043	-0.0221009	0.142661
0.44	-0.0447678	-0.307807	0.464361
0.435	-0.110282	-0.0195387	0.137634
0.43	-0.111109	-0.0171819	0.131073
0.42	-0.112789	-0.030111	0.154218
0.41	-0.117866	-0.0162058	0.1348
0.4	-0.121862	-0.0144479	0.13501
0.39	-0.124955	-0.0192352	0.141607
0.38	-0.131393	-0.00304849	0.122281
0.37	-0.134462	-0.00880651	0.131821
0.365	-0.134091	-0.0263324	0.16287

Table 6.1: Fit coefficients c_n in Eq. 2.40 from fits shown in Fig. 6.17.

6.4 Discussion and conclusions

We have described several dynamical quantities, including those that describe dynamical heterogeneity and the morphology of rearranging regions, that demonstrate a crossover in the dynamics, when the mode coupling temperature is crossed, with relaxation times better approximated by an Arrhenius temperature dependence at lower temperatures. Although it is tempting to describe it as a fragile to strong crossover, whether the dynamical crossover we see is a fragile to strong crossover as originally proposed by Angell [24–26] is open to question. Unlike liquids with energetically favorable tetrahedral structure (such as water, for which the fragile to strong crossover was originally proposed, and silica), the model we investigate does not display a thermodynamic signature of a change in regime in the form of a heat capacity maximum. On the other hand, several glass forming liquids typically described as fragile glass formers do display some form of a crossover at low temperatures [282], as also seen in computer simulations (for, *e. g.*, a model of ortho-terphenyl [291]). A crossover has been predicted as a generic feature in [69] within the RFOT, and in extended mode coupling theory [292]. Our results do indicate a signature in the changes in morphology of rearranging regions, although with some modifications as compared to those envisaged in [69]. In seeking further a structural explanation, it will be interesting to investigate also the morphology of immobile particles, which we have not attempted

in this work, in conjunction with investigations of locally preferred structures [293]. Investigating the Adam-Gibbs relation, we find deviations from the high temperature conformity to the Adam-Gibbs relation at temperatures lower than T_{MCT}, when a harmonic approximation to the vibrational entropy is employed. However, inclusion of anharmonic contributions in estimating the vibrational entropy leads to the conclusion that the Adam-Gibbs relation is valid across the temperature range we study. A more rigorous estimation of the vibrational entropy than what we have presented here should be attempted in light of the results we present here. Another issue to consider in the present system is the possible role of finite size effects. Based on the available results, it has been argued in [41] that the observed dynamical crossover is unlikely to be a result of finite size effects. We haven't addressed this aspect any further in the present work, but with the present day computational resources, this is a question that can be more satisfactorily addressed at the present time. Our work, and related work that has been described, illustrates that exploring the nature of dynamics below the mode coupling crossover is now feasible computationally. Exploration of such low temperature dynamics should help bridge the gap between the temperature range computer simulations have been able to access in the past, and the temperature range relevant for several experimental and theoretical results.

Chapter 7

Conclusions

In this chapter, we summarize the main findings of the thesis, their implications, and the aspects of the works that merit further investigation. The work in the thesis falls under two main themes. One theme is the study of a range of disordered systems under cyclic deformation, and the other is the study of supercooled liquids at very low temperatures.

In the first work chapter, Chapter 3, we have presented the study of the reversible-irreversible transitions in sphere assemblies under the application of oscillatory shear deformation for a range of densities across the isotropic jamming density. The extremum of the densities represents very different systems like low-density colloids or very high-density glasses. Our work shows that even if the systems are very different, the transitions from a reversible state to an irreversible state have similarities and certain differences. Reversible-irreversible transition across the whole density spectrum has been identified by the onset of diffusion. All the transitions have been identified by the discontinuous changes in the appropriate quantities. One very interesting aspect of the work is the identification of a jamming density termed as ϕ_J^{cyc}, a higher density compared to the isotropic jamming density (ϕ_J). The significance of this density is that an unjammed pocket has emerged between ϕ_J and ϕ_J^{cyc} that has facilitated the study of frictionless shear jamming above isotropic jamming density ϕ_J and associated dilatancy. This work leaves some interesting directions to be explored by further investigation. One such direction is establishing a correspondence between cyclic shear jamming (with added friction) and irrevresible transition. This connection could be complementary to the yielding and the irreversible transition at the high density limit. Finally, the question can be asked about how robust the phase diagram is. For a further better understanding of the phase diagram, the inclusion of friction, thermal fluctuation, or noise will be an interesting avenue to explore.

In Chapter 4, we have studied the annealing of the glassy system under oscillatory shear deformation. We have studied the yielding behavior of the system under cyclic shear deformation at a finite rate and a finite temperature. As observed previously for the athermal deformation cases, we also found that the system anneals or accesses the lowest possible energy when the amplitude of the deformation is closest to the respective yielding transition amplitude (γ_y). It has been shown that driving the system with a finite rate and a temperature helps it access lower energies than the energies accessed through athermal driving. But at the temperature regime where the system can be equilibrated by the thermal fluctuations alone, the mechanical driving does not offer a faster sampling. Interestingly, the sheared configurations generated under optimal conditions are equilibrium like in terms of structure, energy, and degree of anisotropy.

With the follow up of the work in Chapter 4, in Chapter 5, we show the overaging of the glassy system under the application of oscillatory deformation. We have found that mechanical perturbation does not offer a faster sampling at a comparatively higher temperature, where the thermal fluctuations can equilibrate the system. But at a relatively lower temperature, where the system enters the aging regime and cannot be equilibrated, mechanical driving makes the relaxation faster. Mechanical driving, along with thermal fluctuation, helps the system access lower energies faster; in other words, it helps the system 'overage'. It is an interesting question to pursue under what conditions mechanical perturbation becomes a more significant component than the thermal fluctuation that helps the system access lower energy minima. It is interesting to find out how overaging changes system properties such as mechanical properties as aging glasses (like polymer glasses) have vast and significant applications.

In Chapter 6, we have studied a dynamical crossover in a model glass former. We have studied different dynamical quantities, dynamical heterogeneity, and morphology of correlated rearrangements. Such dynamical quantities signify a crossover in dynamics in the system around the mode-coupling temperature. Even though the dynamical measurements hint at a non-Arrhenius to Arrhenius transition in an otherwise well known fragile glass-forming liquid, the nature of transition remains different than the extensively studied fragile to strong transition in anomalous liquids. Even though a dynamical crossover is observed, no associated change in thermodynamic quantities has been found. A proper estimate of configurational entropy (with the anharmonic correction added to the estimate of the vibrational entropy) shows that the Adam-Gibbs relation holds reasonably well across the crossover temperature. This work contributes to the recent findings of fragile to strong transitions in a range of systems

that are otherwise known as fragile glass formers at comparatively lower temperatures. The nature of this transition remains to be understood further in the absence of obvious structural changes. This work also emphasizes the role of anharmonicity in the proper enumeration of entropy and demands further refined estimation of the entropy.

Appendix A

Appendix

A.1 Minimization methods and contact numbers

In this section, we describe the dependence of the contact numbers on the minimization methods. Relevant details and definitions of the contact numbers are described.

A.1.1 Dependence of geometric contacts on the minimization protocol

The configurations in the unjamming region have a finite value of Z. This is due to the minimization method used during AQS simulations [294]. We use the FIRE minimization protocol during AQS steps and show that the unjammed configurations so obtained has $Z = 0$. In Fig. A.1 we show how the distribution of the contact numbers changes for different minimization protocols. In Fig. A.2, we show the evolution of the average contact number as a function of γ_{accum}, for CG and FIRE protocol. We observe that the geometric contact number rapidly falls to zero when we use FIRE. By using different tolerance (ϵ) values to identify the geometric contacts (like the mechanical contacts), Z from the CG approaches the Z from the FIRE, see Fig. A.2. Even though FIRE removes overlaps completely, computationally FIRE is almost one order of magnitude slower compared to CG.

A.1.2 Mechanical contacts

In jammed packings especially close to ϕ_J there are always rattler particles. Rattler particles do not belong to the stress carrying rigid network of a jammed packing. The percentage of rattler particles depends on the density of jammed packings and protocol. The higher the packing fraction the lower is the percentage of rattlers. For

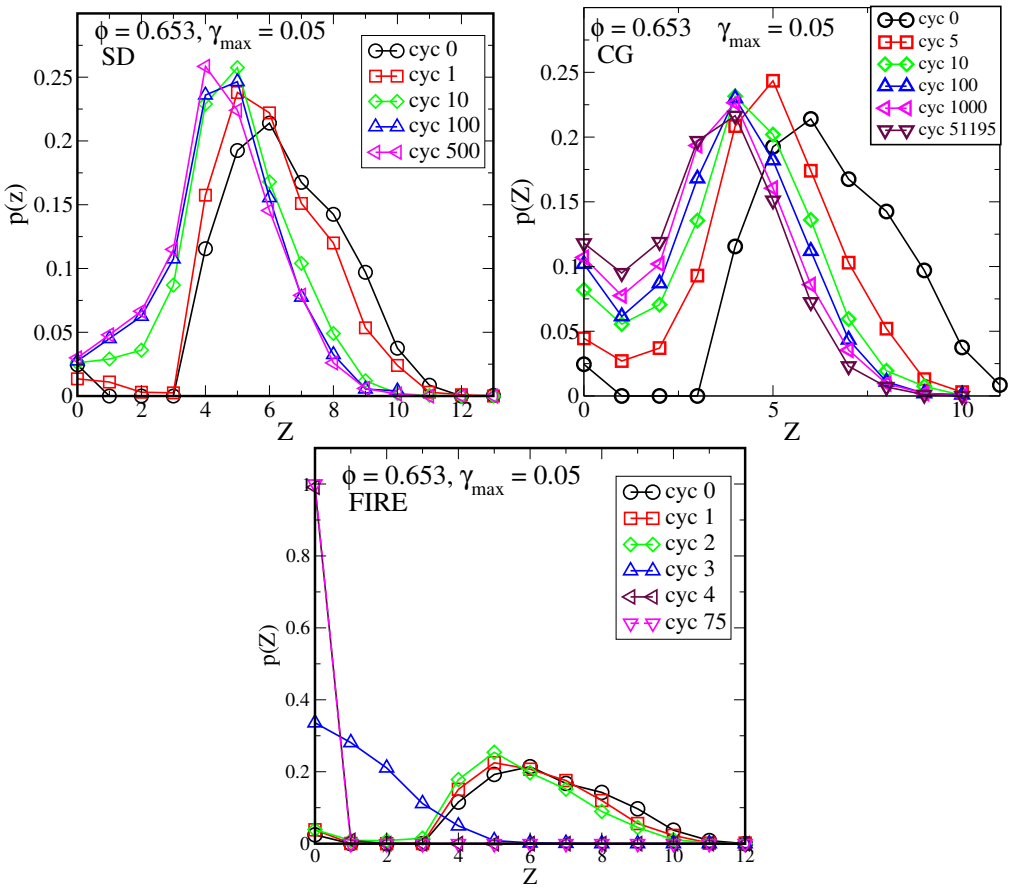

Figure A.1: The distribution of contact numbers shows with the increase of cycles numbers, the peak of the distribution moves slowly to a lower value than 6 with SD and CG minimization. In the case of CG, along with the shift of the peak, the zero contact number increases slowly. In the FIRE method, the average contact number goes to zero pretty fast as the system unjams.

frictionless particles, the geometric criterion for identifying rattlers is that they have contact number $z < D+1$. A more robust criterion is a mechanical one, that is, rattlers are particles that do not carry any forces or stresses. However this mechanical criterion requires us to introduce a tolerance to identify a contact that carry stress due to the minimization protocol and the precision of computation. In Fig. A.3, we show the cumulative distribution of overlaps for a jammed and an unjammed packing. Ideally the tolerance value is $r - \sigma = 0$ but due to the finite precision of the minimization and protocol details we use a tolerance value of 10^{-10} (shown as a vertical dashed line in Fig. A.3). Observe that for a jammed packing, we can clearly see that the two distributions are well separated, *i.e.,* contacts that carry stress and those that do not. We also show the cumulative distribution for a quadruple (quad) precision minimization, see Fig. A.3. We see that with quadruple precision, we can lower the tolerance value but the contacts that carry stress do not change. Note that in the jammed case, the contacts that have small overlaps with double precision computation, are removed when

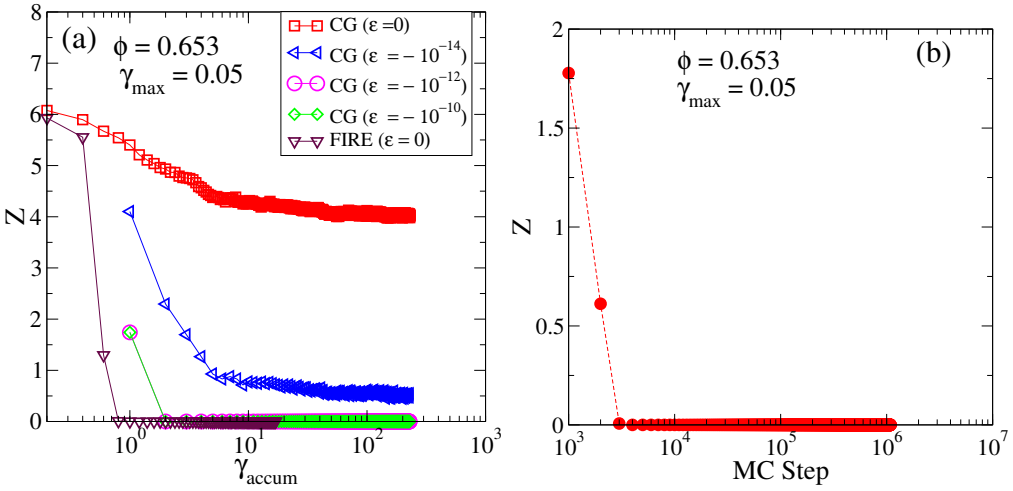

Figure A.2: (a)The average contact number Z as a function of γ_{accum}, shown for $\phi = 0.653$, for the CG method, with different tolerances, and the FIRE method. Compared to the conjugate gradient method, the Fire algorithm performs better minimization and removes all the contacts. (b) Once the system unjams the hard sphere MC simulation also brings down the contact number of the system to zero.

we perform quadruple precision computation. In Fig. A.4, we show the full cumulative distribution of the contacts for a jammed and an unjammed configuration. For an unjammed configuration the plateau is below $2D$ and for a jammed configuration the plateau emerges above $2D$.

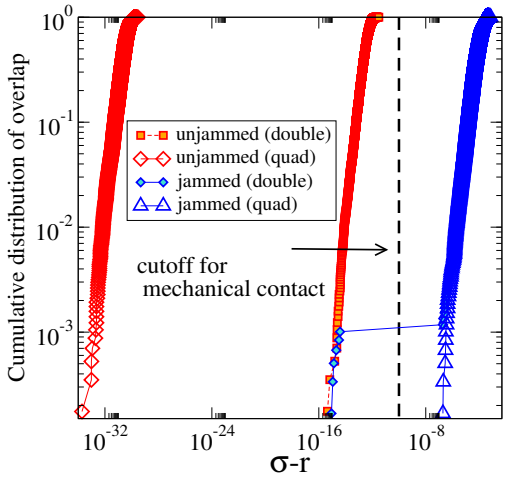

Figure A.3: Cumulative distribution of overlaps for a jammed and an unjammed packing at $\phi = 0.653$, for two precision values. The vertical dashed line shows the tolerance value we use to identify Z_M.

We have shown that the results do not depend on the choice of cutoff. With a better precision of minimization, this cutoff can be shifted to a much lower value. While defining the rattlers, we have calculated the contact network for that given configuration and identify rattlers for that given configuration as particles with less than $D + 1 = 4$ contacts (see above). We do not generate the contact network iteratively,

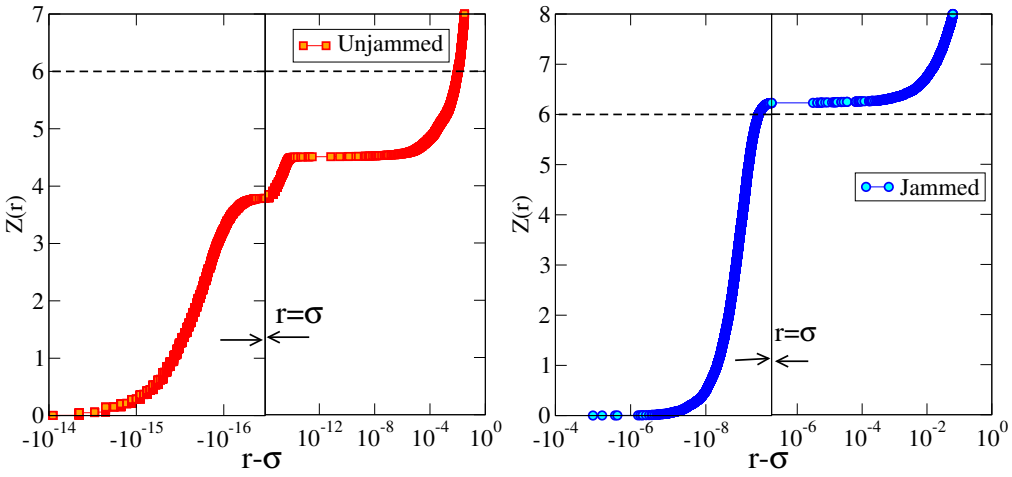

Figure A.4: The full cumulative distribution of contacts (interparticle separation r both above and below σ) for an unjammed and a jammed configuration shows plateau below and above $2D$ respectively. The vertical lines indicate $r = \sigma$.

and thus our procedure is different from Ref. [210]. As reported in [295], where we do such a computation, the iterative or 'bootstrap' procedure generate contact numbers that agree well with the mechanical contact number.

A.1.3 Fraction of non-rattlers at different phases

The fraction of the non-rattlers in the jammed phase (absorbing (A) and yielded phase (Y)) is around 0.95, slightly higher than the fraction of non-rattler percentage (0.82) mentioned [111]. In the unjammed phase the fraction is lower than the cutoff mentioned in [111] as can be expected(see Fig. A.5). At this point, we will mention that in the latter part of this chapter, we have discussed the procedure of counting contacts for the unjammed systems f_{NR} values for the jammed phase (A and Y) are consistent with the f_{NR} value of the initial unsheared jammed configurations. In the study of 2D frictional shear jamming [295], the value of the fraction of non-rattlers (f_{NR}) at the shear jamming transition ranges from (0.8-0.93) depending on the density and protocol.

A.1.4 Contacts below isotropic jamming density ϕ_J

First, we mention the details of how to define contacts for low density systems below isotropic jamming density. Above ϕ_J, we have done structural characterisation of the system in different phases and have identified different phases depending on various contacts. Defining contacts in a similar way for the unjammed phases below isotropic

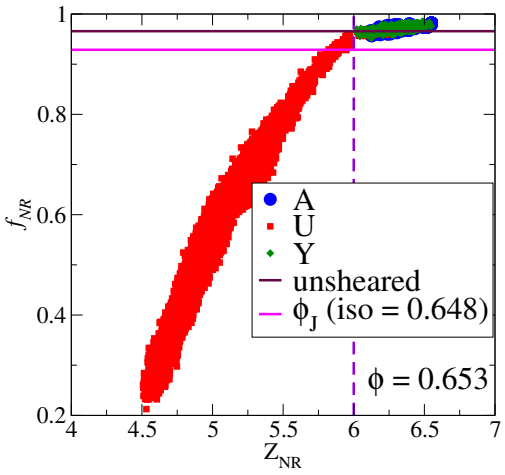

Figure A.5: Fraction of non-rattlers (f_{NR}) *vs* Z_{NR} is shown for a fixed density ($\phi = 0.653$). In the jammed phase (absorbing (A) and yielded phase (Y)), f_{NR} value at $Z_{NR} = 6$ is close to 0.95. The maroon horizontal line represents the fraction of non-rattlers for the initial unsheared jammed configurations. The black line represents the fraction of non-rattlers for the isotropically jammed configurations at ϕ_J. The vertical dashed line corresponds to $Z_{NR} = 6(= 2D)$.

jamming density is not useful. We have seen that for low density configurations, conjugate gradient minimization removes the contacts further away than $r = \sigma$. We have found that contact numbers are zero for comparatively small and intermediate ranges of amplitudes, below ϕ_J. This range of amplitudes span LR and PR phases. Therefore we have performed two rounds of minimization in such cases. First, we take steady state configurations sheared with the minimization method CG. Then we apply further deformation cycles accompanied by the SD minimization method. As shown in Chapter 2, the SD minimization method does not remove the contacts very far apart. So the cumulative distribution of contact numbers $Z(r)$ shows a plateau when plotted as a function of $r - \sigma$. With a proper choice of tolerance of $r - \sigma$ (10^{-12}), we can define contact numbers even for smaller amplitudes (the choice of tolerance and details has been described earlier). We show ($Z(r)$) vs $r - \sigma$ plot for configurations obtained through shearing via CG minimization and configurations obtained through further shearing via SD minimization (see Fig. A.6) for two representative packing fractions ($\phi = 0.627$ and $\phi = 0.638$). That way, we can have a finite value of contact numbers for all the amplitudes in all the phases when minimized using SD.

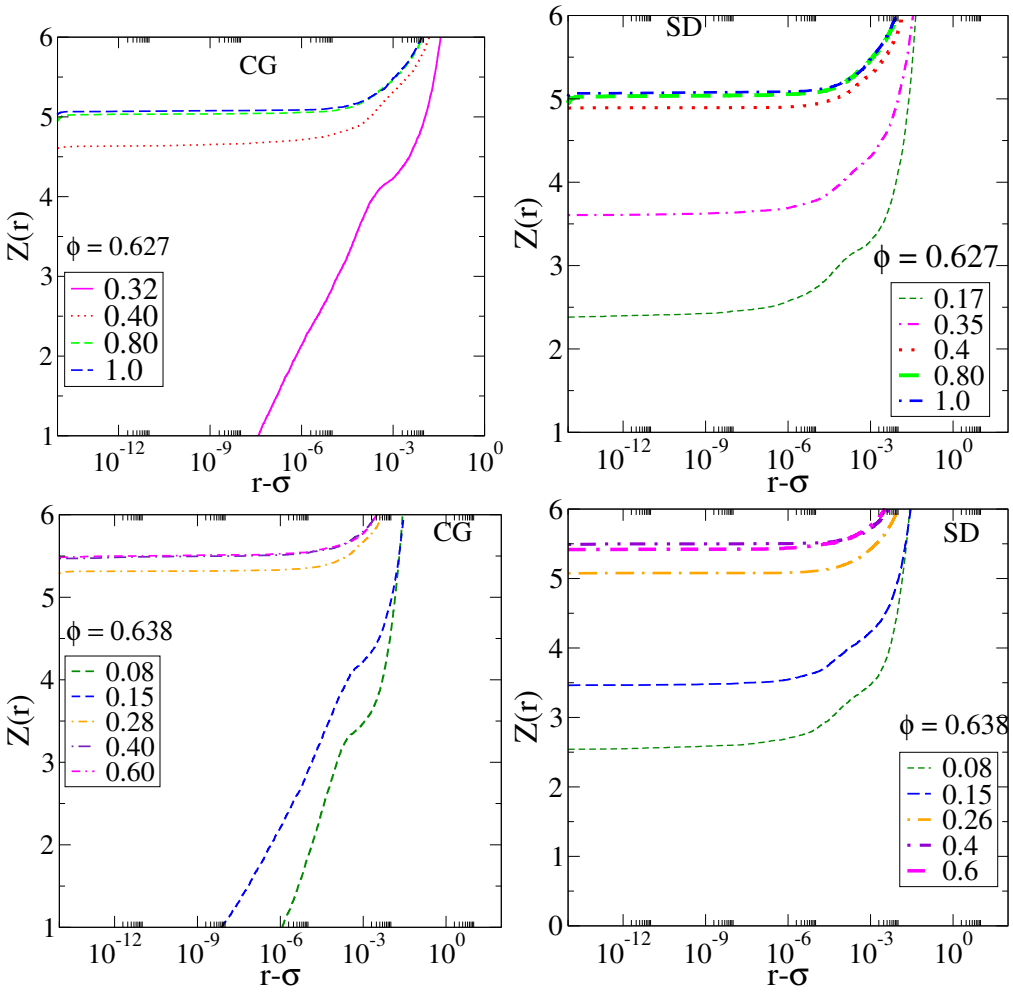

Figure A.6: Cumulative distribution of contact numbers for steady state configurations at $\phi = 0.627$ and 0.638 has been shown. When minimized with SD, $Z(r)$ shows a plateau extended up to 10^{-12}, for smaller amplitudes in contrast to configurations minimized with CG

A.2 Equilibrium properties of binary mixture of Kob-Andersen 80:20 mixture

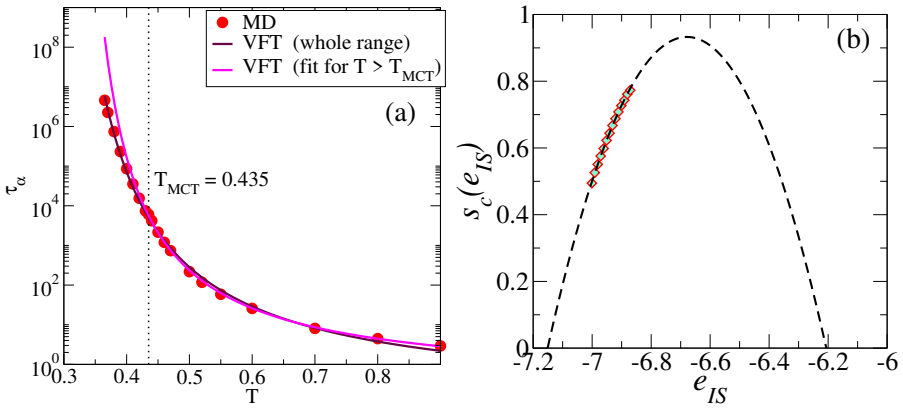

Figure A.7: (*a*) Relaxation times from molecular dynamics simulations *vs.* temperature, and the corresponding fit to the VFT form. (*b*) The configurational entropy density as a function of the inherent structure energy, and a quadratic fit. The extrapolated value of IS energy at which configurational entropy vanishes is (≈ -7.15).

In Fig. A.7 (a), we show VFT fits to the relaxation times (Kob- Andersen 80:20 mixture), first by considering temperatures only for $T > T_{MCT}$ ($\tau_0 = 0.3101$, $K_{VFT} = 0.2243$, $T_{VFT} = 0.2989$). The VFT fits to the high temperature data clearly overestimate the relaxation times for $T < T_{MCT}$. On the other hand, for the VFT fit to the full range ($\tau_0 = 0.1175$, $K_{VFT} = 0.1383$, $T_{VFT} = 0.2592$.), the VFT form does not provide a good description of the data at higher temperatures [240]. Fig. A.7. (b) shows configurational entropy (S_c) vs e_{IS} plot [74] with the lowest estimated value of e_{IS} to be at ≈ -7.15 which configurational entropy vanishes.

A.3 Stress in cyclically sheared glassy configurations

In Fig. A.8 we show the shear stress (σ_{xy}) arising from the interaction of the particles in stroboscopic configurations (at the end of each cycle of strain) obtained by shearing at a rate $\dot{\gamma} = 10^{-5}$, temperature $T = 0.3$ across the yielding transition amplitude (γ_y), which is $\gamma_{max} = 0.035$ for these parameters. As long as the strain amplitude stays below the yielding amplitude, the stroboscopic shear stress values fluctuate around zero, similar to the initial undeformed configurations. Beyond the yielding amplitude, the stroboscopic configurations retain a finite amount of stress (see Fig. A.8(a)). This is also realisable from the evolution of the shear stress within a shearing cycle. The area under the stress-strain curve is negligible when the system is sheared at amplitudes below the yielding transition amplitude. Beyond the yielding amplitude, a finite area under the curve emerges signifying the onset of built-in stress in the system as shown

earlier in Fig. 4.1. We show in Fig. A.8 (b) the distribution of the shear stress per particle in a stroboscopic configuration at a strain amplitude very close to but below the yielding amplitude, which are also seen to be symmetric around zero. Thus, we demonstrate that we are indeed generating low energy structures without any built-in stress.

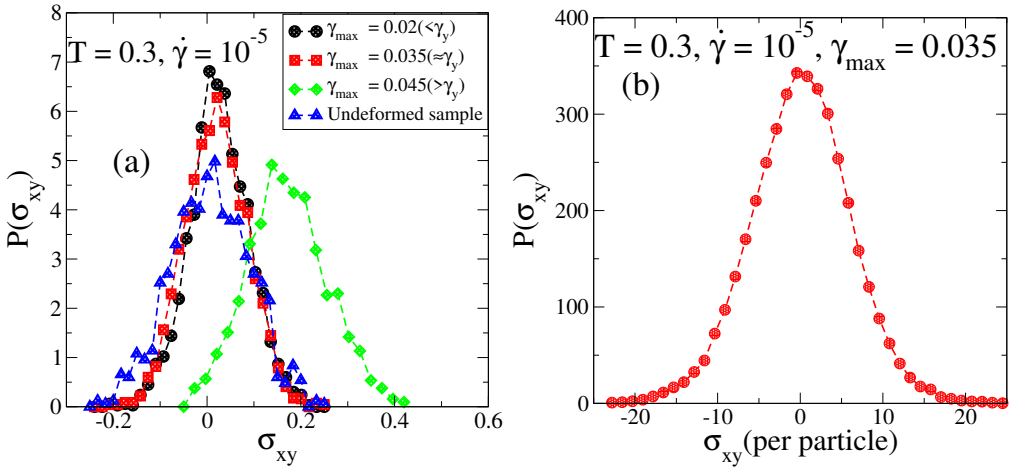

Figure A.8: (*a*) Distributions of the global shear stress of stroboscopic configurations (at the end of each cycle) are shown for different strain amplitudes across the yielding ($\gamma_{max} = 0.035$ in this case) in comparison to the initial undeformed configurations. As long as the strain amplitude is less than or close to the yielding amplitude the shear stress fluctuates around zero in stroboscopic configurations. Beyond yielding, stroboscopic configurations retain a finite mean value of shear stress. (*b*) Distribution of xy components of the stress tensor evaluated for individual particles, in a configuration obtained by shearing close to yielding amplitude ($\gamma_{max} = 0.035$), which is seen to be symmetric around zero.

A.4 wavelength dependence of correlation functions

The $F_s(k,t)$ curves (of binary mixture of Kob-Andersen 80:20 mixture) are shown in Fig. A.9 for several k values, along with fits of the following form

$$F_s(\mathbf{k},t) = (1-f_c)exp(-(t/\tau_s))^n + f_c exp(-t/\tau_\alpha)^{\beta_{kww}} \tag{A.1}$$

. The fit values obtained, of $\tau_\alpha(k)$, $\beta_{kww}(k)$ and $f_c(k)$ are shown in Fig. A.10. The $F_s(k,t)$ curves are shown in Fig. A.9 for several k values, along with fits to the same form as above for $q(t)$. The fit values obtained, of $\tau_\alpha(k)$, $\beta_{kww}(k)$ and $f_c(k)$ are shown in Fig. A.10.

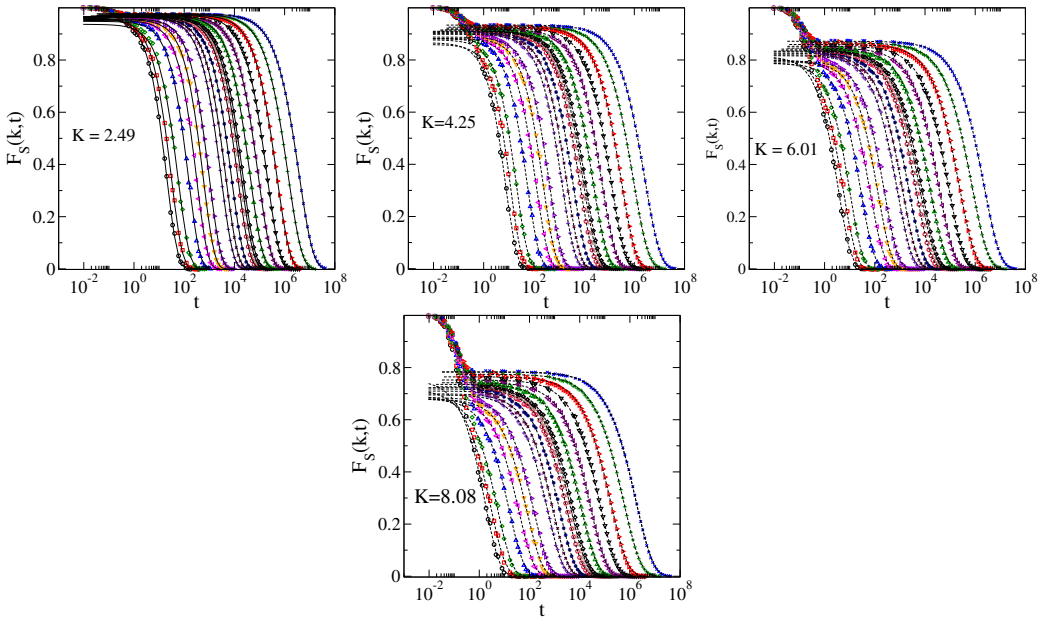

Figure A.9: The self part of the intermediate scattering function $F_s(k,t)$ is shown for a range of k values. The dotted lines are fits to the data.

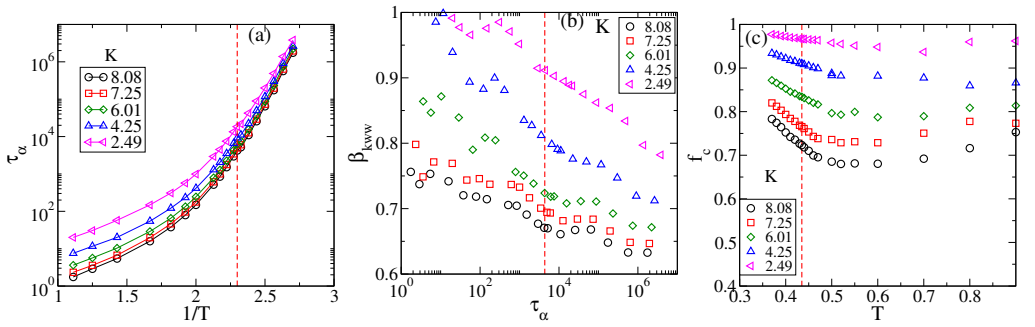

Figure A.10: The variation of relaxation time $\tau_\alpha(k)$, stretching exponent β_{kww} and the non-ergodicity parameter (f_c), obtained from $F_s(k,t)$, are shown for several k values.

List of publications

- Pallabi Das, Vinutha H. A., and Srikanth Sastry. "Unified phase diagram of reversible-irreversible, jamming, and yielding transitions in cyclically sheared soft-sphere packings." Proceedings of the National Academy of Sciences 117.19 (2020): 10203-10209.
- Pallabi Das, Anshul DS Parmar, and Srikanth Sastry. "Annealing glasses by cyclic shear deformation." The Journal of Chemical Physics 157.4 (2022): 044501.
- Pallabi Das, and Srikanth Sastry. "Crossover in dynamics in the Kob-Andersen binary mixture glass-forming liquid." Journal of Non-Crystalline Solids: X (2022): 100098.

Bibliography

[1] J. Ballato and P. Dragic, "Rethinking optical fiber: new demands, old glasses," *Journal of the American Ceramic Society*, vol. 96, no. 9, pp. 2675–2692, 2013.

[2] M. Telford, "The case for bulk metallic glass," *Materials today*, vol. 7, no. 3, pp. 36–43, 2004.

[3] D. Yokoyama, "Molecular orientation in small-molecule organic light-emitting diodes," *Journal of Materials Chemistry*, vol. 21, no. 48, pp. 19187–19202, 2011.

[4] L. Mishnaevsky, K. Branner, H. N. Petersen, J. Beauson, M. McGugan, and B. F. Sørensen, "Materials for wind turbine blades: an overview," *Materials*, vol. 10, no. 11, p. 1285, 2017.

[5] L. L. Hench, "The story of bioglass®," *Journal of Materials Science: Materials in Medicine*, vol. 17, no. 11, pp. 967–978, 2006.

[6] C. A. Angell, "Formation of glasses from liquids and biopolymers," *Science*, vol. 267, no. 5206, pp. 1924–1935, 1995.

[7] M. D. Ediger, "Perspective: Highly stable vapor-deposited glasses," *The Journal of chemical physics*, vol. 147, no. 21, p. 210901, 2017.

[8] A. Banerjee, S. Sengupta, S. Sastry, and S. M. Bhattacharyya, "Role of structure and entropy in determining differences in dynamics for glass formers with different interaction potentials," *Phys. Rev. Lett.*, vol. 113, p. 225701, Nov 2014.

[9] J. E. Hallett, F. Turci, and C. P. Royall, "Local structure in deeply supercooled liquids exhibits growing lengthscales and dynamical correlations," *Nature communications*, vol. 9, no. 1, pp. 1–10, 2018.

[10] L. Pardo, P. Lunkenheimer, and A. Loidl, "Dielectric spectroscopy in benzophenone: The β relaxation and its relation to the mode-coupling cole-cole peak," *Physical Review E*, vol. 76, no. 3, p. 030502, 2007.

[11] J. C. Dyre, "Colloquium: The glass transition and elastic models of glass-forming liquids," *Reviews of modern physics*, vol. 78, no. 3, p. 953, 2006.

[12] P. G. Debenedetti and F. H. Stillinger, "Supercooled liquids and the glass transition," *Nature*, vol. 410, no. 6825, p. 259, 2001.

[13] D. N. Perera and P. Harrowell, "Consequences of kinetic inhomogeneities in glasses," *Physical Review E*, vol. 54, no. 2, p. 1652, 1996.

[14] W. Kob, C. Donati, S. J. Plimpton, P. H. Poole, and S. C. Glotzer, "Dynamical heterogeneities in a supercooled lennard-jones liquid," *Physical review letters*, vol. 79, no. 15, p. 2827, 1997.

[15] C. Donati, J. F. Douglas, W. Kob, S. J. Plimpton, P. H. Poole, and S. C. Glotzer, "Stringlike cooperative motion in a supercooled liquid," *Physical review letters*, vol. 80, no. 11, p. 2338, 1998.

[16] F. W. Starr, J. F. Douglas, and S. Sastry, "The relationship of dynamical heterogeneity to the adam-gibbs and random first-order transition theories of glass formation," *The Journal of chemical physics*, vol. 138, no. 12, p. 12A541, 2013.

[17] B. Doliwa and A. Heuer, "Cage effect, local anisotropies, and dynamic heterogeneities at the glass transition: A computer study of hard spheres," *Physical review letters*, vol. 80, no. 22, p. 4915, 1998.

[18] E. Vidal Russell and N. Israeloff, "Direct observation of molecular cooperativity near the glass transition," *Nature*, vol. 408, no. 6813, pp. 695–698, 2000.

[19] W. K. Kegel, van Blaaderen, and Alfons, "Direct observation of dynamical heterogeneities in colloidal hard-sphere suspensions," *Science*, vol. 287, no. 5451, pp. 290–293, 2000.

[20] C. A. Angell, "Structural instability and relaxation in liquid and glassy phases near the fragile liquid limit," *Journal of non-crystalline solids*, vol. 102, no. 1-3, pp. 205–221, 1988.

[21] Y. S. Elmatad, D. Chandler, and J. P. Garrahan, "Corresponding states of structural glass formers. ii," *The Journal of Physical Chemistry B*, vol. 114, no. 51, pp. 17113–17119, 2010.

[22] D. Kivelson, G. Tarjus, X. Zhao, and S. A. Kivelson, "Fitting of viscosity: Distinguishing the temperature dependences predicted by various models of supercooled liquids," *Physical Review E*, vol. 53, no. 1, p. 751, 1996.

[23] F. Stickel, E. W. Fischer, and R. Richert, "Dynamics of glass-forming liquids. i. temperature-derivative analysis of dielectric relaxation data," *The Journal of chemical physics*, vol. 102, no. 15, pp. 6251–6257, 1995.

[24] C. A. Angell, "Water ii is a "strong" liquid," *The Journal of Physical Chemistry*, vol. 97, no. 24, pp. 6339–6341, 1993.

[25] K. Ito, C. T. Moynihan, and C. A. Angell, "Thermodynamic determination of fragility in liquids and a fragile-to-strong liquid transition in water," *Nature*, vol. 398, no. 6727, pp. 492–495, 1999.

[26] F. W. Starr, C. Angell, and H. Stanley, "Prediction of entropy and dynamic properties of water below the homogeneous nucleation temperature," *Physica A: Statistical Mechanics and its Applications*, vol. 323, pp. 51–66, 2003.

[27] R. Shi, J. Russo, and H. Tanaka, "Origin of the emergent fragile-to-strong transition in supercooled water," *Proceedings of the National Academy of Sciences*, vol. 115, no. 38, pp. 9444–9449, 2018.

[28] L. Lupi, B. Vázquez Ramírez, and P. Gallo, "Dynamical crossover and its connection to the widom line in supercooled tip4p/ice water," *The Journal of Chemical Physics*, vol. 155, no. 5, p. 054502, 2021.

[29] J.-L. Barrat, J. Badro, and P. Gillet, "A strong to fragile transition in a model of liquid silica," *Molecular Simulation*, vol. 20, no. 1-2, pp. 17–25, 1997.

[30] J. Horbach and W. Kob, "Static and dynamic properties of a viscous silica melt," *Phys. Rev. B*, vol. 60, pp. 3169–3181, Aug 1999.

[31] I. Saika-Voivod, P. H. Poole, and F. Sciortino, "Fragile-to-strong transition and polyamorphism in the energy landscape of liquid silica," *Nature*, vol. 412, no. 6846, pp. 514–517, 2001.

[32] A. Saksaengwijit, J. Reinisch, and A. Heuer, "Origin of the fragile-to-strong crossover in liquid silica as expressed by its potential-energy landscape," *Phys. Rev. Lett.*, vol. 93, p. 235701, Dec 2004.

[33] S. Sastry and C. A. Angell, "Liquid–liquid phase transition in supercooled silicon," *Nature materials*, vol. 2, no. 11, p. 739, 2003.

[34] V. V. Vasisht, "Study of supercooled silicon liquid-liquid critical point structural and dynamical properties," Master's thesis, Jawaharlal Nehru Centre for Advanced Scientific Research, 2009.

[35] V. V. Vasisht, *Phase behaviour of supercooled liquid silicon*. PhD thesis, Jawaharlal Nehru Centre for Advanced Scientific Research, Bengaluru, 2013.

[36] N. Jakse, A. Pasturel, S. Sastry, and C. A. Angell, "Response to âĂIJcomment on âĂŸdynamic aspects of the liquid-liquid phase transformation in siliconâĂŹâĂĽâĂİ [j. chem. phys. 130, 247102 (2009)]," *Journal of Chemical Physics*, vol. 130, p. 247103, 2009.

[37] P. H. Poole, F. Sciortino, U. Essmann, and H. E. Stanley, "Phase behaviour of metastable water," *Nature*, vol. 360, no. 6402, pp. 324–328, 1992.

[38] S. Wei, P. Lucas, and C. A. Angell, "Phase change alloy viscosities down to tg using adam-gibbs-equation fittings to excess entropy data: A fragile-to-strong transition," *Journal of Applied Physics*, vol. 118, no. 3, p. 034903, 2015.

[39] J. Orava, D. W. Hewak, and A. L. Greer, "Fragile-to-strong crossover in supercooled liquid ag-in-sb-te studied by ultrafast calorimetry," *Advanced Functional Materials*, vol. 25, no. 30, pp. 4851–4858, 2015.

[40] S. Ashwin and S. Sastry, "Low-temperature behaviour of the kob–andersen binary mixture," *Journal of Physics: Condensed Matter*, vol. 15, no. 11, p. S1253, 2003.

[41] D. Coslovich, M. Ozawa, and W. Kob, "Dynamic and thermodynamic crossover scenarios in the kob-andersen mixture: Insights from multi-cpu and multi-gpu simulations," *The European Physical Journal E*, vol. 41, no. 5, p. 62, 2018.

[42] H. Zhang, X. Wang, H.-B. Yu, and J. F. Douglas, "Dynamic heterogeneity, cooperative motion, and johari–goldstein beta-relaxation in a metallic glass-forming material exhibiting a fragile-to-strong transition," *The European Physical Journal E*, vol. 44, no. 4, pp. 1–30, 2021.

[43] L. Ortlieb, T. S. Ingebrigtsen, J. E. Hallett, F. Turci, and C. P. Royall, "Relaxation mechanisms in supercooled liquids past the mode–coupling crossover: Cooperatively re–arranging regions vs excitations," *arXiv preprint arXiv:2103.08060*, 2021.

[44] K. Schmidt-Rohr and H. Spiess, "Nature of nonexponential loss of correlation above the glass transition investigated by multidimensional nmr," *Physical Review Letters*, vol. 66, no. 23, p. 3020, 1991.

[45] J.-P. Hansen and I. R. McDonald, *Theory of simple liquids: with applications to soft matter*. Academic press, 2013.

[46] H. Tanaka, T. Kawasaki, H. Shintani, and K. Watanabe, "Critical-like behaviour of glass-forming liquids," *Nature materials*, vol. 9, no. 4, pp. 324–331, 2010.

[47] K. Vollmayr-Lee, W. Kob, K. Binder, and A. Zippelius, "Dynamical heterogeneities below the glass transition," *The Journal of chemical physics*, vol. 116, no. 12, pp. 5158–5166, 2002.

[48] C. Donati, S. C. Glotzer, P. H. Poole, W. Kob, and S. J. Plimpton, "Spatial correlations of mobility and immobility in a glass-forming lennard-jones liquid," *Phys. Rev. E*, vol. 60, pp. 3107–3119, Sep 1999.

[49] E. R. Weeks, J. C. Crocker, A. C. Levitt, A. Schofield, and D. A. Weitz, "Three-dimensional direct imaging of structural relaxation near the colloidal glass transition," *Science*, vol. 287, no. 5453, pp. 627–631, 2000.

[50] S. C. Glotzer, V. N. Novikov, and T. B. Schrøder, "Time-dependent, four-point density correlation function description of dynamical heterogeneity and decoupling in supercooled liquids," *The Journal of Chemical Physics*, vol. 112, no. 2, pp. 509–512, 2000.

[51] S. Karmakar, C. Dasgupta, and S. Sastry, "Growing length scales and their relation to timescales in glass-forming liquids," *Annu. Rev. Condens. Matter Phys.*, vol. 5, no. 1, pp. 255–284, 2014.

[52] S. Karmakar, C. Dasgupta, and S. Sastry, "Growing length and time scales in glass-forming liquids," *Proceedings of the National Academy of Sciences*, vol. 106, no. 10, pp. 3675–3679, 2009.

[53] S. Sengupta, S. Karmakar, C. Dasgupta, and S. Sastry, "Breakdown of the stokes-einstein relation in two, three, and four dimensions," *The Journal of chemical physics*, vol. 138, no. 12, p. 12A548, 2013.

[54] J. Douglas and D. Leporini, "Obstruction model of the fractional stokes–einstein relation in glass-forming liquids," *Journal of non-crystalline solids*, vol. 235, pp. 137–141, 1998.

[55] G. Tarjus and D. Kivelson, "Breakdown of the stokes–einstein relation in supercooled liquids," *The Journal of chemical physics*, vol. 103, no. 8, pp. 3071–3073, 1995.

[56] S. Sengupta and S. Karmakar, "Distribution of diffusion constants and stokes-einstein violation in supercooled liquids," *The Journal of chemical physics*, vol. 140, no. 22, p. 224505, 2014.

[57] S. K. Kumar, G. Szamel, and J. F. Douglas, "Nature of the breakdown in the stokes-einstein relationship in a hard sphere fluid," *The Journal of chemical physics*, vol. 124, no. 21, p. 214501, 2006.

[58] A. D. Parmar, S. Sengupta, and S. Sastry, "Length-scale dependence of the stokes-einstein and adam-gibbs relations in model glass formers," *Physical review letters*, vol. 119, no. 5, p. 056001, 2017.

[59] M. Adhikari, S. Karmakar, and S. Sastry, "Spatial dimensionality dependence of heterogeneity, breakdown of the stokes–einstein relation, and fragility of a model glass-forming liquid," *The Journal of Physical Chemistry B*, vol. 125, no. 36, pp. 10232–10239, 2021.

[60] T. R. Kirkpatrick and D. Thirumalai, "Comparison between dynamical theories and metastable states in regular and glassy mean-field spin models with underlying first-order-like phase transitions," *Physical Review A*, vol. 37, no. 11, p. 4439, 1988.

[61] W. Kauzmann, "The nature of the glassy state and the behavior of liquids at low temperatures.," *Chemical reviews*, vol. 43, no. 2, pp. 219–256, 1948.

[62] C. Cammarota and G. Biroli, "Ideal glass transitions by random pinning," *Proceedings of the National Academy of Sciences*, vol. 109, no. 23, pp. 8850–8855, 2012.

[63] W. Kob and L. Berthier, "Probing a liquid to glass transition in equilibrium," *Physical review letters*, vol. 110, no. 24, p. 245702, 2013.

[64] M. Ozawa, W. Kob, A. Ikeda, and K. Miyazaki, "Equilibrium phase diagram of a randomly pinned glass-former," *Proceedings of the National Academy of Sciences*, vol. 112, no. 22, pp. 6914–6919, 2015.

[65] S. Chakrabarty, S. Karmakar, and C. Dasgupta, "Dynamics of glass forming liquids with randomly pinned particles," *Scientific reports*, vol. 5, no. 1, pp. 1–10, 2015.

[66] G. Adam and J. H. Gibbs, "On the temperature dependence of cooperative relaxation properties in glass-forming liquids," *The journal of chemical physics*, vol. 43, no. 1, pp. 139–146, 1965.

[67] T. Kirkpatrick, D. Thirumalai, and P. G. Wolynes, "Scaling concepts for the dynamics of viscous liquids near an ideal glassy state," *Physical Review A*, vol. 40, no. 2, p. 1045, 1989.

[68] V. Lubchenko and P. G. Wolynes, "Theory of structural glasses and supercooled liquids," *Annu. Rev. Phys. Chem.*, vol. 58, pp. 235–266, 2007.

[69] J. D. Stevenson, J. Schmalian, and P. G. Wolynes, "The shapes of cooperatively rearranging regions in glass-forming liquids," *Nature Physics*, vol. 2, no. 4, pp. 268–274, 2006.

[70] R. Richert and C. Angell, "Dynamics of glass-forming liquids. v. on the link between molecular dynamics and configurational entropy," *The Journal of chemical physics*, vol. 108, no. 21, pp. 9016–9026, 1998.

[71] R. J. Speedy, "The hard sphere glass transition," *Molecular Physics*, vol. 95, no. 2, pp. 169–178, 1998.

[72] G. Johari, "A resolution for the enigma of a liquidâĂŹs configurational entropy-molecular kinetics relation," *The Journal of Chemical Physics*, vol. 112, no. 20, pp. 8958–8969, 2000.

[73] A. Scala, F. Starr, E. La Nave, and et al., "Configurational entropy and diffusivity of supercooled water," *Nature*, vol. 406, pp. 166–169, 2000.

[74] S. Sastry, "The relationship between fragility, configurational entropy and the potential energy landscape of glass-forming liquids," *Nature*, vol. 409, no. 6817, p. 164, 2001.

[75] S. Sengupta, S. Karmakar, C. Dasgupta, and S. Sastry, "Adam-gibbs relation for glass-forming liquids in two, three, and four dimensions," *Physical review letters*, vol. 109, no. 9, p. 095705, 2012.

[76] M. Ozawa, C. Scalliet, A. Ninarello, and L. Berthier, "Does the adam-gibbs relation hold in simulated supercooled liquids?," *The Journal of chemical physics*, vol. 151, no. 8, p. 084504, 2019.

[77] M. Goldstein, "Viscous liquids and the glass transition: a potential energy barrier picture," *The Journal of Chemical Physics*, vol. 51, no. 9, pp. 3728–3739, 1969.

[78] A. Cavagna, "Supercooled liquids for pedestrians," *Physics Reports*, vol. 476, no. 4-6, pp. 51–124, 2009.

[79] L. Berthier and G. Biroli, "Theoretical perspective on the glass transition and amorphous materials," *Reviews of Modern Physics*, vol. 83, no. 2, p. 587, 2011.

[80] S. F. Swallen, K. L. Kearns, M. K. Mapes, Y. S. Kim, R. J. McMahon, M. D. Ediger, T. Wu, L. Yu, and S. Satija, "Organic glasses with exceptional thermodynamic and kinetic stability," *Science*, vol. 315, no. 5810, pp. 353–356, 2007.

[81] L. Berthier, P. Charbonneau, E. Flenner, and F. Zamponi, "Origin of ultrastability in vapor-deposited glasses," *Physical review letters*, vol. 119, no. 18, p. 188002, 2017.

[82] L. Yu, "Surface mobility of molecular glasses and its importance in physical stability," *Advanced drug delivery reviews*, vol. 100, pp. 3–9, 2016.

[83] Y. Qiu, L. W. Antony, J. J. de Pablo, and M. Ediger, "Photostability can be significantly modulated by molecular packing in glasses," *Journal of the American Chemical Society*, vol. 138, no. 35, pp. 11282–11289, 2016.

[84] H. Yu, M. Tylinski, A. Guiseppi-Elie, M. Ediger, and R. Richert, "Suppression of β relaxation in vapor-deposited ultrastable glasses," *Physical review letters*, vol. 115, no. 18, p. 185501, 2015.

[85] H.-B. Yu, Y. Luo, and K. Samwer, "Ultrastable metallic glass," *Advanced Materials*, vol. 25, no. 41, pp. 5904–5908, 2013.

[86] I. Lyubimov, M. D. Ediger, and J. J. de Pablo, "Model vapor-deposited glasses: Growth front and composition effects," *The Journal of chemical physics*, vol. 139, no. 14, p. 144505, 2013.

[87] I. Lyubimov, L. Antony, D. M. Walters, D. Rodney, M. Ediger, and J. J. de Pablo, "Orientational anisotropy in simulated vapor-deposited molecular glasses," *The Journal of chemical physics*, vol. 143, no. 9, p. 094502, 2015.

[88] D. Gazzillo and G. Pastore, "Equation of state for symmetric non-additive hard-sphere fluids: An approximate analytic expression and new monte carlo results," *Chemical Physics Letters*, vol. 159, no. 4, pp. 388–392, 1989.

[89] T. S. Grigera and G. Parisi, "Fast monte carlo algorithm for supercooled soft spheres," *Physical Review E*, vol. 63, no. 4, p. 045102, 2001.

[90] A. Ninarello, L. Berthier, and D. Coslovich, "Models and algorithms for the next generation of glass transition studies," *Physical Review X*, vol. 7, no. 2, p. 021039, 2017.

[91] L. Berthier, D. Coslovich, A. Ninarello, and M. Ozawa, "Equilibrium sampling of hard spheres up to the jamming density and beyond," *Physical review letters*, vol. 116, no. 23, p. 238002, 2016.

[92] L. Berthier, P. Charbonneau, D. Coslovich, A. Ninarello, M. Ozawa, and S. Yaida, "Configurational entropy measurements in extremely supercooled liquids that break the glass ceiling," *Proceedings of the National Academy of Sciences*, p. 201706860, 2017.

[93] A. D. Parmar, M. Ozawa, and L. Berthier, "Ultrastable metallic glasses in silico," *Physical Review Letters*, vol. 125, no. 8, p. 085505, 2020.

[94] P.-H. Lin, I. Lyubimov, L. Yu, M. Ediger, and J. J. de Pablo, "Molecular modeling of vapor-deposited polymer glasses," *The Journal of Chemical Physics*, vol. 140, no. 20, p. 204504, 2014.

[95] P. Leishangthem, A. D. Parmar, and S. Sastry, "The yielding transition in amorphous solids under oscillatory shear deformation," *Nature communications*, vol. 8, p. 14653, 2017.

[96] P. Das, A. D. Parmar, and S. Sastry, "Annealing glasses by cyclic shear deformation," *arXiv preprint arXiv:1805.12476*, 2018.

[97] S. Duane, A. Kennedy, B. J. Pendleton, and D. Roweth, "Hybrid monte carlo," *Physics Letters B*, vol. 195, no. 2, pp. 216 – 222, 1987.

[98] M. van Hecke, "Jamming of soft particles: geometry, mechanics, scaling and isostaticity," *Journal of Physics: Condensed Matter*, vol. 22, no. 3, p. 033101, 2009.

[99] J. D. Bernal, "A geometrical approach to the structure of liquids," *Nature*, vol. 183, no. 4655, pp. 141–147, 1959.

[100] A. J. Liu and S. R. Nagel, "Jamming is not just cool any more," *Nature*, vol. 396, no. 6706, pp. 21–22, 1998.

[101] T. C. Hales, "A proof of the kepler conjecture," *Annals of mathematics*, vol. 162, no. 3, pp. 1065–1185, 2005.

[102] C. S. OâĂŹHern, L. E. Silbert, A. J. Liu, and S. R. Nagel, "Jamming at zero temperature and zero applied stress: The epitome of disorder," *Physical Review E*, vol. 68, no. 1, p. 011306, 2003.

[103] P. Chaudhuri, L. Berthier, and S. Sastry, "Jamming transitions in amorphous packings of frictionless spheres occur over a continuous range of volume fractions," *Physical review letters*, vol. 104, no. 16, p. 165701, 2010.

[104] M. Ozawa, T. Kuroiwa, A. Ikeda, and K. Miyazaki, "Jamming transition and inherent structures of hard spheres and disks," *Physical review letters*, vol. 109, no. 20, p. 205701, 2012.

[105] J. C. Maxwell, "L. on the calculation of the equilibrium and stiffness of frames," *The London, Edinburgh, and Dublin Philosophical Magazine and Journal of Science*, vol. 27, no. 182, pp. 294–299, 1864.

[106] M. Cates, J. Wittmer, J.-P. Bouchaud, and P. Claudin, "Jamming, force chains, and fragile matter," *Physical review letters*, vol. 81, no. 9, p. 1841, 1998.

[107] D. Bi, J. Zhang, B. Chakraborty, and R. Behringer, "Jamming by shear," *Nature*, vol. 480, no. 7377, pp. 355–358, 2011.

[108] Y. Zhao, J. Barés, H. Zheng, J. E. Socolar, R. P. Behringer, *et al.*, "Shear-jammed, fragile, and steady states in homogeneously strained granular materials," *Physical review letters*, vol. 123, no. 15, p. 158001, 2019.

[109] H. A. Vinutha and S. Sastry, "Force networks and jamming in shear-deformed sphere packings," *Physical Review E*, vol. 99, no. 1, p. 012123, 2019.

[110] H. A. Vinutha and S. Sastry, "Disentangling the role of structure and friction in shear jamming," *Nature Physics*, vol. 12, no. 6, p. 578, 2016.

[111] N. Kumar and S. Luding, "Memory of jamming–multiscale models for soft and granular matter," *Granular Matter*, vol. 18, no. 3, p. 58, 2016.

[112] V. Babu, D. Pan, Y. Jin, B. Chakraborty, and S. Sastry, "Dilatancy, shear jamming, and a generalized jamming phase diagram of frictionless sphere packings," *Soft Matter*, vol. 17, no. 11, pp. 3121–3127, 2021.

[113] M. L. Falk and J. S. Langer, "Dynamics of viscoplastic deformation in amorphous solids," *Physical Review E*, vol. 57, no. 6, p. 7192, 1998.

[114] C. E. Maloney and A. Lemaître, "Amorphous systems in athermal, quasistatic shear," *Physical Review E*, vol. 74, no. 1, p. 016118, 2006.

[115] V. Chikkadi and P. Schall, "Nonaffine measures of particle displacements in sheared colloidal glasses," *Physical Review E*, vol. 85, no. 3, p. 031402, 2012.

[116] M. L. Falk and J. S. Langer, "Deformation and failure of amorphous, solidlike materials," *Annu. Rev. Condens. Matter Phys.*, vol. 2, no. 1, pp. 353–373, 2011.

[117] J. D. Eshelby, "The determination of the elastic field of an ellipsoidal inclusion, and related problems," *Proceedings of the royal society of London. Series A. Mathematical and physical sciences*, vol. 241, no. 1226, pp. 376–396, 1957.

[118] G. Picard, A. Ajdari, F. Lequeux, and L. Bocquet, "Elastic consequences of a single plastic event: A step towards the microscopic modeling of the flow of yield stress fluids," *The European Physical Journal E*, vol. 15, no. 4, pp. 371–381, 2004.

[119] G. Parisi, I. Procaccia, C. Rainone, and M. Singh, "Shear bands as manifestation of a criticality in yielding amorphous solids," *Proceedings of the National Academy of Sciences*, vol. 114, no. 22, pp. 5577–5582, 2017.

[120] A. Wisitsorasak and P. G. Wolynes, "On the strength of glasses," *Proceedings of the National Academy of Sciences*, vol. 109, pp. 16068–16072, 2012.

[121] D. Fiocco, G. Foffi, and S. Sastry, "Oscillatory athermal quasistatic deformation of a model glass," *Phys. Rev. E*, vol. 88, p. 020301, Aug 2013.

[122] I. Regev, J. Weber, C. Reichhardt, K. A. Dahmen, and T. Lookman, "Reversibility and criticality in amorphous solids," *Nature communications*, vol. 6, p. 8805, 2015.

[123] J. Lin, T. Gueudré, A. Rosso, and M. Wyart, "Criticality in the approach to failure in amorphous solids," *Physical review letters*, vol. 115, no. 16, p. 168001, 2015.

[124] T. Kawasaki and L. Berthier, "Macroscopic yielding in jammed solids is accompanied by a nonequilibrium first-order transition in particle trajectories," *Physical Review E*, vol. 94, no. 2, p. 022615, 2016.

[125] P. K. Jaiswal, I. Procaccia, C. Rainone, and M. Singh, "Mechanical yield in amorphous solids: A first-order phase transition," *Physical review letters*, vol. 116, no. 8, p. 085501, 2016.

[126] I. Procaccia, C. Rainone, and M. Singh, "Mechanical failure in amorphous solids: Scale-free spinodal criticality," *Physical Review E*, vol. 96, no. 3, p. 032907, 2017.

[127] P. Urbani and F. Zamponi, "Shear yielding and shear jamming of dense hard sphere glasses," *Physical review letters*, vol. 118, no. 3, p. 038001, 2017.

[128] G. P. Shrivastav, P. Chaudhuri, and J. Horbach, "Yielding of glass under shear: A directed percolation transition precedes shear-band formation," *Physical Review E*, vol. 94, no. 4, p. 042605, 2016.

[129] F. Varnik, L. Bocquet, and J.-L. Barrat, "A study of the static yield stress in a binary lennard-jones glass," *The Journal of chemical physics*, vol. 120, no. 6, pp. 2788–2801, 2004.

[130] H. Bhaumik, G. Foffi, and S. Sastry, "The role of annealing in determining the yielding behavior of glasses under cyclic shear deformation," *Proceedings of the National Academy of Sciences*, vol. 118, no. 16, 2021.

[131] M. Ozawa, L. Berthier, G. Biroli, A. Rosso, and G. Tarjus, "Random critical point separates brittle and ductile yielding transitions in amorphous materials," *Proceedings of the National Academy of Sciences*, vol. 115, pp. 6656–6661, June 2018.

[132] K. Martens, L. Bocquet, and J.-L. Barrat, "Spontaneous formation of permanent shear bands in a mesoscopic model of flowing disordered matter," *Soft Matter*, vol. 8, no. 15, pp. 4197–4205, 2012.

[133] S. Sastry, "Models for the yielding behavior of amorphous solids," *Phys. Rev. Lett.*, vol. 126, p. 255501, Jun 2021.

[134] A. D. Parmar, S. Kumar, and S. Sastry, "Strain localization above the yielding point in cyclically deformed glasses," *Physical Review X*, vol. 9, no. 2, p. 021018, 2019.

[135] H. Bhaumik, G. Foffi, and S. Sastry, "Avalanches and structural change in cyclically sheared silica glass," *arXiv preprint arXiv:2108.07469*, 2021.

[136] D. Fiocco, G. Foffi, and S. Sastry, "Oscillatory athermal quasistatic deformation of a model glass," *Physical Review E*, vol. 88, no. 2, p. 020301, 2013.

[137] D. Mollison, "Spatial contact models for ecological and epidemic spread," *Journal of the Royal Statistical Society: Series B (Methodological)*, vol. 39, no. 3, pp. 283–313, 1977.

[138] D. Pine, J. P. Gollub, J. Brady, and A. Leshansky, "Chaos and threshold for irreversibility in sheared suspensions," *Nature*, vol. 438, no. 7070, p. 997, 2005.

[139] L. Corte, P. Chaikin, J. P. Gollub, and D. Pine, "Random organization in periodically driven systems," *Nature Physics*, vol. 4, no. 5, p. 420, 2008.

[140] G. I. Menon and S. Ramaswamy, "Universality class of the reversible-irreversible transition in sheared suspensions," *Physical Review E*, vol. 79, no. 6, p. 061108, 2009.

[141] E. Tjhung and L. Berthier, "Hyperuniform density fluctuations and diverging dynamic correlations in periodically driven colloidal suspensions," *Physical review letters*, vol. 114, no. 14, p. 148301, 2015.

[142] R. Mari, E. Bertin, and C. Nardini, "Absorbing phase transitions in systems with mediated interactions," *arXiv preprint arXiv:2105.15027*, 2021.

[143] R. Jeanneret and D. Bartolo, "Geometrically protected reversibility in hydrodynamic loschmidt-echo experiments," *Nature Communications*, vol. 5, no. 1, pp. 1–8, 2014.

[144] S. F. Edwards and R. Oakeshott, "Theory of powders," *Physica A: Statistical Mechanics and its Applications*, vol. 157, no. 3, pp. 1080–1090, 1989.

[145] J. B. Knight, C. G. Fandrich, C. N. Lau, H. M. Jaeger, and S. R. Nagel, "Density relaxation in a vibrated granular material," *Phys. Rev. E*, vol. 51, pp. 3957–3963, May 1995.

[146] E. R. Nowak, J. B. Knight, E. Ben-Naim, H. M. Jaeger, and S. R. Nagel, "Density Fluctuations In Vibrated Granular Materials," *Phys. Rev. E*, vol. 57, no. 2, pp. 1971–1982, 1998.

[147] K. Asencio, M. Acevedo, I. Zuriguel, and D. Maza, "Experimental study of ordering of hard cubes by shearing," *Physical review letters*, vol. 119, no. 22, p. 228002, 2017.

[148] A. Yu, X. An, R. Zou, R. Yang, and K. Kendall, "Self-assembly of particles for densest packing by mechanical vibration," *Physical review letters*, vol. 97, no. 26, p. 265501, 2006.

[149] D. J. Lacks and M. J. Osborne, "Energy landscape picture of overaging and rejuvenation in a sheared glass," *Physical review letters*, vol. 93, no. 25, p. 255501, 2004.

[150] D. Fiocco, G. Foffi, and S. Sastry, "Encoding of memory in sheared amorphous solids," *Physical review letters*, vol. 112, no. 2, p. 025702, 2014.

[151] M. Adhikari and S. Sastry, "Memory formation in cyclically deformed amorphous solids and sphere assemblies," *The European Physical Journal E*, vol. 41, no. 9, p. 105, 2018.

[152] C. E. Packard, E. R. Homer, N. Al-Aqeeli, and C. A. Schuh, "Cyclic hardening of metallic glasses under hertzian contacts: Experiments and stz dynamics simulations," *Philosophical Magazine*, vol. 90, no. 10, pp. 1373–1390, 2010.

[153] C. Deng and C. A. Schuh, "Atomistic mechanisms of cyclic hardening in metallic glass," *Applied Physics Letters*, vol. 100, no. 25, p. 251909, 2012.

[154] C. Scalliet and L. Berthier, "Rejuvenation and memory effects in a structural glass," *Physical review letters*, vol. 122, no. 25, p. 255502, 2019.

[155] P. Refregier, E. Vincent, J. Hammann, and M. Ocio, "Ageing phenomena in a spin-glass: effect of temperature changes below tg [154]," *Journal de Physique*, vol. 48, no. 9, pp. 1533–1539, 1987.

[156] J. H. Schmertmann, "The mechanical aging of soils," *Journal of Geotechnical Engineering*, vol. 117, no. 9, pp. 1288–1330, 1991.

[157] F. Myers, M. FA, C. FC, and S. SS, "Mechanically enhanced aging of glassy polymers.," 1976.

[158] T. Bennin, E. Xing, J. Ricci, and M. Ediger, "Rejuvenation versus overaging: The effect of cyclic loading/unloading on the segmental dynamics of poly (methyl methacrylate) glasses," *Macromolecules*, vol. 53, no. 19, pp. 8467–8475, 2020.

[159] V. Viasnoff, S. Jurine, and F. Lequeux, "How are colloidal suspensions that age rejuvenated by strain application?," *Faraday Discussions*, vol. 123, pp. 253–266, 2003.

[160] W. Kob and H. C. Andersen, "Testing mode-coupling theory for a supercooled binary lennard-jones mixture i: The van hove correlation function," *Physical Review E*, vol. 51, no. 5, p. 4626, 1995.

[161] D. J. Durian, "Foam mechanics at the bubble scale," *Physical review letters*, vol. 75, no. 26, p. 4780, 1995.

[162] L. Berthier and T. A. Witten, "Compressing nearly hard sphere fluids increases glass fragility," *EPL (Europhysics Letters)*, vol. 86, no. 1, p. 10001, 2009.

[163] E. Bitzek, P. Koskinen, F. Gähler, M. Moseler, and P. Gumbsch, "Structural relaxation made simple," *Physical review letters*, vol. 97, no. 17, p. 170201, 2006.

[164] A. Lees and S. Edwards, "The computer study of transport processes under extreme conditions," *Journal of Physics C: Solid State Physics*, vol. 5, no. 15, p. 1921, 1972.

[165] W. G. Hoover, "Canonical dynamics: Equilibrium phase-space distributions," *Physical review A*, vol. 31, no. 3, p. 1695, 1985.

[166] G. J. Martyna, M. L. Klein, and M. Tuckerman, "Nosé–hoover chains: The canonical ensemble via continuous dynamics," *The Journal of chemical physics*, vol. 97, no. 4, pp. 2635–2643, 1992.

[167] T. S. Ingebrigtsen, J. C. Dyre, T. B. Schrøder, and C. P. Royall, "Crystallization instability in glass-forming mixtures," *Phys. Rev. X*, vol. 9, p. 031016, Aug 2019.

[168] S. Auer and D. Frenkel, "Quantitative prediction of crystal-nucleation rates for spherical colloids: A computational approach," *Annual Review of Physical Chemistry*, vol. 55, no. 1, pp. 333–361, 2004.

[169] W. G. Hoover, A. J. Ladd, R. B. Hickman, and B. L. Holian, "Bulk viscosity via nonequilibrium and equilibrium molecular dynamics," *Physical Review A*, vol. 21, no. 5, p. 1756, 1980.

[170] D. J. Evans and G. P. Morriss, "Nonlinear-response theory for steady planar couette flow," *Phys. Rev. A*, vol. 30, pp. 1528–1530, Sep 1984.

[171] P. J. Daivis and B. Todd, "A simple, direct derivation and proof of the validity of the sllod equations of motion for generalized homogeneous flows," *The Journal of chemical physics*, vol. 124, no. 19, p. 194103, 2006.

[172] K. B. Lipkowitz and D. B. Boyd, "Books published on the topics of computational chemistry," *Reviews in Computational Chemistry, Volume 17*, pp. 255–357, 2001.

[173] S. Karmakar, C. Dasgupta, and S. Sastry, "Short-time beta relaxation in glass-forming liquids is cooperative in nature," *Physical review letters*, vol. 116, no. 8, p. 085701, 2016.

[174] F. Sciortino, W. Kob, and P. Tartaglia, "Inherent structure entropy of supercooled liquids," *Phys. Rev. Lett.*, vol. 83, pp. 3214–3217, Oct 1999.

[175] S. Sastry, "Onset temperature of slow dynamics in glass forming liquids," *PhysChemComm*, vol. 3, pp. 79–83, 2000.

[176] F. Sciortino, "Potential energy landscape description of supercooled liquids and glasses," *Journal of Statistical Mechanics: Theory and Experiment*, vol. 2005, p. P05015, may 2005.

[177] T. Mason, J. Bibette, and D. Weitz, "Yielding and flow of monodisperse emulsions," *Journal of Colloid and Interface Science*, vol. 179, no. 2, pp. 439–448, 1996.

[178] E. Brown and H. M. Jaeger, "The role of dilation and confining stresses in shear thickening of dense suspensions," *Journal of Rheology*, vol. 56, no. 4, pp. 875–923, 2012.

[179] I. R. Peters, S. Majumdar, and H. M. Jaeger, "Direct observation of dynamic shear jamming in dense suspensions," *Nature*, vol. 532, no. 7598, p. 214, 2016.

[180] R. Mari, R. Seto, J. F. Morris, and M. M. Denn, "Shear thickening, frictionless and frictional rheologies in non-brownian suspensions," *Journal of Rheology*, vol. 58, no. 6, pp. 1693–1724, 2014.

[181] M. Wyart and M. Cates, "Discontinuous shear thickening without inertia in dense non-brownian suspensions," *Physical review letters*, vol. 112, no. 9, p. 098302, 2014.

[182] A. J. Liu and S. R. Nagel, "The jamming transition and the marginally jammed solid," *Annu. Rev. Condens. Matter Phys.*, vol. 1, no. 1, pp. 347–369, 2010.

[183] J. Ren, J. A. Dijksman, and R. P. Behringer, "Reynolds pressure and relaxation in a sheared granular system," *Physical review letters*, vol. 110, no. 1, p. 018302, 2013.

[184] C. Coulais, A. Seguin, and O. Dauchot, "Shear modulus and dilatancy softening in granular packings above jamming," *Physical review letters*, vol. 113, no. 19, p. 198001, 2014.

[185] M. Baity-Jesi, C. P. Goodrich, A. J. Liu, S. R. Nagel, and J. P. Sethna, "Emergent so (3) symmetry of the frictionless shear jamming transition," *J. Stat. Phys.*, pp. 1–14, 2016.

[186] R. P. Behringer and B. Chakraborty, "The physics of jamming for granular materials: a review," *Reports on Progress in Physics*, vol. 82, no. 1, p. 012601, 2018.

[187] H. A. Vinutha and S. Sastry, "Geometric aspects of shear jamming induced by deformation of frictionless sphere packings," *Journal of Statistical Mechanics: Theory and Experiment*, vol. 2016, no. 9, p. 094002, 2016.

[188] S. Karmakar, E. Lerner, and I. Procaccia, "Statistical physics of the yielding transition in amorphous solids," *Physical Review E*, vol. 82, no. 5, p. 055103, 2010.

[189] Y. Jin, P. Urbani, F. Zamponi, and H. Yoshino, "A stability-reversibility map unifies elasticity, plasticity, yielding, and jamming in hard sphere glasses," *Science advances*, vol. 4, no. 12, p. eaat6387, 2018.

[190] T. Divoux, M. A. Fardin, S. Manneville, and S. Lerouge, "Shear banding of complex fluids," *Annual Review of Fluid Mechanics*, vol. 48, pp. 81–103, 2016.

[191] D. Bonn, M. M. Denn, L. Berthier, T. Divoux, and S. Manneville, "Yield stress materials in soft condensed matter," *Reviews of Modern Physics*, vol. 89, no. 3, p. 035005, 2017.

[192] V. V. Vasisht, G. Roberts, and E. Del Gado, "Emergence and persistence of flow inhomogeneities in the yielding and fluidization of dense soft solids," 2017.

[193] E. A. Jagla, F. P. Landes, and A. Rosso, "Viscoelastic effects in avalanche dynamics: A key to earthquake statistics," *Physical review letters*, vol. 112, no. 17, p. 174301, 2014.

[194] J. T. Uhl, S. Pathak, D. Schorlemmer, X. Liu, R. Swindeman, B. A. Brinkman, M. LeBlanc, G. Tsekenis, N. Friedman, R. Behringer, *et al.*, "Universal quake statistics: From compressed nanocrystals to earthquakes," *Scientific reports*, vol. 5, p. 16493, 2015.

[195] D. J. Jerolmack and K. E. Daniels, "Viewing earthâĂŹs surface as a soft-matter landscape," *Nature Reviews Physics*, pp. 1–15, 2019.

[196] Y. Sun, A. Concustell, and A. L. Greer, "Thermomechanical processing of metallic glasses: extending the range of the glassy state," *Nature Reviews Materials*, vol. 1, no. 9, p. 16039, 2016.

[197] N. V. Priezjev, "The effect of cryogenic thermal cycling on aging, rejuvenation, and mechanical properties of metallic glasses," *Journal of Non-Crystalline Solids*, vol. 503, pp. 131–138, 2019.

[198] C. Ness, R. Mari, and M. E. Cates, "Shaken and stirred: Random organization reduces viscosity and dissipation in granular suspensions," *Science advances*, vol. 4, no. 3, p. eaar3296, 2018.

[199] C. F. Schreck, R. S. Hoy, M. D. Shattuck, and C. S. OâĂŹHern, "Particle-scale reversibility in athermal particulate media below jamming," *Physical Review E*, vol. 88, no. 5, p. 052205, 2013.

[200] I. Regev, T. Lookman, and C. Reichhardt, "Onset of irreversibility and chaos in amorphous solids under periodic shear," *Physical Review E*, vol. 88, no. 6, p. 062401, 2013.

[201] N. C. Keim, J. D. Paulsen, Z. Zeravcic, S. Sastry, and S. R. Nagel, "Memory formation in matter," *Reviews of Modern Physics*, vol. 91, no. 3, p. 035002, 2019.

[202] J. R. Royer and P. M. Chaikin, "Precisely cyclic sand: Self-organization of periodically sheared frictional grains," *Proceedings of the National Academy of Sciences*, vol. 112, no. 1, pp. 49–53, 2015.

[203] M. O. Lavrentovich, A. J. Liu, and S. R. Nagel, "Period proliferation in periodic states in cyclically sheared jammed solids," *Physical Review E*, vol. 96, no. 2, p. 020101, 2017.

[204] J. D. Paulsen, N. C. Keim, and S. R. Nagel, "Multiple transient memories in experiments on sheared non-brownian suspensions," *Physical review letters*, vol. 113, no. 6, p. 068301, 2014.

[205] N. C. Keim and S. R. Nagel, "Generic transient memory formation in disordered systems with noise," *Physical review letters*, vol. 107, no. 1, p. 010603, 2011.

[206] N. V. Priezjev, "Heterogeneous relaxation dynamics in amorphous materials under cyclic loading," *Phys. Rev. E*, vol. 87, p. 052302, May 2013.

[207] S. Dagois-Bohy, E. Somfai, B. P. Tighe, and M. van Hecke, "Softening and yielding of soft glassy materials," *Soft matter*, vol. 13, no. 47, pp. 9036–9045, 2017.

[208] K. Nagasawa, K. Miyazaki, and T. Kawasaki, "Classification of the reversibleâĂŞirreversible transitions in particle trajectories across the jamming transition point," *Soft Matter*, vol. 15, pp. 7557–7566, 2019.

[209] L. Berthier and T. A. Witten, "Glass transition of dense fluids of hard and compressible spheres," *Physical Review E*, vol. 80, no. 2, p. 021502, 2009.

[210] N. Kumar, S. Luding, and V. Magnanimo, "Macroscopic model with anisotropy based on micro–macro information," *Acta Mechanica*, vol. 225, pp. 2319–2343, Aug 2014.

[211] M. Wyart, S. R. Nagel, and T. A. Witten, "Geometric origin of excess low-frequency vibrational modes in weakly connected amorphous solids," *EPL (Europhysics Letters)*, vol. 72, no. 3, p. 486, 2005.

[212] J. Zhang, T. Majmudar, A. Tordesillas, and R. Behringer, "Statistical properties of a 2d granular material subjected to cyclic shear," *Granular Matter*, vol. 12, no. 2, pp. 159–172, 2010.

[213] M. Otsuki and H. Hayakawa, "Shear jamming, discontinuous shear thickening, and fragile state in dry granular materials under oscillatory shear," *arXiv preprint arXiv:1810.03846*, 2018.

[214] D. Ishima and H. Hayakawa, "Dilatancy and compaction in a pressure control granular system under an oscillatory shear," *arXiv preprint arXiv:1902.04759*, 2019.

[215] R. Möbius and C. Heussinger, "(ir) reversibility in dense granular systems driven by oscillating forces," *Soft matter*, vol. 10, no. 27, pp. 4806–4812, 2014.

[216] M. M. Bandi, H. G. E. Hentschel, I. Procaccia, S. Roy, and J. Zylberg, "Training, memory and universal scaling in amorphous frictional granular matter," *EPL (Europhysics Letters)*, vol. 122, p. 38003, jun 2018.

[217] C. Ness and M. E. Cates, "Absorbing-state transitions in granular materials close to jamming," *arXiv preprint arXiv:2001.10228*, 2020.

[218] M. Mungan, S. Sastry, K. Dahmen, and I. Regev, "Networks and hierarchies: How amorphous materials learn to remember," *Physical review letters*, vol. 123, no. 17, p. 178002, 2019.

[219] H. Vinutha and S. Sastry, "Force networks and jamming in shear deformed sphere packings," *arXiv preprint arXiv:1705.10109*, 2017.

[220] I. Regev and T. Lookman, "Yield in amorphous solids: The ant in the energy landscape labyrinth," *arXiv preprint arXiv:1701.04020*, 2017.

[221] M. Ediger and P. Harrowell, "Perspective: Supercooled liquids and glasses," *The Journal of Chemical Physics*, vol. 137, no. 8, p. 080901, 2012.

[222] L. Santen and W. Krauth, "Absence of thermodynamic phase transition in a model glass former," *Nature*, vol. 405, no. 6786, p. 550, 2000.

[223] W. Kob, C. Brangian, T. Stühn, and R. Yamamoto, "Equilibrating glassy systems with parallel tempering," in *Computer Simulation Studies in Condensed-Matter Physics XIII*, pp. 153–166, Springer, 2001.

[224] W. G. T. Kranendonk and D. Frenkel, "Computer simulation of solid-liquid coexistence in binary hard-sphere mixtures," *Journal of Physics: Condensed Matter*, vol. 1, pp. 7735–7739, oct 1989.

[225] Q. Yan, T. S. Jain, and J. J. De Pablo, "Density-of-states Monte Carlo simulation of a binary glass," *Phys. Rev. Lett.*, vol. 92, no. 23, pp. 1–4, 2004.

[226] K. Hukushima and K. Nemoto, "Exchange monte carlo method and application to spin glass simulations," *Journal of the Physical Society of Japan*, vol. 65, no. 6, pp. 1604–1608, 1996.

[227] S. Singh, M. Ediger, and J. J. De Pablo, "Ultrastable glasses from in silico vapour deposition," *Nature materials*, vol. 12, no. 2, p. 139, 2013.

[228] R. Gutiérrez, S. Karmakar, Y. G. Pollack, and I. Procaccia, "The static lengthscale characterizing the glass transition at lower temperatures," *EPL (Europhysics Letters)*, vol. 111, p. 56009, sep 2015.

[229] C. Brito, E. Lerner, and M. Wyart, "Theory for swap acceleration near the glass and jamming transitions," *arXiv preprint arXiv:1801.03796*, 2018.

[230] W.-T. Yeh, M. Ozawa, K. Miyazaki, and L. Berthier, "Glass stability changes the nature of yielding under oscillatory shear," *arXiv preprint arXiv:1911.12951*, 2019.

[231] N. V. Priezjev, "Molecular dynamics simulations of the mechanical annealing process in metallic glasses: Effects of strain amplitude and temperature," *Journal of Non-Crystalline Solids*, vol. 479, pp. 42–48, 2018.

[232] K. M. Salerno and M. O. Robbins, "Effect of inertia on sheared disordered solids: Critical scaling of avalanches in two and three dimensions," *Physical Review E*, vol. 88, no. 6, p. 062206, 2013.

[233] C. Liu, E. E. Ferrero, F. Puosi, J.-L. Barrat, and K. Martens, "Driving rate dependence of avalanche statistics and shapes at the yielding transition," *Physical review letters*, vol. 116, no. 6, p. 065501, 2016.

[234] N. V. Priezjev, "Accelerated relaxation in disordered solids under cyclic loading with alternating shear orientation," *Journal of Non-Crystalline Solids*, vol. 525, p. 119683, 2019.

[235] V. Lubchenko and P. G. Wolynes, "Barrier softening near the onset of nonactivated transport in supercooled liquids: Implications for establishing detailed connection between thermodynamic and kinetic anomalies in supercooled liquids," *The Journal of chemical physics*, vol. 119, no. 17, pp. 9088–9105, 2003.

[236] V. Lubchenko and P. G. Wolynes, "Theory of aging in structural glasses," *The Journal of chemical physics*, vol. 121, no. 7, pp. 2852–2865, 2004.

[237] S. Plimpton, "Fast parallel algorithms for short-range molecular dynamics," *Journal of computational physics*, vol. 117, no. 1, pp. 1–19, 1995.

[238] G. B. McKenna, "Mechanical rejuvenation in polymer glasses: factor fallacy ?," *J. Phys. Condens. Matter*, vol. 15, p. S737, 2003.

[239] M. Nicodemi and A. Coniglio, "Aging in out-of-equilibrium dynamics of models for granular media," *Phys. Rev. Lett.*, vol. 82, pp. 916–919, Feb 1999.

[240] P. Das and S. Sastry, "Crossover in dynamics in the kob-andersen binary mixture glass-forming liquid," *Journal of Non-Crystalline Solids: X*, p. 100098, 2022.

[241] V. V. Krishnan, K. Ramola, and S. Karmakar, "Annealing effects of multidirectional oscillatory shear in model glass formers," *arXiv preprint arXiv:2112.07412*, 2021.

[242] M. Adhikari, M. Mungan, and S. Sastry, "Yielding behavior of glasses under asymmetric cyclic deformation," *arXiv preprint arXiv:2201.06535*, 2022.

[243] N. C. Keim, J. D. Paulsen, and S. R. Nagel, "Multiple transient memories in sheared suspensions: Robustness, structure, and routes to plasticity," *Physical Review E*, vol. 88, no. 3, p. 032306, 2013.

[244] C. Reichhardt and C. J. Reichhardt, "Jamming, fragility and pinning phenomena in superconducting vortex systems," *Scientific Reports*, vol. 10, no. 1, pp. 1–11, 2020.

[245] N. V. Priezjev, "Slow relaxation dynamics in binary glasses during stress-controlled, tension-compression cyclic loading," *Computational Materials Science*, vol. 153, pp. 235–240, 2018.

[246] Y. G. Chung and D. J. Lacks, "Sheared polymer glass and the question of mechanical rejuvenation," *The Journal of chemical physics*, vol. 136, no. 12, p. 124907, 2012.

[247] A. V. Lyulin and M. Michels, "Time scales and mechanisms of relaxation in the energy landscape of polymer glass under deformation: direct atomistic modeling," *Physical review letters*, vol. 99, no. 8, p. 085504, 2007.

[248] K. Lad, N. Jakse, and A. Pasturel, "Signatures of fragile-to-strong transition in a binary metallic glass-forming liquid," *The Journal of chemical physics*, vol. 136, no. 10, p. 104509, 2012.

[249] C. Zhang, L. Hu, Y. Yue, and J. C. Mauro, "Fragile-to-strong transition in metallic glass-forming liquids," *The Journal of chemical physics*, vol. 133, no. 1, p. 014508, 2010.

[250] R. Alvarez-Donado, S. Cajahuaringa, and A. Antonelli, "Revisiting the fragile-to-strong crossover in metallic glass-forming liquids: Application to cu x zr x al 100- 2 x alloy," *Physical Review Materials*, vol. 3, no. 8, p. 085601, 2019.

[251] C. Zhou, L. Hu, Q. Sun, H. Zheng, C. Zhang, and Y. Yue, "Structural evolution during fragile-to-strong transition in cuzr (al) glass-forming liquids," *The Journal of chemical physics*, vol. 142, no. 6, p. 064508, 2015.

[252] C. A. Angell, "Strong and fragile liquids," *Relaxation in Complex Systems, K. L. Ngai and G. B. Write (eds)*, pp. 3–12, 1985.

[253] L.-M. Martinez and C. Angell, "A thermodynamic connection to the fragility of glass-forming liquids," *Nature*, vol. 410, no. 6829, pp. 663–667, 2001.

[254] A. L. Greer, K. F. Kelton, and S. Sastry, *Fragility of Glass-Forming Liquids*. Hindustan Book Agency, New Delhi, 2013.

[255] H. E. Stanley, *Liquid Polymorphism*, vol. 152. Wiley Online Library, 2013.

[256] S. Wei, F. Yang, J. Bednarcik, and et al., "LiquidâĂŞliquid transition in a strong bulk metallic glass-forming liquid," *Nature communications*, vol. 4, p. 2083, 2013.

[257] S. V. Sukhomlinov and M. H. MÃijser, "Anomalous system-size dependence of properties at the fragile-to-strong transition in a bulk-metallic-glass forming melt," *Computational Materials Science*, vol. 156, pp. 129–134, 2019.

[258] E. Flenner and G. Szamel, "Dynamic heterogeneities above and below the mode-coupling temperature: Evidence of a dynamic crossover," *Journal of Chemical Physics*, vol. 138, p. 12A523, 2013.

[259] E. Flenner and G. Szamel, "Hybrid monte carlo simulation of a glass-forming binary mixture," *Phys. Rev. E*, vol. 73, p. 061505, Jun 2006.

[260] P. Rein ten Wolde, M. J. Ruiz-Montero, and D. Frenkel, "Numerical calculation of the rate of crystal nucleation in a lennard-jones system at moderate undercooling," *The Journal of chemical physics*, vol. 104, no. 24, pp. 9932–9947, 1996.

[261] F. Alvarez, A. Alegra, and J. Colmenero, "Relationship between the time-domain kohlrausch-williams-watts and frequency-domain havriliak-negami relaxation functions," *Physical Review B*, vol. 44, no. 14, p. 7306, 1991.

[262] S. F. Swallen and M. Ediger, "Self-diffusion of the amorphous pharmaceutical indomethacin near t g," *Soft Matter*, vol. 7, no. 21, pp. 10339–10344, 2011.

[263] S. F. Swallen, K. Traynor, R. J. McMahon, M. Ediger, and T. E. Mates, "Self-diffusion of supercooled tris-naphthylbenzene," *The Journal of Physical Chemistry B*, vol. 113, no. 14, pp. 4600–4608, 2009.

[264] M. D. Ediger, "Spatially heterogeneous dynamics in supercooled liquids," *Annual Review of Physical Chemistry*, vol. 51, no. 1, pp. 99–128, 2000.

[265] A. T. Ogielski, "Dynamics of three-dimensional ising spin glasses in thermal equilibrium," *Phys. Rev. B*, vol. 32, pp. 7384–7398, Dec 1985.

[266] S. Sastry, P. G. Debenedetti, and F. H. Stillinger, "Signatures of distinct dynamical regimes in the energy landscape of a glass-forming liquid," *Nature*, vol. 393, no. 6685, p. 554, 1998.

[267] G. A. Appignanesi, J. A. Rodríguez Fris, R. A. Montani, and W. Kob, "Democratic particle motion for metabasin transitions in simple glass formers," *Phys. Rev. Lett.*, vol. 96, p. 057801, Feb 2006.

[268] S. Karmakar, C. Dasgupta, and S. Sastry, "Length scales in glass-forming liquids and related systems: a review," *Reports on Progress in Physics*, vol. 79, p. 016601, 2016.

[269] E. Rössler, "Indications for a change of diffusion mechanism in supercooled liquids," *Phys. Rev. Lett.*, vol. 65, pp. 1595–1598, Sep 1990.

[270] D. Thirumalai and R. D. Mountain, "Activated dynamics, loss of ergodicity, and transport in supercooled liquids," *Physical Review E*, vol. 47, no. 1, p. 479, 1993.

[271] F. H. Stillinger and J. A. Hodgdon, "Translation-rotation paradox for diffusion in fragile glass-forming liquids," *Physical review E*, vol. 50, no. 3, p. 2064, 1994.

[272] L. Andreozzi, A. Di Schino, M. Giordano, and D. Leporini, "A study of the debye-stokes-einstein law in supercooled fluids," *Journal of Physics: Condensed Matter*, vol. 8, no. 47, p. 9605, 1996.

[273] M. T. Cicerone and M. D. Ediger, "Enhanced translation of probe molecules in supercooled o-terphenyl: signature of spatially heterogeneous dynamics?," *The Journal of chemical physics*, vol. 104, no. 18, pp. 7210–7218, 1996.

[274] L. Berthier, D. Chandler, and J. P. Garrahan, "Length scale for the onset of fickian diffusion in supercooled liquids," *EPL (Europhysics Letters)*, vol. 69, no. 3, p. 320, 2004.

[275] L. Berthier, "Time and length scales in supercooled liquids," *Physical Review E*, vol. 69, no. 2, p. 020201, 2004.

[276] J. Kim and T. Keyes, "On the breakdown of the stokes- einstein law in supercooled liquids," *The Journal of Physical Chemistry B*, vol. 109, no. 45, pp. 21445–21448, 2005.

[277] S.-H. Chong and W. Kob, "Coupling and decoupling between translational and rotational dynamics in a supercooled molecular liquid," *Physical review letters*, vol. 102, no. 2, p. 025702, 2009.

[278] P. Charbonneau, Y. Jin, G. Parisi, and F. Zamponi, "Hopping and the stokes–einstein relation breakdown in simple glass formers," *Proceedings of the National Academy of Sciences*, vol. 111, no. 42, pp. 15025–15030, 2014.

[279] Q. Yan, T. S. Jain, and J. J. de Pablo, "Density-of-states monte carlo simulation of a binary glass," *Phys. Rev. Lett.*, vol. 92, p. 235701, Jun 2004.

[280] I. Saika-Voivod, F. Sciortino, and P. H. Poole, "Free energy and configurational entropy of liquid silica: Fragile-to-strong crossover and polyamorphism," *Phys. Rev. E*, vol. 69, p. 041503, Apr 2004.

[281] S. Sastry, "Liquid limits: Glass transition and liquid-gas spinodal boundaries of metastable liquids," *Phys. Rev. Lett.*, vol. 85, pp. 590–593, Jul 2000.

[282] C. A. Angell, K. L. Ngai, G. B. McKenna, P. F. McMillan, and S. W. Martin, "Relaxation in glassforming liquids and amorphous solids," *Journal of Applied Physics*, vol. 88, no. 6, p. 3113, 1998.

[283] S. Sengupta, *Investigations of the role of spatial dimensionality and interparticle interactions in model glass-formers.* PhD thesis, JNCASR, Bengaluru, India, Mar. 2013.

[284] K. Broderix, K. K. Bhattacharya, A. Cavagna, A. Zippelius, and I. Giardina, "Energy landscape of a lennard-jones liquid: Statistics of stationary points," *Phys. Rev. Lett.*, vol. 85, pp. 5360–5363, Dec 2000.

[285] L. Angelani, R. Di Leonardo, G. Ruocco, A. Scala, and F. Sciortino, "Saddles in the energy landscape probed by supercooled liquids," *Phys. Rev. Lett.*, vol. 85, pp. 5356–5359, Dec 2000.

[286] T. B. Schröder, S. Sastry, J. C. Dyre, and S. C. Glotzer, "Crossover to potential energy landscape dominated dynamics in a model glass-forming liquid," *The Journal of Chemical Physics*, vol. 112, no. 22, pp. 9834–9840, 2000.

[287] D. Coslovich, A. Ninarello, and L. Berthier, "A localization transition underlies the mode-coupling crossover of glasses," *SciPost Phys.*, vol. 7, p. 77, 2019.

[288] P. H. Handle and F. Sciortino, "Potential energy landscape of tip4p/2005 water," *The Journal of Chemical Physics*, vol. 148, no. 13, p. 134505, 2018.

[289] P. H. Handle and F. Sciortino, "The adam–gibbs relation and the tip4p/2005 model of water," *Molecular physics*, vol. 116, no. 21-22, pp. 3366–3371, 2018.

[290] L. Berthier, M. Ozawa, and C. Scalliet, "Configurational entropy of glass-forming liquids," *The Journal of Chemical Physics*, vol. 150, no. 16, p. 160902, 2019.

[291] A. Rinaldi, F. Sciortino, and P. Tartaglia, "Dynamics in a supercooled molecular liquid: Theory and simulations," *Phys. Rev. E*, vol. 63, p. 061210, May 2001.

[292] S.-H. Chong, S.-H. Chen, and F. Mallamace, "A possible scenario for the fragile-to-strong dynamic crossover predicted by the extended mode-coupling theory for glass transition," *Journal of Physics: Condensed Matter*, vol. 21, p. 504101, nov 2009.

[293] D. Coslovich, "Locally preferred structures and many-body static correlations in viscous liquids," *Phys. Rev. E*, vol. 83, p. 051505, May 2011.

[294] D. Krijgsman and S. Luding, "Simulating granular materials by energy minimization," *Computational particle mechanics*, vol. 3, no. 4, pp. 463–475, 2016.

[295] H. A. Vinutha, K. Ramola, B. Chakraborty, and S. Sastry, "Timescale divergence at the shear jamming transition," *Granular Matter*, vol. 22, no. 1, pp. 1–8, 2020.